



HAL
open science

Etude des mécanismes de génération des stries dans le procédé de découpe laser d'aciers

Koji Hirano

► **To cite this version:**

Koji Hirano. Etude des mécanismes de génération des stries dans le procédé de découpe laser d'aciers. Mécanique [physics.med-ph]. Arts et Métiers ParisTech, 2012. Français. NNT: . pastel-00751668

HAL Id: pastel-00751668

<https://pastel.hal.science/pastel-00751668>

Submitted on 14 Nov 2012

HAL is a multi-disciplinary open access archive for the deposit and dissemination of scientific research documents, whether they are published or not. The documents may come from teaching and research institutions in France or abroad, or from public or private research centers.

L'archive ouverte pluridisciplinaire **HAL**, est destinée au dépôt et à la diffusion de documents scientifiques de niveau recherche, publiés ou non, émanant des établissements d'enseignement et de recherche français ou étrangers, des laboratoires publics ou privés.

École doctorale n° 432 : SMI, Sciences des Métiers de l'Ingénieur

Doctorat ParisTech

THÈSE

pour obtenir le grade de docteur délivré par

l'École Nationale Supérieure d'Arts et Métiers

Spécialité " Mécanique - Matériaux "

présentée et soutenue publiquement par

Koji HIRANO

le 14 Septembre 2012

Study on striation generation process during laser cutting of steel

Directeur de thèse : **Rémy FABBRO**

Jury

Mme Simone MATTEI, Professeur, Université de Bourgogne
M. Alexander KAPLAN, Professeur, Université de Lulea, Suède
M. Marc MEDALE, Professeur, Université Aix-Marseille
M. El-Hachemi AMARA, Directeur de recherche, CDTA, Algérie
M. Francis BRIAND, Expert Procédés, Air Liquide Welding
M. Rémy FABBRO, Directeur de recherche, PIMM, CNRS/ Arts et Métiers ParisTech

Rapporteur
Rapporteur
Examineur
Examineur
Examineur
Examineur

**T
H
È
S
E**

Acknowledgments

First of all, I would like to thank the PIMM Laboratory at Arts et Métiers ParisTech and the Directors, M. Thierry BRETHERAU and M. Gilles REGNIER, who welcomed me to the laboratory for this PhD study.

I express my heartfelt thanks to the supervisor of this thesis, Rémy FABBRO (CNRS/Arts et Métiers ParisTech). Tremendous hours of discussion with him lead to important and original results of this study. Many fruitful ideas, suggestions, and sometimes critical comments, which were issued from his vast knowledge and experience, helped navigate this study in proper direction. I am sure that this three years' experience will also be really helpful for my ongoing career as a researcher.

I would like to thank Nippon Steel Corporation and relevant members who gave me this chance to study at Arts et Métiers ParisTech. I am really grateful to the company not only for the financial support to this research but also for constant cares during my two years' stay in Paris from 2009 to 2011.

It is a great honour for me that Prof. Simone MATTEI (University of Burgundy) and Prof. Alexander KAPLAN (Luleå University of Technology) accepted to read my thesis and to make a report as jury members of the defence. I am quite grateful to Prof. Marc MEDALE (Polytech' Marseille), Dr. El-Hachemi AMARA (Centre for Development of Advanced Technologies) and Dr. Francis BRIAND (Air Liquid Welding) for participating in the jury and examining my dissertation.

I would like to give my great thanks to Frédéric COSTE for his support in various experiments at the disc laser platform in PIMM. I am grateful also to other members of the laser team: Maryse MULLER, Matthieu SCHNEIDER, Kevin VERDIER, Corinne DUPUY, Emilie LE GUEN, Mariette NIVARD and Cyril GORNY, who supported me in preparing experimental instruments, operating experiments and analysing samples.

I deeply thank Dr. Francis BRIAND and his colleagues at Air Liquid Welding for performing an important comparative laser cutting experiment with their fibre and CO₂ lasers. My special thanks go to Petr YUDIN (Khristianovich Institute of Theoretical and Applied Mechanics; now at École Polytechnique Fédérale de Lausanne) for valuable discussion and instruction on visualisation technique of melt film dynamics on kerf fronts. I express my gratitude to Shun KOJIMA (PHOTRON LTD.) for technical support for use of a high speed video camera. I would like to give my sincere thanks to Dr. Laurent Limat (CNRA/Paris Diderot University) and his team members for useful discussion and their comments on dynamics of melt accumulations on kerf sides. I also convey my thanks to Dr. Ken-ichi Sugioka (Tohoku University) for helpful comments and advice for some aspects of fluid mechanics.

I would like to express my gratitude to those who helped me begin and perform numerical simulations: Prof. Marc MEDALE (Polytech' Marseille), Dr. Partick NAMY (SIMTEC), support team members at COMSOL France, Dr. Charline TOUVREY (CEA), and Maxim TROSHIN (Tomsk Polytechnic University). Although I could not include many results of numerical simulations in this thesis, their valuable support will serve me to develop this study further in terms of numerical simulations.

Members in Nippon Steel Corporation also helped me conduct this study. I am thankful to Hirofumi IMAI for discussion on experimental results, Masaomi YOSHIKAWA and members at the technical support section for analyses of cut samples, and Masato SUGIURA for useful advice on temperature measurement of melt surfaces.

I express my deep thanks to members at PIMM laboratory: Patrice PEYRE, Laurent BERTHE, Pascal AUBRY, Neila HFAIEDH, Béatrice ROULEAU, Anass NIFA, Elise GAY, Myriam GHARBI,

Jeremie GIRARDOT, Rezak MEZARI, Thierry MALOT, Yann ROUCHAUSSE, and all the other members at PIMM laboratory, not only for scientific discussion but also for relaxing daily conversations. Friendly and comfortable atmosphere of the laboratory makes my two years stay in Paris an unforgettable joyful memory.

Finally, I express my special thanks to my wife Emiko, who has supported strongly my life during this tough period, and to my parents, who constantly encouraged me back from Japan.

Contents

List of symbols	5
Chapter 1. Introduction	9
Chapter 2. Fundamental physical processes	15
2.1 Absorption	17
2.2 Heat conduction	21
2.3 Hydrodynamics	26
2.4 Coupled analytical models	31
2.5 Summary	32
Chapter 3. Review of theoretical studies on instability in melt ejection process	35
3.1 Model for oxygen laser cutting	37
3.2 Time dependent models for inert gas laser cutting	37
3.3 On origin of striations	40
3.4 Summary	42
Chapter 4. Experimental observations of striation generation process	43
4.1 Experimental setup	48
4.2 Observations of striation initiation from surface	54
4.3 Observations of downward development of striations	70
4.4 Summary	73
Chapter 5. Discussions	75
5.1 Inclination angle of kerf front	77
5.2 Instability in the central part (Hump generation)	78
5.3 Instability on kerf sides (Initiation of striations)	81
5.4 Surface roughness	83
5.5 Influence of operating parameters	85
5.6 Downward development of striations	87
5.7 Summary	88
Chapter 6. Wavelength dependence of striations	91
6.1 Comparative cutting experiments with a fibre and a CO ₂ laser	96
6.2 Mechanisms of the wavelength dependence of striations	101
6.3 Summary and conclusions	111
Chapter 7. Conclusions	113
Annex 1. Measurement of absorptivity	119
A1.1 Measurement of angular dependence	121
A1.2 Temperature dependence of absorptivity	122
A1.3 Absorptivity on kerf front during laser cutting	122
A1.4 Summary	124
Annex 2. Study on recoil pressure	127
A2.1 Recoil pressure during laser material processing	129
A2.2 Theoretical background	131
A2.3 Methods of experiments	135
A2.4 Results	137
A2.5 Discussion	141
A2.6 Conclusion	144

Annex.3. Revised piston model	145
A3.1. Formulation for laser drilling	147
A3.2. Calculation examples	149
A3.3. Summary	151
Annex.4. Analysis of heat conduction process	153
A4.1. Surface heating with a static laser beam	155
A4.2. Melting with a moving laser beam	157
A4.3. Summary	161
References	163
List of publications	169

List of symbols:

A	Laser absorptivity
A_m	Constant
A_p, A_s	Laser absorptivity for p and s-polarisation
b	Kerf width
b	Non-dimensional parameter
Bo	Bond number
c	Speed of light
c	Constant
Ca	Capillary number
C_{ps}, C_{pl}	Heat capacity of solid and melt
d_c	Fibre core diameter
d_k	Kerf width
D	Beam diameter
E_a	Activation energy
f	Friction coefficient
f	Ratio of heat conduction loss to axial heating
g	Gravity
h	Planck constant
h	Sample thickness
h_f, h_e	Characteristic depth for roughness formation
I_{abs}	Absorbed intensity
I_L	Incident laser intensity
l	Droplet length
\dot{m}	Mass evaporation rate
n	Refractive index
k	Extinction coefficient
k	Constant
k_B	Boltzmann constant
K	Heat conductivity
L_m, L_f	Latent heat of melting
L_v	Latent heat of evaporation
M	Mach number
M^2	Beam quality parameter
m	Mass per atom
n_x, n_y, n_z	Components of surface normal
p	Pressure
p_{sat}	Saturated vapour pressure

p_r	Recoil pressure
p_g	Partial pressure of surrounding gas
P_{amb}, P_0	Ambient pressure
P_{res}	Stagnation pressure
Pe	Péclet number
P_g	Assist gas pressure
P, P_L	Incident laser power
q_{cond}	Heat flux across kerf front
q_w	Heat flux lost into solid
Q	Nozzle flow rate
r_k	Kerf radius
r_l, r_0	Laser beam radius
r_m	Curvature radius of rim part
R	Curvature radius of melt deformation
R	Perfect gas constant
Re	Reynolds number
R_z	Surface roughness
$S(\alpha)$	Stability function
St	Stefan number
T_0	Initial temperature
T_{hump}	Period of hump generation
T_m	Melting temperature
T_s	Surface temperature
T_v	Evaporation temperature
u	Downward displacement velocity of melt accumulation
U_e	Mean velocity of ejected melt
U, V	Components of melt velocity
V, V_c	Cutting velocity
V_{chain}	Displacement velocity of a chain element
V_d	Drilling velocity
V_g, v_g	Gas flow velocity
V_{hump}	Hump velocity
V_m	Speed of lateral melt ejection
V_v	Ejection speed by evaporation
W	Width of unstable side region
z_f, Z_f	Defocusing distance

α	Local inclination angle of kerf front
α_{ave}	Mean inclination angle
α_{eq}	Inclination angle in equilibrium condition
α_{thr}	Threshold inclination angle
β	Inclination of melt accumulation surface
β_R	Fraction of recondensed particles
β_m, β_p	Recombination rates
γ	Adiabatic exponent
γ	Euler constant
δ	Size of melt droplet
δ_m, δ_{me}	Thickness of melt layer
ε	Surface emissivity
η_l, μ_m	Melt viscosity
σ	Surface tension coefficient
Δ	Overlap length
ΔH_v	Enthalpy of phase transition from liquid to vapour per atom
ΔP	Pressure difference
Δt	Characteristic interaction time of a melt accumulation
Δt	Laser pulse irradiation time
Δt_a	Accumulation period
Δt_f	Characteristic time of solidification
Δy	Characteristic penetration of heat into solid
Φ	Azimuthal angle from cutting direction
Φ_α	Angle of incidence of laser beam
κ	Thermal diffusivity
λ_L	Laser wavelength
λ	Striation wavelength
ρ_g, ρ_s	Density of gas and solid
ρ_l, ρ_m	Liquid density
ρ_0	Air density in normal condition
τ, τ_g	Shear stress by assist gas

Chapter 1. Introduction

Résumé

Depuis son invention pendant les années 1960, la découpe laser de l'acier a largement été utilisée dans l'industrie en raison de son avantage lié à la vitesse de traitement ou à sa capacité d'automatisation. L'un des problèmes de la qualité dans la découpe laser est la génération des stries sur les surfaces coupées. Récemment ce sujet a attiré beaucoup d'attention, puisqu'on l'a observé que les nouveaux lasers prometteurs, à fibre ou à disque, n'offraient pas la même qualité que les lasers conventionnels CO₂ lors de la découpe de fortes épaisseurs d'acier. Si ce problème pouvait être résolu, ces nouveaux lasers pourraient remplacer avantageusement les lasers CO₂ grâce à une réduction des coûts et à une productivité plus élevée. Ce problème n'a pas été résolu jusqu'à maintenant, malgré des efforts de différents groupes de recherche dans le monde. La raison fondamentale de cette situation est qu'en fait nous ne comprenons toujours pas le mécanisme de la génération des stries en découpe laser avec un gaz inerte. Il y a eu des nombreux modèles théoriques pour expliquer ce phénomène, mais une conclusion claire et définitive n'a jamais été obtenue, en partie en raison du manque de vérifications expérimentales appropriées.

Objectifs et plan de la thèse :

L'objectif principal de cette étude est de clarifier le mécanisme de la génération des stries dans la découpe laser d'aciers, lors de l'emploi d'un gaz d'assistance inerte. Les stries doivent être probablement liées à une instabilité de l'écoulement du métal fondu autour et le long du front avant de la saignée. Cette étude a donc débuté par l'observation de l'hydrodynamique du métal fondu sur le front de la saignée. Une caméra vidéo rapide a été utilisée afin de capturer le processus rapide de l'éjection de liquide. Sur un côté de la saignée, on trouve généralement des stries le long des flancs de la saignée, qui partent de la surface supérieure et descendent vers la surface inférieure avec plus ou moins de déformation. Ce fait expérimental suggère que l'origine de l'instabilité de l'écoulement de liquide devrait être dans une région située près de la surface supérieure. Ainsi, la première étape des observations expérimentales s'est concentrée sur l'hydrodynamique sur la partie supérieure d'un front de la saignée. L'écoulement observé montre de fortes instabilités dans les parties centrale, ainsi que sur le côté de la saignée. Ces instabilités ont été étudiées par la suite dans le cadre d'une étude paramétrique où les principaux paramètres opératoires ont pu être variés. Dans une deuxième série d'expériences, le développement le long du front de la saignée de ces instabilités créées à partir de la surface supérieure a été analysé, à l'aide d'une observation transverse de cet écoulement.

Dans le chapitre 2, les processus physiques fondamentaux de la découpe laser de l'acier sont décrits et réexaminés. Dans le chapitre 3, les études théoriques sur l'instabilité de l'écoulement du métal fondu sur un front avant de la saignée et sur la génération des stries sont passées en revue. Celles-ci deviendront une base pour l'interprétation et la discussion des phénomènes observés. Dans le chapitre 4, des observations expérimentales de l'écoulement de métal liquide autour le front avant de la saignée sont présentées. Les résultats sont interprétés et discutés dans le chapitre 5 suivant. Dans le chapitre 6, la très importante controverse sur l'origine de la différence de qualité de coupe entre des lasers à fibre/disque et à CO₂ est discutée au vu des mécanismes de génération des stries mis en avant et présentés dans les chapitres précédents et une solution à ce problème est proposée.

Introduction

The year 2010 celebrated the 50 years anniversary of laser, which must be one of the greatest inventions in the 20th century both in terms of science and technology. Laser material processing is an area of industrial applications of lasers. A number of applications have been developed: welding, cutting, drilling, surface treatment, and so on. Most applications utilise a laser as a heat source, exploiting its advantages of high power density, excellent focusability, capability of precise position control of a focus spot, ability of processing without a contact tool, and so forth. Although its history is relatively young, laser material processing has been applied to a wide range of spectrum from precise texturing of surfaces in the order of sub-micron to welding and cutting of heavy section materials in the order of several tens of millimetres.

Another aspect of laser material processing is that technologies of equipment such as lasers and optics advance with a fast pace. Recent rapid development of high power disc and fibre lasers is such a good example. These types of lasers show good scalability of laser powers with excellent beam quality. Recently it has been successfully shown in a test laboratory that a 20 kW laser beam can be emitted from a fibre with a core diameter as small as 50 μm [Ness 2012]. The rapid development of laser sources with high power and good beam quality has opened a number of interesting applications. Remote ablation cutting is such a good example. High power density and large focal distance, both of which are realised by an excellent beam quality, enables us to cut materials from a remote distance without assist-gas [Lütke 2008]. Although the concept had been proposed in the époque of CO₂ laser [Krasnyukov 1998], the technology was widely introduced in industries only after the arrival of high power fibre and disc lasers.

This study investigates fundamental physical processes of laser cutting of steel. The industrial importance of steel laser cutting is clear; laser cutting accounts for about 70 % of all the applications of laser material processing, and steel is no doubt one of the primary target materials. The first laser cutting of steel was tried in 1967 [Sullivan 1967, Arata 1967], only 7 years after the invention of lasers. Since then, laser cutting has widely been applied to cut steel sheets, owing to its advantage of processing speed, no requirement for post-processing, or capability of automation. Different aspects of laser cutting with CO₂ lasers are described in a book [Powell 1998] from viewpoints of industrial application. As regards steel, ordinary laser cutting can be applied to a thickness range up to about 20 mm. Above this range, plasma or gas cutting is often utilised. This thickness limit of about 20 mm is imposed by a limit of laser power. The output power of CO₂ lasers with a beam quality good enough to laser cutting is limited at around 8 kW.

Figure 1-1 shows a schematic of laser cutting process. In the equilibrium state, the laser beam is absorbed on kerf front. (A “kerf” is the space from which the material is removed in the cutting process.) The molten material which is produced on the kerf front is blown off from the bottom part of the kerf by a mechanical force from an assist gas jet that is provided from a nozzle, which is usually placed coaxially with the laser beam. The laser beam and the assist-gas nozzle are displaced with a given cutting velocity V_c . Then a cut kerf is created. In laser cutting of steel, two kinds of assist-gas are generally used. For ordinary carbon steel, oxygen is mainly used. The oxidation reaction of Fe into FeO can provide energy that can be utilised for cutting in addition to the energy provided by the laser beam. For stainless steel, inert gas such as nitrogen is normally used. This is because some oxide materials such as CrO which are created by reaction with oxygen gas are highly viscous and difficult to eject from the kerf.

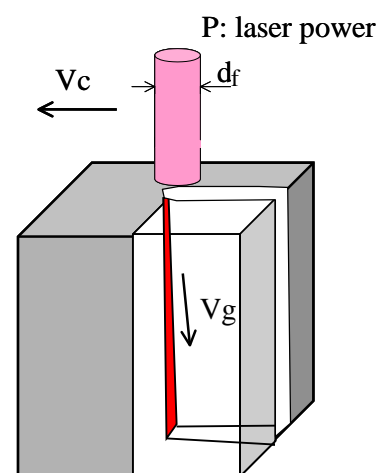


Figure 1-1 Principle of laser cutting

The present study focuses on striation generation process in laser cutting of steel. An example of striations is shown in figure 1-2. Striations are periodic surface structures that are left on kerf sides

after the laser cutting process. In general, striations start from the top of the kerf side and continue to the bottom. Surface roughness created by these striations is one of the important quality factors in laser cutting of steel and is to be minimised. Recently this topic has become more and more important, because it has been revealed that new promising fibre or disc lasers cannot offer the same quality as conventional CO₂ lasers in case of thick steel cutting [Wandera 2006, Himmer 2007]. If this problem can be solved, the present limit of cut thickness (~ 20 mm) will be raised with fibre and disc lasers. Lasers will take over conventional gas or plasma cutting machines, offering us better finishing quality or possibility of automation.

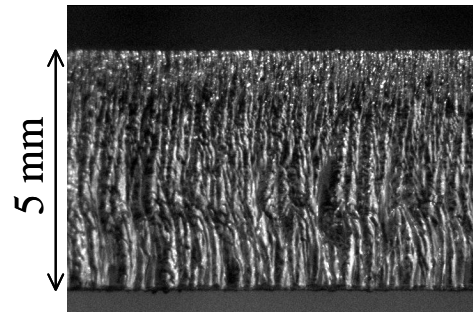


Figure 1-2 An example of striations left on kerf sides.

However, the problem is that we do not fully understand the striation generation mechanism in laser cutting of steel in spite of research efforts since the 1960's. For the case of using oxygen, which provides the exothermic energy, a model of cyclic activation and extinction of oxygen combustion, which was proposed by Arata *et al.* [Arata 1979], was raised up to the level of numerical modelling [Ermolaev 2009]. Creation of striations on kerf sides were successfully explained by this model. Although the mechanism of striation generation for the other case with inert gas might seem simpler, in that it involves only heat input by laser beam, the mechanism has remained unknown for several decades. The generation of striations must be attributed to a time-dependent fluctuation of melt flow around kerf front. A number of complex theories have been proposed to explain this phenomenon, but there is no agreement or conclusion, because of a lack of experimental verifications.

Recently high speed video filming technique has emerged as a powerful tool to investigate physical processes during laser material processing. In laser welding, for example, many interesting results concerning melt flow, spatter and plume ejection, hump formation, and so on, have been obtained [Fabbro 2005, Fabbro 2006, Weberpals 2010-1, Kawahito 2007, Schuster 2009, Eriksson 2011]. In laser cutting, however, it seems that the capability of the high speed video observation has not been exploited enough, probably because of difficulty to have a vision inside kerfs. Meanwhile, we can mention a recent study by Yudin *et al.* [Yudin 2007], who developed a technique to observe melt flow inside a kerf through a glass plate, which was attached onto a sample. Rose's alloy [Yudin 2007] and mild steel [Grigory 2010] were cut in the experiments. It was confirmed that striations are developed by intermittent downward displacement of melt accumulations along kerf sides. However, precise observation of the top part of the kerf was not realised, so that it could not be revealed why the melt accumulations are generated from the top surface.

In view of these situations, this work aims to reveal the mechanism of striation generation during inert gas laser cutting of steel based on experimental observations of hydrodynamics of molten liquid on a kerf front using a high speed video camera. The outline of this thesis is briefly summarised as follows.

In the next chapter 2, fundamental physical processes involved in laser cutting of steel are explained and discussed. The process of inert gas laser cutting of steel is composed of three fundamental processes: absorption of laser beam on kerf front, heat conduction and melting of the kerf front surface, and molten liquid ejection from the kerf by an assist-gas jet. These individual processes, however, have not been fully understood. In this study we re-examine several aspects. First, experimental investigation of the absorptivity is carried out. It is shown that the well-known Fresnel absorption law provides a good estimation of the absorptivity in laser cutting process. Then peculiarity of heat conduction process near the sample surface is discussed. We demonstrate that a kerf front profile near the top and bottom surfaces is deviated from the one which is obtained from a 1D approximation of the heat conduction equation. Finally it is revealed that the recoil pressure hardly contributes to melt ejection when the surface temperature is lower than the boiling temperature, as opposed to the commonly believed presumption. These new findings are utilised in discussions on the mechanism of

striation generation process.

In chapter 3, a review of theoretical studies on instability of melt flow and striation generation process is presented. Although we have not reached a conclusion on the mechanism of the striation generation, the review of the previous theoretical models becomes a basis for theoretical analyses performed in this work. Various models that have been proposed are categorised into three types: the models which only treat fluctuations of gas-liquid interface; those which only deal with fluctuations of solid-liquid interface; and those which consider both of them. Generally, the models analyse a response of the system when a small perturbation is added to a kerf front, and predict resonant oscillation of the system or transient transport of the perturbation. However, the problem is that the origin of this small perturbation is unknown. There are many hypotheses: unavoidable fluctuations of operating parameters of laser beam and assist-gas, strong interaction between melt film and assist-gas jet, peculiarity of heat conduction process near the sample surface, and surface tension of molten metal. To conclude on this mechanism, experimental investigations are being required.

The chapter 4, the first main part of this study, is thus devoted to experimental observations of hydrodynamics of molten liquid on a kerf front with a high speed video camera. First, the hydrodynamics is visualised from the above of the sample, in order to clarify initiation of melt flow instabilities from the sample surface. The observation reveals unstable nature of the melt flow, which depends strongly on the cutting velocity. Molten droplets, so called humps and melt accumulations, are generated at the surface in the central and side parts of the kerf front, respectively, in low cutting velocity ranges. They are displaced downwards along the kerf front. It is clearly observed that striations are created as a result of this dynamics of melt accumulations on kerf sides. Also different characteristics are found between the instabilities in the centre and side parts of the kerf front, in terms of the frequency of the instability and the velocity range where the instability appears. A parametric study is also conducted in order to investigate dependence of the instability on various operating parameters. In the second configuration of the observation, melt film dynamics on a kerf front is visualised laterally through a glass plate. The result demonstrates that humps in the central part can also disturb the dynamics of the melt accumulations and influence quality of striations.

The origin of the melt flow instability and its relevance to striation generation process are discussed in the next chapter 5. We consider that the melt flow instabilities observed both in the central and side parts of the kerf front is caused by surface tension force which retains humps or melt accumulations at the surface while their size is small. A theoretical analysis of a force balance between the surface tension and the force induced by assist-gas jet predicts well the order of the pitch of the instabilities. The instability disappears for a high cutting velocity, since the surface tension can join two successive melt droplets along kerf front. An analysis shows scaling of instability by α ; there exists a threshold angle above which the instability disappears. The different characteristics observed in the central and side parts can be explained by a geometrical effect. The instabilities observed in the two parts can thus be explained coherently by a single mechanism of the surface tension effect. We consider that striations are created by local melting of solid surface due to heat transfer from the melt accumulations on kerf sides. We estimate surface roughness from a theoretical analysis of the heat conduction process and the result shows reasonable agreement with experimental results. The results of lateral observations through a glass plate indicate that the stability of the central flow also affects striation generation process. As discussed above, the inclination angle of the front is a key parameter that controls this stability.

In chapter 6, we investigate the above-mentioned interesting problem of cut quality difference between CO₂ and fibre/disc lasers, based on the mechanism of striation generation revealed in the previous chapters. First, we compare laser cutting of stainless steel with a fibre and a CO₂ lasers. It is revealed that degradation of the cut surface quality for the 1 μm wavelength occurs for a range of low α , less than 3 degrees. Then the mechanism of the laser wavelength dependence is discussed. We propose two mechanisms which can cause the wavelength dependence: stability of melt flow in the central part and dynamics of melt accumulations along kerf sides. The validity of each mechanism is confirmed by

analytical modelling of related physical processes. Both of the mechanisms are caused by the dependence of the absorption characteristics on laser wavelength. We finally propose that a possible way to improve cut quality for the 1 μm wavelength is to use a laser beam with the radial polarisation, which offers better absorption on a kerf front for a low α less than 3 degrees.

Finally, conclusions and future prospects are presented in Chapter 7.

Chapter 2. Fundamental physical processes

Résumé

Le processus de découpe laser avec un gaz inerte peut être présenté en trois étapes. D'abord, la puissance laser du faisceau incident est absorbée à la surface du matériau. Puis le transfert de chaleur dans le matériau et la fusion de la surface se produisent, enfin, le matériau fondu est éjecté de la saignée par le jet de gaz d'assistance. En fait, ces processus sont fortement couplés entre eux. Afin de modéliser le processus complet de découpe laser, plusieurs équations liées à chacun de ces processus doivent être résolues d'une façon auto-consistante. Malgré cette difficulté, un grand nombre de modèles ont été proposés, principalement en régime stationnaire, et certains ont permis de prévoir la capacité de découpe (l'épaisseur coupée ou la vitesse maximum de coupe pour des paramètres donnés). Cependant, le succès de ces modèles théoriques ne garantit pas la validité des différentes hypothèses faites dans chacun des processus physiques considérés. Par exemple, la capacité de découpe prévue n'est pas dépendante de la dynamique du métal fondu. De même, les processus non-stationnaires, tels que ceux décrivant la génération de stries, doivent dépendre de paramètres plus « fins » que ceux utilisés pour la description du régime stationnaire. Ainsi dans ce chapitre, les processus physiques présents au cours de ces trois étapes sont décrits en détail et plusieurs aspects sont réexaminés : On discutera la validité de la loi d'absorption de Fresnel, le détail du processus de conduction de chaleur près de la surface supérieure, et le rôle de la pression de recul dans le procédé d'éjection du métal fondu.

2.1 Processus d'absorption :

Le premier processus qui se produit dans la découpe laser est l'absorption du rayonnement laser sur un front avant de la saignée. Non seulement cette absorption peut être directe, mais des mécanismes secondaires tels que la diffusion du faisceau par des particules métalliques et/ou l'absorption du faisceau par un plasma induit peuvent se produire pendant la découpe laser. Ces effets secondaires seront négligés dans cette étude parce que la vaporisation est généralement très limitée dans les conditions optimales de découpe laser avec un gaz inerte.

Bien qu'un certain nombre d'études aient supposé une loi d'absorption de type « Fresnel » pour le processus d'absorption, peu d'expériences ont été effectuées pour vérifier la validité de cette loi. Ainsi dans cette étude, plusieurs expériences fondamentales ont été effectuées pour étudier la validité de cette loi (Annexe 1). Ces expériences montrent que cette loi devrait s'appliquer sur une gamme d'angles d'incidence élevée, ce qui est le cas de la découpe laser, et aussi qu'elle peut être utilisée pour une gamme de températures élevées, supérieures à la température de fusion T_m . L'absorptivité dans le processus de découpe en conditions réelles a été estimée à partir de la mesure de la puissance transmise à travers la saignée et un accord raisonnable avec la loi théorique de Fresnel a été obtenu. Ainsi on peut conclure que la loi d'absorption de Fresnel est une bonne approximation pour évaluer l'absorptivité d'un faisceau laser sur le front avant de la saignée.

2.2 Processus de conduction :

Le processus suivant est le transfert de chaleur dans le matériau. Le matériau est chauffé puis fondu. Ceci détermine une puissance laser qui est nécessaire pour découper une épaisseur donnée et un profil approximatif du front avant de la saignée. Ces paramètres peuvent être évalués et sont basés sur un bilan de puissances. Par exemple l'angle α d'inclinaison du front avant de la saignée peut être estimé à partir d'un bilan de puissances par unité d'épaisseur du matériau, composé de la puissance laser absorbée et de la puissance nécessaire pour fondre le matériau. La puissance absorbée par unité d'épaisseur augmente avec l'angle d'inclinaison α . D'autre part, la puissance nécessaire à la fusion se compose d'une puissance nécessaire à la fusion de la partie centrale de la saignée et de la puissance perdue par conduction vers les parties latérales, à l'extérieur donc de la saignée. Cette somme augmente avec la vitesse de découpe V_c . Ainsi une augmentation de la vitesse V_c augmente α , qui sera l'un des paramètres les plus importants dans la discussion qui suit sur l'instabilité de l'écoulement de liquide.

L'analyse ci-dessus s'est concentrée sur la conduction de chaleur dans une section du matériau, située à l'intérieur de l'échantillon et dont la surface de la saignée est quasi-parallèle à l'axe du faisceau laser. Cette approximation ne peut pas être valide dans les régions situées près de la surface supérieure, où le flux thermique, dans une direction verticale, est alors modifié. Cet aspect est étudié pour la première fois, et il est nécessaire de le faire, car il peut être lié à l'initiation de stries à partir de la surface supérieure. La modification du profil du front avant de la saignée issue de la considération de ce flux thermique vertical a été analysée pour une distribution « top-hat » de la tâche focale de faisceau laser. On montre alors que le profil de la saignée au niveau de la surface supérieure ne peut pas être droit comme habituellement considéré lors d'une approximation 1D, mais doit s'arrondir au niveau de la jonction du front avant et de la face supérieure.

2.3 Hydrodynamique du liquide éjecté :

Enfin, le processus qui intervient après le transfert de chaleur et la fusion, est l'éjection du matériau fondu de la saignée par un jet de gaz intense, généralement coaxial au faisceau laser. Dans les études théoriques issues de la bibliographie, deux principaux mécanismes ont été considérés dans ce processus d'éjection du liquide métallique: l'éjection verticale liée au gaz d'assistance et l'éjection latérale résultant de la pression de recul générée par le laser. Cependant, notre étude expérimentale sur la pression de recul (Annexe 2) a clairement démontré pour la première fois que l'éjection latérale par la pression de recul pouvait être négligée tant que la température de surface de la couche liquide est inférieure à la température d'ébullition du matériau. Ce résultat nous permet alors de nous concentrer uniquement sur l'éjection par le gaz d'assistance dans les discussions suivantes, ce qui simplifiera considérablement les analyses.

Dans une condition typique de découpe laser d'acier avec un gaz inerte, la pression du gaz d'assistance est au moins de l'ordre de 10 bar. Ceci induit une distribution du champ de vitesses dans ce gaz issu de la buse très complexe, en partie en raison de la présence d'ondes de choc. Les caractéristiques de cet écoulement complexe ont déjà été étudiées expérimentalement et numériquement et on peut considérer que les caractéristiques de cet écoulement sont plutôt bien connues. L'écoulement supersonique du gaz étant assez sensible aux paramètres opératoires, nous avons par conséquent choisi d'utiliser un jet de gaz en régime subsonique pour la suite de cette étude.

Il y a deux mécanismes entraînant l'éjection du métal fondu par le gaz d'assistance, qui sont discutés: le gradient de pression du gaz et la contrainte de cisaillement. La dynamique d'éjection du liquide peut être obtenue par la résolution des équations de Navier-Stokes. Ce qui est relativement difficile, du fait de la présence d'une surface libre de l'interface gaz-liquide et également d'un champ de vitesse du gaz assez complexe, comme mentionné précédemment. Jusqu'à présent, ces modèles théoriques ont été limités au cas 2D et supposent un gradient de pression constant, ou une contrainte de cisaillement constante avec généralement un nombre de Reynolds faible. Si on admet une contrainte de cisaillement constante issue de l'écoulement, la vitesse de la couche liquide est être donnée par $(\tau\delta_m/2\eta_l)$ (τ : la contrainte de cisaillement, δ_m : l'épaisseur de la couche liquide, η_l : la viscosité du liquide).

On discute également plusieurs modèles théoriques qui prennent en considération l'ensemble des processus rappelés ci-dessus: l'absorption d'un faisceau laser sur le front avant de la saignée inclinée, la conduction de chaleur, l'hydrodynamique du métal fondu sur le front avant. Ces modèles, indépendamment de leur dimension 2D ou 3D, visent à obtenir un profil du front avant de la saignée dans l'état stationnaire pour un ensemble donné des paramètres opératoires. Le profil obtenu doit satisfaire toutes les équations différentielles représentatives des différents phénomènes physiques, qui doivent être résolues d'une façon consistante. Ces modèles semi-analytiques permettent généralement de prévoir les profondeurs coupées maximum ou les vitesses maximum de coupe observées expérimentalement. Ils ne sont cependant pas capables de prévoir et ni de quantifier l'état des stries, puisqu'ils supposent un état stationnaire, la génération de stries étant un processus essentiellement instationnaire.

Introduction

The process of inert gas laser cutting of steel in a quasi-stationary regime can be divided into three processes, as schematically designated using bold arrows in figure 2-1: (i) power of the laser beam is absorbed on the kerf front; (ii) heat transfer occurs and the kerf front surface is melted; (iii) the produced melt film is blown off from the kerf by an assist-gas jet. Actually these processes are coupled to each other. In order to model the entire laser cutting process, several sets of differential equations related to each process have to be solved self-consistently. In spite of this difficulty, a number of models have been proposed as steady state laser cutting models, which have succeeded to predict cutting capacity (i.e. maximum cutting thickness or maximum cutting speed for a given laser condition).

In spite of this success, it seems that different assumptions made in modelling have to be re-examined. One reason is that the success of the theoretical models does not guarantee the validity of different assumptions made in each of the physical processes. For example, as mentioned in the following, the predicted cutting capacity is not influenced strongly by a way of modelling of melt film dynamics. It should also be pointed out that time-dependent phenomena such as striation generation process, which is the topic of this thesis, should be more sensitive to model assumptions than the characteristics under stationary condition.

Therefore, in this chapter, physics of the above three processes is described and several aspects are reinvestigated. Among these are: the validity of Fresnel absorption law, peculiarity of heat conduction process near sample surface, and the role of recoil pressure in melt ejection process. It is shown from experimental measurements of absorptivity that the Fresnel law can be applied to laser cutting, where the incidence angle of laser beam is quite large and the surface temperature of the absorbing kerf surface is kept high over the melting temperature. As regards heat conduction process, it is pointed out that two dimensional approximation of heat conduction process on a plane perpendicular the laser beam axis, which has been often used in the previous studies, is not appropriate in the regions near the top and bottom surfaces. Discrepancy of the kerf front profile from this approximation is discussed. Finally, we conclude from a result of an experimental investigation of recoil pressure that lateral ejection of melt film from the central part of kerf front to kerf side regions can be neglected when the surface temperature of kerf front is below the boiling temperature.

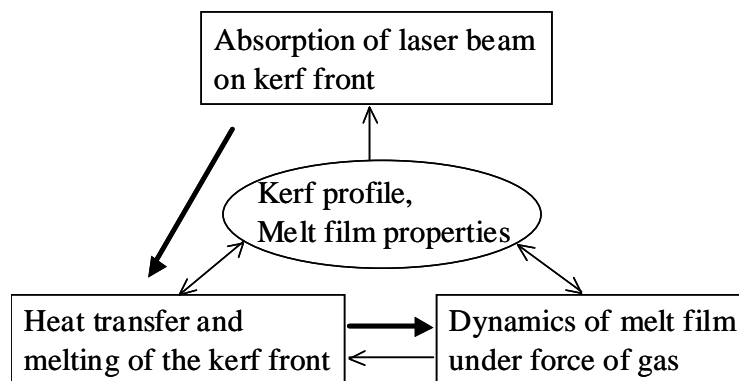


Figure 2-1 Relation among different fundamental phenomena

2.1 Absorption

Laser cutting process begins with absorption of laser beam and heating material on the kerf front. The incoming laser beam is not absorbed by 100%, but is partially reflected. According to the Fresnel absorption theory of electric magnetic waves at an interface of two different materials (air and steel are considered here.), the absorptivity A primarily depends on the refractive index n and the extinction coefficient k [Dausinger 1993]:

$$A = \frac{A_p + A_s}{2} \quad (2-1),$$

$$A_p = \frac{4n \sin \alpha}{(n^2 + k^2) \sin^2 \alpha + 2n \sin \alpha + 1} \quad (2-2),$$

$$A_s = \frac{4n \sin \alpha}{n^2 + k^2 + 2n \sin \alpha + \sin^2 \alpha} \quad (2-3).$$

Here A_p and A_s are the absorptivities for the p-polarisation and the s-polarisation, respectively. The absorptivity A in eq.(2-1) assumes the random polarisation of the incoming laser beam. As is clear from eqs.(2-1) to (2-3), the absorptivity A depends on n and k , which are determined by the laser wavelength and the surface temperature of kerf front surface, and also on the local inclination angle α of the kerf front. Please refer to figure 2-3 for the definition of α . Please note that α is different from the incidence angle ϕ_α that is defined as the angle between the incident direction of the laser beam and the normal of kerf front surface. As can be seen in figure 2-2, angular dependence of absorptivity of steel is different for laser wavelengths of 1 μm and 10 μm .

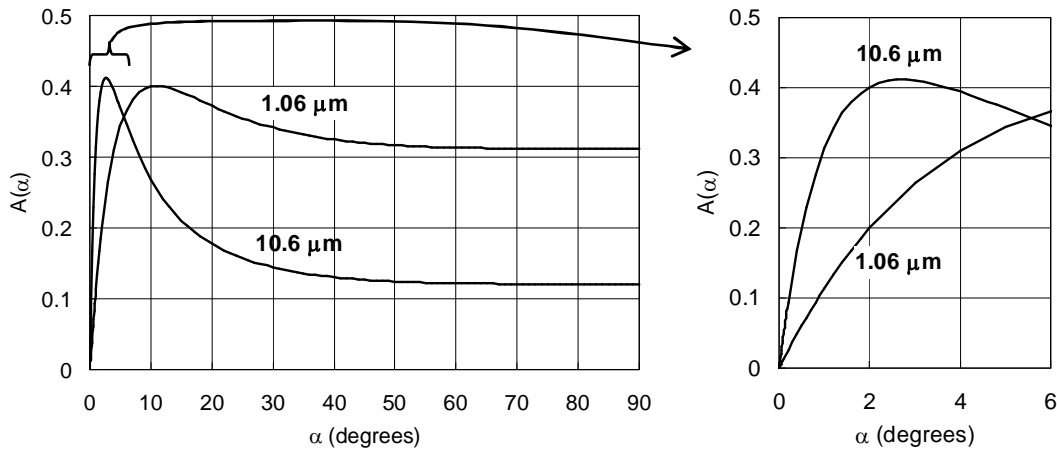


Figure 2-2 Absorptivity predicted from the Fresnel Law for the two wavelengths.

The above Fresnel formula has widely been used in the previous papers on laser cutting [Mahrle 2009, Powell 2011]. However, there remains room for doubt to apply the expression directly to the cutting process, where the absorbing surface has high temperature. It should be noted that the Fresnel absorption law is applicable for ideally smooth surface at room temperature. According to the previous experiments in our laboratory, the absorptivity measured for 1 μm was as high as 80% for drilling [Schneider 2006], and 60% for welding [Fabbro 2005], while the absorptivity for 1 μm is predicted to be below 50% as shown in figure 2-2. For cutting with a CO_2 laser, the measured absorptivity was 60-70% in the case of oxygen laser cutting [Miyamoto 1991], and another experiment conducted in our laboratory suggests that the absorptivity is around 50% for stainless steel cutting by a CO_2 laser with nitrogen gas [Mas 2003-1].

To verify the applicability of the Fresnel absorption formula to laser cutting process, two types of experiments were conducted. The object of the first experiment was to confirm the angular dependence of the absorptivity, especially for low α , which is usually encountered in laser cutting. The details are explained in the Annex 1. Angular dependence of the absorptivity for a disc laser beam (Laser wavelength: 1.03 μm) was measured for a sheet of pure iron. The sample was placed above an integrating sphere and the reflected light was collected in the integrating sphere. The measurement was carried out for the two polarisations s and p. The surface temperature of the sample must have been below the melting point T_m , because melting could not be found after the measurement with a laser

pulse irradiation. The results show reasonable agreement with the theoretical predictions of eqs.(2-2) and (2-3). The absorptivity for both the p and s polarisations exhibit increase with the increase of α , and the absorptivity was much higher for the p-polarisation than for the s-polarisation. The present result agrees with a previous work [Touvrey 2006], where the increase of absorptivity was confirmed with the increase of α for Tantalum.

The second experiment was conducted to investigate influence of temperature dependence of the absorptivity. The details of this experiment are explained in the Annex 2. A sample of pure iron was placed under an integrating sphere, which collected the reflected light from the sample surface. The incidence angle ϕ_α of the laser beam was about 5 degrees ($\alpha = 85$ degrees). Time evolution of the absorptivity was measured during a single pulse irradiation by a disc laser beam. In another experiment with the same laser irradiation condition, the surface temperature of the irradiated spot was measured as a function of time by pyrometry using a high speed video camera. Combining these two results, the temperature dependence of the absorptivity could be estimated. The result shows that the absorptivity for pure iron is almost constant up to the boiling point T_v . The previous studies have shown that the absorptivity of steel for the 1 μm wavelength does not change so much up to 1400 $^\circ\text{C}$ [Dausinger 1993], and up to 2650 K [Kraus 1986]. The result in this work demonstrated for the first time that this extrapolation is valid up to T_v .

The results of the above two experiments support the validity of the theoretical Fresnel absorption law for laser cutting with a 1 μm laser beam. That is, it is reasonable to extend the absorption law to a region of low α using the values n and k that are obtained by an experiment with a high α near 90 degrees. Also, the influence of the temperature change is negligibly small.

Next the absorptivity in real cutting process was measured experimentally to confirm that the absorptivity can certainly be estimated from the Fresnel absorption law. To obtain the absorptivity during the cutting process, we measured power transmitted through a kerf (Figure 2-3). The details of this measurement are described in Annex 1. The transmitted power is composed of two components: the power reflected on the kerf front and transmitted downwards, and the power directly transmitted without any interaction with the kerf front. The measurement of the surface area of the kerf front intercepting the laser beam allowed us to distinguish the two components and as a result to estimate the absorptivity on the kerf front. The measured absorptivity was around 60%. The value is slightly higher than the value predicted from the Fresnel absorption law. But it seems reasonable to conclude that the Fresnel law approximately describes the absorption during laser cutting of steel.

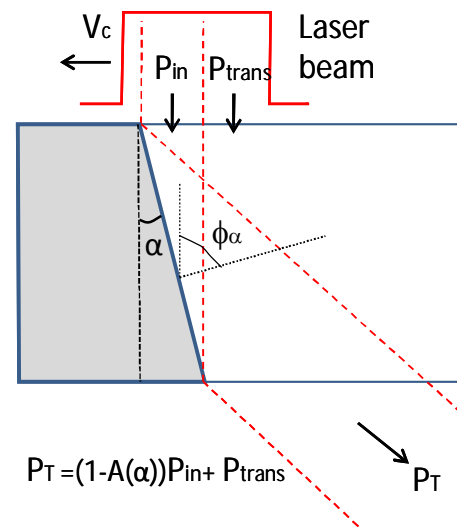


Figure 2-3 Measurement of absorptivity.

In conclusion, the experimental results obtained in this study show reasonable agreement with the Fresnel absorption formula. Thus the Fresnel law will be assumed in the following discussion.

Then a question arises. Why was the absorptivity as high as 80 % obtained in laser drilling of steel [Schneider 2006]? It is likely that multi-reflection effect could have caused an apparent increase of the absorptivity. In this experiment, the reflectivity was measured at about 0.1 ms after the initiation of laser pulse. This was because 0.1 ms was needed for a complete rise up of the laser power. The depth of the hole at 0.1 ms can be estimated from an integral of drilling velocity over 0.1 ms. At a peak power of 5 kW, for example, the drilling velocity V_d in the equilibrium state was measured to be 2.5 m/s. Considering the fact that the characteristic time to reach the equilibrium regime ($\sim \kappa/V_d^2$) is much

smaller than the characteristic time of the rise up of the laser power (0.1 ms), one can assume that the instantaneous drilling velocity is determined by the beam intensity at the same time. If we approximate the rise up of the power to 5 kW is linear and the drilling velocity is proportional to the beam intensity, the depth at 0.1 ms is estimated to be $(1/2) \times (0.1 \text{ ms}) \times (2.5 \text{ m/s}) \approx 125 \text{ }\mu\text{m}$. This is not negligible compared with the beam diameter of 330 μm . One can thus expect that multi-reflection could have increased the effective absorptivity.

Up to now direct absorption of laser beam has only been discussed. Let us mention here other heat transfer mechanisms: scattering of the laser beam and the inverse bremsstrahlung. When the scattering or the inverse bremsstrahlung occurs, the kerf front would be heated from the secondary heat source in any case, in a more homogenised manner than the direct absorption of the laser beam. These secondary absorption processes might be important for a discussion on the difference of cut surface quality between fibre/disc and CO₂ lasers. In this study, however, they are neglected for the following reasons.

The scattering effect is more important for a 1 μm laser beam than a 10 μm CO₂ laser beam, since the scattering intensity increases with a decrease of the laser wavelength λ_L [Hansen 1994, Lacroix 1998, Greses 2004]. Scattering effects such as power attenuation and diffusive scattering were confirmed in experiments with 1 μm YAG laser beams [Matsunawa 1985, Greses 2004] for welding regime where no assist gas jet was applied. In conventional laser cutting with assist gas, however, density of metallic particles above a kerf front is expected to be too small to cause appreciable scattering, because of a lower temperature ($T_s < T_v$) and a stream of the assist-gas jet which blows out the particles.

The attenuation coefficient for the inverse bremsstrahlung increases with λ_L^2 . It can be negligible for a 1 μm laser beam [Lacroix 1997, Mahrle 2006] but may have to be accounted for a 10 μm CO₂ laser beam. A previous study of laser cutting of thin sheets with a continuous wave CO₂ laser shows that extremely high power density in the order of 100 MW/cm² involves plasma formation during laser cutting process [Petring 1991]. In this regime, dependence of cutting velocity on the laser beam polarisation disappears. This suggests that the Fresnel absorption formula is not valid anymore. A possible explanation is the depolarisation of the laser beam by laser-induced plasma. It is also possible that heat transfer from the laser-induced plasma is dominant over the direct absorption from the laser beam.

In a lower intensity range, however, plasma formation is considered to be negligible. To see this point, let us refer to a recent experimental measurement of temperature on kerf front surface [Onuseit 2011]. In this experiment, the surface temperature was determined from emission spectrum from the surface, which was supposed to be a grey body. It was found that any emission line of neutral Fe atoms was not observed for a temperature range $T_s < T_v$. This suggests that plasma was not formed in this temperature range. Of course, T_s can reach T_v and plasma may be ignited. However, the above study also showed that excess of the temperature over T_v was observed only around the bottom part of a 2 mm thick sample and for a cutting speed near the process limit [Onuseit 2011]. It was confirmed also that when $T_s > T_v$, the quality of cut surfaces became worse. Horisawa *et al.* [Horisawa 2000] reported a similar result from cutting experiments of 3 mm mild steel sheet. Bright blue plasma originating from N₂ and N₂⁺ was observed when the cutting speed was set too high. It was reported that an explosive evaporation of molten material was observed almost simultaneously with the plasma formation and the molten material was scattered diffusively, independently of direction of assist-gas jet. The plasma formation was correlated with a bad quality of the kerf surface.

The above experimental results indicate that the plasma formation generally degrades the cut surface quality in laser cutting and suggest that it can be negligible for laser cutting with moderate laser beam intensity at least for an optimal cut velocity range where best cut surface quality can be obtained. Considering an experimental fact that the difference fibre/disc and CO₂ lasers for thick section cutting can be identified in a wide velocity range, we can conclude that the plasma effect should not be the main mechanism for the quality difference.

2.2 Heat conduction

2.2.1 Global energy balance

Let us consider first the dependence of the inclination angle α of the kerf front on the cutting velocity V_c . This can be considered from the equation of power balance per unit length along kerf depth, which is written as

$$p_a = p_s + p_m + p_l \quad (2-4)$$

All the terms have the dimension of W/m. The term p_a in the left side is the energy input to the system per unit depth. It can be approximated using the incident laser intensity I_L , the absorptivity A , the radius r_k of the kerf front ($r_k \approx d_f/2$) and the mean tilting angle α :

$$p_a = A(\alpha)I_L(2r_k)\tan\alpha \quad (2-5)$$

We have taken $(2r_k)$ as the characteristic length of the part along the kerf front which receives laser beam, neglecting its dependence on depth from the surface. The first and second terms on the right hand side of (2-4) represent the powers necessary to melt the solid material in the axial region in front of the kerf front (see figure 2-4) and to heat it further to T_l , which is the mean temperature of liquid:

$$p_s = \rho_s V(2r_k)[C_{ps}(T_m - T_0) + L_m] \quad (2-6)$$

$$p_m = \rho_l V(2r_k)C_{pl}(T_l - T_m) \quad (2-7)$$

Here T_0 is the initial temperature, T_m is the melting temperature, and L_m is the latent heat, and ρ_s (ρ_l), and C_{ps} (C_{pl}) are the density and heat capacity of solid (liquid), respectively. The third term in the right hand side of eq.(2-4) is the power lost by heat conduction into the solid parts outside of the axial region, which can be expressed as [Schulz 1993]

$$p_l = 4K(T_m - T_0)\left(\frac{Pe}{2}\right)^{0.3} \quad (2-8)$$

Here K is the thermal conductivity of the material. And

$$Pe = \frac{r_k V_c}{\kappa} \quad (2-9)$$

is the non-dimensional Péclet number. From eqs.(2-4)-(2-9), one obtains

$$A(\alpha)I_L(2r_k)\tan\alpha = 2\kappa[\rho_s C_{ps}(T_m - T_0) + \rho_s L_m + \rho_l C_{pl}(T_l - T_m)]Pe + 4K(T_m - T_0)\left(\frac{Pe}{2}\right)^{0.3} \quad (2-10)$$

The right hand side is a monotonous increasing function of Pe , which is proportional to V_c . Thus the expression shows that for a given conditions of I_L and r_k , the angle α increases monotonously with the increase of V_c .

2.2.2 Analysis of kerf front profile

For a top-hat intensity distribution, eq.(2-10) predicts a straight kerf front with a constant inclination angle α all along the front. However, a kerf front profile near the top and bottom surfaces is deviated from the straight line. The analysis limited on a 2D plane as in figure 2-4 is not valid in the top and bottom regions, since heat flux in the direction of the thickness of the sample has to be taken into account. Let us analyse this modification of the kerf front profile from the straight line.

Figure 2-5 shows the 2D model considered in the following. The plane shown in the figure corresponds to the central symmetric plane of the kerf. Laser beam has top-hat intensity distribution with the constant intensity of I_L (W/m^2). The laboratory frame where laser beam is fixed is adopted. The material, which flows from the left with constant velocity V_c (m/s), is heated as it approaches the kerf front (surface "3"). It is assumed that the material disappears as soon as the temperature of the material reaches T_m and it absorbs the latent heat. This means that the melt layer is neglected in the analysis. This simplification should be justified when the thickness of the melt layer is kept small

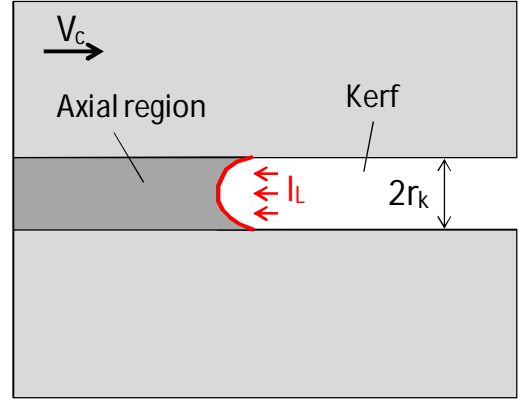


Figure 2-4 Cross-section of a kerf front.

owing to rapid ejection assisted by a strong gas jet. Another assumption is the 100 % absorption of the laser beam without any reflection on the kerf front.

2.2.3 Formulation of the problem

Time dependent two dimensional heat transfer process is considered. Taking into account the convection term due to the displacement of material with the cutting speed of V_c , the heat conduction equation is expressed as

$$\frac{\partial T}{\partial t} + V_c \frac{\partial T}{\partial x} = \kappa \left(\frac{\partial^2 T}{\partial x^2} + \frac{\partial^2 T}{\partial z^2} \right) \quad (2-11).$$

Here

$$\kappa = \frac{K}{\rho C_p}$$

is the thermal diffusion coefficient (ρ : density, C_p : heat capacity, and K : thermal conductivity). Temperature dependence of these parameters is neglected in order to make analytical investigation easier and to see more clearly the dependence of the characteristic of the profile on operating conditions.

As already mentioned, only the solid part is taken into account; a part of the material is assumed to disappear instantaneously as soon as its temperature reaches T_m and it absorbs the latent heat for melting. In this case, the boundary condition on the surface 3 of the inclined kerf front (see figure 2-5) is given by

$$T = T_m \quad \text{on surface 3} \quad (2-12).$$

Another boundary condition on the surface 3 concerns the continuity of the heat flux:

$$K \left(n_x \frac{\partial T}{\partial x} + n_z \frac{\partial T}{\partial z} \right) + \rho L_m V_c n_x = I_L (-n_z) \quad \text{on surface 3} \quad (2-13).$$

The second term in the left hand side represents the heat flux consumed for latent heat during the removal process. The boundary condition on the surface 2 is expressed as

$$\begin{aligned} -K \frac{\partial T}{\partial z} &= I_L & x > x_0 & \quad \text{on surface 2} & (2-14), \\ &= 0 & x \leq x_0 & \end{aligned}$$

considering the top-hat intensity distribution. The surface 1 serves as inlet and the temperature can be defined as

$$T = T_0 \quad \text{on surface 1} \quad (2-15),$$

where T_0 is the room temperature.

In the following we look for a stationary solution of the kerf front profile which satisfies eqs.(2-11)-(2-15) for a given set of V_c and I_0 .

2.2.4 1D approximation

Before going into detailed analysis of the problem, it is worthwhile to mention one-dimensional approximation of the problem to grasp a rough profile of the kerf front. Let us consider the case in figure 2-6(a) where the laser beam is irradiated only on the kerf front ($x = x_0$ in figure 2-5). We consider the energy balance in the sliced part in figure 2-6(a), which is in deep part (large z) where heat exchange with top surface region is neglected. One can estimate the inclination angle α of the kerf front from the following energy balance equation expressed per unit thickness.

$$I_L \tan \alpha = \rho [C_p (T_m - T_0) + L_m] V_c \quad (2-16).$$

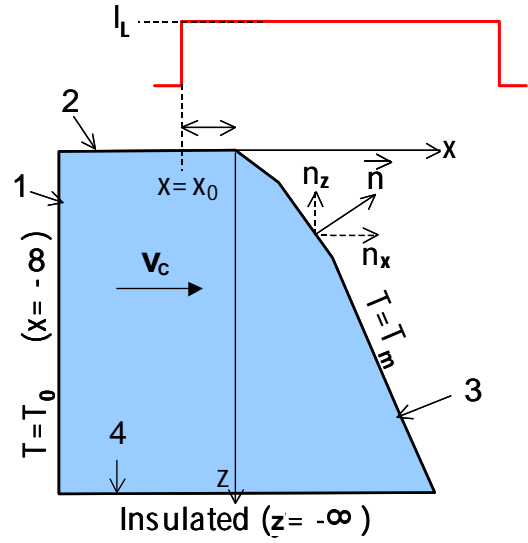


Figure 2-5 Setting of problem

An important outcome of eq.(2-16) is that the angle α increases with the cutting velocity V_c and decreases with the laser intensity I_L .

This non-dimensional parameter $\tan\alpha$ is important, since it is the parameter that governs the characteristic of the solution. If we also introduce other non-dimensional parameters for time and space,

$$\begin{aligned}\xi &= \frac{x}{\left(\frac{\kappa}{V_c}\right)}, & \zeta &= \frac{z}{\left(\frac{\kappa}{V_c}\right)} \\ t' &= \frac{t}{\left(\frac{\kappa}{V_c^2}\right)} & & (2-17). \\ T' &= \frac{(T - T_0)}{(T_m - T_0)} \\ St &= \frac{C_p(T_m - T_0)}{L_m}\end{aligned}$$

then eqs.(2-11) to (2-15) are rewritten as follows.

$$\frac{\partial T'}{\partial t'} + \frac{\partial T'}{\partial \xi} = \frac{\partial^2 T'}{\partial \xi^2} + \frac{\partial^2 T'}{\partial \zeta^2} \quad (2-11')$$

$$T' = 1 \quad \text{on surface 3} \quad (2-12')$$

$$n_\xi \frac{\partial T'}{\partial \xi} + n_\zeta \frac{\partial T'}{\partial \zeta} + n_\xi St^{-1} = \frac{(-n_\zeta)(1 + St^{-1})}{\tan \alpha} \quad \text{on surface 3} \quad (2-13')$$

$$-\frac{\partial T'}{\partial \zeta} = \frac{1 + St^{-1}}{\tan \alpha} \quad x > x_0 \quad \text{on surface 2} \quad (2-14')$$

$$= 0 \quad x \leq x_0$$

$$T' = 0 \quad \text{on surface 1} \quad (2-15')$$

which are no more dependent on V_c nor I_0 . This means that, if the non-dimensional parameter $\tan\alpha$ is the same, the characteristic of the solution of eqs.(2-11)-(2-15) stays the same, except that there will be some modification in scale factors of space and time given by (2-17). Thus in the following we investigate the dependence of the profile on this parameter.

It can be noted here that the inclination angle α of the front certainly plays a significant role in real physical processes. For example, Fabbro proposed that α is a crucial parameter, which determines the degree of interaction between gas vapour jet emitted from a keyhole front and the back melt surface of the keyhole during laser welding [Fabbro 2010]. As an example of such interaction, Weberpals *et al.* showed that ejection angle of spatters from a keyhole is correlated with α [Weberpals 2008].

2.2.5 Temperature drop near surface

The simple straight line profile in figure 2-6 of the 1D approximation cannot be the solution of (2-11)-(2-15), because the temperature distribution on the surface 3 cannot be kept constant at T_m due to heat flux in the direction of the thickness of the sample. Real temperature distribution suffers from a slight drop around the corner A. We analyse in the following this modification of the temperature field in this region.

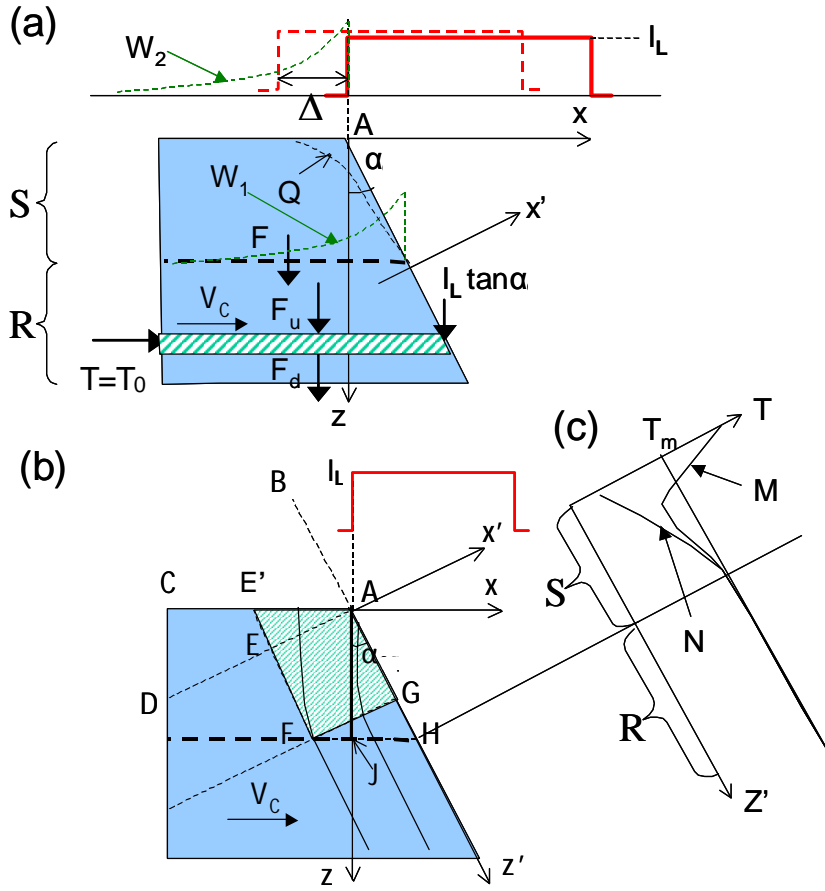


Figure 2-6 1D approximation

To begin with, we introduce the expression of 1D temperature field, which can be applied to the region below the line FJH in figure 2-6(b). We transform the coordinate, by setting x' axis perpendicular to the kerf front surface as shown in figure 2-6(b):

$$x' = x \cos \alpha - z \sin \alpha$$

$$z' = x \sin \alpha + z \cos \alpha$$

If a stationary condition is assumed eq.(2-11) can be transformed as follows.

$$V_c \cos \alpha \frac{\partial T}{\partial x'} + V_c \sin \alpha \frac{\partial T}{\partial z'} = \kappa \left(\frac{\partial^2 T}{\partial x'^2} + \frac{\partial^2 T}{\partial z'^2} \right)$$

The 1D solution should not depend on z' . Thus,

$$V_c \cos \alpha \frac{\partial T}{\partial x'} = \kappa \frac{\partial^2 T}{\partial x'^2} \quad (2-11'')$$

The boundary condition (2-14) is transformed as

$$K \frac{\partial T}{\partial x'} \Big|_{x'=0} + \rho L_m V_c \cos \alpha = I_L \sin \alpha \quad (2-14'')$$

By assuming the solution in the form $T(x') = B \exp(kx')$, the coefficients B and k can easily be determined from the above two expressions (2-11'') and (2-14''). Using also (2-16), we obtain the solution of the 1D temperature field.

$$T(x') = (T_m - T_0) \exp \left\{ \frac{(V_c \cos \alpha) x'}{\kappa} \right\} \quad (2-18)$$

In the region near the top surface, the heat transfer is modified due to the existence of the top surface, and thus the temperature distribution deviates from the solution (2-18) of the 1D approximation. Two regions are shown in figure 2-6(a); the lower R where the one-dimensional approximation is valid and S near the top-surface, where it fails. Let us define F as the heat flux from S to R. Using the fact that the temperature field in R is expressed by (2-18), the flux F in the dimension of [W/m] can be calculated in the following manner.

$$\begin{aligned}
K \frac{\partial T}{\partial z} &= K(\sin \alpha) \frac{\partial T}{\partial x'} \Big|_{x'=x \cos \alpha} \\
&= K(T_m - T_0) \left(\frac{V_c \sin \alpha \cos \alpha}{\kappa} \right) \exp \left\{ \left(\frac{V_c \cos^2 \alpha}{\kappa} \right) x \right\}
\end{aligned} \tag{2-19}$$

$$\begin{aligned}
F &= K \int_{-\infty}^0 \frac{\partial T}{\partial z} dx \\
&= K(T_m - T_0) \tan \alpha
\end{aligned} \tag{2-20}$$

The curve W_1 in figure 2-6(a) illustrates distribution of $K(\partial T/\partial z)$. The integrated heat flux F defined as in the above can be considered as a function of z. Please note that in the region R, the flux F is constant. For example, in the derivation of (2-16), we used the fact that the flux flowing to the slice across the upper segment is equal to the flux that pours out from the lower segment ($F_u = F_d$ in figure 2-6(a)). However, this is not the case in the region S. At $z = 0$, $F(z=0) = 0$ in the present case of thermally insulated top-surface. Due to this lack of heat flux from the top-surface, the temperature on the kerf front surface in the region S becomes less than T_m . Schematic distribution of the temperature is shown as N in figure 2-6(c).

Now let us estimate the characteristic length of the region R where the temperature drop occurs. Taking into account the fact that the one-dimensional temperature field has its contours parallel to the z' direction, we consider AEFG in figure 2-6(b), where the influence of the top-surface appears. Recalling that heat flow is driven by gradient of temperature field, we can say that the meaningful energy flow happens when the temperature T is about the same order as $(T_m - T_0)$. So we take $(\kappa/(V_c \cos \alpha))$, the characteristic distance of the field of T, as the length of the segment AE, out of which the energy flows.

$$\overline{AE} = \frac{\kappa}{V_c \cos \alpha} \tag{2-21}$$

The characteristic length of AG, which represents length over which the temperature decrease occurs, is defined by the diffusion length during the time Δt that corresponds to the time needed to travel from E to A. (In reality, the material does not travel to the x' direction, but this assumption should be appropriate, as the principal direction of the temperature gradient is in the x' direction.) That is,

$$\Delta t = \frac{\overline{AE}}{V_c \cos \alpha} \tag{2-22}$$

$$\overline{AG} = \sqrt{\kappa \Delta t} = \frac{\kappa}{V_c \cos \alpha} = \overline{AE} \tag{2-23}$$

It can be said that every point which traverses through the region AE'FG in figure 2-6(b) suffers from temperature drop. Recalling that real velocity is in the direction of x, not of x' , one obtains the length of AH, which represents the characteristic distance of the region of the temperature drop.

$$\overline{AH} = \overline{AG} + \overline{GH} = \frac{\kappa}{V_c \cos \alpha} (1 + \tan \alpha) \quad (2-24)$$

We define δ_2 as the length of AJ, which is the projection of AH to z axis.

$$\delta_2 = \overline{AJ} = (1 + \tan \alpha) \left(\frac{\kappa}{V_c} \right) \quad (2-25)$$

It is evident that in order to avoid this temperature drop near the top-surface, the heat flux must be applied also from top-surface. This is realised by overlapping the laser beam with the top-surface, by displacement of the laser beam to the (-x) direction, as the dotted red line in figure 2-6(a). Considering the energy balance in the region S, the flux F in (2-20) should be applied from the surface to compensate the temperature decrease. This corresponds to the overlap length

$$\Delta = \frac{F}{I_L} = \frac{\tan^2 \alpha_{eq}}{(1 + St^{-1})} \left(\frac{\kappa}{V_c} \right) \quad (2-26).$$

We have not yet arrived at the stationary solution of the kerf front profile, however, because with this straight kerf front geometry and with the beam overlap Δ , the temperature around the corner point A becomes higher than T_m , although the surface temperature averaged over the S region becomes T_m . The distribution M in figure 2-6(c) illustrates the resulting temperature distribution. To obtain the constant temperature T_m all over the kerf front, the profile must be rounded as PQ drawn in figure 2-7. With this modification, the energy input from the laser beam is redistributed from the surface to the inclined kerf front by the decrease of the overlap length on the top-surface and the increase of the local inclination angle α of the front in the top part. This should be able to lead to the constant temperature distribution. To obtain the accurate profile of the front, however, a numerical simulation is required.

Up to now, we discussed only temperature field near the top surface. Temperature field near the bottom surface is also deviated from the solution of the 1D approximation. It can be concluded from a simple energy balance consideration that the profile of the bottom part is also rounded as P'Q' shown in figure 2-7 and the displacement of P' from the straight line of the 1D solution is given also by Δ .

The peculiarity of the kerf front profile near the top surface analysed in this section may be related to generation of melt flow instability from the surface. For example, Golubev stated that melt ejection becomes intermittent when the overlap distance Δ becomes small compared with the characteristic length (κ/V_c) of the temperature field along the cutting direction [Golubev 2004]. This point will be discussed in section 3.3.

2.3 Hydrodynamics

2.3.1 Mechanisms of melt ejection

Molten material created on a kerf front is pushed down on the front and is ejected from the kerf. In the previous theoretical studies, two principal mechanisms were considered in the ejection process. One is vertical ejection by assist-gas force and the other is lateral ejection by recoil pressure (figure 2-8). However, our experimental study on the recoil pressure (Annex 2) clarified that lateral ejection by the recoil pressure can be neglected as far as the surface temperature of the melt layer is below the boiling point of the material. Thus we will focus on the ejection by assist-gas in the following discussion of the analyses of the melt layer.

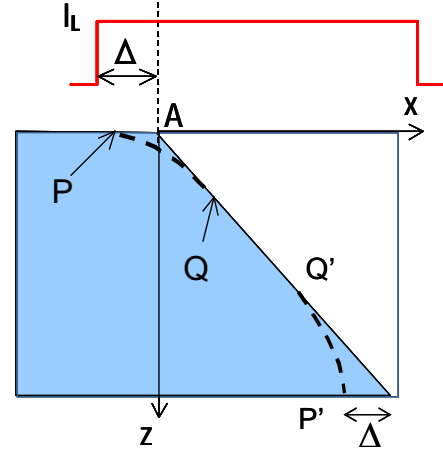


Figure 2-7: Compensation of the temperature drop and modification of the kerf front profile.

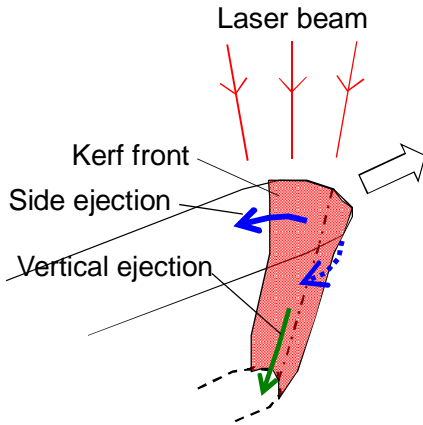


Figure 2-8 Ejection of molten material from the kerf.

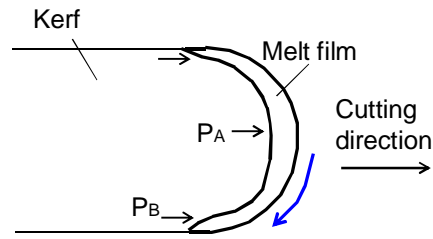


Figure 2-9 Cross section of a kerf front viewed from the above.

The reason why the recoil pressure does not contribute to the ejection process is briefly explained in the following. First of all, one must note that driving force of the lateral ejection is the pressure difference between the central point and the side point on a cross-section of the kerf front (figure 2-9).

$$V_m = \sqrt{\frac{2(P_A - P_B)}{\rho_m}} \quad (2-27)$$

The result of the study in Annex 2 suggests that the pressure P_A , which is a function of the temperature T_{sA} at A, is approximated as

$$\begin{aligned} P_A &= P_{A0} & (T_{sA} < T_1) \\ &= 0.6 p_{sat}(T_{sA}) & (T_{sA} > T_1) \end{aligned} \quad (2-28)$$

where P_{A0} is the pressure at A induced by the assist-gas even at room temperature. The temperature T_1 is given by

$$P_{A0} = 0.6 p_{sat}(T_1) \quad (2-29)$$

Figure 2-10 shows dependence of P_A on T_{sA} for the case of $P_{A0} = P_{amb} = 1$ bar. Obviously P_{B0} depends on the surface temperature T_{sB} at B in the same way (P_{B0} is the pressure at B induced by the assist-gas.). The important conclusion is that, when temperatures T_{sA} and T_{sB} are both less than T_v , $P_A = P_{A0}$ and $P_B = P_{B0}$, so that recoil pressure cannot generate a driving force for side ejection. Of course, $(P_A - P_B)$ can generally take a non-zero value depending on assist-gas pressure field inside the kerf. But the lateral melt flow generated from this pressure difference has nothing to do with the recoil pressure.

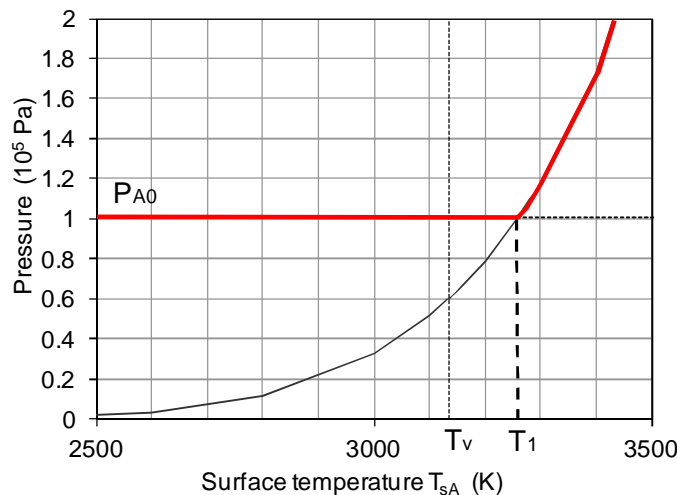


Figure 2-10 Temperature dependence of P_A .

2.3.2 Characterisation of gas flow field

There are two driving forces for melt ejection from a kerf by the force of assist-gas during laser cutting of steel: the pressure gradient and the shear stress [Vicanek 1987-2]. It is thus important to evaluate distributions of the gas velocity $v_g(x)$ and the gas pressure $p(x)$ inside a kerf front. A number of works have been conducted to characterise the gas field. Let us begin with a short overview of the previous studies.

In inert gas laser cutting we use high pressure for assist gas, typically more than 10 bar. As is well known, when the stagnation pressure P_{res} in a nozzle satisfies

$$\frac{P_{res}}{P_{amb}} > \left(\frac{2}{1+\gamma} \right)^{\left(\frac{\gamma}{1-\gamma} \right)} \quad (= 1.89 \text{ for } \gamma = 1.4) \quad (2-30),$$

a free jet from the nozzle becomes supersonic. Here γ ($= 1.4$ for N_2) is the adiabatic exponent. Moreover, when

$$\frac{P_{res}}{P_{amb}} > \left(1 - \frac{1-\gamma^2}{2\gamma} \right)^{\left(\frac{\gamma}{\gamma-1} \right)} \quad (= 2.81 \text{ for } \gamma = 1.4) \quad (2-31),$$

the jet involves a shock-wave. The pressure distribution around the kerf front becomes quite non-linear in this case.

An example of experimental measurement of the pressure distribution can be found in [Ward 1984, Fieret 1986-1, Fieret 1986-2]. The pressure distribution of an assist gas jet from circular and non-circular nozzles was measured with a piezoelectric device, which was placed below a pinhole drilled on a workpiece. When a shock was formed the pressure decreased sharply as the stand-off distance from the nozzle exit to the workpiece surface increased. The pressure shows a recovery at a distance if the nozzle pressure is not too high, but if the nozzle pressure becomes higher than ~ 4 bar, this recovery of the pressure cannot be obtained any more. In inert gas laser cutting the pressure is usually higher than 10 bar. The experimental result suggests that the stand-off distance must be very small, and also that the cutting result will be very sensitive to the stand-off distance or the nozzle alignment.

The studies mentioned above measured the total pressure on a workpiece surface. In a real kerf, the pressure distribution should be more or less modified. Although measurement of the pressure distribution inside a kerf is quite challenging, gas flow inside a kerf can be assessed from a shock structure which is observed, for example, with the Schlieren method [Zefferer 1991] or a shadowgraphic technique [Man 1999]. In these measurements, real metallic samples were replaced with glass sheets for visualisation. The results of the observations were correlated with real cutting experiment. For instance, it was reported that a separation of a boundary layer from the kerf wall, which is caused by a positive pressure gradient, reduces efficiency of melt ejection and degrades cut surface quality [Zefferer 1991, Duan 2001-3].

Along with the experiments, theoretical investigations have been carried out on dynamics of free gas jet with a CFD calculation [Chen 2000] or with a mathematical model [Duan 2001-4]. Distribution of supersonic gas flow field inside a cut kerf was also investigated with the mathematical model [Duan 2001-2]. These numerical results as a whole show reasonable agreement with the experimental measurements. These theoretical models can be used to estimate distributions of $v_g(x)$ and $p(x)$ inside a real kerf.

In conclusion of this short review, it can be said that we understand the characteristics of the gas field rather well. In this study, a weak gas jet near subsonic regime will be mainly used, since the supersonic gas flow is really sensitive to operating parameters and is not appropriate for a systematic study where assist gas condition is varied in a wide range. A numerical simulation by Kovalev *et al.* [Kovalev 2008] demonstrates that such a jet with low pressure can propagate inside a kerf for a long distance without a strong decay. The use of a weak gas jet seems to be justified also from a

presumption that complex structure of a supersonic gas flow is not the principal mechanism of the striation generation. In order to improve distribution of gas field, a number of experiments have been carried out with different configurations: Laval nozzles, non-circular nozzles, additional oblique nozzles, and so on. However, striations have never disappeared in spite of these efforts, which suggests that the fundamental cause of striations has little to do with a detailed gas flow structure of a supersonic jet. Of course, it is worthwhile to keep in mind that, once the fundamental mechanism of striation generation has been clarified, it will open a possibility to facilitate further optimisation of the gas field distribution for the improvement of cut surface quality.

2.3.3 Dynamics of melt film ejection

If a kerf front profile and distribution of gas field are given, we can calculate melt film dynamics in principle. The solution is given from three-dimensional Navier-Stokes equations. However, a complex numerical simulation is required to obtain the solution. In this section, simplified analyses are described. As shown in figure 2-11, we assume that the solid-liquid interface is parallel to the axes of laser beam and assist-gas nozzle. The solid part is homogeneously melted at the interface and the inflow rate of material into the melt layer from the melting front is constant at V_c over the entire kerf front.

In the most simplified analysis, thickness δ_m of the melt film is represented by a single value and variation of thickness along the x axis is neglected. If we define at the exit of the kerf the mean velocity U_e of melt ejection and the melt film thickness δ_{me} , mass balance equation can be written as

$$hV_c \approx \delta_{me}U_e \quad (2-32)$$

where h is the sample thickness. Another equation can be obtained from consideration of momentum balance. For example, if the gas force is dominated by a shear stress τ , one obtains:

$$\eta_l \left(\frac{2U_e}{\delta_{me}} \right) \approx \tau \quad (2-33)$$

where η_l is the viscosity of the melt. Here we assumed a linear distribution of the melt flow velocity across the thickness and utilised a fact that the velocity at the melt surface becomes twice as the mean velocity U_e . The analytical expression τ is obtained from consideration of turbulent boundary layer of gas near the interface [Mas 2003-1]:

$$\tau = \frac{f}{4} \frac{\rho_g v_g^2}{2} \quad (2-34)$$

where the coefficient f is a function of the Reynolds number of the gas flow. From eqs.(2-32) to (2-34) one can calculate U_e and δ_{me} for a given condition of h , V_c , v_g and ρ_g .

Vicanek *et al.* [Vicanek 1987-1] carried out a more detailed analysis on the dynamics of molten material inside the melt film using a set of incompressible Navier-Stokes equations:

$$\frac{\partial U}{\partial x} + \frac{\partial V}{\partial y} = 0 \quad (2-35)$$

$$\rho_l \left(U \frac{\partial U}{\partial x} + V \frac{\partial U}{\partial y} \right) = -\frac{dp}{dx} + \eta_l \frac{\partial^2 U}{\partial y^2} \quad (2-36)$$

Boundary conditions are as follows:

$$U = 0, V = V_c \quad \text{at } y = 0 \quad (2-37)$$

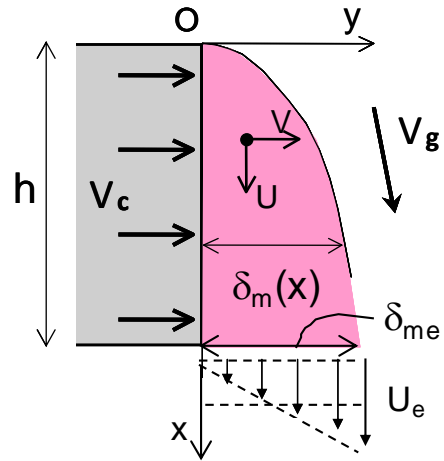


Figure 2-11 Schematic of boundary flow of molten liquid.

$$\eta_l \left(\frac{\partial U}{\partial y} \right) = \tau \quad \text{at } y = \delta_m \quad (2-38)$$

$$\frac{\partial \delta_m}{\partial t} + U \frac{\partial \delta_m}{\partial x} = V \quad \text{at } y = \delta_m \quad (2-39)$$

The first boundary expression concerns inlet of mass flow, as cutting proceeds with the speed of V_c . The next equation is required from a balance of shear stress at the liquid-gas interface. The last one concerns continuity of surface.

In this paper [Vicanek 1987-1], an analytical solution was shown for the case of $Re = (\rho U \delta_m / \eta_l) \rightarrow 0$ (i.e. very small inertia). Under our assumption of neglecting pressure gradient term, the solution becomes

$$U = \frac{1}{\eta_l} \left[\tau y - \frac{\partial p}{\partial x} \left(\delta_m y - \frac{y^2}{2} \right) \right] \quad (2-40)$$

$$V = V_c + \frac{1}{\eta_l} \frac{\partial p}{\partial x} \frac{\partial \delta_m}{\partial x} \frac{y^2}{2} \quad (2-41)$$

$$\frac{\delta_m^3}{\delta_{mp}^3} + \frac{\delta_m^2}{\delta_{m\tau}^2} = 1 \quad (2-42)$$

where

$$\delta_{mp}^3 = \frac{3\eta_l V_c x}{-\partial p / \partial x}, \quad (2-43)$$

and

$$\delta_{m\tau}^2 = \frac{2\eta_l V_c x}{\tau}. \quad (2-44)$$

When the driving force is dominated by shear stress, namely, when

$$\tau \gg \left| \frac{\partial p}{\partial x} \right| \delta_m,$$

the equations (2-40) and (2-42) can be expressed as

$$\delta_m = \sqrt{\frac{2\eta_l V_c x}{\tau}} \quad (2-45)$$

$$U = \frac{\tau}{\eta_l} y \quad (2-46)$$

The velocity along the front averaged over the melt film thickness at the position x can be calculated as

$$\bar{U} = \frac{1}{\delta_m} \int_0^{\delta_m} U dy = \sqrt{\frac{2\tau V_c x}{\eta_l}} \quad (2-47)$$

or

$$\bar{U} = \frac{\tau}{2\eta_l} \delta_m \quad (2-48)$$

These approximate equations have been used in several steady state laser cutting models that are described in section 2.4.

The melt layer thickness δ_m at a depth can be correlated with surface temperature T_s of the melt film at this depth [Mas 2003].

$$\delta_m = \left(\frac{\kappa}{V_c} \right) \ln(1 + \Lambda_m) \quad (2-49)$$

where

$$\Lambda_m = \frac{\rho_l C_{pl} (T_s - T_m)}{\rho_s [C_{ps} (T_m - T_0) + L_m]} \quad (2-50)$$

As can be seen from eqs.(2-45) , (2-49) and (2-50), with an increase of V_c , δ_m as well as T_s are increased.

2.4 Coupled analytical models

There exist several theoretical models which describe steady state laser cutting. These models, regardless of the dimension of 2D or 3D, aim to obtain a kerf front profile in equilibrium state for a given set of operating parameters. The models treat differential equations that describe each of the above processes: absorption of a laser beam, heat conduction, gas flow inside a kerf, and hydrodynamics of the melt film. The resultant kerf front profile and the characteristics of melt flow (thickness, velocity and temperature) have to satisfy all the equations for different phenomena, so the problem has to be solved self-consistently.

The first model of this kind was developed by Schulz *et al.* [Schulz 1989]. The model deals with a three-dimensional kerf front. The calculation process in each of the iterations is summarised as follows. First, gas field is calculated for a kerf front profile that has been determined by the previous iteration. Then, using the information of the kerf front profile and the obtained gas field, Navier-Stokes equations are solved to obtain melt flow field. This yields distribution of melt film thickness over the kerf front. With this information heat conduction calculation is performed to obtain distribution of heat flux injected at each point of the kerf front surface. Finally, the obtained heat flux as well as the laser beam intensity distribution are used to calculate local inclination angle of the kerf front surface. This geometrical information provides a new kerf front profile. These processes are repeated until the change of the kerf front profile becomes negligible.

It was reported that a better agreement with experiments was made possible with consideration of a three-dimensional melt flow. Compared with the above-mentioned 2D model of melt film dynamics by Vicanek [Vicanek 1987-1], the three-dimensional model yielded thinner melt film thickness due to escape of the melt from the central part to the sides of the kerf. The decreased thickness provided a better agreement with experiments and a better estimation of surface temperature of a kerf front [Schulz 1989]. Influence of several operating parameters was investigated with this model. (1) Assist-gas velocity had negligible influence. (2) Reduction of beam diameter with a constant laser beam power resulted in increase of cutting speed. (3) Increase of cutting speed raised inclination angle of a kerf front. When the cutting velocity was increased, however, the kerf front profile in the x-y plane became a rectangular shape. This does not agree with what is observed in a real cutting experiment. It seems that this discrepancy originated from some assumption related to the 3D model.

The second model that has to be referred to is a 3D analytical model developed by Petring [Petring 1994]. In this model, a kerf front profile on the i th thin crosssection parallel to the sample surface is assumed to be semi-circle with radius r_{ki} . Melt layer thickness δ_{mi} is constant all over the semi-circle. Three parameters δ_{mi} , r_{ki} , and the centre of the semi-circle were determined from three balance equations: mass balance of the melt flow, energy balance, and heat flux at kerf sides. The Fresnel absorption law was used to calculate the energy absorbed to a segment of the semi-circle [Petring 1988]. It was shown that results of the calculations under these assumptions reproduce fairly well experimental results. Several differences can be mentioned compared with the model by Schulz *et al.* [Schulz 1989]. Concerning modelling of a melt layer, thickness δ_m of the layer was assumed to be constant along the semi-circle. Also recoil pressure was taken into account to express lateral melt ejection to kerf sides, whereas in the model by Schulz melt ejection was naturally induced from the three dimensional Navier-Stokes equations. As regards the energy balance equation, Petring considered convection of molten material on a kerf front. This convection was neglected in the model by Schulz.

A similar model in 2D was developed by Mas *et al.* [Mas 2003-1, Mas 2003-2]. Two parameters,

inclination angle α_i of the kerf front and melt layer thickness δ_{mi} were defined to express kerf front profile and melt layer thickness distribution. These two parameters were determined from two sets of equations of mass flow balance and energy balance. Melt ejection to kerf sides by recoil pressure was also taken into account as in the model by Petring. Results of the calculations agreed well with experimental results.

Kovalev *et al.* [Kovalev 2001] developed a more complete 2D mathematical model. Heat transfer and melt film dynamics were solved in a fully coupled manner. Although cutting depth was limited to a range less than 0.5 mm, the calculated cutting depth and maximum cutting velocity showed a good correlation with experimental values.

One of the interesting results in [Kovalev 2001] is that the above approximate solutions shown in (2-45)-(2-48) were validated numerically in the range of $Re = 30$. This is quite reasonable; a small Re number means that the melt flow is dominated by viscosity rather than inertia. The distribution of velocity of the melt at some point of z can be equilibrated rapidly to a linear distribution, regardless of the melt flow velocity field in the upstream or of the inflow and outflow conditions.

All of the above-mentioned models take into consideration variation of δ_m as a function of z . This makes the solution process rather complicated and necessitates an iteration process. One way to simplify the problem is to neglect the variation of δ_m and to assume a constant δ_m all along the kerf front from the upper surface to the bottom. This assumption was used in several theoretical studies [Schuöcker 1987, Kaplan 1996, Quintero 2005]. These mathematical models also showed good agreement with experiments.

Another way to simplify the formulation of the melt layer is to disregard it completely. Duan *et al.* [Duan 2001-1] neglected completely melt film dynamics. It was assumed that heated material is removed when the surface temperature reaches a threshold temperature $(T_m+T_v)/2$. Although this assumption might seem crude, the model predicted well the maximum cutting speed experimentally observed.

In summary, a number of mathematical models have been proposed and they have succeeded to predict experimental cut depth or maximum cutting speed. Various methods for the formulation of melt layer have been proposed, but all of the different methods can predict well cut depth or cutting speed. It appears that the cut depth or speed does not depend so much on how the melt film dynamics is modelled. This is not surprising, since the error related to estimation of the averaged temperature of a melt layer front, which directly influence the cut depth or speed according to the energy balance, is not so large. For example, enthalpy required raising temperature up to $(T_m+T_v)/2$ differs from enthalpy that is required only to melt only by 30 %.

These models, however, are not capable to predict striation generation, since they assume an equilibrium state and thus cannot deal with such a time dependent process.

2.5 Summary

Fundamental physical processes involved in laser cutting of steel (laser beam absorption on kerf front, heat transfer and melting of the front, and dynamics of melt film ejection) are explained and discussed.

Concerning the absorption process, several fundamental experiments have been carried out to investigate the applicability of the Fresnel absorption law to laser cutting process. The experimental study on the angular dependence of absorptivity clarified that the law is applicable to a range of high incidence angle, which is usually encountered in laser cutting. The measurement of absorptivity as well as temperature of a surface during laser pulse irradiation showed that the Fresnel law can be extrapolated to a high temperature range over T_m with the complex refractive index obtained at room temperature. In addition, absorptivity in actual laser cutting was evaluated from experimental measurement of power transmitted down through a kerf. The obtained value of absorptivity (~ 60 %)

shows a reasonable agreement with the theoretical Fresnel law. Therefore, it can be concluded that the Fresnel absorption law should be a good approximation to evaluate the absorptivity of laser beam on a kerf front.

Heat transfer process in solid phase was analysed based on power balance equations. The inclination angle α of the kerf front was estimated from a power balance per unit thickness of the sample, including the effect of heat conduction loss. An important result for the upcoming discussion on the instability of the melt flow is that the inclination angle α increases with the cutting velocity V_c . For top-hat intensity distribution of the laser beam, this analysis predicts a straight kerf front with constant α over the sample thickness. This is not exactly true, however, for regions near the top and bottom surfaces, since heat flux along the direction of the laser beam axis is not compatible with the 2D approximation for a plane with unit thickness of the sample. Modification of the kerf front profile due to this consideration of the vertical heat flux was analysed for the top-hat intensity distribution. It was shown that the profile near the top and bottom surfaces is not straight but is rounded. This peculiarity at the top surface may be related to striation initiation from the surface.

Then the process of melt ejection from a kerf by an assist-gas jet was discussed. In the previous theoretical studies, two principal mechanisms were considered in the ejection process. One is vertical ejection by assist-gas force and the other is lateral ejection by recoil pressure. However, our experimental study on the temperature dependence of the recoil pressure clarified for the first time that lateral ejection by the recoil pressure can be neglected as far as the surface temperature of the melt layer is kept below the boiling point of the material. This result enables us to focus on the ejection by assist-gas force in the following analyses of the melt layer. This is very important because it greatly simplifies the analyses.

Finally, we reviewed theoretical steady state laser cutting models which solve self-consistently coupled differential equations for each of the above processes. Although these mathematical models have generally succeeded to predict experimental cut depth or maximum cutting speed, they are not capable to predict striation generation, since they assume an equilibrium state and thus cannot deal with such a time dependent process. In the next chapter we review theoretical models that can deal with time dependent fluctuations in related physical processes.

Chapter 3. Review of theoretical studies on instability in melt ejection process

Résumé

Dans ce chapitre, différents modèles théoriques décrivant diverses instabilités dans le processus de fusion et d'éjection du liquide métallique sont passés en revue. Bien qu'à cette étape dans notre étude, nous ne connaissions pas quel est le modèle adapté à la description de la génération des stries lors du processus de découpe laser, cette revue des différentes hypothèses servira de base à la discussion des mécanismes de génération des stries.

D'abord, le mécanisme de génération des stries lors de la découpe laser sous oxygène, comme gaz d'assistance est expliqué, et il est significatif de noter les différences des mécanismes de génération des stries avec la découpe sous gaz inerte. Puis des modèles qui dépendent du temps et qui décrivent la fusion et l'éjection de liquide pendant la découpe avec un gaz inerte sont abordés. Enfin, plusieurs mécanismes proposés pour la génération des stries sont décrits.

3.1 Découpe sous oxygène :

Contrairement au cas de la découpe laser avec un gaz inerte, le mécanisme de la génération des stries dans le cas particulier de la découpe laser de l'acier sous oxygène est bien compris et admis. Dans ce cas, le fer est oxydé par l'oxygène et l'énergie libérée par cette réaction crée une vague de combustion, qui peut se déplacer plus rapidement que la vitesse de découpe V_c , quand V_c est faible. En conséquence, le front de la vague de combustion oscille par rapport au faisceau laser et cette oscillation produit des stries sur les côtés de la saignée.

3.2 Modèles dépendants du temps en découpe laser sous gaz inerte :

Les modèles qui décrivent des caractéristiques dépendant du temps en découpe laser avec un gaz inerte peuvent être classés suivant trois types :

(i) Modèles qui traitent seulement des fluctuations de l'interface gaz-liquide.

Dans ce cas, l'instabilité d'une surface de métal fondu est provoquée par une interaction entre l'écoulement de liquide et le jet intense du gaz d'assistance. On suppose que l'interface solide-liquide est stable. En d'autres termes, on admet que la vitesse de déplacement du front de fusion est constante et égale à V_c . Vicanek *et al.* [Vicanek 1987-1] ont analysé le développement d'une petite perturbation qui est ajoutée à un écoulement de liquide dans un régime stationnaire. Pour un écoulement contrôlé par un gradient de pression du jet de gaz, ils concluent qu'une petite perturbation peut être amplifiée et que la longueur d'onde à laquelle ce taux de croissance d'amplitude devient maximal correspond à une fréquence de 2,5 kilohertz pour un ensemble typique des paramètres opératoires. Chen et Yao [Chen 1999] ont étudié l'instabilité de l'écoulement basé sur le mécanisme d'une perturbation de la contrainte de cisaillement issue du jet. Ce mécanisme avait également été analysé par Craig *et al.* [Craig 1966].

(ii) Modèles qui analysent seulement des fluctuations de l'interface solide-liquide.

Dans ce cas, une fluctuation apparaît seulement à l'interface liquide-solide. Les instabilités dans la couche de liquide sont négligées. Plusieurs modèles analysent la dynamique de l'interface liquide-solide lorsqu'une petite perturbation est ajoutée à cette interface. Ces modèles étudient l'évolution du front avant de la saignée basée sur la vitesse locale de perçage qui dépend de l'intensité du faisceau laser absorbé localement et de l'angle α d'inclinaison local du front. Quand une petite région (un « plateau », où α est très élevé) apparaît sur le front avant de la saignée, l'intensité absorbée devient alors plus élevée et amplifie l'effet, de sorte qu'un « perçage » local se produit. Cette petite perturbation est alors convectée vers le bas. Ce genre de réponse a été montré analytiquement [Makashev 1992, Niziev 1993] et numériquement [Matsunawa 1997, Semak 1999].

(iii) Modèles qui prennent en considération ces deux types d'effets.

Il y a eu plusieurs modèles qui ont considéré les deux fluctuations mentionnées ci-dessus. Schuöcker [Schuöcker 1987] a analysé un système couplé à l'aide d'un modèle simplifié, et a trouvé une fréquence de résonance, qu'il considère être la fréquence de la génération périodique des stries. Schulz

et al. [Schulz 1999] ont analysé un modèle dynamique plus complet des procédés de fusion et d'éjection du liquide. Ils ont finalement conclu que le front avant de la saignée et la couche liquide dans ce système couplé sont intrinsèquement instables et ont proposé un paramètre c_0 qui pilote le degré de cette instabilité [Poprawe 2010, Vossen 2010].

3.3 Modèles de génération des stries de découpe :

Plusieurs types de mécanismes ont été suggérés théoriquement pour expliquer la génération des stries dans la découpe laser d'acier avec un gaz inerte. La première idée est d'attribuer la création des stries à une fluctuation externe des paramètres opératoires tels que la puissance laser et/ou le débit de gaz, qui perturbent alors les bilans énergétique et d'impulsion. La deuxième proposition concerne l'instabilité hydrodynamique induite dans la couche liquide pendant son interaction avec le jet de gaz. Il semble cependant, que ces deux mécanismes ci-dessus ne sont pas les mécanismes principaux de génération des stries. Dans l'un ou l'autre de ces cas, une perturbation pourrait alors être créée n'importe où sur le front avant de la saignée. En revanche, l'observation expérimentale de ces stries suggère qu'elles sont créées à partir de la surface supérieure, probablement en raison d'une certaine instabilité, et sont ensuite transportées vers le bas avec en fait peu de perturbation. Jusqu'à présent deux mécanismes pour l'initiation des stries de la surface supérieure ont été proposés : L'un des mécanismes concerne la surchauffe de la partie supérieure de la saignée. Cette surchauffe retarde l'éjection du liquide de la surface supérieure. Ce modèle, cependant, n'explique pas l'origine de cette surchauffe. L'autre mécanisme concerne la force de tension superficielle, qui retient le matériau fondu pendant une courte période de temps, à la surface supérieure et il s'en suit ainsi une éjection intermittente du métal fondu. Il est intéressant de noter que cet effet de la tension de surface peut être également à l'origine de la surchauffe de la zone mentionné ci-dessus.

En résumé, un nombre conséquent de modèles théoriques et d'hypothèses concernant ce processus de la génération des stries a été proposé. On ne peut pas dire qu'une conclusion évidente s'impose, et cela principalement en raison d'un manque certain de données expérimentales. Des observations expérimentales sont donc nécessaires et vont faire l'objet du prochain chapitre.

Introduction

In this chapter, different theoretical models on instability in melting and melt ejection processes are reviewed. Although at the present stage we do not know which model is the one that describes striation generation process in a real cutting process, this review of different hypotheses will become a basis of our discussion on the mechanism of striation generation.

First, striation generation process in oxygen laser cutting is explained, since it might be suggestive to note differences from striation generation in inert gas laser cutting. In this special case, the model of cyclic activation and extinction of oxygen combustion which takes place in front of the laser beam can explain striations created on kerf sides.

Then time-dependent models that describe melting and melt ejection processes during inert gas laser cutting are summarised. We describe these models, dividing them into three types: the models which consider only time dependent fluctuation of gas-liquid interface; those which take into account only fluctuation of solid-liquid interface; and those which deal with both of the above. In general, these models predict that, once a small perturbation is added to a stationary kerf front, the perturbation is transported down to the bottom of the kerf front. However, the problem is that the origin of the small perturbation has never been understood. There have been proposed several different mechanisms such as oscillation of operating parameters, interaction between melt film and a strong assist-gas gas jet, peculiarity of heat conduction near the sample surface, and surface tension of the molten material. In order to conclude about the mechanism, however, experimental observations are required.

3.1 Model for oxygen laser cutting

Although this work investigates inert gas laser cutting of steel, it may be worthwhile to mention the mechanism of striation generation process during oxygen gas laser cutting of steel. Figure 3-1 schematically shows the striation generation process proposed by Arata *et al.* [Arata 1979]. In oxygen laser cutting, the following exothermic reaction takes place on a kerf front: $\text{Fe} + (1/2)\text{O}_2 \rightarrow \text{FeO}$. The energy released by this reaction is 272 kJ/mol. When temperature of the kerf front reaches a threshold value T_{th} , this reaction can spread autogenously. Let us suppose that at some instance the temperature of kerf front becomes T_{th} . Then the exothermic reaction is ignited and the kerf front can spread faster than the beam travelling speed V_c . But this reaction ceases when the kerf front moves too far away from the laser beam, into a region where the temperature is not elevated sufficiently. Then the kerf front stops there and waits for the laser beam. As the laser beam catches up the front, the temperature begins to increase again. When the temperature exceeds T_{th} , the process described above is repeated. Such periodic advance of the kerf front leaves an undulating profile structure on kerf sides.

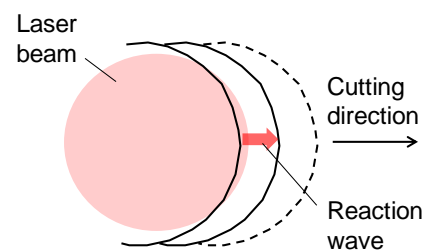


Figure 3-1 Striation generation process during oxygen laser cutting.

This qualitative explanation was successfully validated by a numerical simulation [Ermolaev 2009]. A three dimensional code which couple heat transfer and hydrodynamics was developed with allowance for the exothermic reaction on the kerf front. It was shown that periodic striations appear on cut surfaces at a low cutting velocity V_c , but they disappear at a high V_c . This agrees well with experimental observations [Arata 1979].

3.2 Time dependent models of inert gas laser cutting

A number of models have been proposed to describe time dependent characteristics in inert gas laser cutting. These models can be divided into three types as shown in figure 3-2. In the first type of models (figure 3-2(a)), time dependent fluctuation of gas-liquid interface is only analysed. In the second type (figure 3-2(b)), only fluctuation of solid-liquid interface is considered. In the last type (figure 3-2(c)), both of the above are taken into account. In the following, these different types of models that have been proposed are briefly reviewed.

3.2.1 Fluctuation of gas-liquid interface

In this case, instability of melt film surface is caused by interaction between melt flow and strong assist-gas jet. The solid-liquid interface is assumed to be stable. In other words, the displacement velocity of the melting front is assumed to be constant at V_c .

Vicanek *et al.* [Vicanek 1987-1] analysed influence of a small perturbation that is added to a flow in an equilibrium regime shown in Eqs.(2-40) to (2-44). After a complex calculation, it was concluded that a flow driven by pressure gradient is less stable than a flow driven by shear stress. The growth rate of amplitude for a small perturbation depends on the perturbation frequency and it becomes maximum at about 2.5 kHz for a typical set of operating parameters. This frequency was considered as the frequency of striation generation.

Tsai and Weng [Tsai 1993] added heat transfer process to this model by Vicanek *et al.* The solid liquid interface was assumed to be stable (straight), although the instability in heat transfer process should involve fluctuation of the melting front. They obtained an unrealistic result that melt layer thickness exhibits a sudden drop at a lower part of the kerf, for a high cutting speed. This result may be attributed to the assumption of the stable melting front, which might have been a constraint too strong.

Chen and Yao [Chen 1999] investigated melt film based on a wind-induced shear stress perturbation that had been previously analysed by Craig *et al.* [Craig 1966]. It was argued that liquid film becomes unstable when the wave-induced shear stress perturbation is larger than restoring surface tension force.

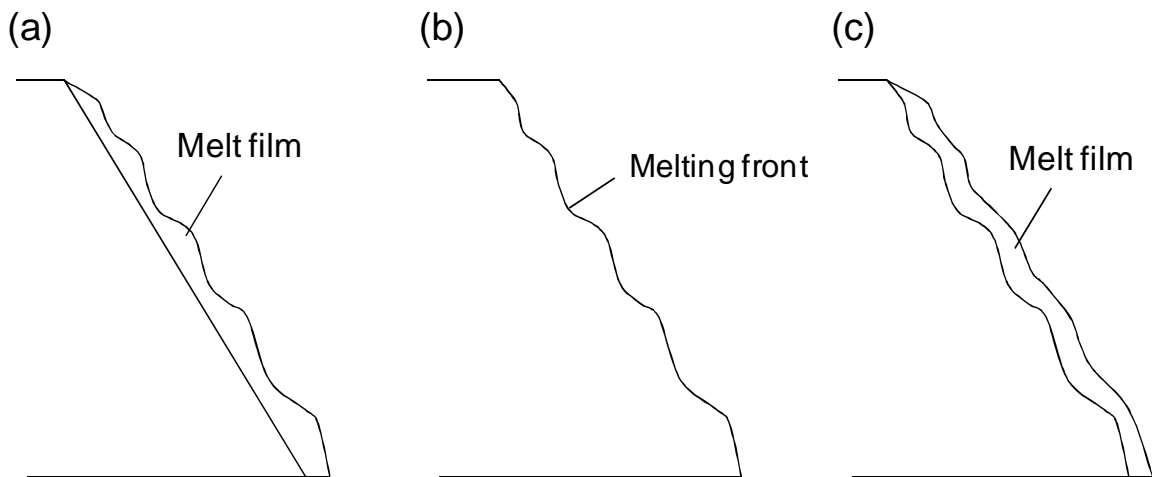


Figure 3-2 Different types of models for fluctuation analysis of melting and melt film dynamics.

3.2.2 Fluctuation of liquid-solid interface

Another approach to investigate time dependent fluctuation is to analyse only solid-liquid interface, or melting front, neglecting instabilities in the melt layer (figure 3-2(b)). There have been proposed several models which analyse dynamics of a kerf front profile when a small perturbation is added to an equilibrium kerf front profile.

Makashev *et al.* [Makashev 1992, Makashev1994] mathematically investigated evolution of a small perturbation created on a two-dimensional kerf front. Advance of a kerf front was expressed based on local drilling velocity that depends on the local laser beam intensity and the local inclination angle of the kerf front. When a shape $\varphi(z)$ of small disturbance is added at $t = 0$ to a stationary shape $x_m^0(z)$ of the kerf front profile, downward transport of this perturbation can be expressed as

$$\varphi = \varphi_0 \left(\int_0^z \frac{dy}{U_s(z)} - t \right) \exp \left(\int_0^z \frac{\theta_s(z)}{U_s(z)} dz \right) \quad (3-1)$$

where

$$\rho L_m U_s(z) = I(x_m^0(z)) \frac{d(\alpha A(\alpha))}{d\alpha} \Big|_{x_m^0} \quad (3-2)$$

and

$$\rho L_m \theta_s(z) = -\alpha A(\alpha) \frac{dI}{dx} \Big|_{x_m^0} \quad (3-3)$$

Where $A(\alpha)$ is the absorptivity dependence with local inclination α . The small perturbation is transported downwards with velocity $U_s(z)$ (in the order of 1 m/s) and the growth rate of its amplitude is given by $\theta_s(z)/U_s(z)$. The function $d(\alpha A(\alpha))/d\alpha$ is positive, so it follows that the sign of (dI/dx) determines the growth or shrink of the perturbation. The amplitude of the perturbation increases when $(dI/dx) < 0$.

Niziev [Niziev 1993] carried out a similar analysis as the analysis by Makashev *et al.* Effects of focus position and polarisation were studied with the developed mathematical model. As regards the focus position, it was recommended that a sample be placed below the focus position. It is likely that eq.(10) in [Niziev 1993] predicts growth of a perturbation when $(dI/dx) > 0$, in the notation of Makashev's model. (= If we assume cutting by a Gaussian beam with its focus position in the middle of the sample, instability is amplified in the upper half of the kerf front). This is contrary to the Makashev's conclusion. The sign of eq.(6) in [Niziev 1993] may have to be reversed.

Matsunawa and Semak [Matsunawa 1997] simulated numerically stability of a keyhole front during laser welding. Although the considered process is different from laser cutting, concept of modelling is the same as the above analytical studies. Local drilling velocity that depends on the absorbed intensity of laser beam was the source of the dynamics of the keyhole front. It was reported that humps which slide down along the front appear only for a low welding velocity. Semak and co-workers [Semak 1999] improved this semi-empirical code to a more complete numerical code by taking into account also melt film and heat transfer in a solid part and obtained essentially the same result as [Matsunawa 1997]. These papers, however, did not investigate thoroughly characteristics of the instability, for example, the threshold velocity under which the keyhole front becomes unstable.

Schulz *et al.* [Schulz 1997] analysed the advance of a kerf front with a one-dimensional model, where a kerf front is represented by a single parameter that denotes melting front position with respect to the cutting direction. Heat conduction into solid part was taken into account. It was argued that a response of the system to a small perturbation depends on a parameter $\Lambda = b_1(Pe/F')$, where b_1 is a constant (= 3/5), and F' is the normalised non-dimensional first derivative of the laser beam intensity distribution with respect to the position, measured at the melting front. It was concluded that the melt front changes its position more rapidly as Λ becomes small.

3.2.3 Coupled model

There have been several models which have considered both of the fluctuations mentioned above. Time dependent fluctuations are investigated by coupled equations for melt film dynamics and thermodynamics.

Schuöcker [Schuöcker 1987] analysed the coupled system with a simplified model, where variables related to a melt film such as ejection velocity, temperature, thickness and so forth are expressed by single representative values, neglecting distributions inside the melt film. Several balance equations on energy, momentum and mass were coupled to investigate the dynamics. The resonant frequency of the system was obtained and it was argued that this frequency corresponds to the frequency of periodic striation generation.

Schulz *et al.* [Schulz 1999] showed a more complete dynamical model of melting and melt ejection processes during laser cutting, although no concrete example of the simulation results was explained in this paper. Recently the stability of the system was analysed with a similar model [Vossen 2010, Poprawe 2010]. It was concluded that this coupled system of a kerf front and a melt layer is inherently

unstable but the system is more stable as the following parameter c_0 becomes small.

$$c_0 = \left(\frac{\delta_{me}}{h} \right) \left(\frac{I_L}{\rho L_m V_c} \right) \left(\frac{d(A(\phi_\alpha) \cos \phi_\alpha)}{d(\cos \phi_\alpha)} \right) \quad (3-4)$$

where δ_{me} is the melt film thickness at the bottom of the kerf, ϕ_α is the angle of incidence of the laser beam ($= 90^\circ - \alpha$).

3.3 On origin of striations

The above-mentioned time dependent models have been used to explain striation generation in inert gas laser cutting. Many explanations have been proposed and we classify them into four categories.

3.3.1 Oscillation of parameters

Schuöcker found a resonance frequency in a coupled system of melt film [Schuöcker 1987]. He claimed that some fluctuation of laser power or gas field can cause the melt film to oscillate at this frequency and this is the cause of striations. Schulz stated also that unavoidable oscillation of the laser processing parameters causes oscillation of the whole system [Schulz 1999].

3.3.2 Gas-melt film interaction

Vicanek *et al.* showed that a melt flow driven mainly by pressure-gradient is unstable and presumed that this instability is the cause of striations [Vicanek 1987-1]. It was argued that the oscillation frequency of the melt flow is given by the frequency at which growth rate of a small perturbation takes the maximum value. In spite of a difference in the physical mechanism that creates instability, Chen *et al.* looked at the problem in almost the same way [Chen 1999]. It was presumed that the melt film oscillation occurs at the frequency where the averaged shear stress applied from gas field takes the minimum value.

Neither of the two explanations in 3.3.1 and 3.3.2 seems to be the fundamental cause of striations for inert gas laser cutting of steel. Experiments show that striations on kerf side start from the top surface and run down quite vertically to the bottom surface. This indicates that some mechanisms of perturbation affect melt flow only near the top surface but that no perturbation occurs in a lower part. If striations were created from oscillation of laser parameters or gas melt film interaction as discussed above, one would not be able to find quite vertical striations that continue to the bottom of the kerf but would see more chaotic traces of melt film oscillations for the entire thickness. This reasoning suggests that the origin of striations must be attributed to some mechanism that perturbs melt flow near the surface.

Moreover it can be pointed out that the striations have excellent regularity in most cases and that typical pitch (wavelength) of striations is in the range of 100 μm regardless of laser oscillator or gas providing system. This also hints that the above explanations cannot be the main mechanism of the striation generation.

3.3.3 Peculiarity of heat conduction at surfaces

Kovalenko proposed that periodic removal of material is the mechanism of striation generation. Although cw laser irradiation was assumed, intermittent drilling from the top surface to the bottom was considered as the removal process. It was presumed that each drilling process is triggered when surface temperature reaches T_{th} , which is higher than T_m . When a laser beam proceeds into a sample, surface temperature increases and melting occurs. Molten material appears but it is not ejected instantaneously. The downward drilling suddenly starts when the surface temperature becomes T_{th} . After a downward stroke of drilling, surface with relatively low temperature is left and the laser beam starts to heat it again. It was predicted that this periodic process occurs only for a low cutting velocity; when cutting speed is higher than a speed of heat conduction wave, the material ejection process becomes stationary. It should be noted that this mechanism of overheating of a sample surface is very similar to the mechanism of striation generation in the case of oxygen-assisted laser cutting.

A similar analysis was carried out by Golubev [Golubev 2004]. Whereas Kovalenko assumed a top hat beam intensity distribution, Golubev assumed a Gaussian distribution. It was argued that the intermittent ejection regime is obtained when the overlap distance Δ of the laser beam with the material is smaller than the characteristic distance (κ/V_c) of the temperature field along the cutting direction inside the solid part. His analysis showed that this unstable regime appears when $Pe < 1\sim 3$ for a typical condition of laser cutting or welding with a Gaussian beam [Golubev 2004, Golubev 1995].

Golubev's analysis seems better than Kovalenko's model, in that the former does not explicitly include T_{th} , whose physical meaning is not evident for inert gas laser cutting. In this context, it may be worthwhile to extend the Golubev's analysis to a top-hat beam intensity distribution. We have already obtained in eq.(2-26) the overlap distance Δ of the laser beam with the material in the case of a top-hat intensity beam. Using the same criterion $\Delta < (\kappa/V_c)$, the intermittent ejection occurs when

$$\tan \alpha_{eq} < \sqrt{1 + St^{-1}} \quad (\approx 1.2 \text{ for steel}) \quad (3-5)$$

This criterion does not include Pe . It is not surprising from a mathematical point of view, however, since one cannot define a characteristic beam size for a top-hat distribution as the beam radius for a Gaussian beam.

The above-mentioned mechanism is promising, since the mechanism is related to a process that occurs near the surface. However, the mechanism depends upon the assumption that there occurs overheating of sample surface over T_m and it is not evident whether this overheating always takes place on the surface. The above-mentioned stationary laser cutting models do not predict overheating; it is usually assumed that at the initiation point of the melt flow at the surface, temperature is exactly equal to T_m and melt film thickness is zero. Another problem of the models by Kovalenko and Golubev is the fact that the instability is predicted only for low speed range below a threshold, while experimentally striations also appear in a wide velocity range.

3.3.4 Surface tension

Makashev proposed a more convincing mechanism for the intermittent removal of material from the surface [Makashev 1992, Makashev 1994]. It was argued that molten material cannot be ejected instantaneously after the generation, because a surface tension force retains the material at the top surface when its size is not large enough. The critical size of a melt droplet for the initiation of its ejection was estimated from a force balance analysis. Figure 3-3 shows a cross section of a kerf front in the central plane of the cutting. A melt droplet is being attached at the surface. As the size of the melt droplet increases, force exerted from a gas jet increases and it finally detaches from the surface. The critical radius δ of the droplet for this initiation of the movement is given by $\Delta P \approx \sigma/\delta$, where ΔP is a pressure drop of the gas field across the droplet and σ is the surface tension coefficient of the droplet. The pressure drop ΔP can be estimated from a decrease of the cross section of the gas flow from b to $(b - \delta)$ due to the existence of the droplet (the initial cross section of the gas flow before entering the kerf was represented by the kerf width b). Assuming that gas flow is described by an adiabatic compressive one-dimensional flow, ΔP can be calculated as

$$\frac{\Delta P}{P} \approx \gamma \frac{M^2}{1 - M^2} \frac{\delta}{b} \quad (3-6)$$

With the relation $\Delta P \approx \sigma/\delta$, one obtains

$$\delta \approx \sqrt{\frac{\sigma b (1 - M^2)}{P \gamma M^2}} \quad (3-7)$$

This size is about $60 \mu\text{m}$ for a typical processing condition for inert gas laser cutting of steel. This roughly agrees with the experimentally obtained striation wavelength.

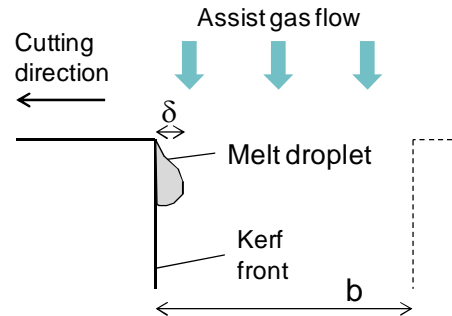


Figure 3-3 Assist gas flow around a melt droplet attached at the top part of the kerf.

3.4 Summary

In this chapter, different theoretical models on instability in melting and melt ejection processes have been reviewed. In contrast to the case of inert gas laser cutting, which is the main interest of this study, the mechanism of striation generation in the special case of oxygen laser cutting has been well understood. In this case, iron is oxidised by the assist-gas of oxygen and the exothermic energy released by this reaction creates a combustion wave. For a low cutting velocity V_c , the combustion front can travel faster than the cutting velocity V_c . As a result, the combustion front oscillates with respect to the laser beam and this oscillation creates striations on kerf sides.

Then time dependent models for inert gas laser cutting have been reviewed. Some models on fluctuation of gas-liquid interface induced by interaction between melt flow and assist-gas jet [Vicanek 1987-1, Chen 1999] predict the existence of a resonant frequency at which the growth rate of amplitude of a small perturbation is maximised. Several other models deal with fluctuation of solid-liquid interface [Makashev 1992, Makashev 1994, Niziev 1993, Matsunawa 1997, Semak 1999] and these models analyse transport of a small perturbation added to a stationary kerf front. An important outcome of these analyses is that the transport velocity and the growth rate of the perturbations are dependent on the intensity distribution of the laser beam and angular dependence of the absorptivity. Lastly there exist models which take into account both of the fluctuations of the gas-liquid and the solid-liquid interfaces. The simplified model by Schuöcker [Schuöcker 1987] predicts a resonant frequency of the whole system, similarly to the above-mentioned models on the film-gas interaction. The more complete model by Schulz and co-workers [Poprawe 2010, Vossen 2010] predicts that the coupled system of a kerf front and a melt layer is inherently unstable. The proposed stability parameter c_0 represents the dependence of the instability on the laser beam intensity distribution and the absorptivity variation as a function of α .

Several types of mechanisms have been suggested theoretically to explain the striation generation in inert gas laser cutting of steel. The first idea is to attribute the striations to external fluctuation of operating parameters such as laser power and gas flow rate, which can change the energy and momentum balances. The second proposal is hydrodynamic instability induced in the melt layer during its interaction with gas jet. It seems, however, that any of the two mechanisms is not the principal mechanism of striation generation. In either case, a perturbation would be created anywhere on a kerf front. In contrast, experimentally obtained striations suggest that striations are created at the top surface, probably from some instability, but are transported downwards with little perturbation. Two mechanisms have been proposed for the initiation of striations from the top surface. One is overheating and resultant delay of melt ejection from the top surface. This model, however, lacks explanation of the origin of the overheating. The other mechanism concerns surface tension force, which holds molten material for a short time at the surface and thus causes the intermittent melt ejection. It should be noted that this effect of surface tension can also be the origin of the above-mentioned overheating of the surface.

In summary, there have been a number of theoretical models and hypotheses for striation generation process during inert gas laser cutting. We have not reached the conclusion, however, because of lack of experimental verification. Experimental observations are thus being required.

Chapter 4. Experimental observations of striation generation process

Résumé

Le processus de génération des stries provient d'une instabilité dans l'écoulement du liquide métallique au niveau du front avant de la saignée. Une compréhension de ce processus de génération des stries nécessite donc une observation expérimentale directe du comportement de cet écoulement, et c'est donc l'objet principal de ce chapitre. Bien que Yudin *et al.* ait déjà constaté le caractère intermittent de l'écoulement du liquide, grâce à une observation transverse de la saignée (en utilisant une lame de verre transparente remplaçant un côté de la saignée), il n'a pas réussi à montrer les détails du processus de génération de cette instabilité. En fait, il s'avère que ces stries sont indépendantes les unes des autres, et comme elles s'écoulent vers le bas, elles doivent donc être générées à partir de la surface supérieure de l'échantillon. C'est donc cette zone qui a tout d'abord été analysée à l'aide d'une caméra vidéo rapide. La génération intermittente de « humps » sur la partie centrale de la saignée et le mouvement d'accumulations de matière fondue (comme de petites gouttelettes) sur le côté de la saignée ont ainsi pu être observés. Ces instabilités sur la partie centrale et sur le côté ont un comportement très différent. Ce résultat significatif n'a pu être obtenu que grâce à une disposition particulière de l'axe d'observation de la caméra vidéo rapide placé à 45°, de la direction de découpe et situé au-dessus du plan de la surface supérieure. Une étude paramétrique a ensuite été effectuée avec cette disposition de la caméra. Par la suite, afin de suivre le développement complet de l'écoulement du haut vers le bas de la saignée, nous avons repris la technique de visualisation transverse (avec la lame de verre). L'axe d'observation étant cette fois placé à 45° de la direction de découpe, dans un plan horizontal, il a été possible de visualiser en même temps l'écoulement sur le front avant de la saignée et sur son côté où les stries sont créées.

4.1 Dispositif expérimental d'observation des stries :

Dans une première série des expériences, on a donc observé l'hydrodynamique de la partie supérieure du front avant de la saignée à l'aide d'une caméra vidéo rapide placée au-dessus de l'échantillon lors de la découpe sous azote de cibles de 3 millimètres d'acier. Le faisceau du laser à disque de 8 kilowatts avait une tache focale de 1,7 millimètre de diamètre, avec une distribution d'intensité de type « top-hat ». Ce diamètre important de la tâche a été choisi afin de mieux visualiser la zone autour du front avant de la saignée et a permis de ce fait de visualiser facilement l'ensemble du processus d'initiation des stries à partir de la surface supérieure. La pression de l'azote dans le réservoir de la buse de découpe était 1,5 bar ; le diamètre de la buse, la distance buse - surface de l'échantillon étaient toutes deux de 3,5 mm.

L'écoulement du liquide montre des instabilités très caractéristiques : sur le front avant, il apparaît des discontinuités de la surface du liquide (que l'on dénommera « humps ») qui se propagent le long de celle-ci avec une vitesse, une fréquence et une amplitude qui dépendent des paramètres opératoires (vitesse de coupe, puissance laser, jet de gaz). De même, sur les côtés de la saignée, plusieurs stries sont formées par la descente quasi verticale d'accumulations de métal fondu. L'un des résultats les plus importants est que ces deux types d'instabilités présentent un comportement très différent. L'angle α d'inclinaison du front de la saignée augmente avec la vitesse de coupe V_c et on verra par la suite que ce paramètre est déterminant pour le régime de stabilité observé.

- Régimes caractéristiques :

Plusieurs régimes caractéristiques de ces instabilités ont été classifiées et dépendent de la vitesse de coupe :

Pour $1 \text{ m/min} < V_c < 2 \text{ m/min}$, à la fois la partie centrale et les côtés de la saignée présentent des discontinuités. L'existence des humps, qui glissent vers le bas le long de la partie centrale du front de la saignée, a été ainsi pour la première fois confirmée dans le processus de découpe laser. Ces humps sont en quelque sorte des plateaux ou des marches, dont l'inclinaison locale est plus importante que l'inclinaison moyenne du front. Par ailleurs, on constate que la vitesse de descente de ces humps est différente de la vitesse moyenne du liquide métallique éjecté. Ce qui montre bien que ces humps ne

transportent pas de la matière, mais représente une propagation d'onde. Pour cette gamme de vitesses de découpe, l'intervalle entre chaque hump est constant et de l'ordre de 70 microns indépendamment de V_c . De même, la dynamique de l'écoulement de liquide sur les côtés est très irrégulière et chaotique. Par exemple, une accumulation de liquide peut fusionner avec une ou plusieurs autres accumulations de liquide, lors de leur descente. On observe également dans ce régime, qu'une accumulation de liquide (donc sur le côté) et un hump (de la partie centrale) peuvent fusionner vers le milieu du front avant et descendent ensuite ensemble. En raison de ce régime chaotique, et de l'interaction possible des humps et des accumulations, les trajectoires de ces accumulations de liquide sont assez irrégulières, ainsi que les stries résultantes.

Pour $2 \text{ m/min} < V_c < 6 \text{ m/min}$, la région centrale du front de la saignée devient stable (les humps ont disparu), mais les flancs de la saignée présentent toujours des stries : Cette coexistence d'un écoulement stable dans la partie centrale et d'un écoulement instable sur les côtés est aussi un résultat original très important. Car dans la plupart des travaux théoriques antérieurs, il a toujours été admis que la partie centrale perturbait naturellement l'écoulement sur les flancs de la saignée ou était même la cause des stries. Ce type d'hypothèses doit donc être rejeté au moins pour ce régime de vitesse de découpe.

Dans cette gamme de V_c , l'écoulement le long des flancs de la saignée est caractérisé par la génération périodique d'accumulations de liquide à partir de la surface supérieure suivi de leur déplacement vers le bas. Alors que Yudin *et al.* [Yudin 2007] avaient déjà observé ce mouvement des accumulations grâce à une visualisation latérale de la saignée (en utilisant un verre transparent), notre observation montre pour la première fois les mécanismes de génération des accumulations et de l'initiation des stries. Chaque déplacement vers le bas d'une accumulation laisse une trace qui constituera la rainure des stries. Ces accumulations peuvent être absorbées par l'écoulement central stable. Quand l'inclinaison α augmente avec V_c , la distance parcourue par les accumulations de liquide, avant de rencontrer l'écoulement central, devient donc plus faible. La longueur de ces stries verticales régulières est ainsi réduite. La longueur d'ondes (ou le pas) des stries est de $199 \mu\text{m}$ à $V_c = 3 \text{ m/min}$. Un résultat important dans cette expérience est aussi que cette longueur d'onde est nettement plus grande que le pas des humps ($70 \mu\text{m}$). On constate par ailleurs une légère diminution de cette longueur d'onde des stries quand V_c augmente.

La largeur de la région instable sur le côté de la saignée diminue lorsque V_c augmente. À 6 m/min , les écoulements sur le front central et sur le côté deviennent tous les deux continus. L'écoulement instable de côté a disparu et est complètement masqué par l'écoulement central stable à $V_c = 6 \text{ m/min}$. Au-delà de cette vitesse aucune strie n'apparaît sur les côtés, bien que nous observions une très faible oscillation du niveau de la surface de l'écoulement central.

Une évolution semblable a été obtenue pour une configuration quasi-bidimensionnelle où une barre rectangulaire (simulant la zone du matériau constituant la partie centrale de la saignée) a été fondue avec le même faisceau laser se déplaçant à la même vitesse. Cette expérience nous permet d'observer uniquement les caractéristiques de l'écoulement central, les côtés de la saignée n'existant pas, donc sans aucune perturbation possible issue des côtés. La dépendance avec la vitesse de découpe de la stabilité de l'écoulement est presque identique à celle observée dans l'expérience normale de découpe. Ceci nous permet de conclure que l'instabilité observée dans la partie centrale du front avant de la saignée, dans le cas des expériences ordinaires de découpe, n'est pas provoquée par une perturbation issue des côtés de la saignée, mais doit être attribuée à une instabilité intrinsèque à l'écoulement central.

- Etude paramétrique des caractéristiques des instabilités :

L'ensemble des caractéristiques de l'écoulement de liquide ont été étudiées pour divers paramètres opératoires: pression de gaz d'assistance, puissance et diamètre du faisceau laser, distribution de l'intensité de la tache focale laser ; pour cette dernière, une distribution d'intensité quasi-gaussienne a été obtenue par défocalisation. La tendance des résultats observés était à peu près identique à celle observée et décrite ci-dessus; à basse V_c , les parties centrale et de côté du front avant de la saignée

sont instables. Lorsque V_c est augmentée, l'écoulement central fini par devenir stable.

On a vérifié que l'inclinaison front α est approximativement proportionnelle au rapport (V_c/I_L). On a vu que l'angle seuil au-dessus duquel l'écoulement central devient continu ne dépend pas de la puissance laser, pour un diamètre de faisceau fixé. On peut donc considérer que c'est l'angle α d'inclinaison qui contrôle la stabilité de l'écoulement. Cet angle seuil diminue avec une diminution du diamètre de faisceau. On a également constaté que la défocalisation changeait assez notablement la stabilité de l'écoulement. Comparé à une distribution de faisceau « top hat », l'écoulement central devient stable pour des vitesses de coupe plus faibles avec une distribution quasi-gaussienne.

Le pas de formation des humps diminue avec une augmentation de la pression de gaz et avec une réduction de diamètre de faisceau. D'autre part, il est indépendant de la puissance laser ou de la distribution d'intensité du faisceau laser.

Il existe une bonne corrélation entre les évolutions du pas des stries λ et de la rugosité R_z . Pour des vitesses V_c supérieures au seuil de stabilité de l'écoulement central, λ et R_z diminuent légèrement avec V_c . On observe un même comportement à toutes les puissances laser, bien que la gamme de vitesses où l'écoulement central est continu dépende de la puissance laser. De même λ et R_z diminuent avec une réduction du diamètre de tache focale. Un autre résultat important est la diminution de λ et R_z lors de la défocalisation.

- Visualisation de la dynamique de formation des stries :

La dernière série d'expériences a porté sur l'analyse du développement des stries à l'aide d'une caméra vidéo rapide, en utilisant une visualisation transverse (méthode de la plaque de verre), mais avec des paramètres opératoires assez proches de ceux utilisés dans un processus réel de découpe laser. La puissance laser et le diamètre de tache étaient de 4 kW et de 0,56 mm, respectivement. La pression de l'azote au niveau de la buse était 10-12 bars. Les vidéos obtenues montrent clairement le rôle de l'interaction entre les deux écoulements discutés jusqu'à présent : Quand l'écoulement central est stable, avec peu de fluctuations, les accumulations de liquide sur les côtés de la saignée descendent sans interruption verticalement vers le bas. Ces accumulations peuvent être absorbées à l'écoulement central qui est stable et les stries périodiques résultantes dans ce cas génèrent une faible rugosité des flancs. Quand l'écoulement central est instable, le déplacement des accumulations de liquide devient également chaotique et interagit avec l'écoulement instable au centre. En conséquence les flancs de découpe ont une qualité dégradée. De même, l'écoulement central devient continu quand la vitesse de découpe est augmentée ou quand on défocalise le faisceau laser.

Tous les différents résultats expérimentaux décrits ci-dessus vont être interprétés et discutés dans le prochain chapitre 5.

Introduction

Striation generation process must be related to some instability of melt flow around a kerf front. Thus the first step towards the clarification of the striation generation process is experimental observation of the instability of the melt flow, and this is the primary object of this chapter. Although Yudin *et al.* [Yudin 2007] already found intermittent nature of melt ejection in laser cutting by lateral observation of a kerf side through a glass plate, the origin of generation of this instability could not be revealed in this study. Riveiro *et al.* [Riveiro 2011] studied melt flow dynamics and influence on cut quality in CO₂ laser cutting of transparent glass. The melt flow dynamics and the dross formation at the bottom surface of the sample were analysed. The striation generation process, however, was not investigated in this work.

In general, a stripe of striations starts from the surface and continues quite vertically to the bottom. It is thus considered that the origin of the melt flow instability should not be located in the middle of a kerf front but in a region near the surface. Therefore in the first experiment, the hydrodynamics on the very top part of the kerf front is observed from the above with a high speed video camera. This configuration of the observation from the above is contrasted to the previous study by Yudin *et al.* [Yudin 2007]. In normal condition of laser cutting, the stand-off distance of the nozzle is so small, typically less than 1 mm, that we cannot observe melt flow on the kerf front. Therefore, we use a larger stand-off distance (3.5 mm) in the experiment. In addition, the assist-gas pressure is set low at 1.5 bar. In spite of these unusual gas conditions, the observed characteristics of the melt flow are not supposed to be so different from those which would be observed for a normal condition. Moreover, the observation angle is deviated by 45 degrees from the cutting direction. This allows us to see differences of melt flows between the central and side parts of the kerf front.

The observation results show striking instability of the melt flow. Intermittent generation of humps and melt accumulations are clearly observed in central and side parts of a kerf front, respectively. One of the important results is that these instabilities in the central and side parts exhibit different characteristics: the instabilities appear in the central and side parts in different cutting velocity ranges and the wavelength of striations is larger than the pitch of humps. Then a parametric study is conducted, varying different operating parameters: assist-gas pressure, laser beam power, laser beam diameter, and intensity distribution at the focus spot. These results will be used in the next chapter to discuss on the origin of the melt flow instabilities. Finally, in order to clarify downward development of the instability initiated at the surface, melt film dynamics is observed laterally through a glass plate. The observation angle is set at 45 degree from the cutting direction also in this experiment. This enables us to observe interaction of melt flows between the central and side parts and its influence to striations left on kerf sides.

4.1 Experimental setup

A laser cutting system with a fibre-delivered 10 kW disc laser beam was established in the laboratory. A picture and a schematic of the experimental setup are shown in figure 4-1 and 4-2, respectively.

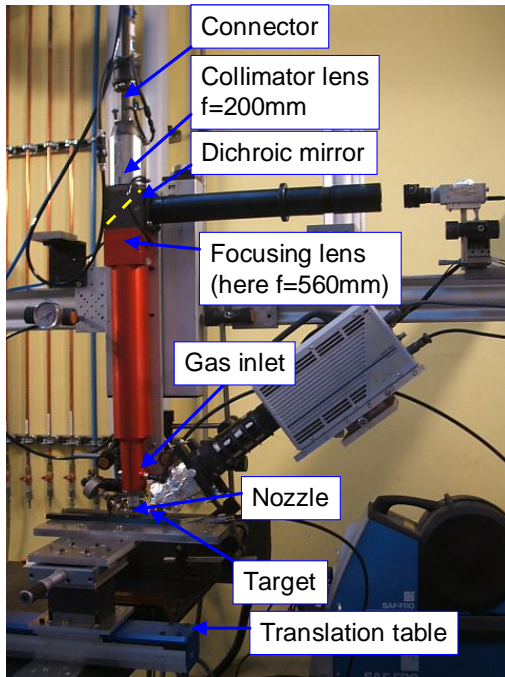


Figure 4-1 Typical experimental configuration

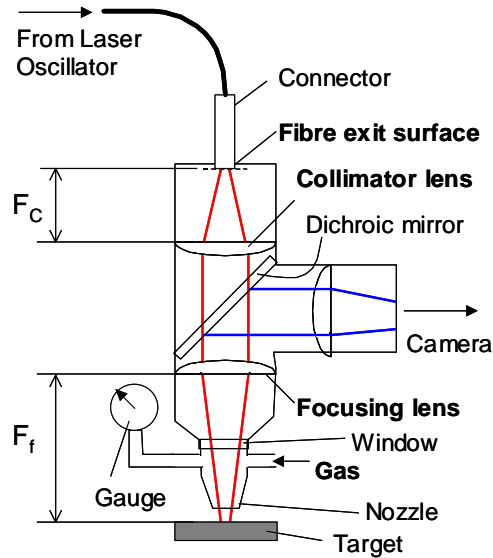


Figure 4-2 Schematic of experimental configuration.

4.1.1 Laser oscillator

A 10kW disc laser system (Trumpf, TruDisc10002) is used in this study [Trumpf WEB]. Disc laser is a type of laser in which thin discs are utilised as laser media. The media of Yb:YAG discs pumped by laser diodes emit light with a wavelength at around 1030 nm. Each disc is cooled by a heat sink from backside. Compared with conventional rod type media, large surface area of thin discs allows good heat dissipation. Consequently disc lasers have good power scalability in terms of beam quality; they can emit laser beams with a good beam product parameter even at high power.

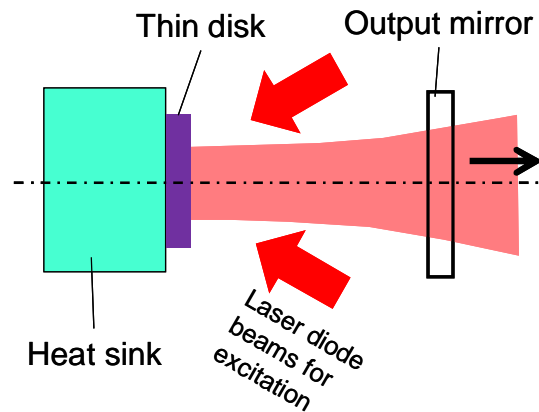


Figure 4-3 Basic concept of the disc laser.

4.1.2 Beam transfer system to target

A multimode fibre is utilised to transfer the laser beam from the oscillator to the processing head. Length of the fibre is typically 20 m. Several fibres with different core diameters $d_c = 200 \mu\text{m}$, $400 \mu\text{m}$, and $600 \mu\text{m}$ are used.

As shown in figures 4-1 and 4-2, the laser beam which comes out from the fibre passes a collimator lens and a focusing lens and reaches the target. The distance between the exit surface of the fibre and the collimator lens is adjusted to F_c , the focal length of the collimator lens, and the distance between the focusing lens and the target surface is set at F_f , the focal length of the focusing lens. In this normal configuration, the diameter of the focused laser beam d_f is given from the following formula of optical imaging.

$$d_f = \frac{F_f}{F_c} d_c \quad (4-1).$$

If the optical systems are free from aberrations, the form of the laser beam spot is exactly the same as that at the exit of the fibre, except the magnification factor expressed by eq.(4-1).

The exit surface of the fibre and the collimation and focusing lenses are all cooled using circulating water flow to avoid unfavourable heat accumulation.

4.1.3 Characterisation of focused beam

(a) Core diameter $d_c = 200 \mu\text{m}$

The power density distribution in the case of $d_c = 200 \mu\text{m}$ was analysed for several planes around the focus position with a commercial PRIMES FocusMonitor [PRIMES WEB]. This device has a small chip with a very tiny hole (diameter = $17 \mu\text{m}$), and a photo detector that measures the power of a small portion of the laser beam transmitted through the hole. By scanning the position of the tiny hole, a power density distribution can be obtained. The advantage of this method is that it allows measuring small focused beam spot directly with a relatively high resolution, which is determined by the hole size, and with a high power used in actual applications.

The results of the caustic analyses for the condition of $F_c = 200 \text{ mm}$ and $F_f = 560 \text{ mm}$ are presented in figure 4-4(a) with several power density distributions at different planes. The power density distribution at the focus is nearly top-hat. The diameter at the focus position was $560 \mu\text{m}$, which is exactly equal to the theoretical value from eq.(4-1).

At defocused positions above and below the focus position, the distribution is not top-hat, but quasi-Gaussian. This is because the plane is deviated from the imaging point of the top-hat distribution at fibre exit. Along with this change in the distribution, the diameter increases with the defocusing distance, following the beam propagation formula.

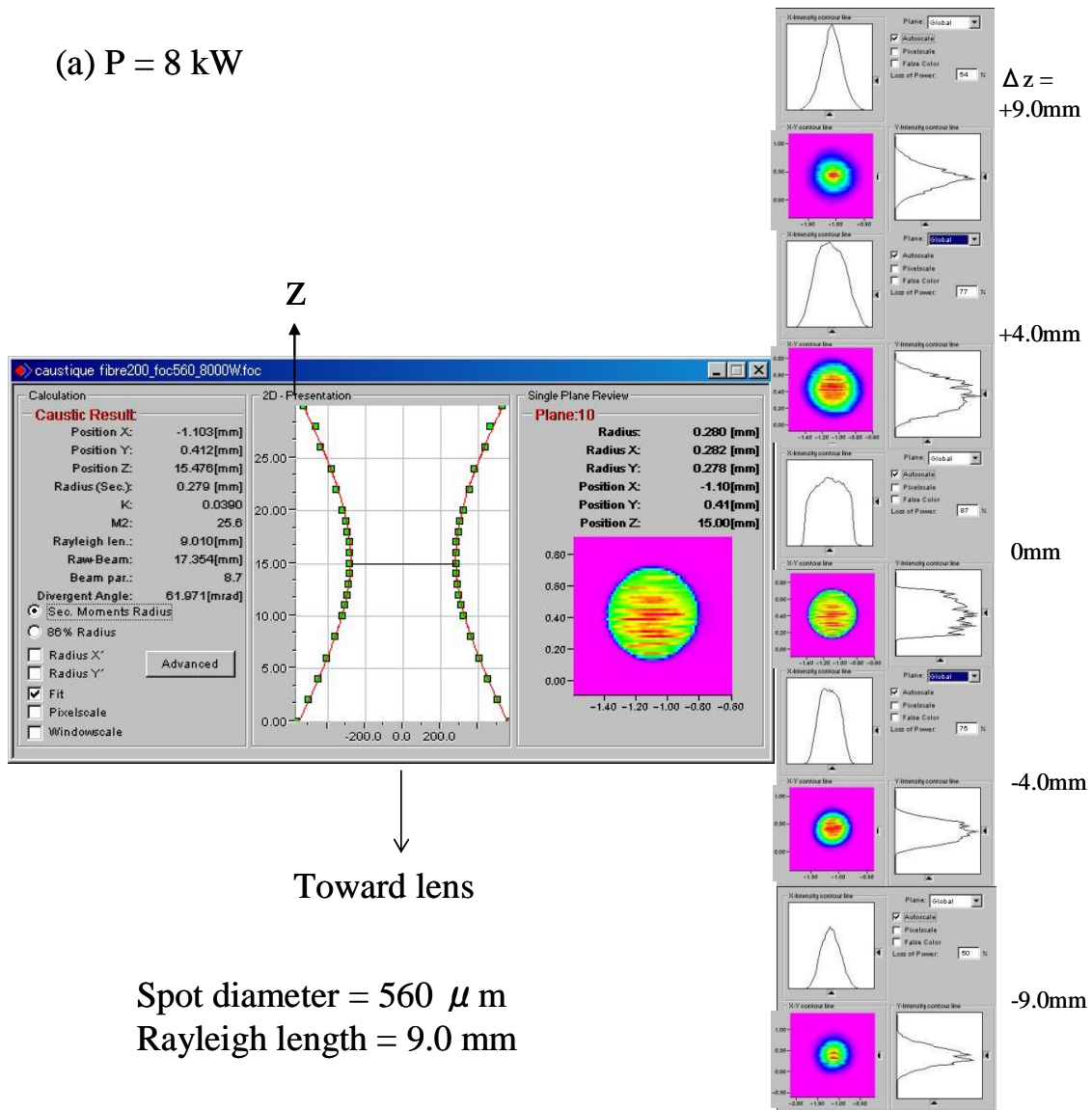
$$d_z = d_f \sqrt{1 + \left(\frac{z}{z_R}\right)^2} \quad (4-2).$$

Here z_R is the focal waist depth. It is defined as the distance of the plane where the diameter of the laser beam increases by a factor of $\sqrt{2}$, as is evident from (4-2). The software of the FocusMonitor conducts fitting with the formula (4-2) using the measured diameters at different planes and determines the Rayleigh length as a result of the best fit. The obtained value is 9.0 mm for the present case. The beam quality parameter M^2 can be calculated as 26 from the following relation.

$$z_R = \frac{\pi d_f^2}{4M^2 \lambda} \quad (4-3).$$

Power dependence of the beam focusing characteristics was also investigated. The power density distributions at focus positions are shown in figure 4-4(b) for different laser powers. One can confirm that the beam diameter at the focus position is kept almost constant even when the power is increased. It is observed that the distribution approaches top-hat with the increase of power, although the change is not so big. Although the focus spot diameter does not change, the beam quality is slightly reduced with an increase of the power: $M^2 = 24$ at 0.5 kW to $M^2 = 26$ at 8 kW .

(a) $P = 8 \text{ kW}$



(b) At focus

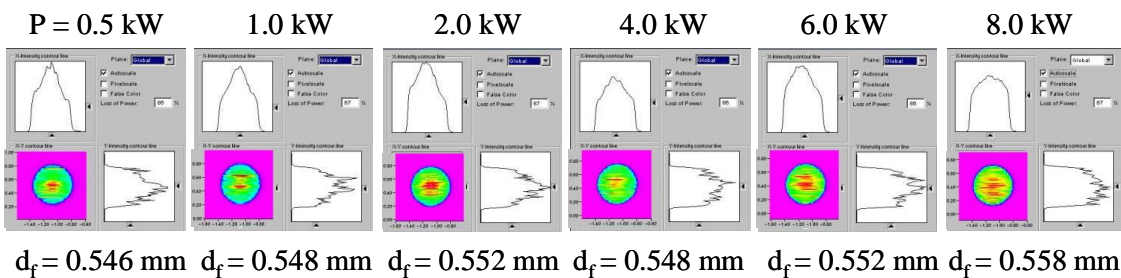


Figure 4-4 Focusing characteristics for the combination of $F_c = 200 \text{ mm}$ and $F_f = 560 \text{ mm}$; (a) caustic measurement for $P = 8 \text{ kW}$ and (b) laser power dependence of the intensity distribution at focus position.

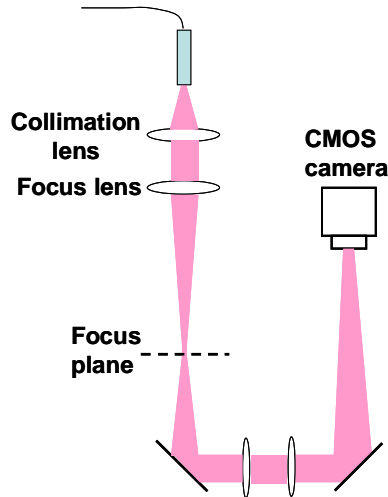


Figure 4-5 Beam profiling system with a CMOS camera.

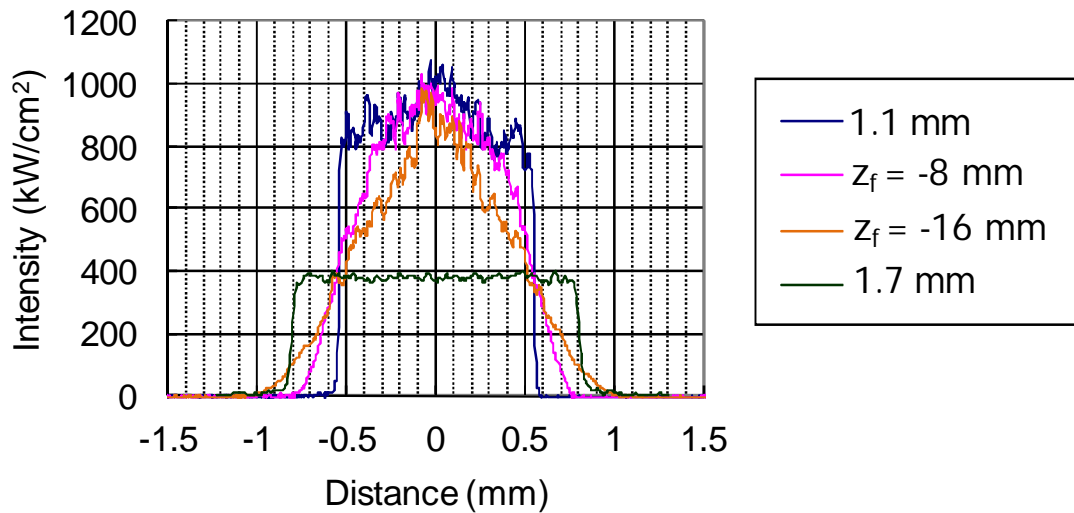


Figure 4-6 Beam intensity distributions for different focus conditions.

(b) Core diameter $d_c = 400 \mu\text{m}$ and $600 \mu\text{m}$

For fibre core diameters $d_c = 400 \mu\text{m}$ and $600 \mu\text{m}$, intensity distributions for different z planes were analysed with a homemade beam analysing system shown in figure 4-5. Intensity distribution on a z plane is imaged onto a detector of a commercial CMOS camera. Figure 4-6 shows intensity distributions at focus and at the defocus distances of $z_f = -8 \text{ mm}$ and $z_f = -16 \text{ mm}$ for $d_c = 400 \mu\text{m}$, and the distribution at focus position for $d_c = 600 \mu\text{m}$. These distributions were utilised in cutting experiments that are explained later. The result shows the same tendency as the case of $d_c = 200 \mu\text{m}$. The beam spot at the focus position has a top-hat intensity distribution and it becomes gaussian-like as z_f is increased from the focus position. The beam diameter at the focus was 1.1 mm for $d_c = 400 \mu\text{m}$ and 1.7 mm for $d_c = 600 \mu\text{m}$.

Figure 4-4 and 4-6 show that as the fibre core diameter increases, the intensity distribution becomes more homogeneous. This is possibly because homogenisation of a beam mode depends on the fibre core diameter. It is expected that the beam mode in the disc laser oscillator has a bell-like distribution. Getting this beam through a fibre homogenise the distribution toward top-hat. It seems, however, that this mode-conversion process does not complete for small core diameters of $d_c = 200 \mu\text{m}$ and $400 \mu\text{m}$, even with the fibre length of $\sim 20 \text{ m}$.

4.1.4 Samples

Low carbon steel and the standard S355 steel are used as cut samples. Chemical compositions of the low carbon steel are shown in Table 4-1.

Table 4-1 Chemical compositions of low carbon steel used in experiments.

										(%)
C	Cr	Cu	Mn	Mo	N	Nb	P	S	Si	
0.013	0.014	0.012	0.25	<0.003	0.004	0.035	0.0049	0.081	<0.003	

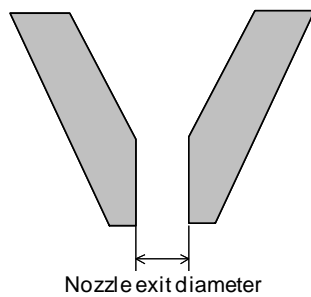


Figure 4-7 Profile of nozzle

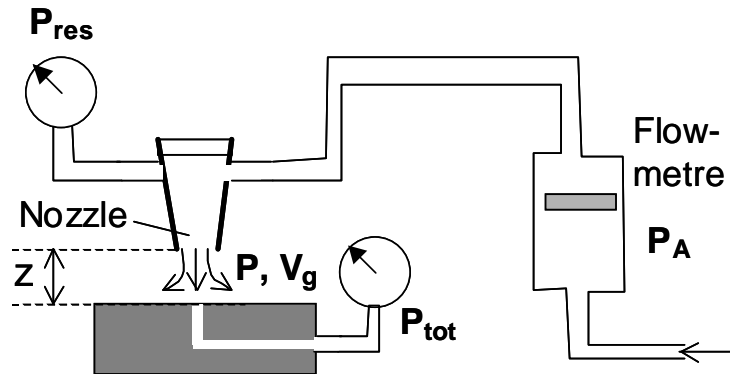


Figure 4-8 Pressure field measurement.

4.1.5 Assist gas

Nitrogen is provided as an assist gas from a commercial nozzle provided by Trumpf. The profile of the nozzle is sketched in figure 4-7. The nozzle exit diameter is 1.5 mm or 3.5 mm. The profile at the exit is straight with no taper. The gas pressure, which is changed as a parameter, is measured by a pressure gauge attached to the reservoir. In this study the assist-gas pressure is defined with this value measured at the reservoir. This represents the pressure value relative to the ambient pressure (1 bar).

Although the pressure in the reservoir gives rough estimation of gas force, it may not exactly represent the pressure applied on the sample surface. This is due to a divergence of the gas flow into free space or shock effect caused by supersonic flow. In view of this, we measured a pressure distribution outside of the nozzle.

The total pressure of the gas field was measured with a homemade apparatus, shown in figure 4-8. The gas was injected to a small hole (0.5 mm in diameter), which is connected to a commercial pressure gauge. This is a well-known Pitot-tube technique, although the technique normally adopts manometer with a tube enclosed with mercury.

Figure 4-9(a) and (b) show the pressure for the nozzle diameters of 1.5 mm and 3.5 mm, respectively. Pressure was measured along the symmetrical centre line of the nozzle as a function of the distance z from the nozzle exit. In the case of $P_{res} = 7.5$ bar for the nozzle diameter 1.5mm ϕ , a rapid decrease of pressure is confirmed for $0 < z < 5$ mm. Formation of shockwave must be the reason of this decay. When the pressure is reduced to 1.5 bar, which is below the threshold pressure for the shock generation (1.89 bar), the pressure is kept almost constant along the symmetric line.

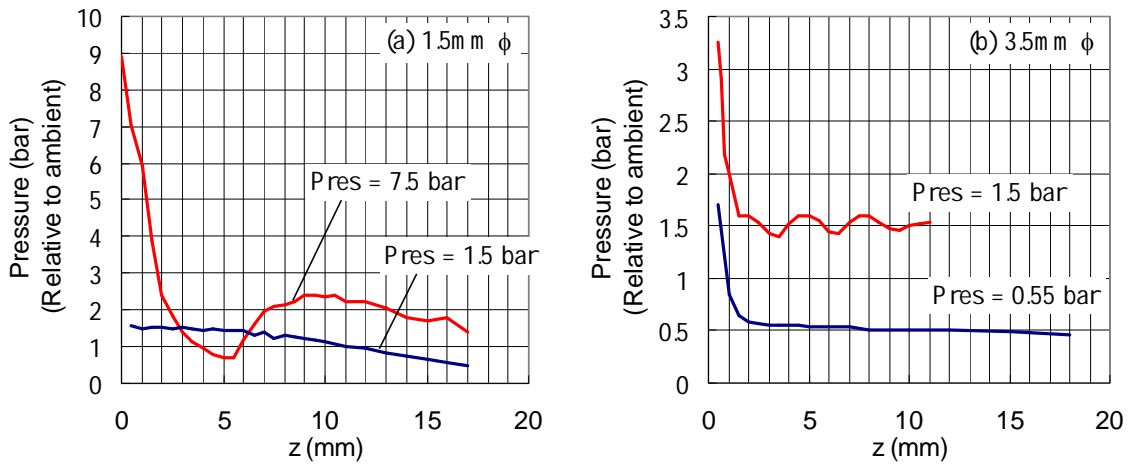


Figure 4-9 Measured total pressures as a function of the distance z from the nozzle exit surface.

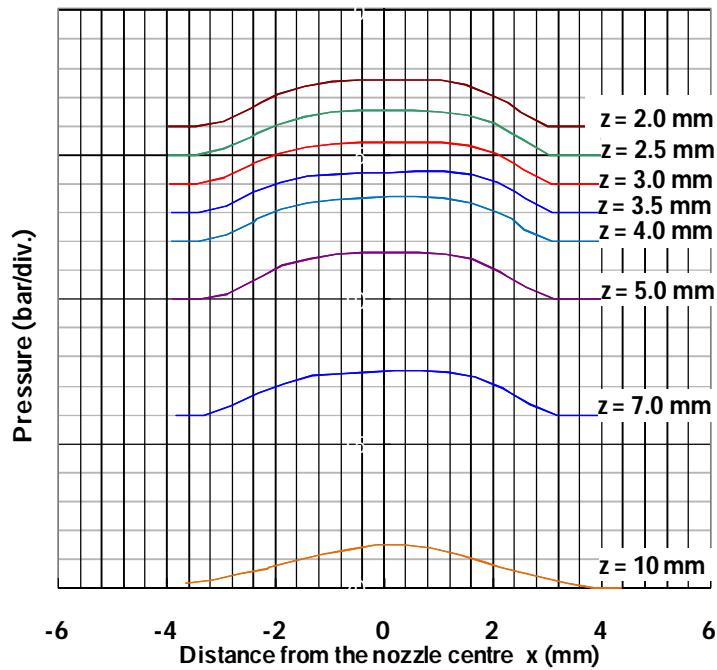


Figure 4-10 Pressure distribution measured at different distances from the nozzle exit surface. (The nozzle diameter = 3.5 mm, $P_{res} = 1.5$ bar)

Let us analyse more details of the gas field at $z = 3.5$ mm in the case of the nozzle diameter 3.5 mm ϕ and $P_{res} = 1.5$ bar. This condition is mainly used in the following experiments. Figure 4-10 shows the pressure distribution as a function of z in the case of the nozzle diameter 3.5 mm ϕ and $P_{res} = 1.5$ bar. The FWHM d_g of the pressure distribution at $z = 3.5$ mm was 4.8 mm. The flow rate was measured to be $Q = 115$ L/min with a standard gas flow meter, taking into account density correction due to the gas pressure. Assuming that the size of pressure distribution corresponds to that of velocity field, the gas velocity at this position can be estimated from the following formula:

$$v_g = \frac{Q}{\left(\frac{\pi d_g^2}{4} \right)} \quad (4-4)$$

which gives $v_g = 1.1 \times 10^2$ m/s.

The static pressure P_{in} at $z = 3.5$ mm is estimated from the Bernoulli's equation for compressible gas flow [Landau 1987]:

$$\frac{\gamma}{\gamma - 1} \frac{P_{in}^{(\gamma-1)/\gamma}}{\rho_0 P_0^{-1/\gamma}} + \frac{1}{2} v_g^2 = \frac{\gamma}{\gamma - 1} \frac{P_{tot}^{(\gamma-1)/\gamma}}{\rho_0 P_0^{-1/\gamma}} \quad (4-5)$$

Here γ is the adiabatic exponent ($=1.4$ for N_2) and ρ_0 is the density of N_2 at ambient pressure $P_0 = 1 \times 10^5$ Pa ($\rho_0 = 1.3$ kg/m³). Inserting to eq.(4-5) these values and the total pressure $P_{tot} = 2.4$ bar (absolute value) measured on the nozzle axis, one obtains $P_{in} = 2.1$ bar (absolute value).

4.1.6 Observation system

For observation of hydrodynamics of molten metal, a commercial high speed camera is used (Photron, FASTCAM/APX-RS). This video camera can take grayscale images with the maximum acquisition rate of 100 kHz. Although the CMOS detector of the camera does not have high sensitivity to the laser wavelength of 1030 nm, a sheet of glass (KG3) is placed in front of a camera lens to protect from the reflected laser light from the irradiation point. As the acquisition rate or the magnification increases, less and less light come into each element of the detector array. Thus commercial halogen projection lamps are utilised to illuminate samples with enough brightness.

Although in most of the observations the observation angle is set off the axis of the laser beam, coaxial configuration is also possible by picking up reflected light with a dichroic mirror.

4.2 Observation of striation initiation from surfaces

The first series of experiments was dedicated to investigate the mechanism of initiation of striations from sample surfaces. Melt flow in the top part of the kerf front was observed with the high speed video camera.

4.2.1 Experimental condition

Using the experimental setup shown in figure 4-11, melt dynamics on kerf fronts were filmed with the

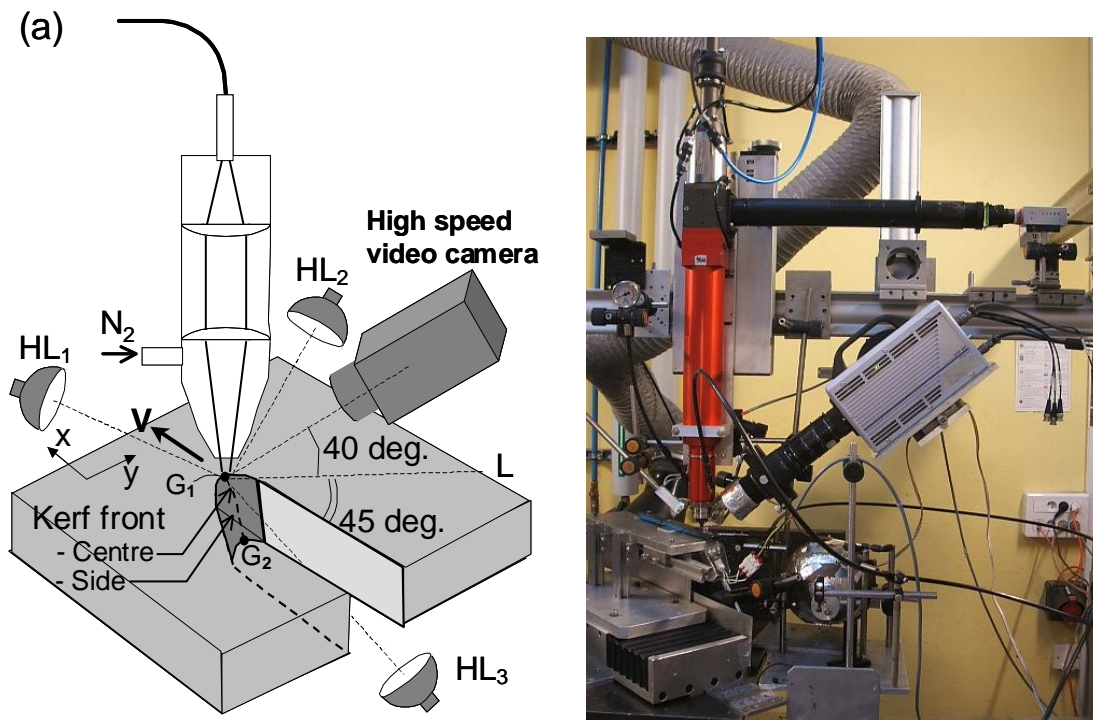


Figure 4-11. (a) Scheme of the experimental setup and (b) its picture. In (a), HL₁₋₃ represent halogen lamps used for illumination.

high speed video camera. Low carbon mild steel was used as samples. The thickness was 3 mm, and the very surface layer of steel oxide had been removed by mechanical polishing to avoid unfavourable perturbations. Nitrogen was used as assist-gas.

The kerf front was observed by the high speed video camera (Photron, FASTCAM/APX-RS) with the acquisition rate of 20 - 50 kHz (depending on operating conditions). In order to clarify the initiation process of striations, the top part of the front was observed from the above, with the angle of 40 degree with respect to horizontal surface. To visualise the central and side parts of the kerf front at the same time, the angle of the observation was deviated by 45 degree from the cutting direction (Please note also our notations concerning parts of the kerf, which are presented in figure 4-11(a)). The spatial resolution of the video images was approximately 10 $\mu\text{m}/\text{pixel}$. As shown in figure 4-11(a), three halogen lamps (HL₁₋₃) were used for illumination; the two HL₁ and HL₂ from the above of the sample to illuminate the sample surface and the side part of the kerf front, respectively, and the other HL₃ from the below through the kerf to illuminate the central part of the front. No wavelength filter was used. The exposure time was set at 0.05 ms, the inverse of the acquisition rate.

The operating conditions are summarised in Table 4-2. First we investigated in detail the hydrodynamics with the standard condition in the first column. Then the dependences on the operating parameters were studied with conditions in the second and the third columns.

Table 4-2 Operation parameters

Parameters	Standard condition	Conditions for parametric study	
Power	8 kW (CW)	2-8 kW (CW)	8 kW (CW)
Spot diameter	1.7 mm	1.7 mm , 1.1 mm	0.56 mm
Intensity profile	Top-hat	Top-hat, Quasi-Gaussian	Top-hat
Gas pressure	1.5 bar	0.2-1.5 bar	1.5 bar
Nozzle diameter	3.5 mm	3.5 mm	1.5 mm
Nozzle standoff	3.5 mm	3.5 mm	2 mm

(a) Standard condition

In the standard condition, the focus spot diameter was 1.7 mm ϕ . As shown in figure 4-6, the intensity profile was nearly complete top-hat.

This focal diameter is larger than diameter typically used (~0.1 mm). It could have been possible to utilise such small focus diameter, but it is a very difficult task to observe the dynamics of phenomenon with sufficient spatial resolution. Instead of increasing the magnification factor of the optical system of the camera, we adopted a much easier way to enlarge the spatial scale of the kerf, in order to have a better visualization and to deduce the mechanism of the striation generation. Despite the increase of diameter, relevant physical processes or mechanisms are not expected to change so much, since most of the physical processes of heat transfer in solid and liquid layer and of hydrodynamics in liquid are scalable in terms of governing mathematical equations.

The stand-off distance of the nozzle was set at a rather large value of 3.5 mm, to assure the vision around the kerf. The pressure of N₂ assist gas in the nozzle was 1.5 bar (relative to the ambient 1 bar), so that the gas flow from the nozzle was free from shock waves, which would have introduced disturbances in the flow. The pressure distribution had a diameter d_g of 4.8 mm measured at FWHM and the distribution was homogeneous within the laser beam diameter d_f (1.7 mm). As was explained in Sec. 4.1.5, the static pressure of gas flow at the sample surface and the velocity of the flow are estimated to be 2.4 bar (absolute value) and $v_g = 1.1 \times 10^2$ m/s, respectively.

As mentioned above, in order to have intact vision and stable gas flow, we used the large stand-off distance and the low pressure as compared with typical conditions utilised in inert gas laser cutting. This means that gas force exerted on melt layer was lower. Nevertheless, striations observed in this study are essentially the same as in practical conditions, as will be shown. Moreover, the influence of gas parameters on the striation generation process will be investigated later.

The cutting speed V_c was varied from 1 m/min to 6 m/min to investigate the evolution of hydrodynamics. The roughness R_z and the wavelength λ of striations were measured along a line parallel to the surface at the depth 0.5 mm below the top surface. We measured also tilting angle α of kerf front with samples obtained after switching-off of the laser beam. The angle was evaluated as the value averaged over the sample thickness, using a straight line which links the two points G_1G_2 on the top and back surfaces (see figure 4-11(a)). In the case where the sample could not be cut through, the lower point G_2 is substituted by the end point of the tilted kerf front. The technique gives rather accurate estimation of α , since melt layer is so thin that it is frozen very rapidly when the laser is turned off. (The thickness δ_{me} of the melt layer can be estimated in the order of 100 μm from the mass balance equation (2-32) $\delta_{me}V_m = hV_c$, where h is the workpiece thickness (3 mm) and V_m is the velocity of continuous melt flow, which will be shown later in figure 4-14.) The freezing time of the melt layer was confirmed experimentally to be roughly 0.2 ms by the high speed video observation. The melt layer moves only several hundred microns after the turn-off of the laser if we multiply the freezing time by the measured velocity V_m (1~3 m/sec).

(b) Conditions for parametric study

In order to investigate dependencies of characteristics of melt flow dynamics on operating parameters, assist-gas pressure, laser beam power, focused spot diameter, and beam intensity profile were changed as shown in Table 4-2. The beam diameter was changed by using a fibre with different core diameter. For the beam diameter of 0.56 mm ϕ , different nozzle diameter and nozzle stand-off distance were selected (see Table 4-2). The observation method with the high speed camera was the same as the standard condition explained in the above. Also as in the experiments of the standard condition, the cutting velocity V_c was varied for each combination of operating parameters.

4.2.2 Standard condition

Typical examples of images acquired for different cutting velocities V_c from 1 m/min to 6 m/min are shown in figure 4-12. As can be seen, liquid flow on the kerf front exhibits strong dependence on V_c . In the following, we describe observed phenomena for several different velocity ranges. For the present operating conditions, the maximum speed to cut through the 3 mm thick sample was $V_c = 3$ m/min. Even in the range of $V_c > 3$ m/min, however, the flow feature observed in this top part of the kerf is considered to be essentially the same as that would be obtained when thinner samples are to be cut properly.

4.2.2.1. Velocity dependence of hydrodynamics

(i) $V_c = 3$ m/min

Let us start from the intermediate case of $V_c = 3$ m/min (figure 4-12(c)). Two different flows can be recognized: the flow in the central region of the kerf front and the flow on the side of the kerf. In the following, we call the former the central flow, and the latter the side flow. We define W , the thickness of the side flow region, as the distance from the kerf side line to the point R on the kerf, which separates the continuous central region and discontinuous side region. In the present case of $V_c = 3$ m/min, $W = 160 \mu\text{m}$.

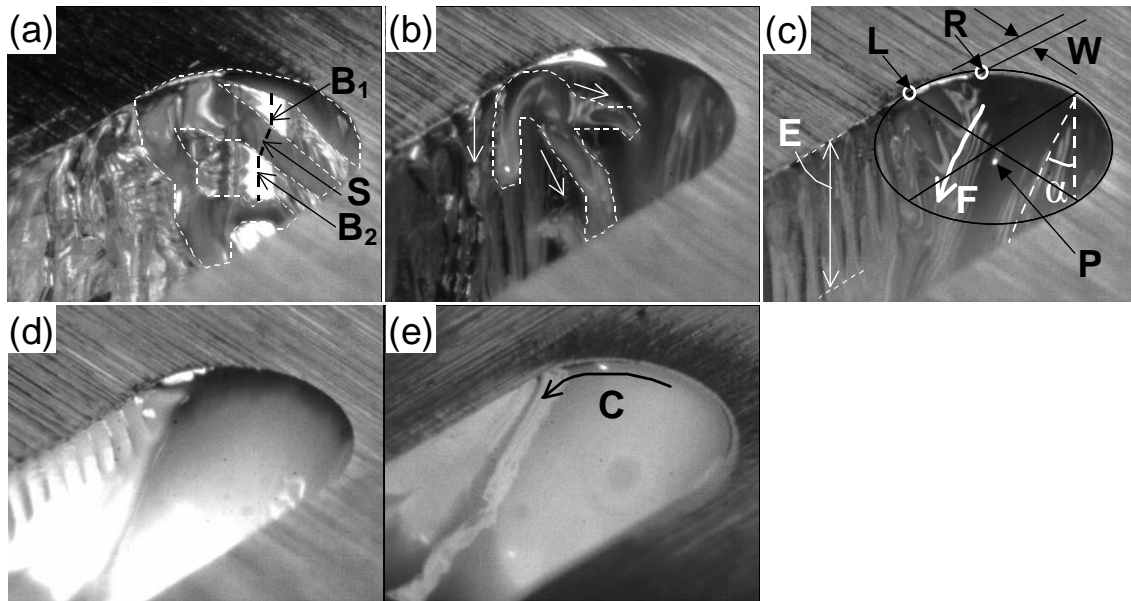


Figure 4-12. Observation result for different velocities V_c . (a) $V_c = 1$ m/min, (b) $V_c = 2$ m/min, (c) $V_c = 3$ m/min, (d) $V_c = 4$ m/min and (e) $V_c = 6$ m/min. For the scale of the images, refer to the kerf width d_k in figure 4-13 ($d_k \sim 1.7$ mm for all the V_c).

The central flow runs continuously and smoothly downwards along the central part of the kerf. The central symmetrical line on the kerf is tilted by an angle α of 26 degree with respect to the beam incident axis (see also figure 4-13). The velocity V_m of the continuous flow is determined as 3.2 m/s using moving particles like P in figure 4-12(c), which appear occasionally (see also figure 4-14). We think that they are some very small inclusions inside the material, but the characteristics such as chemical composition and size are not clear at the present stage.

On the other hand, the flow in the side region between the points L and R in figure 4-12(c) exhibits striking discontinuity and periodicity. The termination point L on the left corresponds to the edge of overlapped region with laser beam, whose position at the surface is shown on figure 4-12(c) by the

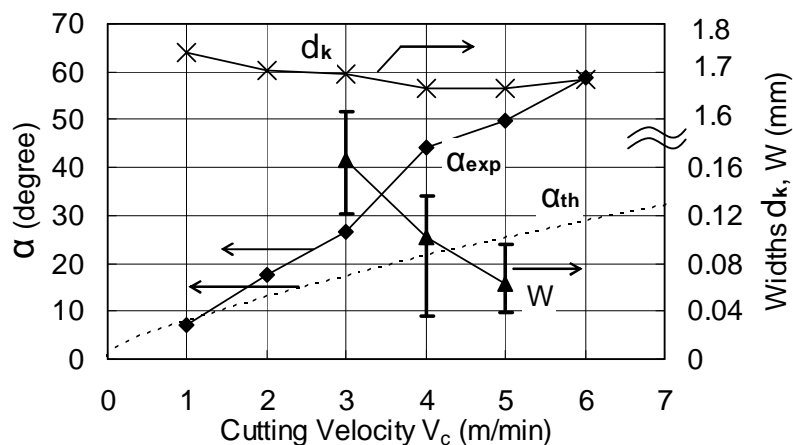


Figure 4-13. Velocity dependence of tilting angle of kerf front; experimental measurement (α_{exp}) and theoretical prediction from the equation (2-10) (α_{th}). Also shown are measured values of kerf width (d_k) and the width of unstable side region (W).

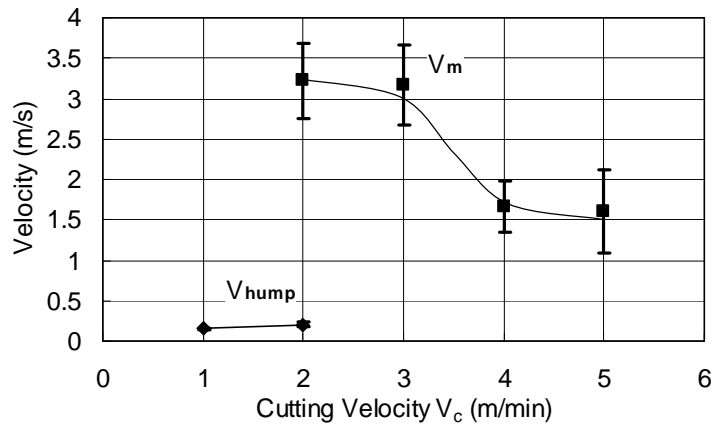


Figure 4-14. Measured velocities of continuous flow (V_m) and humps (V_{hump}) in the central region of the kerf front.

ellipse ($d_f = 1.7$ mm). The point R is located at the separation point of the central and side flows. The very top part of the region is very bright because of specular reflection from the halogen lamp HL₂ (see figure 4-11(a)). Liquid accumulations are generated one by one from the top part and displaced towards the direction shown with F in the figure 4-12(c); they slide down on the sidewall of the kerf until they are absorbed by the central flow. After displacement of each accumulation, one single vertical stripe of striations is created on the sidewall. The depth of region where we observe such vertical striations (distance E in figure 4-12(c)) is determined by the travelling distance of accumulations before joining to the central flow. The average time interval Δt_a of two accumulation generations was measured to be 4 ms. The wavelength λ of striations measured after cutting was 199 μm , which corresponds to the value of $V_c \cdot \Delta t_a = 200$ μm . It is clear that the periodical generation and displacement of accumulations is the origin of the striations. Whereas Yudin *et al.* [Yudin 2007] already observed the downward displacement of the accumulations by lateral visualisation of the kerf side through a transparent glass, our observation has revealed for the first time the processes of the accumulation generation and the striation initiation at the top part of the kerf. More detailed description of the striation generation process is given in the next section 4.2.2.2.

(ii) $3 \text{ m/min} < V_c < 6 \text{ m/min}$

When the velocity is increased from 3 m/min to 5 m/min (figure 4-12(d)), general feature of the flow

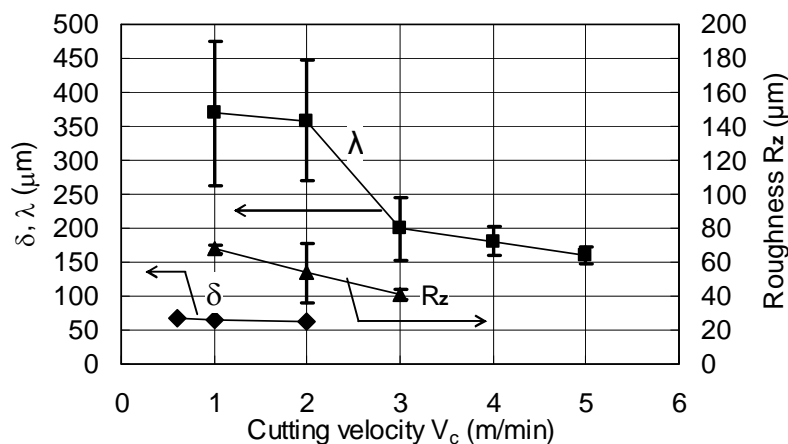


Figure 4-15. Pitch δ of humps in the central part of the kerf front, striation wavelength λ and surface roughness R_z obtained from the experiments.

does not change. The stable central flow and the non-stationary side flow exist and the periodic behaviour of the latter generates regular striations on the side. Meanwhile, characteristic parameters of the flow depend on the cutting velocity V_c . As shown in figure 4-13, the tilting angle α of the front at the centre line increases with V_c and at the same time, the thickness W of unstable side region decreases. Because of this increase of α , the travelling distance of accumulations before meeting the central flow becomes shorter. The depth of region where we observe regular vertical striations is thus reduced. The wavelength of striations slightly decreases with this increase in V_c (see figure 4-15).

(iii) $V_c = 6 \text{ m/min}$

If we further increase V_c to 6 m/min (figure 4-12(e)), the stable central flow covers the entire kerf front, and the periodic generation of accumulations and their downward displacement along the kerf side cannot be observed any more. Correspondingly, no striation appears on the side, although we observe random oscillation of the liquid surface level of the central flow, which creates very thin relief.

Let us mention here some fundamental remarks about the velocity of the continuous central flow. As shown in figure 4-14, the velocity V_m decreases with increasing V_c . At $V_c = 6 \text{ m/min}$, we could not determine the velocity because we found no particles moving downwards. Instead, we found particles moving laterally along the semi-circular kerf shape as designated with C in figure 4-12(e). It is likely that this change of flow is caused by combination of the following two factors. First, as α increases, the deflection of gas flow near the front surface becomes more pronounced. As a result, the tangential force which is applied on the melt surface is considered to be decreased. Second, as the tilting angle α of the front increases with V_c (figure 4-13), the laser beam intensity absorbed on the central part increases. The surface temperature may exceed the boiling temperature. If this is the case, it can be possible that the azimuthal flow to the side by the piston mechanism [Semak 1997] becomes relatively important compared with the downward flow.

(iv) $V_c = 2 \text{ m/min}$

On the other hand, when V_c is decreased from 3 m/min, the central part also begins to show discrete behaviour, as is clear in the case of $V_c = 1 \text{ m/min}$ (figure 4-12(a)). The melt flows down intermittently; parts of surface between the two successive bunches of melt are not even covered with liquid metal. We will define these liquid bunches as humps in this study. The threshold velocity of the appearance of this discontinuity is $V_c = 2 \text{ m/min}$, where the flow in the central region fluctuates between the two regimes of continuous and discontinuous flows. An interesting point is that, at $V_c = 2 \text{ m/min}$, the velocity of continuous flow was observed to be 3.2 m/s, whereas the velocity of humps was 0.2 m/s. It is not surprising to observe this difference, because the evolution of hump is not a mass flow but an evolution of phase as already pointed out [Makashev 1992, Makashev 1994, Matsunawa 1997, Golubev 2004].

The image at $V_c = 2 \text{ m/min}$ shown in figure 4-12(b) is the one typically observed when the central flow is in the continuous regime. Compared with $V_c = 3 \text{ m/min}$, the angle α is decreased (see also figure 4-13). This leads to the extension of perpendicular striations which are left on the kerf side. At the same time, the width W of unstable side flow as well as the accumulation size becomes larger. Travelling paths of the accumulations are more irregular and complex. The accumulation surrounded with a white dotted line in figure 4-12(b) shows such an example: several branches originate from the single accumulation, one of which goes away to the left without being absorbed to the central flow. As a consequence of this kind of irregularity, striation relief which is left on the kerf side is not as regular as in the case of $V_c > 2 \text{ m/min}$.

(v) $V_c = 1 \text{ m/min}$

When we further decrease V_c to 1 m/min, the central flow completely becomes the regime of humps. Now the melt flow is discontinuous on the entire kerf front. The dynamics of the humps and accumulations becomes more and more irregular, and they show stronger interactions to each other. In the central region, humps, which are generated from the top part at every 4 ms, slides down with velocity of 0.15 m/s. Compared with $V_c = 2 \text{ m/min}$, the generation time period T_{hump} is doubled, so that

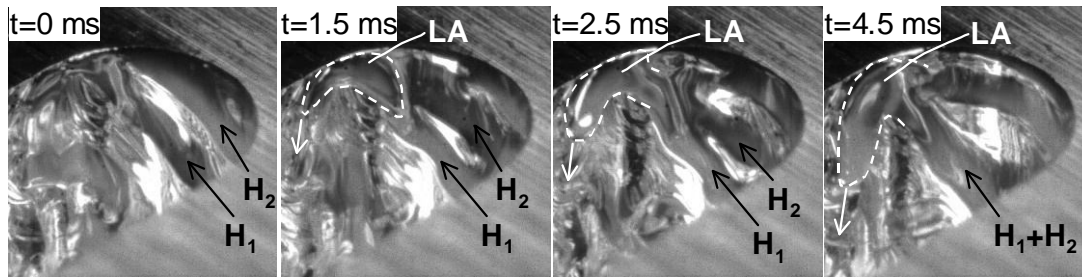


Figure 4-16. Example of melt accumulation dynamics observed for $V_c = 1$ m/min. A merger of two successive humps H_1 and H_2 is shown. The white dotted lines indicate approximate border of the liquid accumulation LA. As for the scale of the images, note that $d_k = 1.74$ mm.

the pitch δ measured along the cutting direction (x-axis) stays at the same value of $70 \mu\text{m}$. Please note that the pitch is defined as $\delta = V_c \cdot T_{\text{hump}}$. It is frequently observed that two successive humps starting from the surface merge in the middle of the front and go down together after that. Such an example can be found in a sequence of images shown in figure 4-16. The two humps H_1 and H_2 are separated at $t = 0$ ms. At $t = 1.5$ ms, however, they begin to interact via the liquid accumulation LA on the side. The merger is initiated and they are completely unified at $t = 4.5$ ms. In figure 4-16 one can observe also a branch of the liquid accumulation (LA) escaping to the left.

Another interesting feature is found in bright regions such as those marked with B_1 and B_2 in figure 4-12(a). These regions are not covered with liquid but are very bright because the light emitted from the halogen lamp HL_3 is specularly reflected in these regions toward the video camera. The centre lines B_1 and B_2 of the two bands have a lag, which indicates that the hump is situated on a small plateau S , whose tilting angle is different from the two parts above (B_1) and below (B_2). This difference of the tilting angle is also suggested from the difference in the brightness. The solid regions are bright since the angle matches that of the specular reflection from HL_3 , while the liquid on S is less bright due to the mismatch of the angle. It has been already discussed that the regime of humps involves such plateaus around the humps [Kovalenko 1985, Makashev 1992, Makashev 1994, Golubev 2004, Matsunawa 1997].

(vi) *Summary of velocity dependence*

Table 4-3 summarises the observed different regimes, which are classified from the viewpoint of instability. When V_c is increased from 1 m/min, the entire region on the kerf front exhibits discontinuity until $V_c = 2$ m/min. In the following intermediate velocity range from 2 m/min to 6 m/min, the central flow becomes continuous, but the side flow is still discontinuous. As V_c increases, the width W of the unstable side region diminishes with the expansion of the stable central region. The side flow in this regime is characterised by periodic generation of accumulations at the top part and their displacement downwards, which is the origin of regular vertical striations created on the kerf sides. And finally, the unstable side region disappears at $V_c = 6$ m/min.

Table 4-3. Velocity dependence of the flows.

	Cutting Velocity V (m/min)		
	$V_c < 2$	$2 < V_c < 6$	$V_c = 6$
Central flow	Unstable	Stable	Stable
Side flow	Unstable	Unstable	Stable

The existence of instability in the central region has been predicted theoretically for low velocity condition [Kovalenko 1985, Golubev 2004]. Meanwhile, an important point firstly shown by the present observation is that there is a regime where we observe simultaneously both the stable and unstable flows, in the central and side regions, respectively. In most of the theoretical works in the past,

it has been assumed that the instability in the central part naturally perturbs the flow in the side region [Kovalenko 1985, Makashev 1992, Makashev 1994, Golubev 2004]. This kind of assumptions should be rejected for the intermediate regime.

4.2.2.2. Process of striation generation

Let us see more precisely the striation generation process. An example of the generation, development and displacement of an accumulation for $V_c = 3$ m/min is shown in figure 4-17. The solid lines indicate the position of the accumulation under consideration at each time. The dotted lines show the position of the precedent accumulation. The dot-dash lines show the border of laser beam overlap region. In the first image at $t = 0$ ms, no accumulation is recognized inside of the white dotted circle, from which the precedent accumulation has just gone out. At $t = 0.5$ ms, the new accumulation is confirmed in this region and it continues to grow up. At $t = 1.5$ ms, one can see that the bottom of the accumulation now touches the central flow. The displacement of this accumulation seems to be dragged by the central flow after this time. The accumulation continues to descend and finally it is sucked into the central flow at $t = 7.0$ ms. After the displacement of such accumulation, one single stripe of the striation structure is left on the kerf side.

Why do the accumulations go down quite vertically? The observation suggests the following two guiding mechanisms on the displacement of accumulations by downward gas force. Firstly the accumulations cannot go beyond the border of the beam (dot-dash lines), because they cannot exist as liquid any more once they do so. The cooling rate of the liquid is very rapid, as will be shown in chapter 5. In addition, there is a geometrical effect. The white dotted ellipse in the image at $t = 2.5$ ms surrounds a vertical line, which corresponds to a ridge of the striations. The height of such ridge can be estimated from the surface roughness. The measured value of R_z is $40 \mu\text{m}$ in this case of $V_c = 3$ m/min (see also figure 4-15). From the images which follow after $t = 2.5$ ms, it appears that the ridge works as a guide, preventing the accumulation from passing over the ridge. Thus the displacement of the present accumulation is again perpendicular to the top surface of the sample, reproducing a new ridge on the other side.

In summary, the observation has clarified for the first time the generation process of vertical striations. This regular process applies to the velocity range of $2 \text{ m/min} < V_c < 6 \text{ m/min}$. For the lowest velocity range ($V_c < 2 \text{ m/min}$), the accumulation is also generated rather periodically at the top part of the kerf, but the irregularity of accumulation trajectory perturbs final relief left on the kerf side.

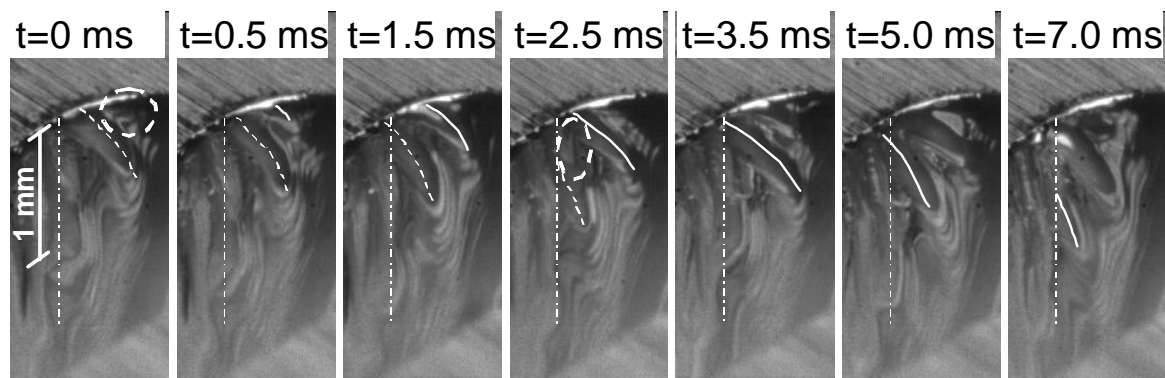


Figure 4-17. Dynamics of an accumulation observed at $V_c = 3$ m/min. The solid and dotted lines show the position of the accumulation under consideration and the precedent accumulation, respectively. The dotted circle at $t = 0$ ms indicates the position of the creation of the accumulations. The dotted ellipse at $t = 2.5$ ms shows a ridge left after the displacement of the precedent accumulation.

4.2.3 2D melting experiments

In order to investigate stability limit of hydrodynamics in the central part of the kerf front, another type of samples were used. The sample was a rectangular bar with the width of 1 mm and the height of 3 mm. They were held as depicted in Figure 4-18. Using exactly the same experimental conditions as the cutting experiment described above, they are melted with the moving laser beam. This experiment allows us to observe hydrodynamics only in the central part of the kerf front without any possible perturbation from the side region. In addition, the melting phenomenon can be regarded as a two-dimensional problem (in the x - z plane in Figure 4-18), considering the facts that the width of the samples is less than the laser beam diameter and that the both sides of the samples are thermally isolated. This simplification will help us to understand fundamentals on the stability of hydrodynamics and also to develop numerical models in the future. In the following, we call this experiment “2D melting experiment” in order to distinguish it from the ordinary cutting experiment with plate samples. It should be mentioned that Schuster *et al.* [Schuster 2009] visualised melting using the same kind of 2D configuration for the case of welding without process gas. While they employed lateral observation, we used the oblique observation from the above, which gives us clearer vision of the hydrodynamics on the kerf front.

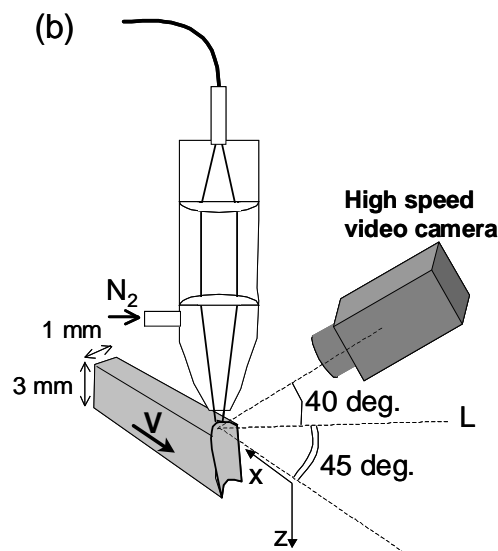


Figure 4-18. Schematics of experimental setup for 2D melting experiment.

The 2D melting experiments were conducted for different laser power $P = 8, 4$ and 2 kW, varying the beam displacement velocity V for each laser power. The images captured for $P = 8$ kW are presented in figure 4-19. The observed velocity dependence was nearly the same as that observed for the flow in the central region of the kerf in the case of the normal cutting experiment. For low velocity condition of $V < 2.5$ m/min, melt accumulations (humps) were observed but for higher velocity range, the melt flow became continuous.

In the images (a) ($V = 1$ m/min) and (b) ($V = 2$ m/min), humps are observed only in the very top part of the kerf front. In the lower part they disappear. This behaviour cannot be observed in the case of normal cutting. The reason is not clear, but we think that the force applied on the kerf surface by the assist gas may be inefficient due to the special geometry used in this experiment. In spite of this difference in the lower part, it is considered that the flow in the upper part, which governs the stability, is essentially the same as the cutting experiment.

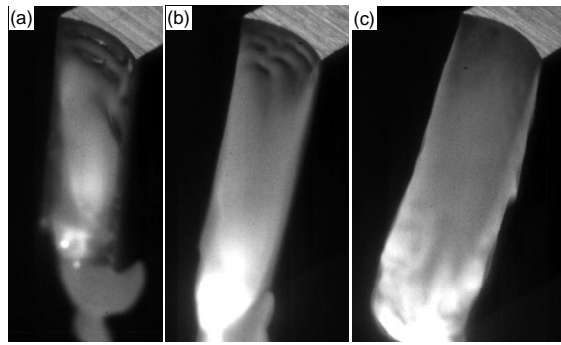


Figure 4-19. Observation results of 2D melting experiments for different velocities V . (a) $V = 1$ m/min, (b) $V = 2$ m/min, and (c) $V = 3$ m/min.

When the laser power was decreased, the threshold velocity below which the flow becomes discontinuous decreased. This result is presented in figure 4-20, where the measured tilting angles are plotted. The vacant and filled marks represent the unstable and stable regimes, respectively. One can see that the threshold velocity is proportional to the laser power. The tilting angle α is roughly proportional to (V/I_L) [Fabbro 2010], where I_L is the laser intensity. Thus the linear dependence of the threshold velocity on the laser power means that the threshold corresponds to the same angle of $\alpha = 13$ degree for all the different laser powers, as can be seen in figure 4-20.

This 2D melting experiment leads us to conclude that the instability observed in the central part of the kerf front in the case of ordinary cutting experiments is not caused by any perturbation from kerf sides but should be attributed to an inherent instability in the central flow.

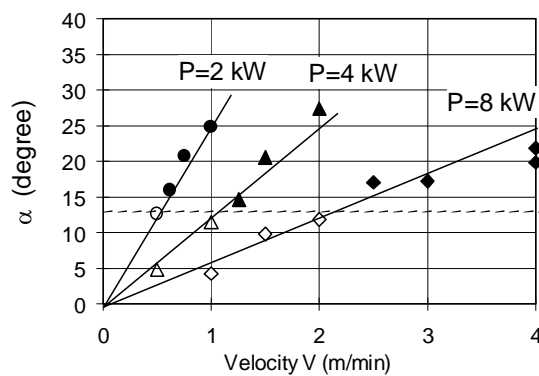


Figure 4-20. Velocity dependence of α obtained in the 2D melting experiment.

4.2.4 Parametric study

In addition to the cutting velocity V_c , several operating parameters were changed in order to investigate dependence of the melt flow on the cutting condition. The varied operating parameters and the investigated quality parameters are summarised in Table 4-4 and 4-5, respectively. The cutting velocity V_c was changed for all combinations of the operating parameters. Melt flow around the kerf front was visualised with the same configuration as the observations for the standard condition (figure 4-11).

Table 4-4 Operating parameters changed.

Parameters	Ranges
Gas pressure	$P_G = 0.2 - 1.5$ bar
Laser power	$P_L = 2 - 8$ kW
Beam diameter	$d_f = 1.7, 1.1, 0.56$ mm
Beam profile	Top-hat, Quasi-Gaussian
Material	Low carbon steel

Table 4-5 Quality parameters investigated.

Symbols	Definitions
α	Averaged inclination angle of the kerf front
V_{hump}	Downward velocity of humps on the kerf front
$\delta (=T_{\text{hump}}*V_c)$	Pitch of humps which appear in the central flow
λ	Striation wavelength
R_z	Roughness on cut surfaces (0.5mm below the surface of sample)

(a) Gas pressure

Pressure dependence was investigated for a fixed laser power (8 kW) and a beam diameter (1.7 mm). Figures 4-21 to 4-25 show measured α , V_{hump} , δ , λ , and R_z , respectively.

- The inclination angle α was almost independent of the pressure (Figure 4-21).
- Figure 4-26 show a comparison of the two static images for 1.5 bar and 0.2 bar in the case of $V_c = 1.5$ m/min. It is seen that thickness of melt layer is larger in the case of 0.2 bar than 1.5 bar. Accordingly, it was found that V_{hump} decreases with a reduction of the gas pressure.
- It was confirmed that δ and λ decrease with increase of the gas pressure (Figures 4-23 and 4-24).
- On the other hand, the roughness R_z hardly depended on the pressure (Figure 4-25).

(b) Laser power

The influence of the laser power was examined with a beam diameter of 1.7 mm and an assist-gas pressure of 1.5 bar. The results are shown in figures 4-27 to 4-31.

- One can confirm from figure 4-27 that α is approximately proportional to (V_c/I_L) , where I_L is the laser beam intensity. The empty marks in the figure indicate that the central flow is stable without humps. When α is larger than around 16 degrees, the central flow becomes continuous, regardless of the power. This behaviour had also been confirmed in a two-dimensional melting experiment with rectangular bars (Figure 4-20).
- V_{hump} increases with laser power if compared at the same V_c (Figure 4-28).
- δ does not depend on the laser power, although the cutting velocity range where the central flow involves humps depends on the laser power (Figure 4-29).
- The striation wavelength λ slightly decreases with the cutting velocity V_c and this decrease occurs in a lower velocity range when laser power is decreased (Figure 4-30).

(a) Dependence on gas pressure

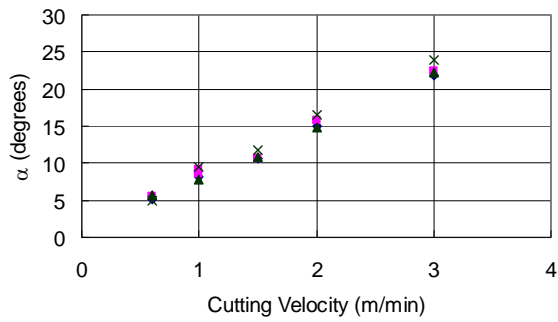


Figure 4-21 Inclination angle α of the front.

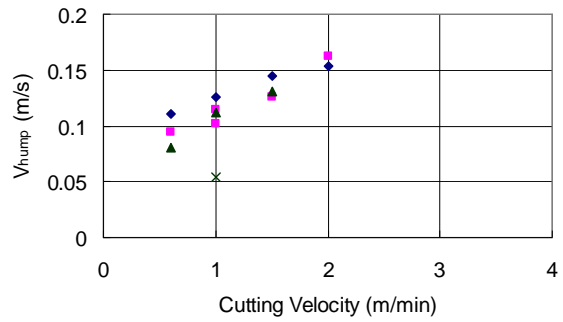


Figure 4-22 Downward velocity of humps.

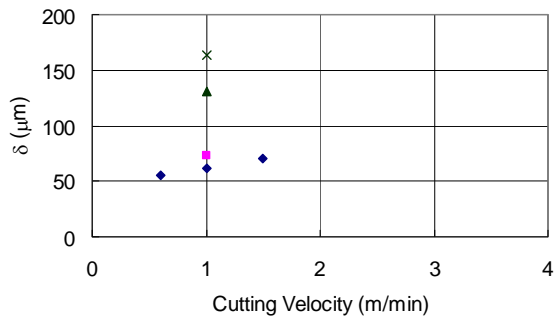


Figure 4-23 Pitch δ of the humps.

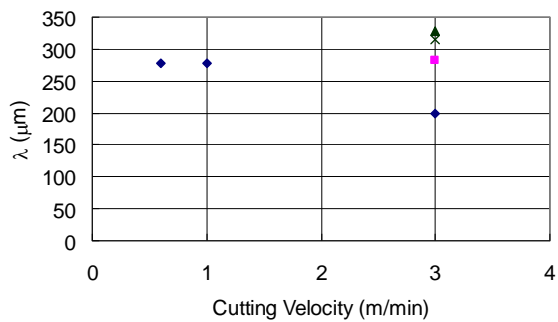


Figure 4-24 Wavelength λ of striations.

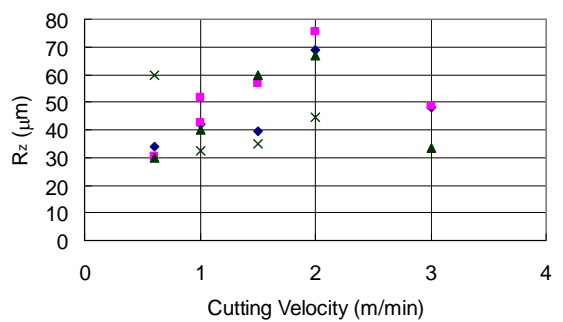


Figure 4-25 Roughness R_z of cut surfaces.

(a) $P_G = 1.5$ bar, $V_c = 1.5$ m/min

(b) $P_G = 0.2$ bar, $V_c = 1.5$ m/min



Figure 4-26 Examples of high speed video images

(b) Dependence on laser power

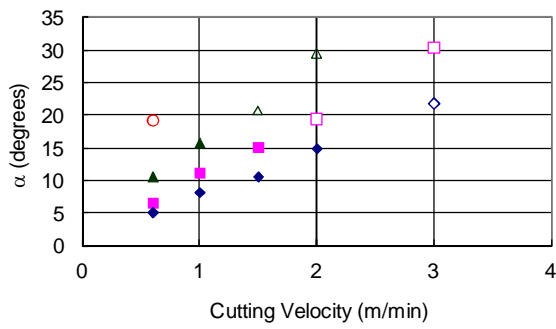


Figure 4-27 Inclination angle α of the front.

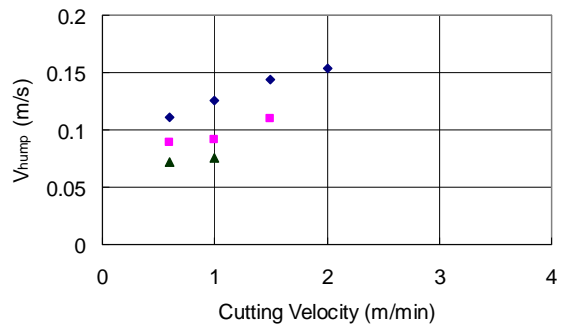


Figure 4-28 Downward velocity of humps.

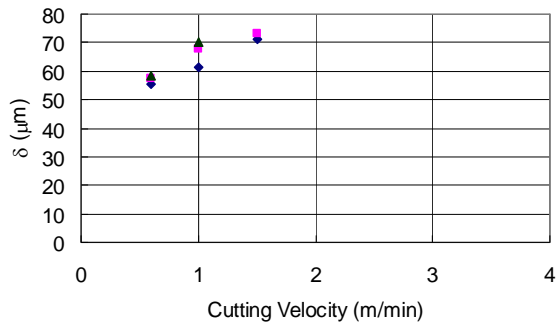


Figure 4-29 Pitch δ of the humps.

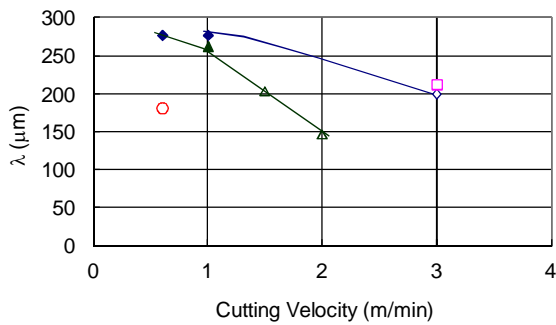
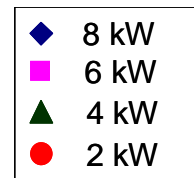


Figure 4-30 Wavelength λ of striations.

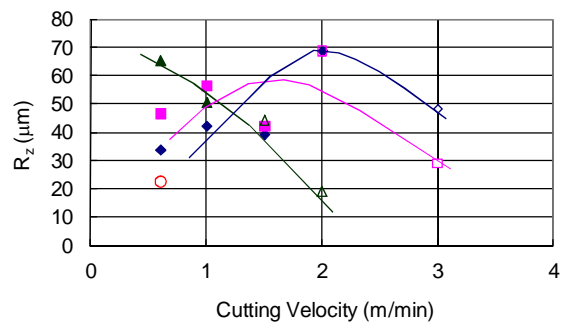


Figure 4-31 Roughness R_z of cut surfaces.

(a) $P_L = 6 \text{ kW}$, $V_c = 1.5 \text{ m/min}$

(b) $P_L = 4 \text{ kW}$, $V_c = 1.5 \text{ m/min}$

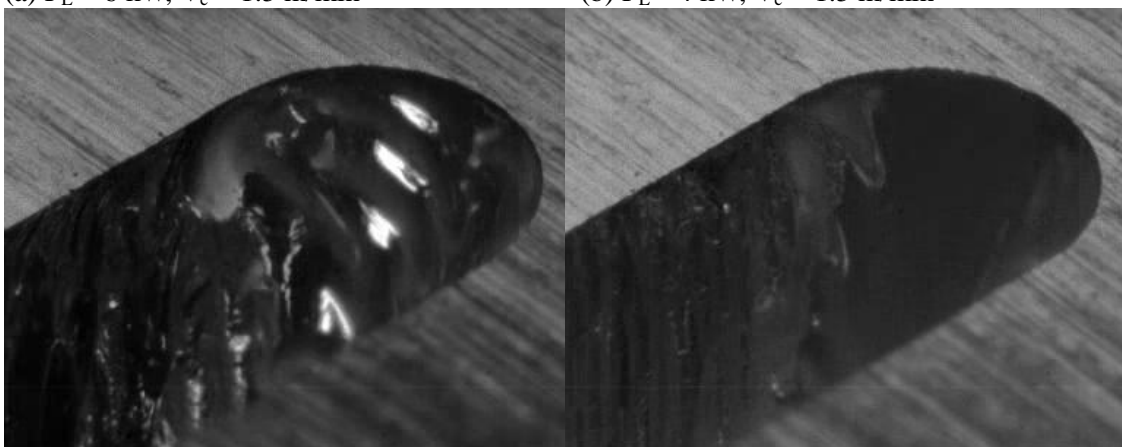


Figure 4-32 Examples of high speed video images

- As shown in figure 4-31, R_z increases with V_c in a low velocity range, becomes maximum at a certain V_c , and then decreases. The velocity at which R_z takes maximum value decreases with a decrease of laser power.

(c) Beam diameter

The Beam diameter was varied from 1.7 mm to 1.1 mm and to 0.56 mm, by changing the core diameter of the transmitting optical fibre from 0.6 mm to 0.4 mm and to 0.2 mm. The pressure of the assist gas was fixed at 1.5 bar. The laser power was 8 kW for all the diameters. The results are shown in figures 4-33 to 4-37.

- As shown in figure 4-33, the angle α decreases with a reduction of the beam diameter for a given cutting velocity. The empty marks mean that a stable flow was observed in the central part. The threshold angle α_{thr} above which the central flow becomes stable becomes smaller as the beam diameter is diminished.
- Characteristics of melt flow instability depend on the beam diameter as shown in figure 4-38. For the diameter d_f of 1.7 mm (figure 4-38 (a)), it appears that humps slide down along the central part rather independently from the accumulations on the sides at least for a length several times of the characteristic distance of δ measured from the surface. On the other hand, when the beam diameter becomes smaller ($d_f = 0.56$ mm; figure 4-38(b)), the amount of melt that flows from side parts to the central region increases compared with the melt that appears and flows down uniquely in the central region. The additional molten material from sides can connect two successive humps in the central region and may result in the suppression of the humps. In fact, it becomes difficult to distinguish humps which are generated in the central part and melt accumulations which are generated in kerf sides.
- It seems that V_{hump} is increased with a decrease of beam diameter if compared at the same V_c (Figure 4-34).
- All of the three parameters δ , λ , and R_z decrease when the beam diameter becomes small (Figures 4-35 to 4-37).

(d) Beam profile

The effect of the beam profile was investigated by defocusing the laser beam from the top-hat homogeneous intensity distribution with the diameter of 1.1 mm. Similar effects were observed by moving the focus position both upwards and downwards, so only the downward defocusing was investigated in details. The defocusing distance z_f was set at -8 mm and -16 mm. The corresponding beam profiles are shown in figure 4-6. In figure 4-39 to figure 4-43, the results are presented.

- The inclination angle α increases with the defocusing distance (Figure 4-39). (Please note that this α is the averaged value over penetration depth.)
- It was found that the defocusing changes drastically melt flow features. As shown in figure 4-44 (b), in the case of a defocused condition, stable central flow that starts from the top surface becomes unstable from a certain depth. The empty marks in the figures indicate that stable central flow is observed at the very top part near the surface. When the focus position is shifted, the central flow becomes stable at a lower cutting velocity.
- V_{hump} and δ are hardly affected by defocusing (Figures 4-40 and 4-41).
- On the other hand, λ and R_z decrease by defocusing, especially in a high cut velocity range (Figures 4-42 and 4-43).

(c) Dependence on beam diameter

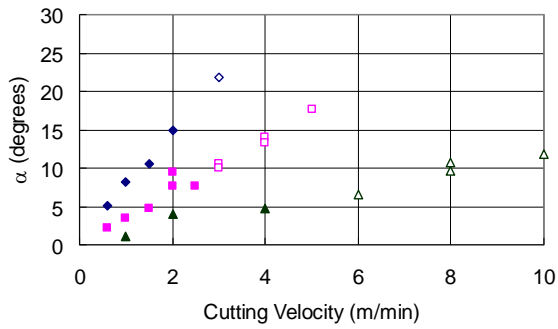


Figure 4-33 Inclination angle α of the front.

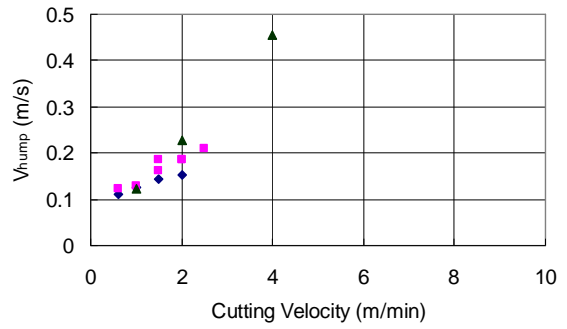


Figure 4-34 Downward velocity of humps.

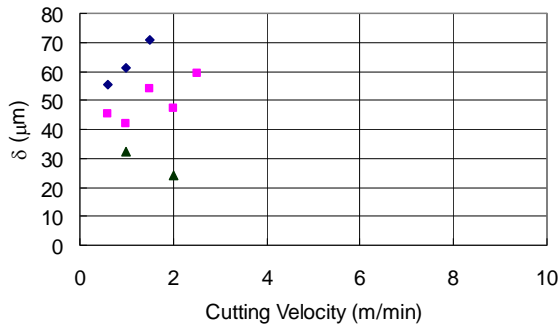


Figure 4-35 Pitch δ of the humps.

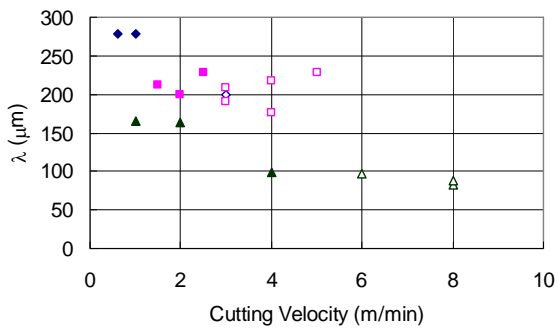
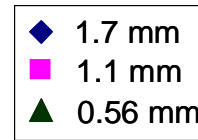


Figure 4-36 Wavelength λ of striations.

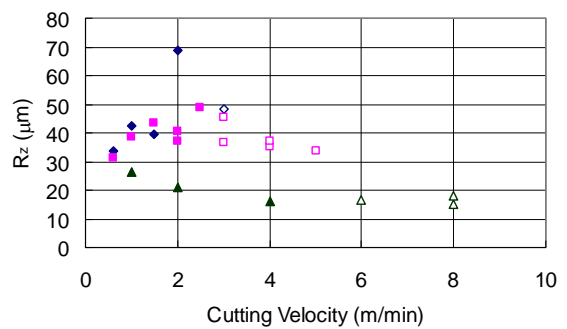


Figure 4-37 Roughness R_z of cut surfaces.

(a) $d_f = 1.7 \text{ mm}$, $V_c = 1 \text{ m/min}$



(b) $d_f = 0.56 \text{ mm}$, $V_c = 4 \text{ m/min}$



Figure 4-38 Examples of high speed video images.

(d) Dependence on beam profile

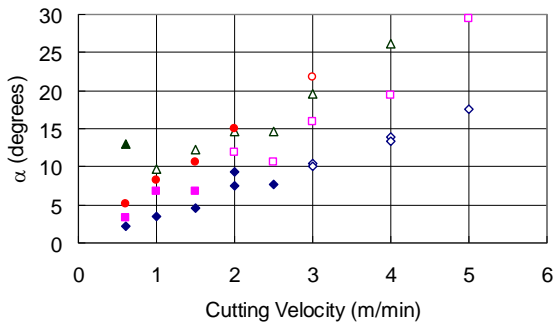


Figure 4-39 Inclination angle α of the front.

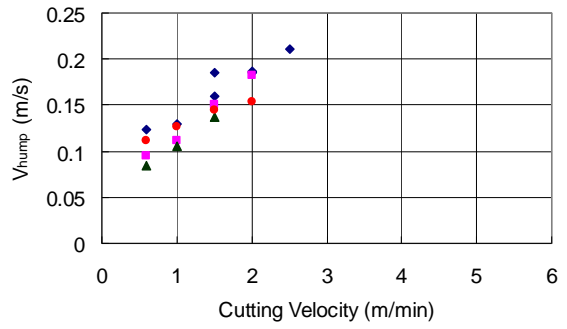


Figure 4-40 Downward velocity of humps.

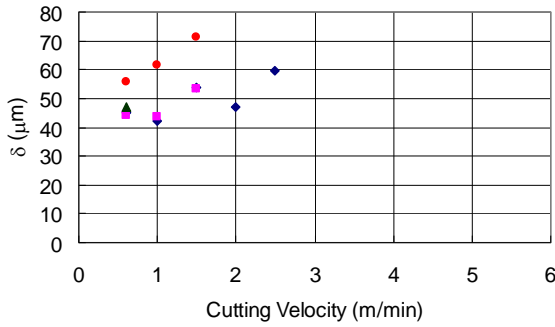


Figure 4-41 Pitch δ of the humps.

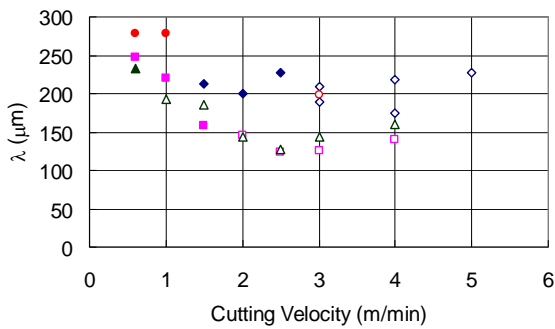
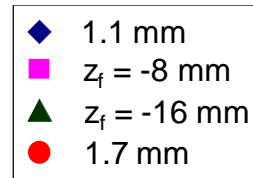


Figure 4-42 Wavelength λ of striations.

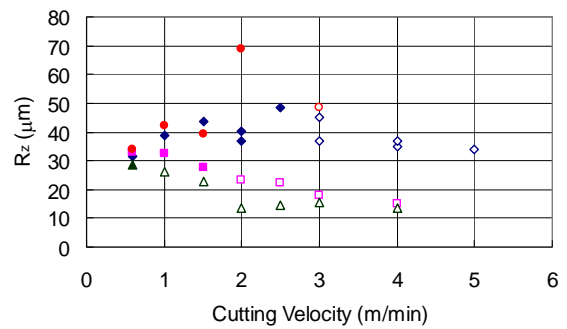


Figure 4-43 Roughness R_z of cut surfaces.

(a) $d_f = 1.7$ mm, $V_c = 1.5$ m/min

(b) $z_f = -16$ mm, $V_c = 1.5$ m/min

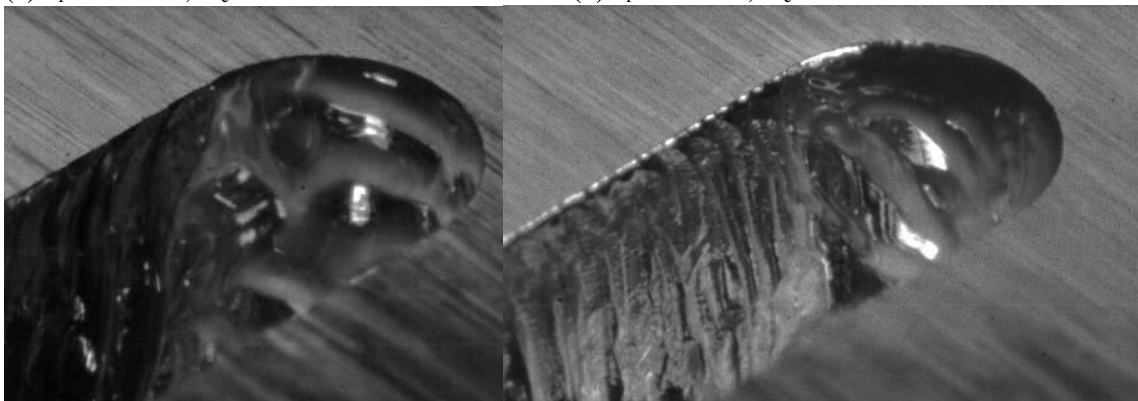


Figure 4-44 Examples of high speed video images.

Summary of the parametric studies

The results of the parametric studies are summarised in Table 4-6, which show tendencies of the changes of the evaluated parameter (α , V_{hump} , δ , λ , R_z) when each of the operating parameters (assist-gas pressure P_G , laser power P_L , beam diameter d_f and defocus distance z_f) is increased.

Another important result is the scaling of the melt flow by α . For a given set of operating parameters, α increases with V_c . When α is smaller than a certain threshold value α_{thr} , melt flow in the central part of the kerf front becomes discontinuous. This threshold value decreases with a decrease of the beam diameter. When α is larger than α_{thr} , the central melt flow becomes continuous. In this range of α , λ and R_z both decrease as α is increased. These results are discussed and interpreted in chapter 5.

Table 4-6 Dependencies of melt flow characteristics on operating parameters.

	$P_G \uparrow$	$P_L \uparrow$	$d_f \uparrow$	defocus \uparrow
α	\rightarrow	\downarrow	\uparrow	\uparrow
V_{hump}	\uparrow	\uparrow	\downarrow	\rightarrow
$\delta (=T_{\text{hump}} * V_c)$	\downarrow	\rightarrow	\uparrow	\rightarrow
λ	\downarrow	\uparrow	\uparrow	\downarrow
R_z	\rightarrow	\uparrow	\uparrow	\downarrow

4.3 Observations of downward development of striations

The observations from above the kerf front described in section 4.2 demonstrated the mechanism of the discontinuities of the central and side flows that depart from the sample surface and also dependencies of the instabilities of the flows on the operating parameters. Practically, the melt flow on the kerf sides determines the surface roughness just below the sample surface. In order to understand further development of striations down to the bottom of the sample, evolution of the melt flow instabilities is further investigated.

Downward development of striations was observed through a glass plate using basically the same method as reported by Yudin and co-workers [Yudin 2007, Yudin 2009, Grigory 2010]. Experimental setup is shown in figure 4-45. The laser beam was irradiated at the interface of a steel sample and a commercial glass sheet with a thickness of 3 mm. It is of course true that the process can be observed without this glass sheet (for example, see [Fushimi 2000]), but the glass is necessary to confine the assist-gas; otherwise, assist-gas jet easily detaches from the steel sample and the melt flow is totally different from the one obtained in real cutting process. We confirmed this point in a preliminary experiment. In the setup shown in figure 4-45, the steel sample and the glass sheet were displaced in the opposite direction. The velocity of the glass sheet was set higher than V_c of the steel sample. These conditions allowed us visualisation with an acceptable quality as reported in [Grigory 2010]. The most important difference from this study is that the observation angle of the high speed video camera was set 45 degrees deviated from the cutting direction in the present experiment. This configuration enabled us to visualise better interactions between melt flows in the central and side parts of the front.

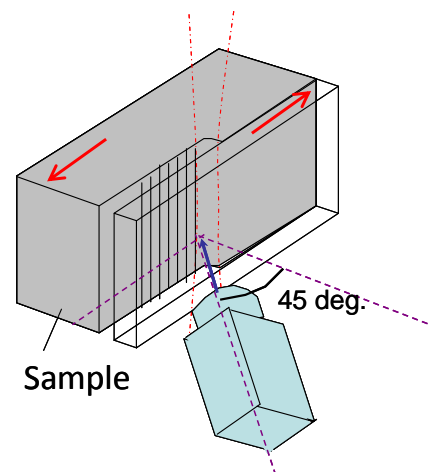


Figure 4-45 Experimental setup for lateral observation of melt flow dynamics through a glass plate.

(a) $V_c = 2$ m/min (b) $V_c = 4$ m/min (c) $V_c = 6$ m/min

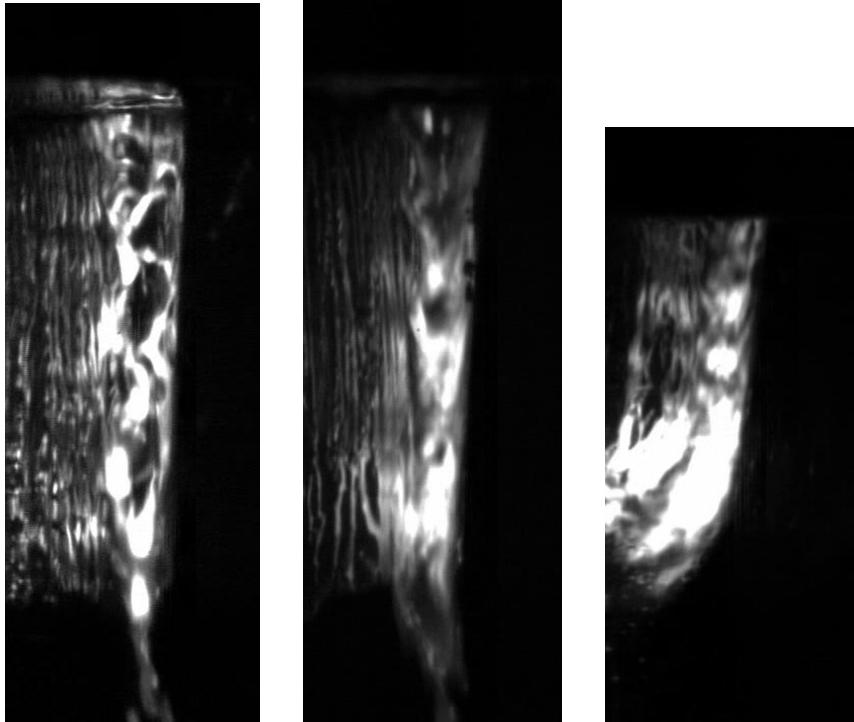


Figure 4-46 High speed video images for different V_c .
($P = 4$ kW, $d = 0.56$ mm, $P_G = 10$ bar, $h = 3$ mm)

Main results of the observations can be summarised as

- 1) When the central flow is unstable from the surface, the central and side flows are rather hard to be distinguished. The downward displacement of melt accumulations (MAs) is chaotic, which can degrade final quality of cut surfaces.
- 2) When the central flow is stable, MAs on the kerf sides are pulled down by the central flow. Resultant regular downward displacement of the MAs leads to a good cut surface quality.

Figure 4-46 show high speed video images obtained with the laser power 4 kW, the beam diameter 0.56 mm, the assist-gas pressure 10 bar, and the sample thickness 3 mm. At $V_c = 2$ m/min, both the central and side flows are unstable from the above. As they slide down the kerf front, they interact to each other and construct an unstable downstream which swings to and from left and right. The striations left on the kerf sides are thus irregular and have a bad quality. At $V_c = 4$ m/min, the central flow becomes almost continuous, whereas the side flow stays unstable. Nevertheless, there exist interactions between the two flows. It can be observed that the melt accumulations are pulled down by the central flow. An important difference from the case of $V_c = 2$ m/min is that the central flow is stable, so the downward displacement of the melt accumulations driven by this stable flow is also stable. As a result, striations that have much more regular pitch and less roughness compared with $V_c = 2$ m/min are left on the kerf sides. At a higher cutting velocity of 6 m/min, the cut velocity is too high and the kerf front is substantially inclined. The lower part of the front is out of the laser beam. Only reflected components of the laser beam contribute to heat the massive melt there. The melt ejection process is unstable and it leaves cut surfaces with a poor quality.

Results of the observations with sample thickness of 5 mm are shown in figure 4-47. For this thickness, the central flow must be in the unstable regime, because the maximum cutting velocity is only 3 m/min. Therefore striations become rough because of the downward unstable melt flow which is generated from the unstable central and side flows initiated from the surface.

As described above, when the central flow is continuous, downward displacement of melt accumulations can be stable, which results in a better quality. As discussed in the previous section, the discontinuity of the central flow can be improved by displacing the focus position. This effect was demonstrated in figure 4-47. By defocusing the focus position from the sample surface ($Z_f = 0$ mm) to 4 mm below ($Z_f = -4$ mm), the central flow can be stabilised to some extent, although it still remains discontinuous. Consequently downward strokes of the melt accumulations to the bottom also appear to be stabilised. For example, in the image for $Z_f = 0$ mm, traces of melt accumulations suggest that some of them detach to the left, deviated from the vertical direction. These traces cannot be found in the image for $Z_f = -4$ mm.

In conclusion, the present lateral observations indicated that not only the side flow but also the central flow affect the quality of striations which are developed down to the bottom surface of the sample. Unstable central flow disturbs downward displacement of the molten material on kerf sides and as a result degrades the surface roughness. On the other hand, when the central flow is stable, melt accumulations are guided downwards by the stable central flow. One can find a stripe of the striations originated at the surface continue to the bottom surface.

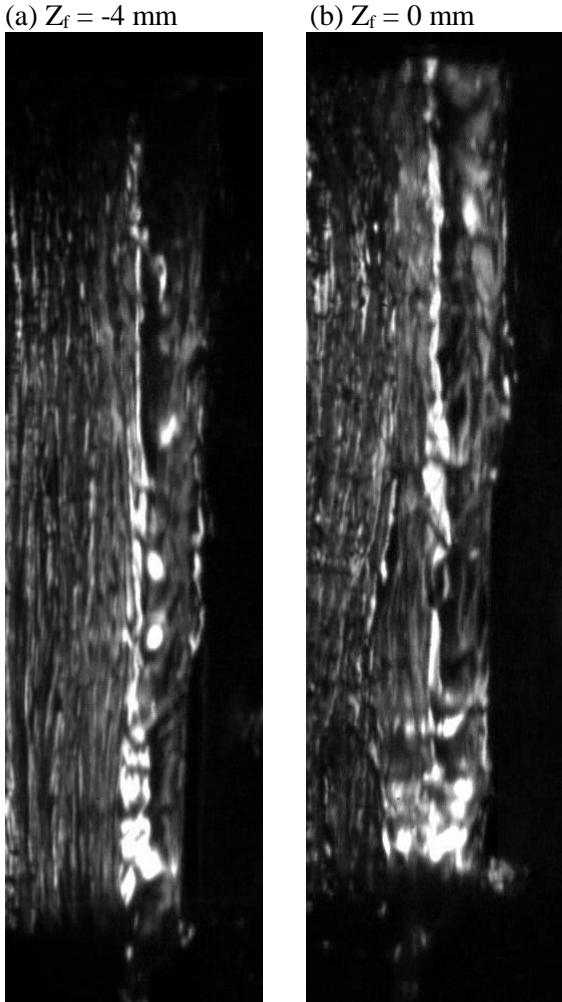


Figure 4-47 High speed video images for different focus positions.
($P = 4$ kW, $d = 0.56$ mm, $P_G = 12$ bar, $h = 5$ mm, $V_c = 2$ m/min)

4.4 Summary

In this chapter, hydrodynamics of melt flow around a kerf front was observed with a high speed video camera, as the first step towards the clarification of the origin of the melt flow instability and striation generation during inert gas laser cutting of steel.

In the first series of the experiments, hydrodynamics in the top part of kerf front was observed from the above of the sample during laser cutting of 3 mm thick mild steel with inert gas of nitrogen. A 8 kW disc laser beam was focused to the diameter of 1.7 mm with the top-hat intensity distribution. We chose this large focus diameter in order to better visualise phenomena around the kerf front. The pressure of nitrogen in the nozzle was 1.5 bar and the nozzle diameter and the stand-off distance were both 3.5 mm.

The melt flow exhibits strong instabilities involving humps, which are bunches of molten material in the central part of the kerf front, and melt accumulations, which appear in the kerf sides of the kerf front. The characteristics of the instabilities can be classified into several regimes depending on the cutting velocity. One of the most important results is that instabilities in the central and side parts exhibit different characteristics in terms of the pitch and the dependence of the stability on the cutting velocity V_c , as explained in the following. The inclination angle α of the kerf front increases with V_c . It will be shown later that the observed velocity dependence of melt flow stability is induced by this change of α .

For $1 \text{ m/min} < V_c < 2 \text{ m/min}$, both the central and side parts of the kerf show discontinuities. The existence of humps, which slide down in the central part of the kerf, was firstly confirmed in laser cutting process. These humps exist on plateau regions where local inclination angle α is quite large. Another interesting finding at the threshold velocity $V_c = 2 \text{ m/min}$ is that the velocity of continuous flow was different from the velocity of humps. This indicates that transport of hump is not a mass flow but an evolution of phase. The pitch δ of humps measured along the cutting direction stays roughly constant at $70 \text{ }\mu\text{m}$ independently of V_c . In this low velocity range, the dynamics of melt flow is very irregular and chaotic. For example, a melt accumulation can be split into several melt accumulations. It was observed also that a melt accumulation on a kerf side and a hump in the central part merge in the middle of the kerf front and go down together. Due to this unstable nature of the trajectories of melt accumulations, rather irregular striations are left on kerf sides.

For $2 \text{ m/min} < V_c < 6 \text{ m/min}$, the central region becomes stable, but the kerf side region is still discontinuous. One of the most important results of the observation is this coexistence of stable flow in the central part and unstable flow in side parts. In most of the theoretical works in the past, it has been assumed that the instability in the central part naturally perturbs the flow in the side region. This kind of assumptions should be rejected at least for this intermediate regime.

In this range of V_c , the side flow is characterised by periodic generation of accumulations from the top part and their displacement downwards. Whereas Yudin *et al.* [Yudin 2007] already observed the downward displacement of the accumulations by lateral visualisation of the kerf side through a transparent glass, our observation has revealed for the first time the processes of the accumulation generation and the striation initiation at the top part of the kerf. Each downward stroke of a melt accumulation leaves a stripe of striations. These accumulations are absorbed into the stable central flow. As α increases with V_c , travelling distance of melt accumulations before meeting the central flow becomes shorter. The depth on a kerf side region where we observe regular vertical striations is thus reduced. The wavelength λ of striations was $199 \text{ }\mu\text{m}$ at $V_c = 3 \text{ m/min}$. An important finding is that this wavelength λ is larger than the pitch δ of humps ($70 \text{ }\mu\text{m}$). The wavelength of striations slightly decreases with an increase of V_c .

The width of the unstable region on the kerf side decreases as V_c is increased. At 6 m/min , both the central and side flows become continuous. The unstable side flow is completely overwhelmed by the stable central flow at $V_c = 6 \text{ m/min}$. At this velocity no striation appears on the side, although we

observe random oscillation of the liquid surface level of the central flow, which creates very thin relief.

A similar observation was made for a two-dimensional configuration where a rectangular bar was melted with a moving laser beam. This experiment enabled us to observe only the characteristic of the central flow without any perturbation from sides. The velocity dependence of the stability of the flow was almost the same as that observed in a normal cutting experiment. This leads us to conclude that the instability observed in the central part of the kerf front in the case of ordinary cutting experiments is not caused by any perturbation from kerf sides but should be attributed to an inherent instability in the central flow.

Then characteristics of the melt flow were investigated, varying various operating parameters: assist-gas pressure, laser beam power, laser beam diameter, and intensity distribution of the beam spot. The beam intensity distribution was changed from the top-hat intensity distribution to a quasi-Gaussian distribution by defocusing. The tendency of the observed results was roughly the same as that observed for the standard condition described above; at a low V_c , both the central and side parts of the kerf front are unstable. As V_c is increased, however, the central flow becomes stable at some point.

It was found that the inclination angle α of the front obeys the approximate law that α is approximately proportional to (V_c/I_L) ; it increases when velocity is increased, when power is decreased, or when diameter is increased. It was found that the threshold angle α_{thr} over which the central flow becomes continuous does not depend on the laser power for a fixed beam diameter. It is thus suggested that the inclination angle α is one of the important parameters that control this flow stability. This threshold angle α_{thr} decreases with a decrease of the beam diameter. It was found also that the defocusing changes drastically melt flow stability. The quasi-Gaussian beam spot lowers the threshold velocity above which the central flow becomes stable.

The pitch δ of humps decreases with an increase of the gas pressure. It was found also that δ decreases with a reduction of beam diameter. On the other hand, δ is independent of the laser power or of the beam intensity distribution.

A good correlation was found in variations of λ and R_z . When V_c is increased from the velocity at which the central flow becomes continuous, λ and R_z slightly decrease with V_c . This behaviour was observed for all the laser powers, although the velocity range for continuous central flow depends on the laser power. It was found also that λ and R_z decrease with a decrease of the spot diameter or with an increase of z_f (i.e. by defocusing).

Finally, downward development of striations was observed by a high speed video camera through a glass plate. The operating parameters were close to those used in real laser cutting process. The laser power and the spot diameter were 4 kW and 0.56 mm, respectively. The pressure of nitrogen was 10-12 bar. The observed video films show that not only the side flow but also the central flow influences final relieves left on kerf sides. When the central flow runs continuously with little fluctuation, melt accumulations on kerf sides go down smoothly to the bottom surface or get assimilated to the stable central flow. Periodic striations with relatively low surface roughness are generated in this case. When the central flow is unstable, downward displacement of melt accumulations becomes chaotic through interactions with the unstable central flow. Consequently one obtains rough cut surfaces. The central flow becomes continuous when the cutting velocity is increased or the focus position is deviated from the sample surface, as stated above.

These experimental results are interpreted and discussed in the next chapter 5.

Chapter 5. Discussions

Résumé

Les résultats des observations précédentes ont indiqué que l'écoulement du liquide sur un front avant de la saignée pouvait présenter une forte instabilité et que l'instabilité sur les côtés de la saignée était la cause de la génération des stries. Dans ce chapitre, l'origine de ces instabilités est discutée et comparée avec les résultats expérimentaux.

L'analyse montre que l'effet de tension superficielle joue un rôle prépondérant dans cette instabilité et nous proposons un modèle physique simple. Ce modèle explique non seulement la génération périodique des humps sur un front avant de la saignée, mais également les différents comportements des instabilités observées sur les parties centrale et les côtés, en particulier leur différence pour la longueur d'onde spatiale caractéristique de ces perturbations et leur dépendance avec V_c . On discute ensuite le processus de génération des stries : les stries résultent du transfert de chaleur à partir des accumulations de liquide vers la partie solide sur les côtés de la saignée, au cours de leur descente. Ce processus de transfert de chaleur est modélisé pour estimer la rugosité finale des surfaces coupées. De plus lorsque l'écoulement central est discontinu, les humps qui apparaissent sur cette partie centrale peuvent perturber le déplacement des accumulations de liquide descendant le long des côtés de la saignée et accentuent la dégradation de la rugosité finale.

Modèle de formation des instabilités observées :

- Formations de humps sur la partie centrale – Discussions :

D'abord, l'origine de la discontinuité observée de la partie centrale du front avant de la saignée est discutée en invoquant l'effet de la tension superficielle. Le matériel fondu à la partie supérieure de la saignée ne peut pas se déplacer sur le long du mur de la saignée instantanément en raison de son maintien par la tension superficielle. La matière fondue ne commence à descendre en glissant sur le mur lorsque sa taille atteint une certaine valeur critique. Cette taille dépend de la pression de gaz d'assistance et du coefficient de la tension superficielle et est accord avec ses valeurs correspondantes expérimentales : diminution avec la pression du gaz d'assistance, et indépendance avec la puissance laser ou sa distribution d'intensité.

Cette discontinuité disparaît quand la vitesse de coupe V_c est augmentée ; cet effet est également conforme au rôle joué par la tension superficielle. Lorsque V_c augmente, la fréquence de génération des humps augmente et la distance entre deux humps consécutifs diminue. Par conséquent l'écoulement de liquide devient continu au-delà d'une certaine vitesse. Une analyse simple montre que la stabilité de l'écoulement de liquide dans la partie centrale ne dépend que de l'angle α d'inclinaison, et au-dessus d'un angle seuil, l'écoulement de liquide devient continu. Cette loi d'échelle a été vérifiée expérimentalement pour des puissances laser variables. On a également observé que cet angle seuil augmente avec le diamètre du faisceau laser. Les observations suggèrent également que la présence des accumulations du liquide sur les côtés de la saignée facilite la fusion de deux humps consécutifs et rendent ainsi l'écoulement continu.

On a vu précédemment que l'angle α d'inclinaison, qui déterminait la stabilité de l'écoulement central, peut être déterminé par une équation de bilan énergétique et il varie proportionnellement à (V_c/I_L) en première approximation. Cette loi d'échelle a été parfaitement confirmée expérimentalement.

- Formation des stries sur les flancs – Discussions :

L'instabilité observée sur les flancs de la saignée peut également être interprétée à l'aide de la tension de la surface. La diminution du pas caractéristique des accumulations de liquide (la longueur d'onde des stries) avec l'augmentation de la pression du gaz d'assistance confirme ce mécanisme. Il faut cependant noter deux principales différences : D'abord, le pas de ces stries est très différent de celui des humps de la région centrale. De plus, cette instabilité subsiste même pour des vitesses de coupe V_c pour lesquelles l'écoulement central devient stable. Cet effet est interprété à l'aide d'une considération géométrique. On montre que le rapport entre le pas de ces stries λ et le pas caractéristique des humps δ est égal à $(2r_k/\delta)^{1/2}$ et est conforme aux résultats expérimentaux : λ est plus grand que δ , et décroît avec

le diamètre du faisceau laser. Le fait que λ soit plus important que δ a pour conséquence que la fréquence de génération des accumulations sur les côtés est plus faible que celle des humps de la partie centrale. Il en résulte donc que la vitesse seuil pour laquelle l'écoulement sur les côtés devient continu est plus élevée que celle assurant la stabilité de l'écoulement central.

On peut donc dire que les principales différences des caractéristiques typiques de ces instabilités observées au centre ou sur les côtés (différence entre λ et δ et dépendance de la stabilité avec V_c) peuvent être correctement interprétées en invoquant le rôle prépondérant de la tension superficielle.

On a également vu que λ diminue avec V_c , lorsque l'écoulement central est continu. Ceci peut aussi s'interpréter en faisant intervenir cet écoulement central continu : pour cette gamme de vitesse, les accumulations de liquide descendent le long des côtés de la saignée et finissent par être absorbées par l'écoulement central continu ; tant que V_c augmente, l'angle α d'inclinaison augmente. En conséquence λ diminue.

Les stries observées résultent de la génération et du déplacement vertical des accumulations de liquide le long des flancs. Cette accumulation de liquide intercepte et absorbe une partie de la puissance laser et en conséquence, de l'énergie est transférée au solide. La région du solide en contact avec l'accumulation de liquide peut donc localement fondre et ceci au cours de la descente de l'accumulation : Il en résulte alors une rainure, caractérisée par une rugosité R_z de la saignée. Une analyse de ce processus de conduction de chaleur vers les parois des flancs de la saignée, prévoit que la rugosité R_z est du même ordre de grandeur que λ , en accord avec les observations expérimentales. Ce modèle proposé est également en accord pour ce qui concerne les diverses corrélations observées dans l'étude paramétrique de λ et R_z : λ et R_z diminuent avec une diminution du diamètre du faisceau laser ou avec une augmentation de α dans la gamme de vitesse où l'écoulement central devient continu.

Les observations latérales de la saignée (avec la méthode utilisant une plaque de verre) ont indiqué que la stabilité de l'écoulement central dans la saignée affecte également la qualité finale des stries. Quand l'écoulement central est continu, il « absorbe » les accumulations de liquide. La réduction de λ et des stries régulières entraînent alors à une meilleure rugosité. Par contre, quand l'écoulement central est discontinu, la dynamique des accumulations de liquide devient chaotique et dégrade la rugosité.

Ces observations nous permettent également d'interpréter l'amélioration de la stabilité de l'écoulement de liquide et de la rugosité lorsqu'une distribution d'intensité gaussienne est utilisée au lieu d'un profil « top-hat ». En fait, dans la périphérie de la distribution gaussienne, où l'intensité est réduite, l'angle α d'inclinaison du profil de la saignée près de la surface est important et donc, comme on l'a vu précédemment, tend à rendre l'écoulement central de cette zone continu. En conséquence, la dynamique des accumulations de liquide sur les côtés est stabilisée, pour les mêmes raisons qui ont été décrites plus haut et donc λ et R_z peuvent être diminuées.

En conclusion de ces expériences, de leur analyse et de leur interprétation, on peut dire que c'est la tension de surface qui joue un rôle déterminant dans la dynamique de l'écoulement du liquide en découpe laser. Elle est responsable de la génération des humps sur la partie centrale et des accumulations de liquide sur les côtés de la saignée et en conséquence de la qualité finale de la découpe. Il faut rappeler que seul Makashev *et al.* [Makashev 1992, Makashev 1994] avait prévu théoriquement certains aspects de ce comportement, bien que leur analyse théorique ait uniquement porté sur un modèle 2D, où seule la partie centrale était concernée. Nous avons vu que notre analyse pouvait expliquer les raisons de la disparition de l'instabilité, en raison de l'effet de cette même tension de surface (fusion de deux humps successifs, ou des accumulations de liquide). De même, c'est la tension superficielle qui contrôle l'éventuelle interaction entre les accumulations de liquide et les humps (possibilité de fusion de ces deux écoulements ou absorption de l'accumulation dans la partie centrale).

Introduction

The observation results presented in chapter 4 revealed that melt flow on a kerf front exhibits strong instability and the instability on kerf sides is the cause of striation generation. In this chapter, origin of the observed instability of melt flow is interpreted and its relevance to striation generation process and cut surface quality is discussed.

First, the observed instability of melt flow in the central and side parts of the kerf front is considered. Experimental results for the standard condition (laser power: 8 kW, beam diameter: 1.7 mm ϕ (with the top-hat intensity distribution), gas pressure: 1.5 bar) are interpreted and analytical models are proposed for the pitch δ of the humps, the wavelength λ and surface roughness R_z for striations. Then the results of the parametric study are analysed and the validity of the proposed analytical models is examined.

Surface tension effect should be the principal cause of the melt flow instabilities that are initiated from top parts of the central and side parts of the kerf front, respectively. Molten material produced at the surface cannot be ejected instantaneously, since surface tension force tends to keep it at the surface while its size is small. A theoretical analysis on a force balance between the surface tension and the force exerted by assist-gas explains well the order of the pitch δ of the intermittent generation of humps. As the cutting velocity is increased, the generation frequency of humps increases and the distance between two adjacent humps along the kerf front decreases. We consider that the melt flow becomes continuous for a high cutting velocity, because surface tension begins to join these humps. Our analysis shows that the stability of the central flow is controlled by the inclination angle α of the front and there exist a threshold angle α_{thr} above which the central flow becomes stable.

As shown in chapter 4, the wavelength λ of striations is larger than the pitch δ of humps in the central part of the kerf front. Also the velocity range where melt flow instability appears in side regions is different from that of the central flow. These results can be interpreted as a result of a geometrical effect. Thus the characteristics of the melt flow instabilities observed both in the central and side parts can be explained coherently by a unique mechanism related to surface tension.

Then striation generation process is discussed. We consider that striations are basically created due to heat transfer from melt accumulations on kerf sides to the solid part. The heat transfer process is analysed to estimate surface roughness of cut surfaces. The surface roughness R_z is theoretically analysed by a simple heat transfer model and the result shows a reasonable agreement with the experimental data.

Finally, downward development of striations is discussed. Observations indicate that not only can the melt accumulations on kerf sides but also instability of the central flow influence striation generation process. When the central flow is discontinuous, humps that appear on the central part can disturb downward displacement of melt accumulations on kerf sides and can degrade surface roughness.

These discussions yield a general description of the instabilities of melt ejection process and relevant striation generation process during inert gas laser cutting of steel.

5.1 Inclination angle of kerf front

It is considered that the tilting angle α of central part of the kerf front plays an important role in determining the stability of the flow, as discussed in the following.

As shown in figure 4-13, the inclination angle α_{ave} averaged over the entire kerf front increases with cutting velocity V_c . This agrees with the theoretical equation (2-10). Although we have unknown parameters $A(\alpha)$ and T_1 in eq.(2-10), let us calculate theoretical values of α with assumption that A is constant at 0.5 regardless of α and also that $T_1 = T_m$. The result is shown in figure 4-13 as the dotted line. The model predicts well the increase of α with V_c . The discrepancy between this tentative plot and the experiment increases as V_c increases and this must be attributed to the assumption of $T_1 = T_m$.

Thus it is implied that the temperature T_1 of melt layer increases monotonously with V_c , as is usually observed in experimental temperature measurements [Arata 1979, Woods 1999].

5.2 Instability in the central part (Hump generation)

Let us consider first the origin of humps, which were observed in the central part. As has been shown in Chapter 4, the humps appear in a low cutting velocity condition. When the cutting velocity is increased, they disappear at a certain velocity. In the following, we discuss the mechanism of generation of the humps and the reason why they disappear at a high cutting velocity. As proposed by Makashev *et al.* [Makashev 1992, Makashev 1994], the instability can be explained from an effect of surface tension. In fact, it will be shown later that the instability which was observed on kerf sides can also be understood as a result of the same surface tension effect. The surface tension is considered to be the primary factor that governs the instability of melt ejection in inert gas laser cutting of steel.

The following discussion for the instability in the central part of the kerf front utilises 2D descriptions, where physical processes are expressed in the intersection of a kerf front and the symmetric plane of cutting process. Such 2D analyses without consideration of kerf sides is justified for the central flow, according to the result of the 2D melting experiment, which shows essentially the same characteristics of the melt flow instability as was observed in normal laser cutting.

5.2.1. Mechanism of generation of humps

We discuss about the force balance between surface tension and dynamic force exerted by gas, in a similar way as in the work by Makashev *et al.* [Makashev 1992, Makashev 1994]. Let us consider the condition which is necessary to trigger the displacement of a hump from the top surface, using a simple model described in figure 5-1(b). At time $t = t_0$, the precedent ejection cycle is over and there rests no melt inside the area of laser beam. As the laser beam proceeds after this time, solid part comes into the beam area and is melted rapidly. When the size of melt accumulation is too small, surface tension force remains larger than the gas force applied from the above, so that the accumulation continues to stay attached at the top. As the laser beam proceeds, more melt is generated and its size grows up. The gas force increases due to the increase of its surface area $\delta \cdot l$, where δ and l are the dimensions of the accumulation (figure 5-1(b)). The accumulation is considered to start to move when the gas force exceeds the surface tension force $\sigma \cdot l$ that retains the accumulation along the distance l . This balance can be expressed as

$$F_s(\delta l) \approx \sigma l \quad (5-1)$$

where F_s is the force per unit area applied on the surface of the accumulation. The applied surface area is measured by the projection to the sample surface ($\delta \cdot l$). The force F_s per unit area is generally composed of viscous friction and static pressure. Makashev *et al.* [Makashev 1992, Makashev 1994] considered that F_s is expressed by pressure drop across the vertical length of the accumulation ($\sim \delta$), which is caused by the reduction of gas flow cross section S due to the existence of the accumulation (eq.(3-6)). However, it is not so evident how to estimate the change ΔS , because the gas flow can expand freely inside the kerf along the cutting direction. Moreover, in the present study, relative variation ($\Delta S/S$) of the cross section, which might be expressed as (δ/r_k) , is so small that the estimation of $(\Delta S/S)$ is very delicate. The relation $(\delta/r_k) \ll 1$ suggests that, instead of considering $(\Delta S/S)$ for the entire gas flow, it should be more appropriate to look at the problem locally; in such a way that force is exerted on an obstacle placed within a homogeneous one-directional flow. According to a classical theory explaining drag force, F_s can be written as [Tritton 1977]

$$F_s \approx C_D \left(\frac{1}{2} \rho_g v_g^2 \right) \quad (5-2)$$

where non-dimensional coefficient C_D is a function of the Reynolds number Re and surface profile of an obstacle: the melt accumulation in the present case. Please note that C_D includes two contributions from the friction drag and the pressure drag. Using (5-1) and (5-2) we obtain

$$\delta \approx \frac{2\sigma}{C_D \rho_g v_g^2} \quad (5-3)$$

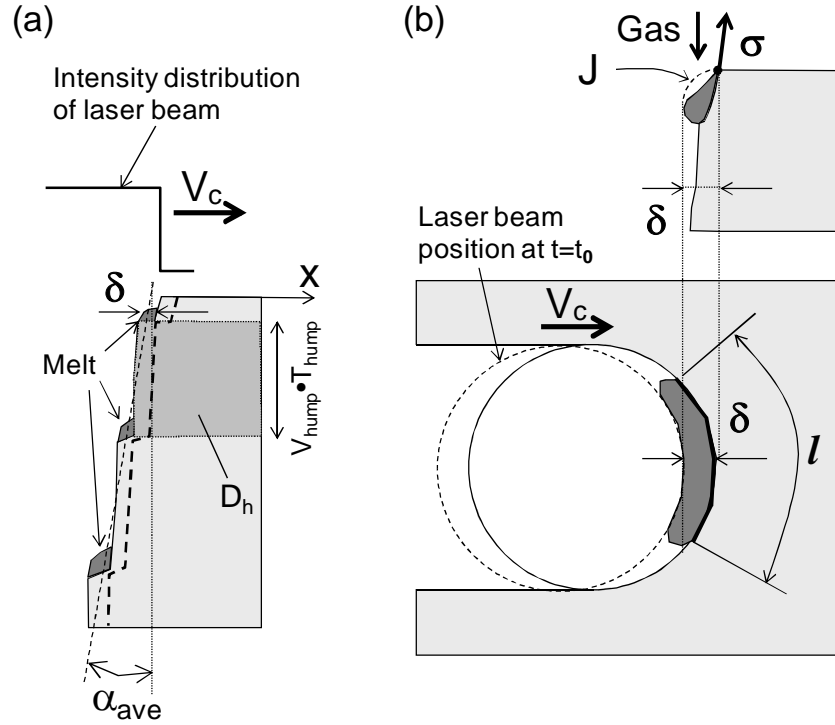


Figure 5-1. Schematics of profiles of solid-liquid interface on the cross section of the central plane of the kerf (a) and of melt accumulation at the top part of the central region of the kerf (b), viewed on the cross section of the central plane (upper) and from the above (lower).

We assume that the surface profile of the accumulation can be approximated as a quarter of a circle with radius δ (J in figure 5-1(b)), and we use the value C_D for flow around a cylinder, which has been widely studied. For the standard gas condition (gas pressure: 1.5 bar) used in this study, Re ($= v_g(2\delta)/\nu$; ν : kinematic viscosity) is about 10^3 , so that we can take $C_D \approx 1$ [Tritton 1977]. From (5-3) we obtain $\delta = 140 \mu\text{m}$ for the conditions in this study [$\sigma = 1.9 \text{ Pa}\cdot\text{m}$ [Kasama 1983], $\rho_g = (P_{in}/P_0)^{1/\gamma} \rho_0$ ($\rho_0 = 1.3 \text{ kg/m}^3$), $v_g = 1.1 \times 10^2 \text{ m/s}$].

The generation of humps is repeated every time when the laser beam proceeds by the distance δ , since heating time is very short. The period of the generation of humps is thus given by

$$T_{hump} \approx \frac{\delta}{V_c} \quad (5-4)$$

The model overestimates δ by a factor of 2, but it successfully predicts that δ is independent of the cutting velocity V_c . This supports the validity of the present model. The discrepancy from the experimental result should be attributed to overestimation of δ in (5-3), which is probably caused by the rough approximation of C_D .

5.2.2. Downward displacement of the humps

Now let us discuss the dynamics of the humps. Figure 5-1(a) schematically shows the cross section of the kerf front at the central symmetric line at some instance.

As was demonstrated experimentally in figure 4-12(a), melt can exist on a small plateau so-called “shelf” [Golubev 2004]. This shelf structure slides down along the kerf front, because the absorbed intensity is higher on the shelf than other part and local drilling occurs there. The downward velocity of the shelves (humps) can be roughly estimated as [Golubev 2004]

$$V_{hump} \approx \frac{AI_L}{\rho_s [C_{ps}(T_m - T_0) + L_m]} \quad (5-5)$$

The equation assumes horizontal shelves ($\alpha \sim 90$ degrees) and neglects preheating in solid and temperature increase over T_m in the melt layer.

Periodical generation and downward displacement of such shelves from the top part generates wavy structure in the solid-liquid interface, which propagates downwards.

As is observed for $V_c = 1$ m/min (figure 4-12(a)), melting tends to occur only in the vicinity of the shelves. The reason can be explained as follows. First let us pay attention to the time-averaged value α_{ave} , which is shown by the dotted line in figure 5-1(a). This mean angle corresponds to the equilibrium tilting angle, which satisfies the power balance (eq.(2-10)). In the following we express this angle as α_{ave} , in order to distinguish it from an instantaneous local inclination angle. Due to the existence of shelves, regions between any two shelves must have local tilting angle that is lower than the time-averaged value α_{ave} , so that the regions between the shelves must be cooled and cannot be melted. Consequently, the melt accumulations (humps) exist only on the shelves and they are transported downwards with the displacement of the shelves. If we take a look at the evolution of the solid-liquid interface at certain depth, the advance of the interface along the cutting direction occurs only when the shelves pass the point.

With the above-mentioned picture of the humps, we can improve the estimation of the downward velocity of the humps. An energy balance is considered with a simplified kerf profile model shown in figure 5-1(a). At $t = 0$, the profile is represented with the solid-line. The profile on the whole advances to the right by δ to the dotted line after the time interval T_{hump} . The energy balance for a thickness of $(T_{hump} \cdot V_{hump})$ (the dark region D_h in figure 5-1(a)) during this time interval can be written as

$$A(\chi)I_L(2r_k)\delta\left(\frac{\delta}{V_c}\right) = \left\{ 2\kappa[\rho_s C_{ps}(T_m - T_0) + \rho_s L_m + \rho_l C_{pl}(T_l - T_m)]Pe + 4K(T_m - T_0)\left(\frac{Pe}{2}\right)^{0.3} \right\} \times (T_{hump} \cdot V_{hump})\left(\frac{\delta}{V_c}\right) \quad (5-6)$$

Here χ is the inclination angle for surface of the humps. With eq.(2-10),

$$V_{hump} = \frac{A(\chi)}{A(\alpha)} \frac{V_c}{\tan \alpha_{ave}} \quad (5-7)$$

Please note that this equation is more precise than eq.(5-5) in that it takes into account the preheat of the solid part (= account for heat conduction). Using a rough approximation that $A(\chi) \approx A(\alpha)$, one obtains

$$V_{hump} \approx \frac{V_c}{\tan \alpha_{ave}} \quad (5-7')$$

With the experimental values of α_{ave} , shown in figure 4-13, eq.(5-7') predicts that $V_{hump} \approx 0.1$ m/s for $V_c = 1 \sim 2$ m/min. These values are in the same order as the velocities observed experimentally (0.1 ~ 0.2 m/s).

Up to now the size δ of humps has been assumed to be constant. However, this is not true. It tends to grow up during the downward movement, because the volume of a solid part scraped from the front wall is continuously added to the melt. This induces additional instability during the downward displacement of the melt, since the force balance (5-1) cannot be satisfied anymore; while the surface tension term is kept constant, the gas force increases with the increase of the melt size. As a result, a part of the melt can easily be expelled from the shelf. This kind of behaviour has been confirmed in the experiment. For low velocity condition such as at $V_c = 1$ m/min (figure 4-12(a)), where the melt ejection is in completely discrete regime, it is frequently observed that a hump falls from the shelf and merges to the precedent hump.

5.2.3. Threshold condition of hump generation

Let us consider why the humps disappear for a high velocity. It is considered that the disappearance of

5.3.1. Wavelength of striations

Now let us estimate the period of the intermittent ejection on the kerf side, which corresponds to the striation wavelength. In the following discussion, we restrict ourselves within the velocity range of $2 \text{ m/min} < V_c < 6 \text{ m/min}$. In this range, λ is well defined; the dynamics of side flow is regular, without perturbation from the central flow, which was observed for $V_c < 2 \text{ m/min}$.

In figure 5-2 is shown the kerf side region seen from the above. At $t = t_0$, the precedent ejection cycle is over, and the kerf profile at the surface almost coincides with the laser beam front (beam centre at C_1). After this moment, laser beam proceeds along the x-axis and solid material in the unstable part, the width of which is defined by W , enters the beam area. It is melted very rapidly from the top surface, but not ejected immediately, and accumulation starts. As in the discussion of the instability in the central region, the accumulation continues until the time when the thickness of the melt accumulation reaches δ , which is given by (5-3), and then ejection occurs. At that time laser beam centre is at C_2 and we can consider that the length of the segment U_1U_2 in figure 5-2 as the characteristic thickness δ of the ejected melt. Using the triangle $C_1C_2U_2$, the pitch λ of striations can be determined from the following geometrical relation:

$$\lambda^2 + (r_k - \delta)^2 = r_k^2 \quad (5-10)$$

Using the fact that $\delta \ll r_k$, one obtains

$$\lambda \approx \sqrt{2r_k\delta} \quad (5-11)$$

It is shown that striation wavelength λ is larger than δ , which defines the pitch of humps in the central part of the kerf front, by a factor of $(2r_k/\delta)^{1/2}$. Substituting into (5-11) the theoretical value of $\delta = 140 \text{ }\mu\text{m}$ obtained from eq.(5-3), λ is found to be $\sim 500 \text{ }\mu\text{m}$. This is more than two times larger than the experimentally obtained wavelength for $2 \text{ m/min} < V_c < 6 \text{ m/min}$ ($\sim 200 \text{ }\mu\text{m}$). However, considering the fact that there has already been the overestimation in δ (about a factor of 2), it can be said that the simple model well predicts the magnitude of λ .

Whereas the expression (5-11) predicts that λ is independent of V_c , experimental result shows that λ slightly decreases with V_c . A possible explanation for this behaviour is a pull-down effect from the central flow: in the velocity range considered, melt accumulations slide down on kerf sides and end up being absorbed into the central flow. As V_c increases, α is raised. This means that the melt accumulations are assimilated into the central flow at an upper point on the kerf sides. This suggests that more interaction occurs between the central flow and melt accumulations through surface tension even when the melt accumulations are near the sample surface. An additional term of the surface tension in the force balance equation may reduce the striation wavelength λ .

The instability persists on kerf sides even when the central flow becomes continuous ($2 \text{ m/min} < V_c < 6 \text{ m/min}$). This can be explained by the difference in size between δ and λ . As in eq.(5-8), if one assumes that the side flow becomes continuous when the distance of two accumulations on kerf sides become equal to the typical size δ of each accumulation, one obtains the following equation:

$$\left(\frac{\lambda}{V_c} \right) \cdot V_{hump} \approx c\delta \quad (5-12)$$

Here the velocity V_{hump} for humps in the central part was used, because little difference was recognised between the downward velocities of humps in the central part and of melt assimilations along kerf sides in high speed video camera observations. Comparing with (5-8), one obtains that the threshold cutting velocity for the disappearance of the instability on kerf sides is larger by a factor of (λ/δ) than that of the instability in the central part. Experimentally the ratio of the threshold velocity was 3 (6 [m/min]/ 2 [m/min]). This value coincides well with the experimental value of (λ/δ) ($\approx 200 \text{ }\mu\text{m} / 70 \text{ }\mu\text{m}$).

5.3.2. Width of instable region on kerf sides

Generalisation of the above discussion enables us to estimate the width W of instable region on kerf

sides. We generalise the pitch p_δ of the melt accumulations as a function of the azimuthal angle ϕ from the cutting direction (see figure 5-2 for the definition of ϕ). Assuming that a melt accumulation at a position of an angle ϕ departs from the surface when the segment B_1B_3 becomes equal to δ , one obtains

$$p_\delta = \delta / \cos\phi \quad (5-13)$$

($p_\delta = B_1B_2$) For an arbitrary cutting velocity V_c , the angle which separates the stable and instable flows can be defined as a point where the distance of two accumulations becomes equal to $c\delta$.

$$\left(\frac{p_\delta}{V_c}\right)V_{hump} \approx c\delta \quad (5-14)$$

We define V_{c1} as the threshold velocity for the disappearance of instability at the centre ($V_{c1} = 2$ m/min for the standard condition). It satisfies

$$\left(\frac{\delta}{V_{c1}}\right)V_{hump} \approx c\delta \quad (5-15)$$

One obtains from eqs.(5-13) to (5-15)

$$\cos\phi \approx \frac{V_{c1}}{V_c} \quad (5-16)$$

From a geometrical relation one obtains

$$\frac{W}{r_k} \approx 1 - \sqrt{1 - \left(\frac{V_{c1}}{V_c}\right)^2} \quad (5-17)$$

This equation predicts a monotonous decrease of W with an increase of V_c , as experimentally observed. It can be considered that the instability on sides disappears when W becomes equal to δ . Letting this cutting velocity V_{c2} , we obtain from eq.(5-17) $(V_{c2}/V_{c1}) \sim (r_k/2\delta)^{1/2}$ (for $\delta \ll r_k$). For conditions of this experiment, (V_{c2}/V_{c1}) is predicted to be 2.5 ($r_k = 0.85$ mm, $\delta = 0.07$ mm), which agrees well with the experimental value of 3 ($V_{c1} = 2$ [m/min], $V_{c2} = 6$ [m/min])

It can be added that consideration of W that is smaller than δ is not necessary, because in this case the accumulation is too thin to be ejected under the given gas condition and thus the melt flow is expected to be continuous in any way.

5.4 Surface roughness

Another practical interest of this model is the estimation of surface roughness due to the striations. The roughness may be approximated by sum of the two distances h_f and h_e defined in figure 5-2:

$$R_z \approx h_f + h_e \quad (5-18)$$

The first term h_f corresponds to thickness of the part F of material (figure 5-2) which is expelled from the laser beam area during the accumulation period and thus is solidified. The height h_f can be easily obtained from geometrical relation:

$$h_f \approx \frac{\lambda^2}{8r_k} \quad (5-19)$$

which is in the order of 6 μm according to the experimental results.

The feasibility of the solidification is validated from the following estimation of the time Δt_f , which is necessary to solidify the part F. The solidification results from heat transfer from the liquid part F to the solid part across the sidewall. If the amount of energy transferred exceeds the energy released during the phase transition from liquid to solid, the part is solidified. Thus the time Δt_f can be estimated from

$$q\Delta t_f \approx \rho_s h_f L_m \quad (5-20)$$

Here we have neglected temperature increase of liquid over T_m . The heat flux q can be written as

$$q \approx K \frac{(T_m - T_0)}{\Delta y} \quad (5-21)$$

where Δy is the characteristic distance of the temperature field along y-axis in the solid side. This distance Δy is estimated from the fact that the power necessary to heat up the width Δy of the solid part along each side of the kerf corresponds to the heat conduction loss p_l given in eq.(2-8). That is,

$$p_l \approx 2\rho_s V_c \Delta y C_{ps} (T_m - T_0) \quad (5-22)$$

Using eq.(2-8),

$$\Delta y \approx \left(\frac{Pe}{2} \right)^{-0.7} r_k \quad (5-23)$$

From (5-20), (5-21) and (5-23), one obtains

$$\Delta t_f \approx \left(\frac{\lambda^2}{8\kappa St} \right) \left(\frac{Pe}{2} \right)^{-0.7} \quad (5-24)$$

where

$$St \approx \frac{C_{ps} (T_m - T_0)}{L_m} \quad (5-25)$$

is the non-dimensional Stefan number ($St \approx 1.8$ for steel). It is estimated that the time Δt_f is about 0.15 ms at $V = 3$ m/min. This time is much shorter than the accumulation period $\Delta t_a = \lambda/V_c$ ($\Delta t_a = 4$ ms at $V_c = 3$ m/min).

The second term h_c in the right hand side of (5-18) represents the melting of the solid region (part E in figure 5-2) due to the heat transfer from the melt accumulation. The phenomenon is quite similar to the above solidification, but the great difference is that now the accumulation within the beam area always absorbs laser intensity, so that melting of the solid part persists as long as the accumulation stays at the top or propagates downwards.

The depth h_c is estimated with a model shown in figure 5-3, which shows intersection of the kerf side and the plane through $C_2U_2U_1$ in figure 5-2. We assume that melt accumulation with thickness of δ suddenly appears at $t = 0$ and it rests at this position until $t = \Delta t_a = \lambda/V_c$. A power balance for the melt droplet with the volume of $(l\delta\lambda)$ can be expressed as

$$AI_L [(e_0 + \delta)\lambda] \approx \rho C_p (l\delta\lambda) \frac{dT}{dt} + \rho L_m (l\lambda)v + q_w (l\lambda) \quad (5-26)$$

Here v is the velocity of the solid-liquid interface to the solid part. The energy absorbed from the laser beam is spent for heating the melt accumulation and melting the solid part and is dissipated as heat conduction deep into the solid part. It is assumed that, without the melt accumulation, the heat flux from the laser beam is balanced with the heat conduction q_w .

$$AI_L (e_0 \lambda) \approx q_w (l\lambda) \quad (5-27)$$

Then we obtain

$$AI_L (\delta \lambda) \approx \rho C_p (l\delta\lambda) \frac{dT}{dt} + \rho L_m (l\lambda)v \quad (5-28)$$

This equation means that additional energy supplied owing to the existence of melt accumulation with the thickness δ is used to heat the melt accumulation and to move the melting front into the solid part. For the sake of simplicity, we neglect the heating time of the melt

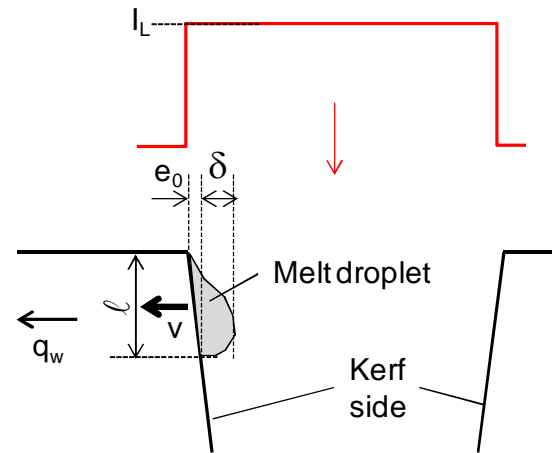


Figure 5-3. Transverse cross section of a kerf in a plane perpendicular to the cutting direction.

accumulation ($\sim \delta^2/\kappa$). This is equivalent to assume that all the additional energy is utilised to melt the solid part. Then the depth h_e ($= v \cdot \Delta t_a$) can be calculated as follows:

$$h_e \approx \frac{AI_L \delta \lambda}{\rho L_m V_c l} \quad (5-29)$$

The roughness is finally obtained as

$$R_z \approx \left(\frac{\lambda}{8r_k} + \frac{AI_L \delta}{\rho L_m V_c l} \right) \lambda \quad (5-30)$$

The length l of a melt accumulation shown in figure 4-12(c) is roughly estimated to be 0.5 ~ 1.0 mm. Thus, with $\delta = 70 \mu\text{m}$, we can approximate δ/l to be ~ 0.1 . Assuming also that $A = 0.5$, the non-dimensional number ($AI_L \delta / \rho L_m V_c l$) is found to be in the order of 1. In eq.(5-30), the second term of erosion (h_e) is much larger than the first term of solidification (h_f). As a result it is predicted that the roughness R_z has the same order as the striation wavelength λ and decreases with the cutting velocity V_c . These theoretical predictions roughly agree with the experimental results.

From the approximate expression of h_e (5-29), principal influence of operating parameters on R_z is deduced. Using also the dependence of λ on δ (eq. (5-11)),

$$R_z \approx 2^{1/2} St \left(\frac{\delta}{l} \right) \delta^{1/2} r_k^{1/2} \left(\frac{AI_L}{\rho(T_m - T_0)V_c} \right) \quad (5-31)$$

If the factor (δ/l) is assumed to be constant, the following three factors show the dependence of R_z . First, δ is a function of σ , ρ_g and v_g , as shown in eq.(5-3). It decreases with the increase of v_g or that of P_{in} , which raises ρ_g . Hence the preparation of appropriate gas condition is an important factor to improve cutting quality, as is a well-known experimental fact. The other two factors represent the dependence on the operating parameters of the laser beam. It is expected that a small beam diameter ($\sim 2r_k$) will decrease R_z . The last factor ($AI_L / \rho C_p (T_m - T_0) V_c$) is related to $\tan \alpha$ as can be seen from eq.(2-10).

5.5 Influence of operating parameters

In the following, influence of operating parameters on characteristics of the instability is discussed based on the results of the parametric study in section 4.2.4.

(a) Gas pressure (Figures 4-21 to 4-26)

First of all, the inclination angle α is almost independent of the pressure (Figure 4-21). In general, a decrease of the pressure causes an increase of melt film thickness, which then increases averaged temperature on the melt surface. This increase of the temperature should be realised by an increase of α , which elevates the energy absorbed per unit thickness. The present result shows, however, that this increase of α is negligible within the investigated parameter range and suggests that the melt surface temperature is little affected with the decrease of the assist-gas pressure.

The fact that α varies little with the pressure indicates that V_{hump} hardly depends on the gas pressure, according to the theoretical equation (5-7'). Nonetheless, we observed a slight decrease of V_{hump} with a reduction of the pressure. As explained in section 5.2.3, the decrease of V_{hump} tends to make the central flow continuous as two adjacent humps are joined. This should be the reason why the melt flow becomes more continuous as the pressure is reduced.

The fact that δ and λ decrease with an increase of the gas pressure (Figures 4-23 and 4-24) strongly supports the proposed mechanism of the instability generation by surface tension. On the other hand, the roughness R_z hardly depends on the pressure (Figure 4-25). This is not consistent with eq.(5-30) which states that R_z is approximately proportional to λ . This is not surprising, however, because the physical model proposed in the previous section 5.4 is supposed to be applicable only to the case where melt accumulations are created and displaced downwards rather regularly. This situation

corresponds to the velocity range $V_c \geq 3$ m/min for the gas pressure of 1.5 bar. For the operating conditions presented in figure 4-25, the dynamics of generation and displacement of melt accumulations is highly chaotic.

(b) Laser power (Figures 4-27 to 4-32)

From figure 4-27, one can confirm that α is approximately proportional to (V_c/I_L) , where I_L is the laser beam intensity. The empty marks in the figure indicate that the central flow is stable without humps. When α is larger than 16 degrees, the central flow becomes continuous, regardless of the power. This behaviour was confirmed also in a two-dimensional melting experiment with rectangular bars. This experimental fact that α determines the stability of the central flow agrees well with the theoretical prediction from eq.(5-9)

When the laser power is lowered, the velocity V_{hump} is decreased if compared with the same cutting velocity. This can be interpreted as a result of an increase of $\tan\alpha_{\text{ave}}$, which decreases V_{hump} according to eq.(5-7').

Although the velocity range where the central flow involves humps depends on the laser power, it is confirmed from figure 4-29 that δ does not depend on the laser power. This is consistent with the theoretical prediction that δ is determined only from the pressure balance between the assist-gas force and the surface tension. This independence of δ and the decrease of V_{hump} with the decrease of the laser power results in the reduction of the threshold velocity over which the central flow becomes continuous.

The wavelength λ of striations slightly decreases with the cutting velocity V_c for a range where the central flow becomes continuous. As discussed in section 5.3.1, a pull-down effect from the central flow can be the reason for this behaviour. When the laser power is lowered, the threshold velocity for the continuous central flow diminishes. Consequently, the slight decrease of λ occurs in a lower velocity range for a lower laser power. In this velocity range, where the central flow becomes stable, R_z decreases with V_c , for all the laser powers. The equation (5-31) suggests that this improvement of R_z is caused by the increase of V_c and also by the decrease of λ .

(c) Beam diameter (Figures 4-33 to 4-38)

The dependence of the inclination angle α on the beam diameter can be interpreted from the approximate scaling law that α_{ave} is proportional to (V_c/I_L) . Since the laser power was fixed at 8 kW, the smaller the beam diameter is, the higher the laser beam intensity I_L becomes. The angle α becomes thus smaller if compared with the same cutting velocity.

The pitch δ of the humps decreases with the beam diameter. This is not consistent with the proposed model which expects that δ is independent of r_k . As already mentioned in section 4.2.4, however, as the beam diameter is decreased, interaction between humps in the central part and melt accumulations in kerf sides becomes strong and this seems to have caused overcounting of the humps.

The threshold angle α_{thr} where the central flow becomes stable becomes smaller as the beam diameter gets smaller. This does not agree with the theoretical prediction that the angle can be uniquely determined independently of the beam diameter. This should also be a result of the stronger interaction between the central and side flows as above. Intervention of melt accumulations to the central flow tends to make flow continuous by increasing interaction between two humps that are generated successively from the surface.

The striation wavelength is also reduced as the beam diameter is decreased (Figure 4-36). The theoretical equation (5.11) predicts that λ is decreased by a factor of 1.7 when the diameter is decreased from 1.7 mm to 0.56 mm. The experimentally obtained reduction ratio, which is about 2 (= 200 $\mu\text{m}/100 \mu\text{m}$), roughly agrees with the theoretical prediction. The decrease of λ with the increase of

V_c can be interpreted by the pull-down mechanism as described above. The roughness R_z is also lowered with the decrease of the beam diameter (Figure 4-37). The reduction factor from 1.7 mm to 0.56 mm is about 2. This agrees with the theoretical model which predicted that R_z is proportional to λ .

(d) *Beam profile* (Figures 4-39 to 4-44)

The inclination angle α increases with the defocusing distance. This α is the averaged value over penetration depth. It increases as the mean laser intensity decreases. A defocused beam has a lower averaged intensity compared with the top-hat intensity at the focus position. Thus the angle α is raised by defocusing. As can be seen in figure 4-14, for the defocusing distance of 16 mm ($z_f = -16$ mm), α is almost the same as the top-hat intensity with the diameter 1.7 mm.

It was found that the beam profile strongly affects the instability of melt flow. A key to understand this influence is the increase of local inclination angle near the top surface. This is caused by a local decrease of laser beam intensity at periphery of the quasi-Gaussian distribution. The increase of the local angle can be observed in both central and side parts of the kerf front. Please note that the angle α shown in figure 4-39 is the value averaged over the sample thickness and it does not represent the local increase of the inclination angle.

The increase of the local inclination angle near the top surface makes melt flow stable. As shown in figure 4-44, even for a low velocity condition in which humps are observed in lower part, the top part is continuous and this stable region spreads almost to kerf sides. This can be interpreted as follows. The local increase of α in the top part makes the velocity of humps slower (see also eq.(5-7')). The distance of two adjacent humps along the front diminishes and the flow becomes continuous. The local inclination angle increases also in side parts of the kerf front, so the same stabilising effect can be found also in the side parts.

The striation wavelength λ decreases by using the quasi-Gaussian intensity distribution. According to the high speed video camera observation, this is considered to be a result of the pull-down effect as discussed above; the use of the quasi-Gaussian beam increases α locally at the top part of the kerf and stabilises the central flow. Melt accumulations are pulled down from this inclined central flow in a stabilised manner. This leads not only to a decrease of λ , but also to a reduction of R_z due to the decreased λ and the regularity of the displacement of melt accumulations. Although this improvement of R_z by defocusing was already observed in several experimental studies [Lüdi 2009, Poprawe 2010, Wandera 2011-1], the mechanism of the improvement has been clarified for the first time in this study.

It is interesting to note that δ is hardly affected by defocusing, although the humps do not appear from the surface but from middle of the front where inclination angle is small. It is likely that the same force balance between the assist-gas pressure and the surface tension can be applied in spite of the slight difference of the position of the instability generation.

5.6 Downward development of striations

The results of the observations of downward developments through a glass plate can be interpreted in the same way as the observation from above the kerf front.

When α is larger than a certain threshold value α_{thr} , the central flow becomes continuous. Melt accumulations generated on kerf sides are displaced downwards, pulled down from the central flow, and assimilated into it. In general, resultant regular striations have a good quality.

When α is smaller than α_{thr} , melt flow over the entire kerf front becomes unstable. The dynamics of humps or melt accumulations is less regular and chaotic. As the depth increases more interactions occur between humps and melt accumulations mediated by surface tension. Irregular growth of their sizes and their trajectory degrades the surface roughness.

The results indicate that the stability of the central flow is one of the important factors that control the final quality of surface roughness. The stability of the central flow can be improved with the use of quasi-Gaussian intensity profile, which was demonstrated in figures 4-39 to 4-44.

It may be interesting to note that no new characteristic was found by this lateral observation compared with the observations from the above of the kerf front. For example, the importance of the stability of the central flow to the final cut surface quality had already been observed in figure 4-12. The dependence of the stability of the central flow on α had also been confirmed in the same figure. This gives an additional support for the use of the large diameter (1.7 mm) and the large stand-off distance of the nozzle from a workpiece (3.5 mm) in the first series of experiments.

5.7 Summary

In this chapter, we discussed the origin of the melt flow instabilities which were observed experimentally and the following striation generation process. Figure 5-4 shows a global schematic picture of the related processes. The inclination angle α of the front controls the stability of melt flow. In the lowest range of α , melt flow over the entire kerf front is unstable. In the intermediate range of α , the central flow becomes continuous but the side flow still involves periodical generation and vertical displacement of melt accumulations. The inclination angle α is basically determined from an energy balance equation and α is proportional to (V_c/I_l) for the first order of approximation. This scaling law was verified in the experiments. Striations are left as a result of generation and downward displacement of the melt accumulations along kerf sides. The theoretical analysis of heat transfer process predicts that R_z has roughly the same magnitude as λ . The stability of melt flow in the central part of the kerf front also affects final quality of striations. When the central flow is continuous, it pulls down the melt accumulations. This reduces λ and creates regular vertical striations, which results in a lower surface roughness R_z . On the other hand, when the central flow is discontinuous, the dynamics of melt accumulations becomes chaotic and results in a higher R_z .

The detailed characteristics of the melt flow instabilities are summarised as follows. Let us begin with the origin of the discontinuity observed in the central part of a kerf front. The observation results suggest that this is caused by a surface tension effect. Molten material created at the top part of the kerf cannot start to move down along the kerf wall immediately due to a surface tension that tends to

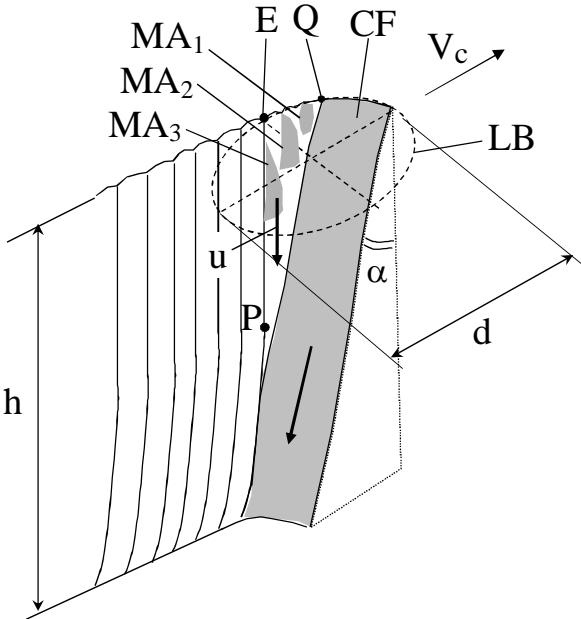


Figure 5-4. Schematic of the striation generation process. (MA: melt accumulation, CF: central flow, LB: laser beam)

hold the melt at the surface. The molten material starts to slide down on the wall when its size reaches a certain critical value. This size depends on the assist gas pressure and surface tension coefficient. The critical size δ of these humps predicted from a theoretical analysis agrees roughly well with the experimentally obtained pitch of humps. This mechanism of surface tension is supported also by the experimental facts that the pitch δ of the humps decreases with an increase of the assist-gas pressure and that δ is independent of laser power or of intensity distribution. The discontinuity in the central flow disappears when the cutting velocity V_c is increased. This can be interpreted also as another surface tension effect. As V_c increases, the generation frequency of the humps increases. As a result, distance of two adjacent humps along the central kerf wall decreases. They begin to merge at a certain velocity and consequently the melt flow becomes continuous. A simple analysis shows that the stability of the melt flow in the central part depends on the inclination angle α . There is a threshold angle α_{thr} above which the melt flow becomes continuous. This scaling was successfully confirmed in experiments where laser power was varied. It was also observed, however, that α_{thr} increases as the beam diameter is expanded. The high speed video observations suggest that intervention of melt accumulations on kerf sides to the humps in the central parts helps to join two adjacent humps and to make the flow continuous.

The instability observed in the side parts of the kerf front can be interpreted in the same way, as the surface tension effect. The decrease of generation pitch of melt accumulations (= wavelength λ of striations) with an increase of assist-gas pressure supports this mechanism. The observation showed, however, two main differences from the instability of the central flow. First, the wavelength λ of striations is different from the pitch δ of humps in the central part. Second, the instability in side parts appears even for a high V_c where the central flow becomes stable. We propose a coherent explanation for these differences. First of all, the difference of the generation pitch can be interpreted from a geometrical effect. It is predicted that the generation pitch of the melt accumulations on the sides is larger by $(2r_k/\delta)^{1/2}$ than the pitch of humps. This roughly agrees with the experimental results. For a given laser condition, λ is larger than δ and λ decreases as laser beam diameter is decreased. The larger pitch in side regions makes the generation frequency of the melt accumulations lower than that of the humps in the central part. Thus, the threshold velocity above which the side flow becomes continuous becomes larger than that for the central flow.

In this way the different characteristics of instabilities in the centre and the sides (the difference between λ and δ and the different velocity dependence of the stability) can successfully be explained based on the unique mechanism of the surface tension effect.

It was observed also that λ slightly decreases with V_c , in a velocity range where the central flow becomes continuous. This can be interpreted as a pull-down effect from the continuous central flow. In this velocity range, melt accumulations generated on kerf sides are displaced downwards on the side walls and are assimilated to the continuous central flow. As V_c increases, the inclination angle α increases. The melt accumulations are pulled down more strongly from the central flow, which results in the decrease of λ .

Striations are left as a result of generation and downward displacement of the melt accumulations (MAs). A melt accumulation absorbs laser power and transfers a part of the power to the solid part. A region of the solid surface in contact with the melt accumulation is locally melted. While the melt accumulation is generated near the top surface and displaced downwards along the kerf side wall, this local melting continues in the contact area. As a result, a stripe of striations is created on the kerf side wall. A theoretical heat conduction analysis predicts that R_z has roughly the same magnitude as λ . This qualitatively agrees with the order of experimental values. The proposed model is supported also by good correlations observed in the parametric study; both λ and R_z decrease with a decrease of the laser beam spot diameter or with an increase of α for the velocity range where the central flow becomes continuous.

The lateral observations of melt flow through a glass plate revealed that the stability of melt flow in the central part of the kerf front also affects final quality of striations. When the central flow is continuous, it pulls down the melt accumulations. Resultant regular striations as well as a reduction of λ lead to a better surface roughness. On the other hand, when the central flow is discontinuous, the dynamics of melt accumulations becomes chaotic and results in a degradation of surface roughness.

The above discussion allows us to interpret the improvement of the stability of melt flow and surface roughness by the use of a Gaussian-like intensity distribution instead of the top hat profile. A low intensity region at the periphery of Gaussian raises inclination angle of the kerf profile near the surface, which tends to make the central flow in this region continuous. As a result, the dynamics of melt accumulations on kerf sides become stable. Moreover, the larger inclination angle of the central part yields a stronger pull-down effect from the central flow to the melt accumulations. Consequently, λ and R_z can be decreased.

On the whole, it was revealed that surface tension plays multiple roles in the dynamics of melt flow on a kerf front. First, the surface tension causes generation of humps and melt accumulations in the central and side parts, respectively. The theoretical model by Makashev *et al.* [Makashev 1992, Makashev 1994] was the one that had well predicted this aspect, although the model was in 2D and thus limited to the central part. In addition, we proposed that the disappearance of these instabilities can also be caused by the same surface tension which tends to merge two successive humps or melt accumulations. Finally, striations and surface roughness can be greatly influenced by interactions driven by surface tension, such as the disturbance on melt accumulations from humps and the pull-down effect on melt accumulations from a continuous central flow.

Chapter 6. Wavelength dependence of striations

Résumé

Lors de la découpe laser de fortes épaisseurs d'acier, donc réalisées à de faibles vitesses de coupe, on s'est rapidement aperçu que la qualité de surface obtenue avec un laser dont la longueur d'onde est de $1\ \mu\text{m}$, était très inférieure à celle obtenue avec un laser CO_2 , dont la longueur d'onde est de $10\ \mu\text{m}$. Malgré les nombreux efforts de recherche entrepris ces dernières années, et les tentatives d'interprétation de cet effet, aucune solution n'est actuellement proposée à ce problème qui représente un très important enjeu industriel. L'une des raisons de cette situation, est probablement que le mécanisme intrinsèque de génération de stries n'était pas compris et donc ne permettait pas d'analyser les conséquences de l'emploi d'un laser avec une longueur d'onde donnée. Compte tenu des résultats de notre étude, nous pensons que cette situation est maintenant différente, car nous avons défini un modèle de génération de stries et donc sa dépendance avec la longueur d'onde laser peut être étudiée dans ce cadre. C'est donc l'objectif de ce chapitre.

6-1 Comparaison expérimentale des découpes par laser à $1\ \mu\text{m}$ et à $10\ \mu\text{m}$:

Nous avons tout d'abord effectué des séries d'expériences semblables de découpes laser avec un laser CO_2 et un laser à fibre. L'objectif de ces comparaisons est non seulement de reconfirmer la différence de qualité de découpe entre ces deux types de laser, mais également d'étudier les paramètres principaux de la saignée, tels que l'angle α de l'inclinaison en variant la vitesse V_c de découpe ; on a vu que cet angle α était un paramètre important qui pilote la stabilité des écoulements. Nous avons utilisé pratiquement les mêmes paramètres opératoires pour ces expériences (la puissance de laser, le diamètre de foyer, la longueur de Rayleigh, la position de foyer et la pression de gaz assistant). Les épaisseurs des échantillons de l'acier inoxydable utilisé (SUS 304) étaient de 3, 5, et 8 mm.

La vitesse maximum de découpe pour le laser à fibre était deux fois plus élevée que celle pour le laser de CO_2 pour l'épaisseur de 3 mm et à peu près identique pour les épaisseurs de 5 et 8 mm. La rugosité des saignées obtenue avec le laser à fibre est à peu près identique à 3 mm, légèrement plus grande à 5 mm, et beaucoup plus importante à 8 mm comparée à celle obtenue avec un laser CO_2 . Ces résultats sur l'augmentation de la vitesse de découpe pour les faibles épaisseurs et de la dégradation de la qualité pour les fortes épaisseurs avec un laser à fibre sont tout à fait conformes aux résultats des études antérieures.

Des différences d'inclinaison du front avant de la saignée ont été mises en évidence pour ces deux longueurs d'onde. On montre ainsi que la dégradation de la qualité pour la longueur d'onde à $1\ \mu\text{m}$ apparaît pour une gamme vitesses inférieures à 1.5 m/min, pour lesquelles l'angle α est faible ($\alpha < 3^\circ$).

6-2 Analyse des effets de la longueur d'onde laser :

En se basant sur le processus de génération de stries présenté dans les chapitres précédents, nous analysons maintenant l'effet de la longueur d'onde laser sur deux mécanismes fondamentaux, à l'aide d'une approche physique appropriée. Dans cette analyse, nous n'examinons que l'influence de la longueur d'onde de laser, en négligeant les probables dépendances complexes des autres paramètres.

- Effet sur la stabilité du front avant :

Nous avons tout d'abord analysé les raisons de la déstabilisation de l'écoulement liquide dans la partie centrale du front avant de la saignée. On rappelle que lorsque l'écoulement central est déstabilisé, la dynamique des accumulations de liquide qui glissent le long des flancs risque d'être également perturbée et les stries qui en résultent sont alors dégradées. L'analyse de la perturbation du profil du front avant de la saignée a été conduite avec un modèle de type « chaîne », où on considère que le front avant de la saignée est constitué de segments de chaîne reliés entre eux et dont on suit la dynamique. On considère que la vitesse locale d'un segment de cette « chaîne » est la somme vectorielle de la vitesse V_c de découpe et d'une vitesse de déplacement du chaînon qui est normale à la surface locale. Cette vitesse de déplacement du chaînon dépend de l'intensité laser absorbée localement, qui est une fonction de l'incidence locale et donc de son inclinaison α . C'est donc la loi

d'absorption de Fresnel, qui dépend aussi de la longueur d'onde laser, qui va déterminer l'intensité absorbée localement et donc la dynamique du front avant.

Notre analyse conduit à définir une fonction de « stabilité » : $S(\alpha) = \frac{\partial^2 F(\alpha)}{\partial \alpha^2} - F(\alpha)$. On constate

que lorsque la fonction $S(\alpha)$ est positive (ou négative), la surface locale se déforme, avec une courbure concave (ou convexe) et une perturbation se développe alors. Pour ces deux types de courbure, la croissance des perturbations s'arrête lorsque l'angle α d'inclinaison local atteint α_0 , tel que $S(\alpha_0) = 0$. Dans le cas de la découpe épaisse (pour lequel on a vu que $\alpha_{eq} < 3$ degrés), l'angle α_0 du point d'arrêt de ce processus de déformation (qui vaut 5,2 degrés, pour la longueur d'onde à 1 μm) est très supérieur à l'angle α_{eq} moyen du front avant ; alors que pour la longueur d'onde à 10 μm , α_0 est alors égal à 1,4 degrés, ce qui est plus proche à α_{eq} . Nous pensons que cet effet explique pourquoi le front avant de la saignée pour un faisceau laser de longueur d'onde 1 μm peut être perturbé beaucoup plus fortement que pour un faisceau laser à 10 μm .

- Effet sur la dynamique des accumulations de liquide :

Nous avons ensuite étudié la dynamique du déplacement vertical vers le bas des accumulations de liquide le long des côtés de la saignée. Ces accumulations de liquide glissent vers le bas tout en absorbant de la puissance de laser, elles peuvent donc transférer une partie de cette puissance à la paroi solide. La région de contact de cette paroi subit une fusion locale et ce processus se poursuit pendant la descente de l'accumulation : Nous considérons que c'est le mécanisme fondamental du processus de génération de stries ; c'est cette dynamique des accumulations de liquide qui va définir les caractéristiques des stries. L'absorptivité du faisceau laser sur les accumulations de liquide est plus élevée pour un faisceau laser à 10 μm en raison de la différence d'absorptivité, qui favorise le 10 μm pour ces incidences très rasantes. La température des accumulations de liquide étant alors plus élevée lorsqu'on utilise un faisceau laser à 10 μm , l'accumulation descendra plus rapidement, sa viscosité devenant plus faible. Le transfert énergétique vers la paroi est alors réduit. Ce mécanisme peut être la raison de la différence de qualité observé entre les lasers à 10 μm et à 1 μm .

Pour estimer ce processus physique, nous avons développé un modèle analytique simple qui détermine le bilan de puissance et le transfert de chaleur dans les accumulations de liquide. La vitesse de descente de l'accumulation a été traitée d'une façon analogue au déplacement observé d'une gouttelette de liquide glissant le long d'une paroi inclinée sous l'effet de la pesanteur. La conclusion de ce modèle montre qu'une augmentation de l'intensité laser absorbée sur les accumulations de liquide peut augmenter leur température et diminuer la rugosité finale. Ce résultat indique donc que, pour ces conditions où les angles d'incidence du laser à la surface des accumulations sont très petits, la plus faible absorptivité du faisceau laser à 1 μm est probablement la raison d'une plus mauvaise qualité finale lors de découpes de fortes épaisseurs.

- Recommandations pour l'amélioration de la qualité de découpe :

De ces considérations, il est alors possible de proposer une solution pour améliorer la qualité de découpe lors de l'emploi d'un laser à 1 μm , qui consiste à utiliser un laser polarisé radialement. Dans ce cas, l'absorptivité sur les côtés de la saignée est alors augmentée, car la polarisation radiale sur les côtés de la saignée se comporte en polarisation P dont on sait qu'elle devient très élevée aux faibles angles d'incidence. Expérimentalement, pour la découpe de l'acier avec un laser CO_2 , il avait déjà été observé que la rugosité pouvait être améliorée par l'emploi d'une polarisation radiale au lieu d'une polarisation circulaire, naturellement générée par un laser [Ahmed 2009]. Mais aucune explication n'avait été donnée. Par ailleurs, pour la longueur d'onde à 1 μm , le problème de la déstabilisation de l'écoulement central ne peut pas être complètement résolu avec une polarisation radiale, car l'angle α_0 du point d'arrêt de la déformation reste assez important (4,8 degrés) pour cette polarisation P. En conclusion, c'est donc la dynamique des accumulations de liquide qui contrôle directement la rugosité finale. Par conséquent, l'emploi d'une polarisation radiale, permettant une meilleure absorption du faisceau laser sur les côtés de la saignée devrait notablement améliorer la qualité de découpe. Il ne nous a pas été possible de tester cette idée, car la transformation optique en polarisation P d'un laser à

1 μm émettant naturellement une polarisation circulaire est assez complexe (et onéreuse). Nous attendons avec impatience qu'une vérification expérimentale de ces idées puisse être réalisée dans un futur proche.

Introduction

Recent progress of high power and high brightness lasers has enabled high throughput and low cost operation in a number of laser material processing applications in industries. Meanwhile, laser cutting of thick-section steel with inert gas, one of the important applications, has so far failed to benefit from this advantage. The problem concerns striations which are created on cut surfaces during laser cutting process. For thickness typically over ~ 4 mm, roughness of cut surfaces obtained with a fibre or disc laser ($\lambda_L \sim 1 \mu\text{m}$) is higher than that achieved with a conventional CO₂ laser ($\lambda_L = 10.6 \mu\text{m}$) [Wandera 2006, Himmer 2007, Hilton 2009, Scintilla 2010]. For example, Scintilla *et al.* [Scintilla 2010] compared laser cutting of steel with a disc and a CO₂ laser using almost the same laser beam diameter and gas condition. For thicknesses of 5 mm and 8 mm, cut surface quality obtained with the disc laser was worse than the one obtained with the CO₂ laser. Considering that the operating conditions were nearly the same, it seems reasonable to infer that the quality difference is attributed to the influence of the laser wavelength on the absorption process and more particularly, the Fresnel absorption.

Whereas wavelength dependence of the Fresnel absorption law has been related to difference in achievable thickness [Mahrle 2009], very few investigations have been made on the mechanism of the difference in the cut surface quality. Poprawe and co-workers observed ripple formations on the kerf front with a $1 \mu\text{m}$ laser beam but not with a $10 \mu\text{m}$ laser beam [Poprawe 2010, Vossen 2010], which they claim is the cause of the quality difference. This correlation between the ripples on the front and the striations on the sides is not so clear; striations appear even in the case of CO₂ laser cutting where the ripple formations were not observed. Petring *et al.* [Petring 2008] has proposed another point of view that multi-reflections, which occur within the kerf in laser cutting with a $1 \mu\text{m}$ beam, can destabilise lower part of kerf sides. According to experimental results, however, the degradation of the surface roughness in the case of a $1 \mu\text{m}$ beam starts at $1 \sim 2$ mm below the top surface [Wandera 2006, Himmer 2007, Hilton 2009, Scintilla 2010], where the laser beam absorption from multi-reflected components is not supposed to be important. Consequently, multi-reflections cannot be the main mechanism.

One of the problems which have hindered a proper understanding of this phenomenon is that, before discussing details of the wavelength effect, we have not understood properly the mechanism of the striation generation process itself. The situation has been changed, however, by direct experimental observations of the process. Yudin and co-workers observed hydrodynamics on kerf sides during laser cutting of Rose's alloy [Yudin 2009] and mild steel [Grigory 2010] by visualization through a glass plate. They confirmed that striations are developed by intermittent downward displacement of melt accumulations along kerf sides. In order to clarify the origin of this intermittent generation of melt accumulations, we observed melt flow dynamics from above the kerf front in laser cutting of steel as described in chapter 4. The results indicated an important role of surface tension, which tends to hold melt accumulations at the top of the kerf side counteracting to assist gas force. Another important phenomenon was found in an intermediate velocity range: melt flow in central part of the kerf front is continuous whereas flow in side parts is discontinuous, and it is this unstable side flow that leads to striation generation. This result indicates the importance of distinction between central and side flows when one considers the influence of the melt flow stability on the striation generation.

The object of this chapter is to discuss this interesting topic of the quality difference observed between the two wavelengths $1 \mu\text{m}$ and $10 \mu\text{m}$ for thick section laser cutting of steel. First, comparative cutting experiments were conducted with a fibre and a CO₂ laser using almost the same operating parameters (laser power, focus diameter, Rayleigh length, focus position and assist-gas pressure) for the two lasers. The object of this experiment is not only to reconfirm the cut surface quality difference, which has been obtained by other research groups, but also to investigate some key parameters such as the inclination angle α while varying the cutting velocity V_c , as in the previous chapters. This is because our experiments and analyses have shown that the angle α is an important parameter that governs the stability of the melt flow. As has been shown by the previous studies, our experiments show that the fibre laser yields a high cutting speed for a thin sample and worse cut quality for a thick sample. The measurement of α revealed for the first time that the degraded cut surface quality for the $1 \mu\text{m}$

wavelength appears for condition of low α ($\alpha < 3$ degrees), which corresponds in this study to a low cutting velocity range less than 1.5 m/min.

Then the mechanism of the wavelength dependence of cut surface quality is theoretically investigated. Based on the striation generation process revealed by the last two chapters we propose as the mechanism two fundamental processes: stability of melt flow in the central part and dynamics of melt accumulations along the kerf sides. For each of the processes, the influence of the wavelength dependence of the absorptivity is verified by analytical modelling of related physical processes. We finally propose utilisation of the radial polarisation for improvement of cut surface quality in the case of the 1 μm wavelength.

6.1 Comparative cut experiments with a fibre and a CO₂ laser

Laser cutting of SUS304 stainless steel was performed with a 5 kW fibre laser and a 4 kW CO₂ laser in Air Liquid Welding Company. The laser powers at the focus positions were the same at 3.7 kW for both lasers. Focusing characteristics which were measured by a commercial PRIMES Focus Monitor [PRIMES WEB] are shown in figure 6-1. The focus diameter was 250 μm for both of the wavelengths. Also the Rayleigh lengths were approximately the same (3.1 mm for the fibre laser and 3.4 mm for CO₂). Please note, however, that the intensity distributions at the focus positions were different; top-hat for the fibre laser and quasi-Gaussian for the CO₂. Thicknesses of SUS 304 samples were 3, 5, and 8 mm. The focus positions were varied for each thickness. The focus positions were at 1, 4, and 5 mm below the surface for the thicknesses of 3, 5, and 8 mm, respectively. These values were optimised for the fibre laser by preliminary cutting trials, and the same values were used also in cutting with the CO₂ laser. The assist-gas was nitrogen with the pressure of 16 bar (relative value to the ambient pressure) at the reservoir. The nozzle diameter and the stand-off distance from the workpiece surface were 2.5 mm and 1 mm throughout the series of experiments. The cutting speed was varied from 20% to 100% of the maximum cutting velocity for each sample thickness and laser wavelength.

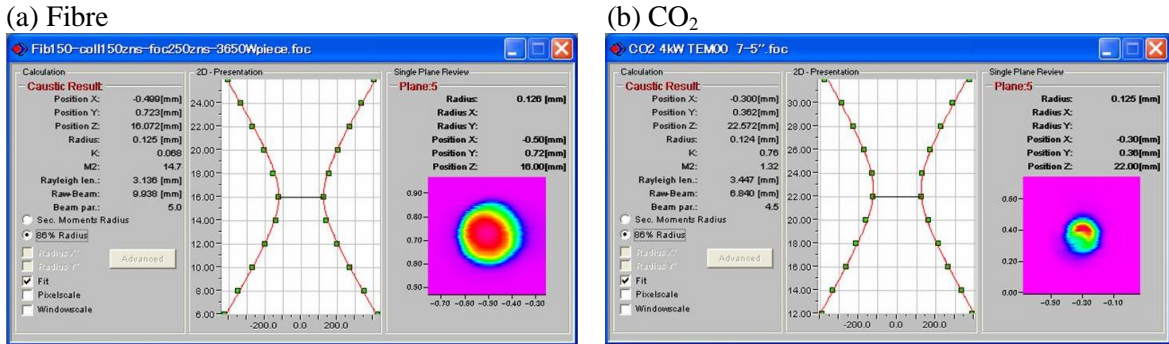


Figure 6-1 Characteristics of the focused beams of the two lasers.

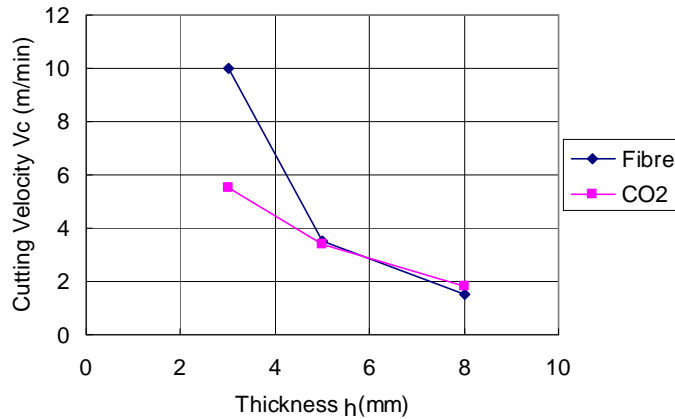


Figure 6-2 Maximum cutting velocities for each thickness.

(a) Maximum cutting velocity

The maximum cutting speeds for different thicknesses and lasers are shown in figure 6-2. For thin sheets ($h = 3$ mm), the maximum velocity of the fibre laser is twice as fast as that of the CO₂ laser. But this advantage of the fibre laser diminishes as the thickness increases and the maximum speed becomes about the same for the thicknesses of 5 mm and 8 mm. This result agrees with what has been reported in the literature.

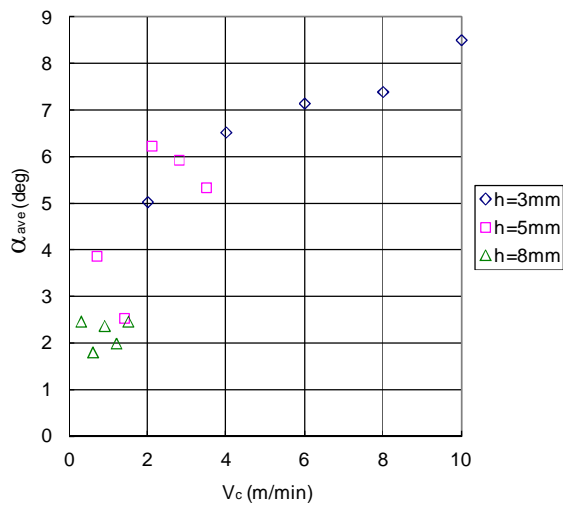
(b) Inclination angle of the front

The inclination angle α of the central part of the kerf front is shown in figure 6-3. These values were measured either by observing from above of the kerf front (solid marks) or by observing a polished cut surface of the central plane of laser cutting (empty marks). The two methods give nearly the same angles. The values are averaged ones over the sample thickness, because in these measurements the kerf front is approximated by a straight segment that connects two points on the top and bottom surfaces.

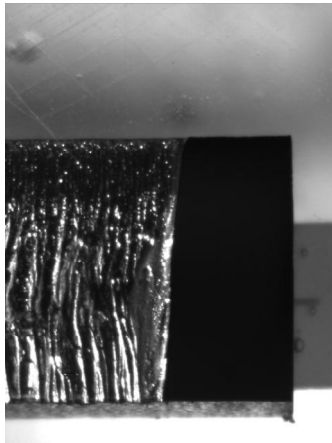
As a global tendency, α increases with V_c for any thickness and wavelength. This agrees well with the theoretical prediction that local α is proportional to $(V_c/A(\alpha)I_L)$ under the condition that heat conduction loss is neglected. This relation suggests also that local α is influenced by the local laser beam intensity that is determined by the focal position and the beam intensity distribution. As can be seen in the kerf front profiles shown in figure 6-3, rather straight kerf profile is obtained with the fibre laser, whereas the kerf profile in the case of the CO₂ laser exhibits rounded profile in the lower part of the kerf, especially at a high velocity. This result can be related to the difference in the beam intensity distribution. Moreover, in the case of the fibre laser, the increase rate of α with V_c is saturated with the increase of V_c . This may be a result from the Fresnel absorption characteristics: $A(\alpha)$ increases with α in the range of $0 < \alpha < 10$ (deg), for the case of the 1 μm wavelength.

One of the important outcomes is that in the case of the maximum thickness 8 mm, α is lower than 3 degrees for the 1 μm wavelength and around 3 degrees for CO₂ laser. The Fresnel absorption law predicts that the absorption of the laser beam is less efficient for the 1 μm in this region of α . The maximum cutting speed, however, is the same (see figure 6-2). This apparent contradiction will be discussed in the next section.

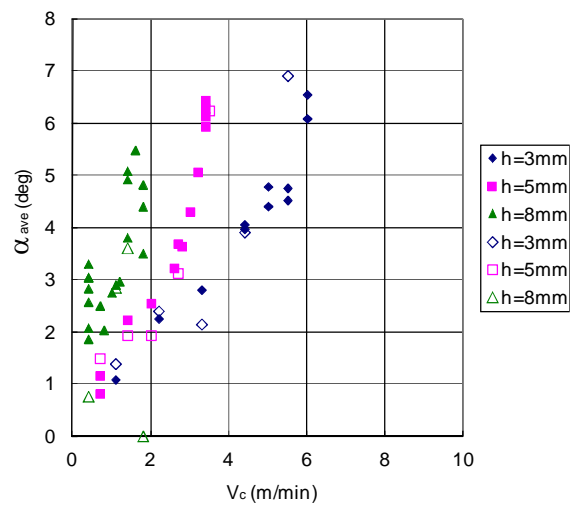
(a) Fibre laser



Fibre, $h = 5$ mm, $V_c = 2.8$ m/min.



(b) CO₂ laser



CO₂, $h = 5$ mm, $V_c = 2.7$ m/min.

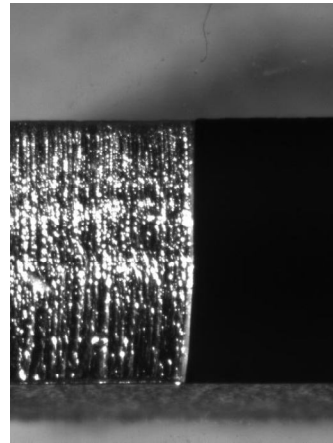


Figure 6-3 Averaged inclination angle of the kerf fronts (top) and examples of cut surfaces (bottom).

(c) Cut surface quality

Cut surfaces and surface roughnesses are compared in figures 6-4 to 6-7. As already reported in the literature, the 1 μ m wavelength yields a poor surface quality for thicker samples. Figure 6-7 and figure 6-3 indicate that the poor quality is obtained in the low velocity range less than 1.5 m/min which corresponds to the α region less than 3 degrees.

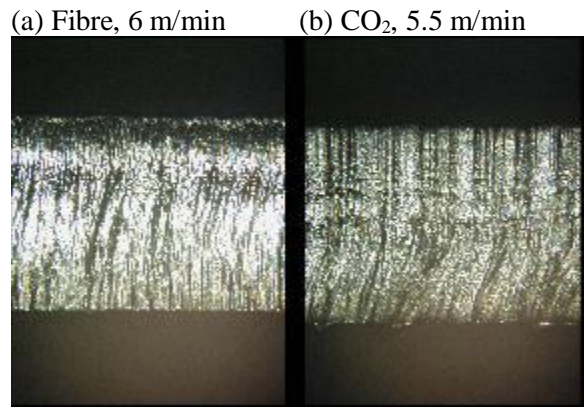


Figure 6-4 Cut surfaces of 3 mm thick samples.

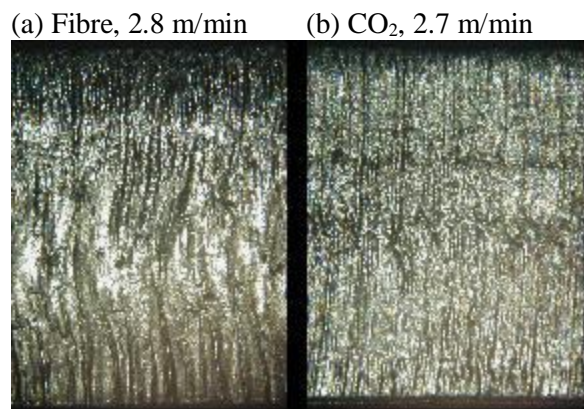


Figure 6-5 Cut surfaces of 5 mm thick samples.

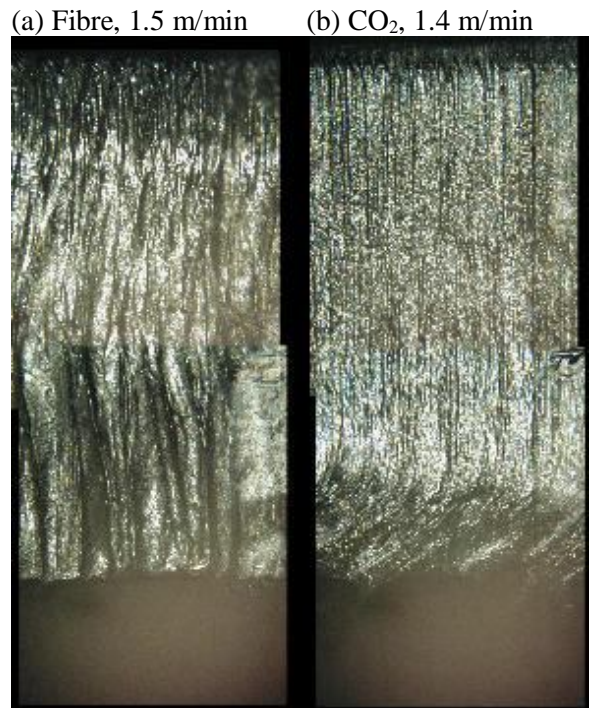
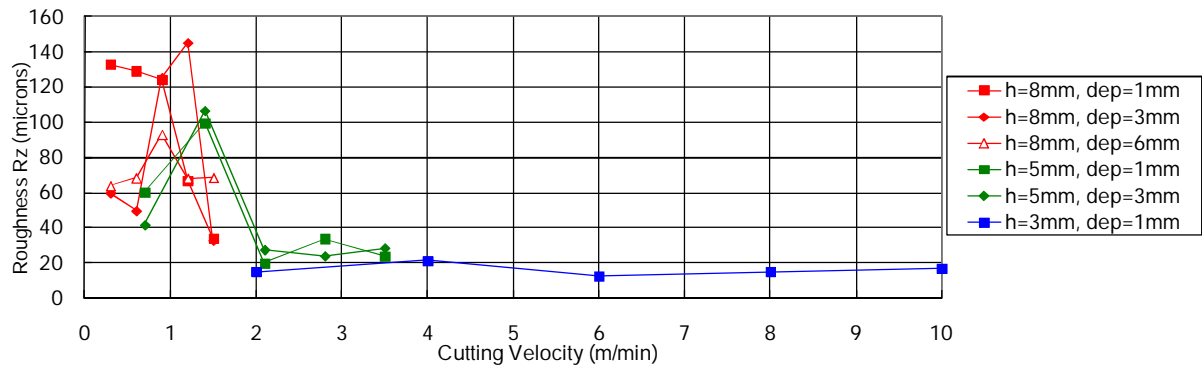


Figure 6-6 Cut surfaces of 8 mm thick samples.

(a) Fibre



(b) CO₂

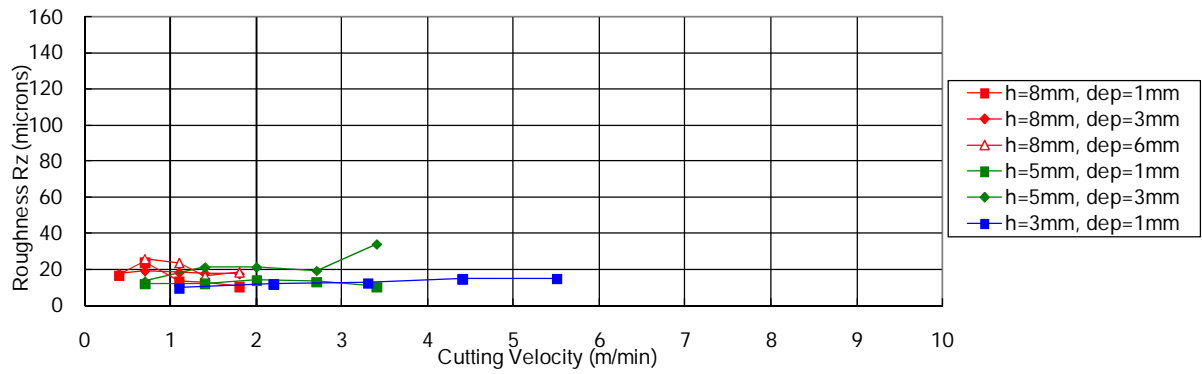


Figure 6-7 Roughness of cut surfaces measured for each thickness h of the sample and for each depth (dep) from the surface.

6.2 Mechanisms of the wavelength dependence of striations

Now physical mechanisms for this interesting and important problem of the wavelength dependence are investigated. First, striation generation process is described, based on a 3D structure of melt flow on a kerf front, which was revealed for the first time by our experimental observations. Two fundamental processes are suggested to explain the difference in the cut surface quality: destabilisation of the melt flow in the central part of the kerf front and downward displacement of discrete melt accumulations along the side parts of the front. Then each of the processes is analyzed using a simplified analytical model. The results show that in both processes, different angular dependence of the absorptivity of the laser beam can result in the quality difference. Finally we propose use of radial polarisation to improve the quality with the 1 μm wavelength.

6.2.1 Mechanism of striation generation

Let us refer to figure 5-4 which shows a schematic of melt flow on a kerf front and striation generation process which have been revealed in the previous chapters. We pay attention to the three-dimensional structure of the melt flow on the kerf front, considering the results of our experimental observation, which revealed the importance of the distinction of the flows in the central and side parts. This point is contrasted with most of the existing mathematical models described in chapter 3, where only processes in the central plane of cutting were described.

In the top part of the kerf, the discontinuity comes from discrete melt accumulations (MAs hereafter) that are generated periodically and displaced downwards along the kerf sides. Our observation showed that the MAs are created one by one along an arc EQ in figure 5-4 and displaced downwards almost vertically along the line EP. This line corresponds to the limit of overlapped region of laser beam and the kerf side. As was discussed in chapter 5, the periodical creation of the MAs is caused by surface tension that tends to retain the MAs at the top surface, and the period of the creation of MAs is determined by force balance between the surface tension and assist gas force.

In lower part of the kerf front, melt flow in the central part can interfere with the side flow as shown in figure 5-4. For example, our observation for the standard condition (section 4.2.2) revealed that in an intermediate velocity region ($V = 2 \sim 6$ m/min), the MAs, which slide down periodically along the kerf side, are absorbed into continuous central flow. Below this intersection point, the striations left on the kerf side are mainly determined by the stability of the central flow. The possibility of the interception of MAs by the central flow depends on inclination angle α of the kerf front, downward velocity u of MAs, and so on. When cutting velocity V_c is increased, for instance, α increases and thus the interception is more likely to occur.

Now let us consider the regime of thick section cutting with a 1 μm laser beam, which is the main interest of the present study. In this regime, the central part of the front is expected to be discontinuous, because α is so small. Concerning the stability of the central flow for a 1 μm disc laser beam, it was experimentally shown that, when $\alpha < 16$ degrees, humps appear in the central part. (Throughout this thesis, the term hump is used for a melt droplet that appears in the central part of the kerf front in order to distinguish the one from a melt accumulation in the side part, which is called as such.) In general, the maximum value of α can be estimated from (d_f/h) (h : thickness of specimen, d_f : laser beam diameter) [Mahrle 2009]. For a typical condition of thick section cutting ($h \geq 4$ mm, $d_f \sim 200$ μm), one obtains $\alpha < 3$ degrees. The angle is so small that the central part is likely to be unstable. This regime of humps for thick section cutting was reported also in [Poprawe 2010]. The humps in the central part can affect striations, since melt flow on the entire kerf front is discontinuous and the humps in the central part can disturb downward movement of MAs on the side through interaction caused by surface tension and can end up in the increase of surface roughness on the kerf sides. This kind of interaction between the central and side flows was observed in our experiments (section 4.2.2) for a low velocity range ($V_c < 2$ m/min).

Then what is the reason of the quality difference between the 1 μm and 10 μm wavelengths? The above discussion leads us to propose two fundamental processes: the destabilisation of the melt flow

in the central part, which can disturb the process of downward displacement of MAs and the downward displacement itself, which directly results in striation generation. Each of these two processes is examined in the following. Although there are many parameters that can alter the characteristics of the two processes, we focus on the influences of different wavelengths to clarify the principal mechanism that leads to the quality difference.

6.2.2 Stability of melt flow in the central part of the kerf front

First we consider the wavelength dependence of the stability of the melt flow in the central part of the kerf front. The interest of the problem is not limited to the quality problem related to cutting applications. For example, in keyhole laser welding, it is well known that more spatters are generated with a 1 μm laser beam than with a 10 μm beam. This may be caused by strong metal vapour jet which is emitted from humps on the keyhole front wall.

In spite of its importance, the wavelength dependence of the stability of a cut front or a keyhole front has been scarcely investigated. Koch *et al.* [Koch 2010] compared evolutions of keyholes for the two wavelengths with a numerical simulation. The keyhole front was found to be stable for a 10 μm beam but unstable for a 1 μm beam, by changing only the input data of the Fresnel absorption formula. In these simulations, however, constant values of 0.1 and 0.4 were added to the absorption formula for 1 μm and 10 μm beams, respectively. The validity of this operation is not obvious. Poprawe and co-workers mathematically analyzed the melt film stability [Poprawe 2010, Vossen 2010]. They found the parameter c_0 that measures the degree of the stability (see eq.(3-4)). According to this parameter, the system is more stable as $\partial(A \sin \alpha) / \partial(\sin \alpha)$ becomes small. Here A is the absorptivity, which depends on the local inclination angle α of the front. Using the Fresnel absorption formulae, however, it is easy to show that this derivative term is larger for the 10 μm wavelength than for the 1 μm in the range of $\alpha < 3$ degrees, which applies to thick section cutting. It appears that the proposed stability parameter does not correctly represent the wavelength dependence experimentally observed.

In the present study, the stability of the kerf front is investigated with a simple analytical model, which was used in the past for investigations of keyhole front profiles during laser welding [Matsunawa 1997, Kaplan 1994, Fabbro 2000-1, Fabbro 2000-2]. We analyze the kerf front in the central plane of cutting, which is shown in Figure 6-8(a). The front is represented by a set of chains and the dynamics of the front profile is expressed by displacement of nodes that connect the chains. In the frame attached to the laser beam, displacement velocity of a chain is written as

$$\vec{V}_{chain} = \vec{V}_c + \vec{V}_p. \quad (6-1)$$

Here \vec{V}_c is the cutting speed and \vec{V}_p is the local processing velocity that is expressed by

$$\vec{V}_p = -(kI_L A(\alpha) \sin \alpha) \vec{n}_\alpha, \quad (6-2)$$

where \vec{n}_α is the normal unit vector of the chain (The subscript α denotes the inclination angle of the chain.), I_L is the laser beam intensity and k is a linear constant [Fabbro 2000-1, Fabbro 2000-2], which is determined from the energy balance. In fact, if we assume that the surface temperature of the kerf front is equal to the melting temperature T_m , it is easily shown from an energy balance equation that $k^{-1} \approx \rho C_p (T_m - T_0) + \rho L_m$ within the present 2D approximation (ρ : density, C_p : heat capacity, T_0 : ambient temperature, L_m : latent heat of melting). Using eqs.(6-1) and (6-2), the velocity V_{chain} , which is defined as the component of \vec{V}_{chain} normal to the chain, is calculated as

$$V_{chain} \equiv \vec{V}_{chain} \cdot \vec{n}_\alpha = V_c \cos \alpha - kI_L F(\alpha), \quad (6-3)$$

where the function F is defined as

$$F(\alpha) \equiv A(\alpha) \sin \alpha, \quad (6-4)$$

for the ease of formulation. By setting $V_{chain} = 0$, the angle α_{eq} in the stationary condition is determined:

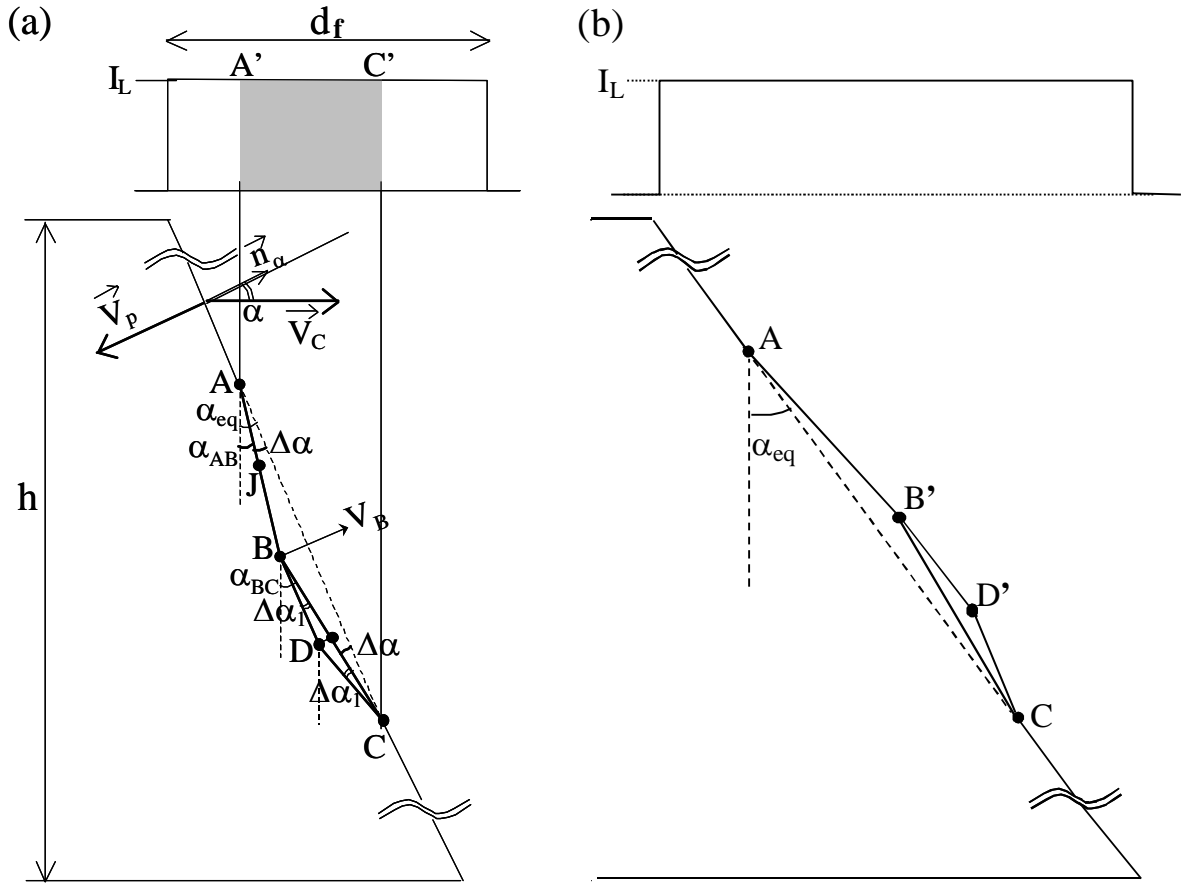


Figure 6-8. The 2D model of kerf front profiles. Evolution of the profile depends on the sign of the stability function $S(\alpha)$ (see eq.(6-7)), where α is the local inclination angle of the front. (a) When $S(\alpha) > 0$, a concave mode can develop: the node B moves to the left from the line AC, and then the node D to the left from the line BC. (b) When $S(\alpha) < 0$, an inverted convex mode develops as from the line AC to $AB'C$ and then to $AB'D'C$.

$$A(\alpha_{eq}) \tan \alpha_{eq} = \frac{V_c}{kI_L}. \quad (6-5)$$

Please note that this is a general equilibrium equation for a moving surface subjected to various combinations of I_L and V_c . For example, this equation can also be applied to a keyhole front wall during welding process [Fabbro 2000-1, Fabbro 2000-2] with slight modification of the coefficient k . Since $A(\alpha)\tan\alpha$ increases monotonously with α , α_{eq} is uniquely determined from eq.(6-5) for a given combination of I_L and V_c . For simplicity, we assume that the laser intensity is constant at I_L , and consequently kerf front is straight with a constant α_{eq} . As shown in eq.(6-5), α_{eq} increases with V_c . As far as the maximum value of α_{eq} is concerned, it can be estimated independently from eq.(6-5), geometrically by (d_f/h) , which is typically smaller than 3 degrees for thick section cutting. The following discussion assumes a constant value of α_{eq} (< 3 degrees).

Now let us discuss the stability of the kerf front profile. As shown in Figure 6-8(a), we consider a small perturbation that displaces the node B to the left (= to the opposite direction of $\vec{n}_{\alpha_{eq}}$) from the straight line corresponding to α_{eq} . The two chains AB and BC, which are assumed to have the same length, are tilted by $(\alpha_{eq} - \Delta\alpha)$ and $(\alpha_{eq} + \Delta\alpha)$, respectively. The velocity component of the node B perpendicular to the straight line AC can be evaluated from the average of the velocities of the two chains AB and BC, which are calculated in the same way as eqs.(6-1) and (6-2):

$$\begin{aligned}
V_B &= \frac{1}{2} \left[\left(\vec{V}_c - kI_L F(\alpha_{eq} - \Delta\alpha) \vec{n}_{\alpha_{eq} - \Delta\alpha} \right) \cdot \vec{n}_{\alpha_{eq}} + \left(\vec{V}_c - kI_L F(\alpha_{eq} + \Delta\alpha) \vec{n}_{\alpha_{eq} + \Delta\alpha} \right) \cdot \vec{n}_{\alpha_{eq}} \right] \\
&= V_c \cos \alpha_{eq} - \frac{kI_L}{2} \left[F(\alpha_{eq} - \Delta\alpha) \cos \Delta\alpha + F(\alpha_{eq} + \Delta\alpha) \cos \Delta\alpha \right] \\
&\approx -\frac{kI_L}{2} \left(\frac{\partial^2 F(\alpha)}{\partial \alpha^2} - F(\alpha) \right) \Big|_{\alpha=\alpha_{eq}} \Delta\alpha^2 + \left(V_c \cos \alpha_{eq} - kI_L F(\alpha_{eq}) \right)
\end{aligned} \tag{6-6}$$

In order to obtain the final expression, we have neglected terms of the fourth order of $(\Delta\alpha)^4$ and higher. According to eqs.(6-3)-(6-5), the second term in the right hand side of eq.(6-6) is zero. Defining another function S:

$$S(\alpha) = \frac{\partial^2 F(\alpha)}{\partial \alpha^2} - F(\alpha), \tag{6-7}$$

one obtains

$$V_B \approx -\frac{kI_L}{2} S(\alpha_{eq}) \Delta\alpha^2. \tag{6-8}$$

As will be shown in the following, $S(\alpha)$ is the key parameter that governs destabilisation and it determines a type of unstable modes that can appear. This “stability” function $S(\alpha)$ is shown in Figure 6-9 for the two wavelengths of 1.06 μm and 10.6 μm . For this calculation, the complex refractive indices of iron at $T = T_m$ were taken from [Dausinger 1993] and these values are shown in Table 6-1. The random polarisation was assumed in the calculation. The stability function $S(\alpha)$ takes a positive value at $\alpha = 0$. It decreases with α and passes zero at some angle. We call this angle α_0 that satisfies $S(\alpha_0) = 0$. α_0 is 1.4 degrees for 10.6 μm and 5.2 degrees for 1.06 μm . For $\alpha > \alpha_0$, $S(\alpha)$ stays negative for both wavelengths.

Table 6-1 The complex refractive indices ($n + ik$) used in the calculation of the stability function $S(\alpha)$ [Dausinger 1993]

Wavelength	n	k
1.06 μm	3.6	5
10.6 μm	14.8	15.5

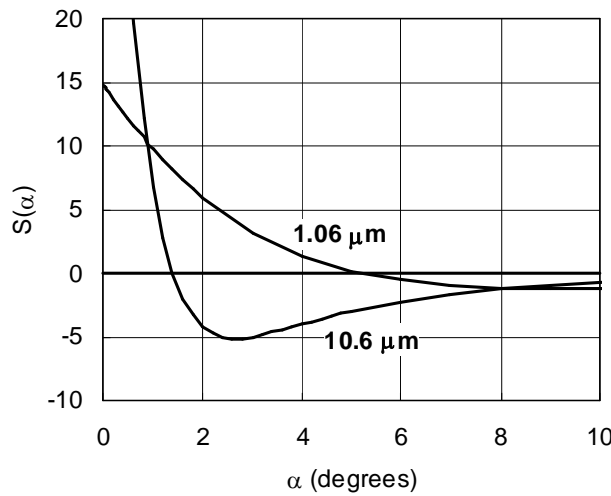


Figure 6-9. The angular dependences of the stability function $S(\alpha)$ (defined by Eq. (6-7)) for the two wavelengths of 1.06 μm and 10.6 μm .

(a) The case of $S(\alpha_{eq}) > 0$

First let us consider the case where $S(\alpha_{eq}) > 0$ ($\alpha_{eq} < \alpha_0$). The equation (6-8) shows that $V_B < 0$ in this case. Therefore, once the node B is displaced to the left, it gains velocity to the left. Thus the perturbation is amplified. The relation $V_B < 0$ applies also to the case where the node B is moved to the right, which corresponds to the case of $\Delta\alpha < 0$ for Figure 6-8(a). The relation $V_B < 0$ means that the node B is pulled back to the equilibrium position on the straight line AC. In this case ($\Delta\alpha < 0$), the perturbation is suppressed.

When the node B is displaced to the left, the perturbation can be amplified more and more. To see this point, let us continue the same discussion as above for the two sets of sub-chains BD-DC, and AJ-JB. First, we consider the case where D and J are both on the straight segments BC and AB, respectively. The velocity component V_{D0} of the node D normal to the segment BC is written as

$$V_{D0} = V_c \cos \alpha_{BC} - kI_L F(\alpha_{BC}) \quad (6-9)$$

Since $\alpha_{BC} > \alpha_{eq}$, one obtains $V_{D0} < 0$ from the relation $(V_c/kI_L) = A(\alpha_{eq}) \tan \alpha_{eq} < A(\alpha_{BC}) \tan \alpha_{BC}$. The velocity component V_{J0} of the node J along $\vec{n}_{\alpha_{AB}}$ at the same moment is found to be positive, since $\alpha_{AB} < \alpha_{eq}$. This difference of the sign between V_{D0} and V_{J0} represents initiation of downward transport of the perturbation of ABC.

Now let us consider a small perturbation of $\Delta\alpha_1$ added to the segment BC. Then the velocity component V_D normal to the segment BC is modified as

$$\begin{aligned} V_D &= \frac{1}{2} \left[\left(\vec{V}_c - kI_L F(\alpha_{BC} - \Delta\alpha_1) \vec{n}_{\alpha_{BC} - \Delta\alpha_1} \right) \cdot \vec{n}_{\alpha_{BC}} + \left(\vec{V}_c - kI_L F(\alpha_{BC} + \Delta\alpha_1) \vec{n}_{\alpha_{BC} + \Delta\alpha_1} \right) \cdot \vec{n}_{\alpha_{BC}} \right] \\ &\approx -\frac{kI_L}{2} S(\alpha_{BC}) \Delta\alpha_1^2 + V_{D0} \end{aligned} \quad (6-10)$$

We obtain the relation $V_D < V_{D0} < 0$. Therefore, once the point D is displaced by a small amount of distance to the left from the straight segment BC, the point can travel to the left faster than V_{D0} . This makes the section BDC more bended with the segment DC more inclined. Therefore, the initial small perturbation of ABC, can be amplified while transported downwards. There appears a region like DC, where the local α becomes higher and higher. This process of bending continues as far as $S(\alpha) > 0$, until the local angle α reaches α_0 ($S(\alpha_0) = 0$). After this moment, there will only be the downward transport of the perturbation without further amplification.

(b) The case of $S(\alpha_{eq}) < 0$

Next we consider the case of $S(\alpha_{eq}) < 0$ ($\alpha_{eq} > \alpha_0$). The same discussion as above leads us to conclude that the perturbation to the right as AB'C in Figure 6-8(b) increases, since the velocity component $V_{B'}$ of the point B' along $\vec{n}_{\alpha_{eq}}$ is positive. The segment B'C tends to be bended further as B'D'C in Figure 6-8(b). The local inclination angle α of the segment D'C becomes smaller than α_{eq} . The growth of the perturbation thus decreases the local α and it stops when α reaches α_0 .

In summary, the above discussion shows that, whatever the initial equilibrium inclination angle α_{eq} is, the kerf profile is inherently unstable (except the case where α_{eq} is exactly equal to α_0). When $\alpha_{eq} < \alpha_0$, $S(\alpha_{eq}) > 0$ and the concave mode as in Figure 6-8(a) develops with the increase of α . On the other hand, when $\alpha_{eq} > \alpha_0$, $S(\alpha_{eq}) < 0$ and the convex mode is amplified with the decrease of α (Figure 6-8(b)). For both cases, the development of the perturbation is terminated when the local α becomes equal to α_0 . It might be surprising that the kerf front is only stable when local α is exactly equal to α_0 . It seems that this result is caused partly by simplifications used in this model. For example,

consideration of surface tension will add a damping effect against the perturbations and should enlarge a stable region of α around α_0 .

In spite of the simplified assumptions, our model allows us to discuss the interesting point of the wavelength dependence of the stability of the kerf profile as follows. We focus on the low α_{eq} condition for thick section cutting (typically when $\alpha_{eq} < 3$ degrees).

(i) The case of 10 μm

In the case of 10.6 μm , $S(\alpha)$ changes its sign at $\alpha_0 = 1.4$ degrees. According to the above discussion, when $\alpha_{eq} < 1.4$ degrees, $S(\alpha) > 0$, so the concave mode develops. There appears a region where $\alpha > \alpha_{eq}$, but the increase of the local α stops at $\alpha_0 = 1.4$ degrees. When $1.4 < \alpha_{eq} < 3$ degrees, on the other hand, $S(\alpha) < 0$. The convex mode appears in this case and the development ceases if the local α is decreased to the same value of 1.4 degrees. In any case, the difference of the angle between α_0 and α_{eq} is small, and thus the corresponding perturbation along the kerf front is small and cannot grow so large.

(ii) The case of 1 μm

For 1.06 μm , $S(\alpha)$ becomes zero at $\alpha_0 = 5.2$ degrees and is always positive for $\alpha_{eq} < 3$ degrees. The concave mode appears and this continues to develop until the local α reaches α_0 . Because of the larger value of α_0 , the profile is perturbed much more strongly than the case of 10.6 μm . This is considered to be the fundamental reason why the front profile in the case of the 1 μm wavelength tends to be less stable than 10 μm . It can be added here that α_0 is about the half of the Brewster angle for each wavelength, so the stability is closely related to wavelength dependence of the Brewster angle.

Although the present model predicts that the local inclination angle can be stagnated at 5.2 degrees for 1 μm , more perturbed profiles with much larger α can be observed experimentally. The proper description of this successive development after 5.2 degrees is left for a future work, but it seems possible that the initial perturbation developed up to 5.2 degrees can trigger larger deformation of the profile. Once a so-called shelf or step, where α is locally very high, comes out, strong drilling occurs on the shelf due to higher absorbed intensity. This localized drilling transports the shelf downwards. In the case of welding, strong metal vapour jet emitted from the shelf can destabilise melt pool dynamics. For the striation generation process in laser cutting, localized melt on the shelf, which we call a hump, can disturb the dynamics of the downward displacement of MAs along the kerf side.

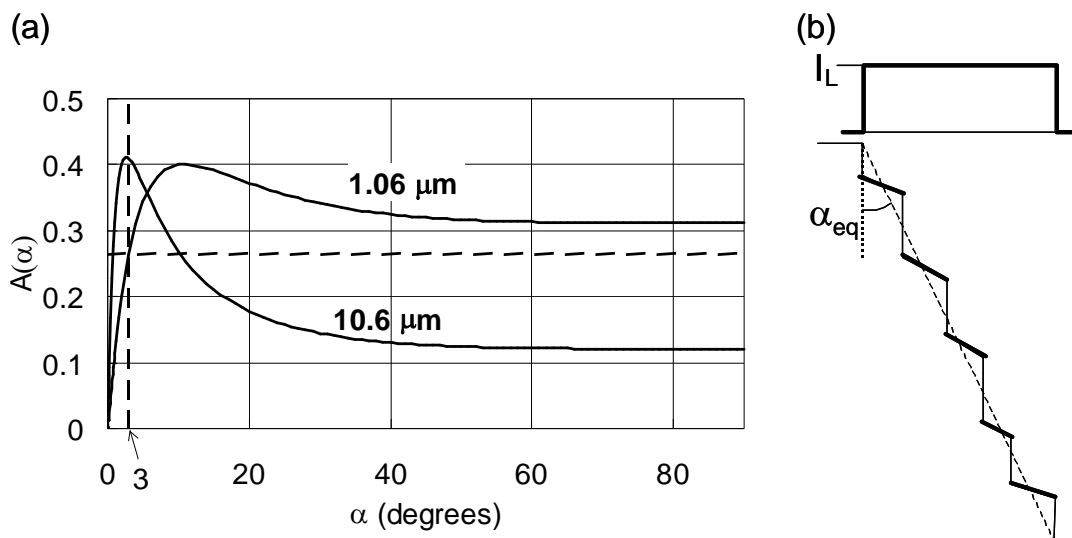


Figure 6-10. (a) The angular dependences of the absorptivity $A(\alpha)$ for the two wavelengths of 1.06 μm and 10.6 μm at $T = T_m$ [Dausinger 1993]. (b) A model kerf profile in the case of the regime of humps.

A closer look at the above analysis shows that the perturbation is amplified due to the fact that bending is favourable in terms of energy efficiency. That is, when the straight line AC in Figure 6-8(a) is bended, averaged absorptivity for the laser beam section A'C' increases. It is interesting to note that for 1 μm this effect can also be observed in a larger scale, in the energy efficiency of the whole cutting process. Let us consider the absorptivity for a model profile for the hump regime shown in Figure 6-10(b). The profile is composed of vertical walls and inclined parts of shelves. The laser beam is then irradiated only on the shelves, where local inclination angle α is much larger than α_{eq} . According to the angular dependence of the absorptivity for 1 μm shown in Figure 6-10(a), the absorptivity always increases when α is increased from α_{eq} that is situated in the range of $\alpha_{\text{eq}} < 3$ degrees. Consequently, when the unstable hump regime is established from the destabilisation effect discussed above in the case of 1 μm , the averaged absorptivity can be raised, compared with the case of straight profile with a constant inclination angle α_{eq} . In fact, the increase of the effective absorptivity has already been suggested experimentally: Wandera *et al.* [Wandera 2011-2] reported that less laser power is required to cut 10 mm thick stainless steel with a fibre laser than with a CO₂ laser for the same cutting velocity. Scintilla *et al.* [Scintilla 2010, Scintilla 2011] investigated the maximum cutting speed to cut samples of different thicknesses for the two wavelengths, and confirmed that the maximum cutting speed reached by a disc laser is higher than a CO₂ laser even for 8 mm thick steel. Also, one must note that the averaged values of α_{eq} for these thicknesses (10 mm, 8 mm) are so small that $A(\alpha_{\text{eq}})$ for the averaged angle α_{eq} is higher for CO₂ laser (see Figure 6-10(a)).

Finally it should be noted that there is another mechanism for the generation of humps. As discussed in chapter 5, when α_{eq} is small, humps are generated periodically from the surface due to combined effect of surface tension and thermal instability. Obviously this mechanism does not depend on the wavelength. Another important difference is that, according to this mechanism, humps are generated only from the surface, whereas humps can emerge anywhere on the kerf front in the case of the destabilisation of the front profile discussed above.

6.2.3 Downward displacement of melt accumulations along kerf sides

Let us discuss the influence of the laser beam wavelength on the dynamics of the downward displacement of MAs along kerf sides and on the roughness of striations. As discussed in chapter 5, the surface roughness is created after the displacement of MAs, which are generated periodically at the top part of the kerf side. The striation wavelength λ , which corresponds to the width of each of the MAs along the cutting direction, is determined from a balance between force exerted by assist gas and surface tension that retains the accumulations. The downward displacement is almost vertical and the MAs continue to receive laser energy during their downward displacement. Each MA transfers a part of this energy to the solid part. As a result, local melting of the solid part in the contact area creates a stripe of striations.

In thick section cutting, inclination angle of kerf sides is very small, generally less than the angle α_{eq} of the front. For such a small angle, the absorptivity of the laser beam on the MAs along the sides is higher for 10 μm than for 1 μm (see Figure 6-10(a)). The MAs in the case of CO₂ laser are thus expected to have higher temperature and consequently lower viscosity. Resultant higher displacement velocity of MAs may reduce the total energy consumed for the local melting during the period of the downward displacement and thus leads to lower surface roughness. This aspect of the temperature dependence of the melt ejection has been pointed out in the past, but the regime of discrete MAs on the kerf side has never been considered. In the following, we examine this rather complex problem with a simplified analytical model and discuss the impact of the temperature of MAs on the final quality of surface roughness.

In section 5.4, we estimated the surface roughness R_z with an analytical model. In this analysis we did not take into account vertical displacement of melt accumulations. It was assumed that an accumulation stays at the surface for a period $\Delta t_a (= \lambda/V_c)$. We considered melting of solid surface by this static melt accumulation during the period Δt_a . The result should predict the surface roughness just

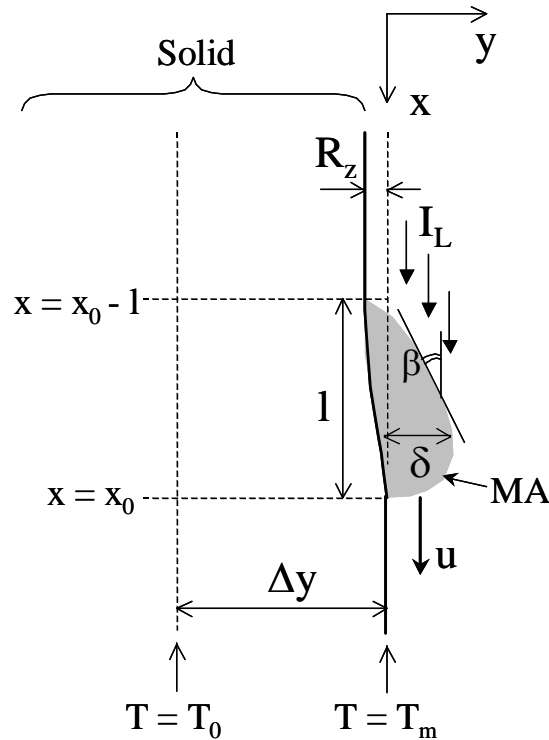


Figure 6-11. The 2D model of the striation generation process. The solid part is melted due to heat transfer from the melt accumulation (MA) sliding down along the kerf side wall.

below the surface. Considering the experimental fact that the degradation of R_z in the case of a $1 \mu\text{m}$ laser beam starts from $1 \sim 2 \text{ mm}$ below the top surface, however, we need here another model which take into account the dynamics of the downward displacement of the melt accumulation and its influence on the melting of the solid surface, in order to predict R_z in a lower part of the kerf.

The model that is investigated is shown in Figure 6-11. For simplicity we assume that the stationary condition is reached. A MA slides down along the kerf side wall with a constant velocity u . It receives laser intensity and transfers a part of the energy to the solid part. As a result, the solid part is eroded by the depth of R_z . The prediction of R_z is the final goal of this analysis. The MA is assumed to be a deformed droplet, whose characteristic width, thickness and length are given by λ , δ and l , respectively. The width λ corresponds to the striation wavelength, and δ represents thickness of the MA at the surface, which is also related to the force balance between the surface tension and assist gas. According to our observation described in chapter 4, it seems reasonable to assume that λ and δ are constant. We regard the problem as 2D, reducing the dimension along λ . The length l of MA increases during the downward displacement, since gradual melting of solid part provides additional volume to MA. Modelling of this complex hydrodynamics is beyond the scope of this work, however, and we assume a constant value of l .

First let us describe the temperature field in the solid part. Before the passage of a MA, the solid part is already pre-heated by heat conduction from the travelling laser beam and the surface temperature reaches T_m , the melting temperature. The initial temperature field inside the solid has the penetration depth Δy , which is approximated by $\Delta y \approx r_k(\text{Pe}/2)^{-0.7}$ (r_k : kerf radius, Pe : Péclet number ($= r_k V_s / \kappa$)), as in eq.(5-23). Here the y axis is taken perpendicularly to the solid-liquid interface. The temperature field is approximated by a linear distribution as the bold line in Figure 6-12.

Now we examine energy balances around a MA under the condition that the equilibrium is established. The temperature T of the MA is represented by the value at the centre of the MA. The first equation comes from the heat flux boundary condition at the surface of the MA:

$$I_L A(\beta) \sin \beta \approx K \frac{T - T_m}{\delta/2}, \quad (6-11)$$

where I_L is the laser intensity, β is the inclination angle of the MA's surface, and K is the heat conductivity. Please note that the increase of the absorbed intensity in the left hand side results in the temperature increase of the MA. The second equation concerns the Stefan condition along the solid-liquid interface.

$$K \frac{T - T_m}{\delta/2} \approx \rho L_f v + q_w, \quad (6-12)$$

where v is the velocity of the melting front into the solid part, and q_w is the heat flux lost into the solid. Considering that the melting front advances by R_z during the solid-liquid interaction over the distance l , v can be expressed as

$$v \approx \frac{R_z}{\Delta t} \quad (6-13)$$

where $\Delta t \approx (l/u)$ is the interaction time.

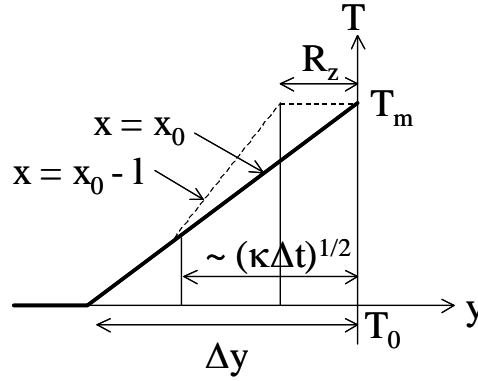


Figure 6-12. Temperature field inside the solid.

The heat flux q_w is determined from the temperature gradient in the solid part. The bold line in Figure 6-12 is the approximate temperature distribution along the line $x = x_0$ shown in Figure 6-11, which corresponds to the moment when the MA arrives. During the interaction time Δt with the MA, heat flux from the MA penetrates into the solid and the solid-liquid interface moves into the solid part by R_z . Considering that the penetration depth of temperature diffusion can be approximated with $\sim(\kappa\Delta t)^{1/2}$, the temperature field after Δt , along the line $x = x_0 - l$ in Figure 6-11, can be approximated as the dotted line in Figure 6-12. Please note that the temperature field outside the thickness $\sim(\kappa\Delta t)^{1/2}$ is not modified in this approximation. One can then calculate the heat flux q_w at the solid-liquid interface from the temperature gradient:

$$\begin{aligned} q_w &= K \left. \frac{dT}{dy} \right|_{y=-R_z} \\ &\approx \frac{1}{1 - \frac{R_z}{\sqrt{\kappa\Delta t}}} \frac{K(T_m - T_0)}{\Delta y} \\ &\approx \frac{1}{1 - R_z \sqrt{\frac{u}{\kappa l}}} \frac{K(T_m - T_0)}{\Delta y} \end{aligned} \quad (6-14)$$

q_w is increased by the factor $(1 - R_z(u/\kappa l)^{1/2})^{-1}$, compared with the heat flux $(\approx K(T_m - T_0)/\Delta y)$ before the

arrival of the MA. When the interaction time Δt is smaller, that is, when the length l of the MA is shorter or the velocity u is larger, q_w becomes larger. From eqs.(6-12) and (6-13), one can see that v and R_z become smaller, which means that the melting is restrained.

Finally we consider kinetics of the MA from a force balance equation. As already mentioned, higher T leads to lower viscosity μ and higher u . In order to estimate the order of u under the shear stress applied on the surface of MA from assist gas, we refer to a result of an experimental study on droplets sliding down along an inclined surface [Podgorski 2001]. In this study, a rather general law was found: $Ca \sim A_m Bo$, where A_m ($\approx 0.005 \pm 0.002$) is a constant, $Ca = \mu u / \sigma$ is the capillary number and $Bo = \rho g \sin \theta V^{2/3} / \sigma$ is the Bond number (σ : surface tension coefficient; θ : inclination angle of the surface; V : volume of the droplet). Replacing the force term ($\rho V g \sin \theta$) with $\tau_g(\lambda l)$, which represents the shear force by assist-gas in our case, we obtain

$$u \approx \frac{A_m \tau_g l}{\mu}. \quad (6-15)$$

It can be mentioned here that dimensionally eq.(6-15) is equivalent to the well-known Newton type viscous friction stress that works on the liquid-solid surface, although in the present case, the droplet slips on the solid surface with the velocity u . The temperature dependence of the viscosity μ is expressed by the Arrhenius law:

$$\mu = \mu_0 \exp\left(\frac{E_a}{RT}\right), \quad (6-16)$$

where E_a and R are the activation energy and the gas constant, respectively.

With non-dimensional parameters $L' = L/r_k$ ($L = l, \delta, R_z$), $u' = u/V_c$, $T' = (T - T_m)/(T_m - T_0)$, $I' = I_L / \rho C_p (T_m - T_0) V_c$, $\varepsilon = E_a / RT_m$, eqs.(6-11), (6-12) and (6-15) are rewritten as

$$I'A(\beta) \sin \beta \approx \frac{2}{Pe} \frac{T'}{\delta'}, \quad (6-17)$$

$$\frac{2T'}{\delta'} \approx \left(\frac{Pe}{St}\right) \frac{R'_z u'}{l'} + \frac{1}{1 - \sqrt{Pe} R'_z \sqrt{\frac{u'}{l'}}} \left(\frac{Pe}{2}\right)^{0.7}, \quad (6-18)$$

$$u' \approx l' \exp\left(\frac{\varepsilon T'}{1 + T'}\right) \left[\frac{A_m \tau_g}{\mu_m \left(\frac{V_c}{r_k}\right)} \right], \quad (6-19)$$

where

$$\mu_m = \mu_0 \exp\left(\frac{E_a}{RT_m}\right) \quad (6-20)$$

is the viscosity at the melting temperature. The non-dimensional parameter $b \equiv (A_m \tau_g r_k / \mu_m V_c)$ is about 2.5 ± 1 , if we take the values of $\tau_g \approx 500$ (Pa), $\mu_m \approx 5 \times 10^{-3}$ (Pa·s), $V_c = 20$ (mm/s), $r_k = 100$ (μm) and $A_m \approx 0.005 \pm 0.002$. Finally we obtain

$$u' \approx b l' \exp\left(\frac{\varepsilon T'}{1 + T'}\right). \quad (6-21)$$

$\varepsilon (= E_a / RT_m)$ is about 3 for steel.

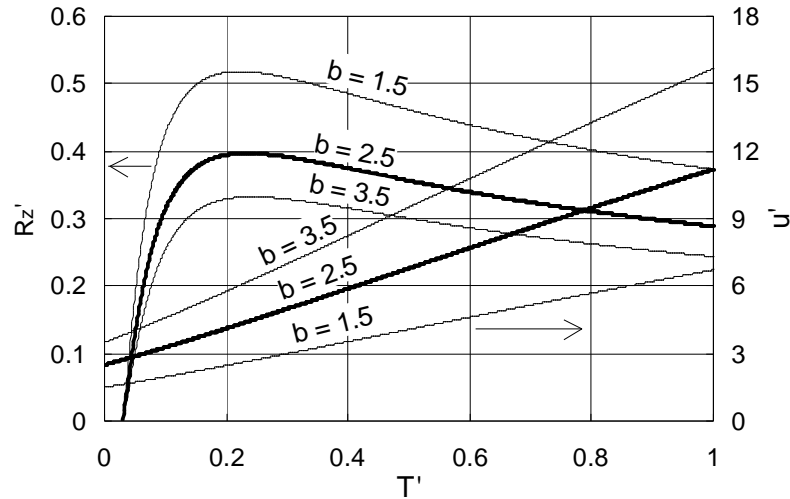


Figure 6-13. Calculated R_z' and u' as a function of T' for different values of b .

Figure 6-13 shows the dependencies of R_z' and u' on T' calculated from eqs.(6-18) and (6-21) with $\delta' = 0.1$, $l' = 1.0$ and $b = 2.5$. The curves are shown also for $b = 1.5$ and 3.5 to see the influence from the variation of A_m . It is confirmed that these curves have the same tendency as the case of $b = 2.5$, so we discuss only this case in the following. When $T' < 0.23$ ($T < 2.2 \times 10^3$ K), R_z' increases with the increase of T' . In this temperature region, u' does not increase strongly with T' , whereas the heat flux through the solid-liquid interface does increase with T' . This increment of the heat flux is consumed to melt more volume per unit time, which is proportional to $(u'R_z')$, and thus R_z' is increased. As u' and R_z' increase, however, the heat conduction loss to the solid part (the second term in the right hand side of eq.(6-18)) begins to grow up and the heat flux that can be used to melt the solid is decreased. Consequently R_z' takes the maximum at $T' = 0.23$. After this point, R_z' decreases with T' mainly due to the reduction of the viscosity with the increase of T' . For this temperature region, the present simplified model predicts that R_z decreases with T' , and this can explain the worse quality of cut surfaces obtained with a $1 \mu\text{m}$ beam.

Considering striking difference observed between $1 \mu\text{m}$ and $10 \mu\text{m}$, however, it seems that the difference predicted by this model is underestimated. Moreover, in reality, the roughness might decrease with the increase of temperature also in the range of $T' < 0.23$. One way to improve the present model is to take into account the evolution of the geometry of the MA and its effect on the kinetics of the MA. This point will be investigated in a future work.

6.3 Summary and conclusions

The cut surface quality difference which had been observed in laser cutting of thick section steel with $1 \mu\text{m}$ and $10 \mu\text{m}$ laser beams was investigated in this chapter. First, comparative cutting experiments were conducted with a fibre and a CO_2 laser using almost the same operating parameters. As in the previous studies, cut surface quality obtained with the fibre laser was worse than that obtained with the CO_2 laser for a large thickness. The inclination angle α of the kerf front was examined for the first time in this work and it was revealed that the degraded cut surface quality for the $1 \mu\text{m}$ wavelength appears for a low α ($\alpha < 3$ degrees).

Then the wavelength dependence was theoretically investigated from the aspects of the two fundamental processes.

First we analyzed the destabilisation of the melt flow in the central part of the kerf front. When the

central flow is destabilised, the dynamics of melt accumulations which slides down the wall is disturbed. Consequently, striations, which result from this downward displacement of the melt accumulations, are degraded. The analysis of kerf front profile was conducted with the chain model, where the dynamics of the kerf front was expressed by displacement of a small segment of chain. Local velocity of a chain at some instance depends on the cutting velocity V_c and the absorbed intensity. The dependence of the Fresnel absorption law on the laser wavelength influences the absorbed intensity and thus the dynamics of the front. Using the stability function

$$S(\alpha) = \frac{\partial^2 F(\alpha)}{\partial \alpha^2} - F(\alpha),$$

it is concluded that when the stability function $S(\alpha_{eq})$ is positive (negative)

the concave (convex) mode of perturbation appears and develops. For both modes, the growth of the perturbations stops when the local inclination angle reaches α_0 , which satisfies $S(\alpha_0) = 0$. In the case of thick section cutting ($\alpha_{eq} < 3$ degrees), the stopping angle α_0 for 1 μm (5.2 degrees) is far away from the mean angle α_{eq} of the cutting front, whereas α_0 for 10 μm (1.4 degrees) is very close to the operating range of α_{eq} . This explains why the cutting front for a 1 μm laser beam is perturbed much more strongly than that for a 10 μm beam.

Then we investigated the dynamics of downward displacement of MAs along kerf sides. Melt accumulations slide down the kerf wall while absorbing laser power. The melt accumulations transfer a part of this power to the solid part. As discussed in chapter 5, the contact area of the solid surface is locally melted and this melting continues down to the bottom of the kerf as the melt accumulations go down. This is considered to be the fundamental mechanism of the striation generation process. It is obvious that the dynamics of melt accumulations strongly influences characteristics of striations. The absorptivity of laser beam on melt accumulations is higher for a 10 μm laser beam due to the different angular dependence of the absorptivity. Higher temperature of melt accumulations for a 10 μm beam can be the mechanism of the quality difference.

We developed a simple analytical model which analyses power balance in the above-mentioned heat transfer process around the melt accumulation. The downward velocity of a melt accumulation was incorporated to the model, based on the result of an experimental investigation of velocity of a droplet on an inclined surface. The result of model calculations shows that an increase of the absorbed intensity on the MAs can increase their temperature and decrease the surface roughness. This result indicates that the lower absorptivity for very small inclination angle of the kerf sides can be the reason for the worse quality obtained for thick section cutting with a 1 μm laser beam.

From these considerations, we finally propose that a possible solution to improve the quality for 1 μm is to utilise lasers with the radial polarisation. The absorptivity on the kerf side can be increased because the radial polarisation works as the favourable p-polarisation on the side. To the best of our knowledge, the interest of the use of the radial polarisation on the cut surface quality has never been pointed out, while relevant theoretical discussions have focused on improvement of capacity of the cutting process in terms of cut thickness or cutting velocity [Niziev 1999, Zaitsev 2005]. Please note that the cutting capacity is determined mainly by the absorptivity on the central part of the kerf front and not by the absorptivity on the side, which is the present interest. Experimentally, for CO₂ laser cutting of steel, it has already been reported that the surface roughness can be improved with the use of radial polarisation compared to the ordinary circular polarisation [Ahmed 2009]. For the 1 μm wavelength, the problem of the destabilisation of the central flow may not be completely solved with the radial polarisation, because the stopping angle α_0 is still kept high at 4.8 degrees even for the absorption of the p-polarisation. Nevertheless, it is the dynamics of MAs that is directly related to the final surface roughness. Therefore, with the radial polarisation, a better absorption of the laser beam on kerf sides should improve the quality to some extent. We are looking forward to seeing experimental verifications in near future.

Chapter 7. Conclusions

Conclusion Générale

Le mécanisme de la génération des stries lors de la découpe laser d'aciers avec un gaz inerte a été étudié dans cette thèse. En utilisant des observations de la dynamique du métal fondu sur le front avant de la saignée avec une caméra vidéo rapide et des investigations théoriques des processus physiques relatifs, nous avons réussi à clarifier ces mécanismes fondamentaux de génération de stries, mécanisme non élucidé depuis quelques dizaines d'années, en dépit de son importance scientifique et industrielle.

Les principaux résultats peuvent se résumer ainsi :

Les stries sont provoquées par les instabilités de l'écoulement de liquide qui apparaissent dans la partie centrale et sur le côté de la saignée. La génération intermittente de « humps » sur la partie centrale et d'accumulations de liquide sur le côté du front de la saignée est la cause fondamentale de l'instabilité de l'écoulement de liquide. Cette génération intermittente résulte de la force de la tension superficielle, qui tend à maintenir une gouttelette de métal fondu à la surface supérieure de l'échantillon, en s'opposant à pression dynamique du gaz d'assistance, tant que la taille de la gouttelette est petite. Une équation d'équilibre entre les forces générées par le gaz d'assistance et par la tension superficielle définit le pas δ des humps. Le pas définissant l'apparition des accumulations de liquide, qui est aussi égal à la longueur d'onde des stries λ observées, est plus grand que δ en raison d'un effet géométrique. Les valeurs et évolutions de δ et λ ainsi prévues sont assez conformes à celles obtenues expérimentalement. Ce modèle est également conforté par d'autres résultats expérimentaux qui montrent en particulier que δ et λ diminuent avec l'augmentation de la pression du gaz d'assistance et qu'ils sont indépendants de la vitesse V_c de découpe.

Les instabilités dans les parties centrale et de côté du front avant disparaissent pour des vitesses V_c élevées. Ceci résulte de la fusion de deux humps consécutifs, puisque la distance entre eux le long du front avant de la saignée diminue avec l'augmentation de V_c . Dans le cas des accumulations de liquide, la distance de deux accumulations le long du côté de la saignée est plus grande que celle des humps de la partie centrale pour une vitesse de coupe V_c donnée, de sorte que la vitesse seuil au-dessus de laquelle l'écoulement de liquide devient continu est plus grande pour les accumulations de liquide. C'est pourquoi les écoulements sur le centre et sur le côté deviennent stables pour différentes vitesses V_c . Une analyse théorique montre que la stabilité de l'écoulement central ne dépend que de l'angle d'inclinaison α du front avant; il existe un angle de seuil au-dessus duquel l'écoulement central devient continu. Cette loi d'échelle est confirmée expérimentalement et cet angle seuil ne dépend pas de la puissance de laser.

En résumé, les caractéristiques des instabilités observées expérimentalement, y compris les différences de comportement entre la partie centrale et le côté de la saignée, peuvent être expliquées avec cohérence par le seul effet de la tension de la surface.

Des stries sont produites par les accumulations de liquide, créées initialement à la surface supérieure de l'échantillon et qui se déplacent vers le bas le long des parois de la saignée. Chaque descente d'une accumulation de liquide laisse une rainure, une strie, car cette accumulation de liquide fond localement la paroi de la saignée en y transférant une partie de l'énergie qu'elle absorbe du faisceau laser. Une modélisation de ce processus de conduction de chaleur a montré que la rugosité R_z est du même ordre que λ . Ceci est conforté par le fait expérimental que λ et R_z varient d'une façon analogue quand les différents paramètres opératoires varient. La dynamique de la descente du déplacement des accumulations affecte fortement le relief final des côtés, ainsi que la rugosité R_z . Cette dynamique dépend aussi de la stabilité de l'écoulement central. Lorsque l'écoulement central est stable, les accumulations de liquide peuvent descendre sans perturbation et les stries résultantes sont presque verticales, assez régulières et relativement lisses. Quand α est grand, les accumulations de liquide peuvent être absorbées par l'écoulement central en raison de la tension superficielle. Par conséquent λ et R_z diminuent dans ce cas. D'autre part, quand l'écoulement central devient instable, les humps

produits dans la partie centrale peuvent fortement interférer avec les accumulations de liquide. Les trajectoires des accumulations sont alors perturbées, et la qualité finale de la surface est irrégulière et dégradée.

L'angle α d'inclinaison du front avant est le paramètre déterminant la stabilité de l'écoulement de liquide et de la qualité finale des stries. Un contrôle possible de cette stabilité est d'utiliser une distribution d'intensité quasi-gaussienne du faisceau laser au lieu d'un profil homogène de type « top-hat ». L'augmentation locale de α au niveau de la surface supérieure stabilise l'écoulement central. Cet écoulement central peut alors stabiliser les accumulations de liquide sur les côtés de la saignée en les absorbant plus rapidement en raison de l'augmentation locale de α . Dans ce cas, λ et R_z peuvent être réduites.

Basé sur cette clarification du mécanisme de génération de stries, il nous été possible d'aborder le sujet très intéressant de la différence de qualité de découpe observée entre des longueurs d'onde laser à 1 μm et à 10 μm . Nous avons mis en avant deux facteurs qui peuvent affecter le processus de génération de stries. Ces deux facteurs concernent la dépendance de la loi d'absorption avec la longueur d'onde laser : Le premier facteur concerne l'absorption du faisceau laser sur les côtés de la saignée. Pour un faisceau à 10 μm l'intensité laser absorbée est plus élevée, de sorte que la vitesse de descente des accumulations de liquide devient plus rapide en raison d'une viscosité inférieure. Cet effet peut réduire la rugosité. L'autre facteur concerne la stabilité de l'écoulement central. On montre que le profil du front avant de la saignée obtenu par un faisceau laser à 10 μm est plus stable que celui obtenu par un faisceau à 1 μm . Ceci peut également expliquer une qualité meilleure obtenue avec un faisceau laser à 10 μm . Finalement, on propose l'utilisation d'une polarisation radiale pour améliorer la qualité de découpe lors de l'emploi d'un faisceau laser à 1 μm .

Quelques perspectives et travaux futurs :

Tout d'abord, il serait intéressant d'effectuer les visualisations semblables à celles que nous avons faites, de l'hydrodynamique du métal fondu lors de l'emploi d'un laser à CO_2 . Les résultats devraient permettre une meilleure compréhension de la dépendance des diverses observables expérimentales de la qualité de découpe avec la longueur d'onde et complèteraient les données pour une meilleure vérification des modèles analytiques proposés au chapitre 6.

La réalisation des simulations numériques de la dynamique d'écoulement de liquide devraient aider à une compréhension plus complète de ces différents processus multi-physique complexes. Plusieurs modèles analytiques proposés dans ce travail, ont permis de donner des explications qualitatives pour certains résultats expérimentaux. Cependant, pour obtenir des analyses quantitatives sur certains paramètres, par exemple sur la rugosité, il faut tenir compte du couplage complexe de tous ces différents processus physiques en régime instationnaire et tridimensionnel (l'absorption du faisceau laser, la thermique induite et les changements de phase, l'hydrodynamique complexe, ...). Par exemple, notre discussion sur la stabilité des écoulements de liquide est uniquement basée sur les aspects d'hydrodynamique. Il est possible que le processus de transfert de chaleur influence également la stabilité, comme Kovalenko et Golubev l'ont proposé. En outre, notre analyse relativement simple du transfert de chaleur dans le processus de génération des stries présenté dans cette thèse a négligé la convection ou la distribution de la température à l'intérieur d'une accumulation de liquide. Les simulations numériques qui peuvent prendre en considération ces différents points permettront de comparer avec une bien meilleure précision les caractéristiques des stries avec les données expérimentales.

Il existe déjà de nombreux codes numériques pour le soudage laser. Ces codes peuvent également s'appliquer au processus de la découpe laser [Schmidt 2011]. Le groupe de Mr. Amara au CDTA à Alger, a déjà commencé à simuler le processus de découpe de laser en collaboration avec notre laboratoire en prenant en compte une description multi-physiques des phénomènes [Amara 2012]. Ces simulations sont assez délicates, en particulier en ce qui concerne la description de l'écoulement du jet de gaz compressible, en régime turbulent, pour des conditions réalistes de découpe. Cependant, les

résultats expérimentaux de notre étude, suggèrent que les processus fondamentaux que nous avons mis en avant ne sont pas modifiés dans le cas d'un jet de gaz à faible pression. On peut ainsi aborder ces investigations en supposant un écoulement incompressible du gaz. Ce genre d'investigations numériques permettra de confirmer les différents schémas proposés dans cette thèse, et contribuera non seulement à une meilleure compréhension du procédé de génération des stries mais également à une optimisation de différentes conditions de l'opération.

Conclusions and future perspectives

In this study, the mechanism of striation generation during inert gas laser cutting of steel was investigated. Based on experimental high speed video film observations of melt film dynamics along kerf fronts and theoretical investigations of related physical processes, we succeeded to clarify the fundamental mechanisms of the striation generation, which has remained unknown for several decades in spite of its industrial importance. The main results are summarised as in the following.

Striations are caused by instabilities of melt flow that appear in the central and side parts of the kerf front. Intermittent generation of humps and melt accumulations from the top part in the central and side regions of the kerf front is the fundamental cause of the melt flow instability. This intermittent generation is caused by surface tension force, which tends to retain a hump or a melt accumulation at the surface, counteracting to the assist gas force, while the size of the hump or the melt accumulation is not large enough. A force balance equation between the assist-gas force and the surface tension determines the pitch δ of humps. The pitch of melt accumulations, which is equal to the wavelength λ of striations, becomes larger than δ due to an additional geometrical effect. Theoretically predicted values of δ and λ agree with those experimentally obtained. This model is also supported by experimental facts that both δ and λ decrease with increasing assist-gas pressure and that they are independent of the cutting velocity V_c .

The instabilities in the central and side parts of the front disappear for high cutting velocity V_c . This is caused by a merger of two adjacent humps, since the distance between them along the kerf front diminishes with an increase of V_c . In the case of the melt accumulations on kerf sides, the distance of two accumulations along the kerf side is larger than that for humps in the central part at a given V_c , so that the threshold velocity above which the melt flow becomes continuous is higher for the side flow. This is why the central and side flows become stable in different ranges of V_c . According to a theoretical analysis, the stability of the central flow depends only on the inclination angle α of the front; there exists a threshold angle α_{thr} above which the central flow becomes continuous. This scaling law is supported by an experimental result that α_{thr} does not depend on the laser power.

In summary, characteristics of the instabilities experimentally observed, including the differences between the central and side flows, have been successfully explained coherently by the unique mechanism of the surface tension effect.

Striations are basically generated by melt accumulations, which are created at the surface and are displaced downwards along kerf side walls. Each stroke of melt accumulation leaves a stripe of striations, because the melt accumulation melts locally the kerf side surface by transferring a part of the energy which it absorbs from the laser beam. A theoretical analysis of this heat conduction process showed that R_z is in the same order as λ . This is supported by an experimental fact that λ and R_z vary in almost the same manner when different operating parameters are varied. The dynamics of downward displacement of the melt accumulations strongly affects final relief of kerf sides and thus R_z . This dynamics depends on the stability of the central flow. When the central flow is stable, melt accumulations can slide down to the bottom surface and striations are nearly vertical, quite regular and relatively smooth. When α is large, the melt accumulations can be pulled down from the central flow by surface tension force. Consequently λ decreases and so does R_z . On the other hand, when the central flow becomes unstable, humps generated in the central part can interfere strongly with the melt accumulations. Trajectories of the melt accumulations are perturbed. Consequently, irregular and rough surfaces are left on kerf sides.

As stated above, the inclination angle α of the front is the key parameter which controls the stability of the melt flow and final quality of striations. One way to control the stability is to use a Gaussian-like intensity distribution instead of a top-hat beam profile. The local increase of α near the surface stabilises the central flow. Moreover, the stabilised central flow can pull down melt accumulations on kerf sides more strongly owing to the increase of α . Thus both λ and R_z can be reduced.

Based on the striation generation mechanism which has been clarified, we investigated the interesting topic of the cut surface quality difference between 1 μm and 10 μm wavelengths. We have pointed out two fundamental processes that can affect the striation generation process. One is the laser beam absorption on the kerf sides. For a 10 μm beam the absorbed intensity is higher, so that downward velocity of melt accumulations becomes faster due to a lower viscosity. This can reduce the surface roughness. The other factor is the stability of the central flow. It was shown that a kerf front profile for a 10 μm laser beam is more stable than that for a 1 μm beam for a low angle α of the inclination that appear in thick section cutting. This can also be the explanation for the better quality obtained with a 10 μm laser beam. The laser wavelength dependence of each of the processes was verified by analytical modelling of related physical processes. Both of the processes are related to the laser wavelength dependence of the angular dependence of the Fresnel absorption law. We finally proposed that a possible way to improve the quality for the 1 μm wavelength is to use a laser beam with the radial polarisation.

Finally let us mention about future prospects. First of all, it will be interesting to carry out similar high speed video film observations for cutting with a CO_2 laser. The results will lead to a better understanding of the wavelength dependence of cut surface quality and will provide data for verification of the analytical models proposed in chapter 6.

Second, numerical simulations of melt film dynamics are required to understand more properly this complicated multi-physics phenomenon. Several analytical models that were proposed in this work have succeeded to give qualitative explanations to experimental results. In order to make quantitative explanations on cut surface quality, however, one has to take into account coupling among different physical processes (absorption of a laser beam, thermodynamics, melt film dynamics). For example, our discussion on stability of a melt flow was based solely on hydrodynamics. However, it can be possible that heat transfer process also influences the stability, as Kovalenko and Golubev proposed. Another aspect that should be improved by a numerical simulation is modelling of the dynamics of a melt accumulation or a hump along a kerf front. Convection or temperature distribution inside these melt droplets should be important to predict characteristics of striations.

There exist already a number of numerical codes for laser welding. Basically these codes can be applied also to laser cutting process [Dobler 2011]. The group at CDTA in Algeria has started numerical simulations of laser cutting in collaboration with our laboratory, taking into account the aspect of multi-physics [Amara 2012]. One of the difficulties in modelling cutting process is how to incorporate a compressive gas flow. The results of this study, however, suggest that fundamental processes are not altered by the use of a weak gas jet. Thus one may start from an incompressive gas flow. This kind of numerical investigations will contribute not only to a better understanding of the striation generation process but also to an optimisation of various operating conditions.

Annex 1. Measurement of absorptivity

Résumé

L'absorption de la puissance de faisceau laser sur le front avant de la saignée constitue le seul apport énergétique dans la découpe laser acier sous un gaz inerte. Trois paramètres principaux caractérisent le processus de l'absorption laser dans la découpe laser: l'angle d'incidence du faisceau laser avec le front avant incliné, la haute température de la surface de liquide sur le front de la saignée et la longueur d'onde laser. Dans la plupart des analyses théoriques du processus de découpe laser, on suppose que la loi d'absorption de Fresnel peut décrire l'absorptivité de cette surface. Cependant, il y a peu de travaux qui ont étudié la validité de cette loi dans le cadre de la découpe laser pour ces conditions.

Pour vérifier la validité de la formule de Fresnel au processus de découpe laser, deux types d'expériences ont été conduits. La première expérience a permis de confirmer la dépendance angulaire de l'absorptivité, particulièrement pour un angle d'incidence élevé (ou faible angle d'inclinaison du front avant de la saignée). La dépendance angulaire de l'absorptivité pour un faisceau de laser à disque (la longueur d'onde laser : $1.03 \mu\text{m}$) a été mesurée en utilisant comme matériau une feuille de fer pur inclinée. L'échantillon a été placé au-dessus d'une sphère intégrante et la lumière réfléchie est recueillie par cette sphère. La mesure a été effectuée pour les deux polarisations S et P. La température de surface de l'échantillon devait être inférieure à la température de fusion T_m , car aucune trace de liquide n'a été trouvée après les tirs laser. Les mesures montrent un accord tout à fait raisonnable avec la théorie: l'absorptivité des polarisations P et S augmentent avec une diminution d'angle d'incidence et elle est beaucoup plus importante pour la polarisation P que pour la polarisation S. Ces résultats sont conformes à des travaux antérieurs [Touvrey 2006], où l'augmentation de l'absorptivité a également été confirmée, avec du tantale, lorsque l'angle d'incidence diminue.

La deuxième expérience a été conduite pour étudier la dépendance de l'absorptivité avec la température de surface d matériau. Un échantillon de fer pur a été placé sous une sphère intégrante qui récupère la lumière réfléchie de la surface de l'échantillon. L'angle d'incidence du faisceau laser était d'environ 5 degrés (c'est-à-dire $\alpha = 85$ degrés). La variation temporelle de l'absorptivité a été mesurée pendant l'irradiation d'un laser à $1 \mu\text{m}$. Dans une autre expérience avec les mêmes conditions d'irradiation laser, la température de surface de la tache irradiée a été mesurée en fonction du temps par pyrométrie, en utilisant une caméra vidéo rapide. En combinant ces deux résultats, la dépendance avec la température de l'absorptivité a pu être estimée. Le résultat montre que l'absorptivité pour le fer pur est presque constante jusqu'à la température d'ébullition T_v . Les études précédentes ont montré que l'absorptivité de l'acier pour une longueur d'onde à $1 \mu\text{m}$ ne variait pratiquement pas jusqu'à $1400 \text{ }^\circ\text{C}$ [Dausinger 1993] et jusqu'à 2650 K [Kraus 1986]. Le résultat dans ce travail a montré pour la première fois que cette dépendance pouvait être extrapolée jusqu'à T_v .

Les résultats de ces deux expériences ci-dessus confirment donc la validité de la loi théorique d'absorption de Fresnel pour une longueur d'onde à $1 \mu\text{m}$ et une surface de fer pur. Il est donc raisonnable d'extrapoler la loi d'absorption pour les très faibles angles d'inclinaison α , avec les valeurs des indices n et k qui ont été déterminés par ces expériences expérience utilisant des angles α plus importants. De plus, l'influence du changement de température s'est avérée relativement négligeable pour ne pas en tenir compte.

Ensuite l'absorptivité au cours d'un processus réel de découpe laser a été mesurée pour confirmer que cette absorptivité pouvait être estimée à partir de la loi d'absorption de Fresnel pour ces conditions. Pour mesurer l'absorptivité pendant le processus de découpe, la puissance transmise sous la pièce est récupérée par une sphère intégrante. La puissance transmise résulte de deux composantes : la puissance réfléchie sur le front avant de la saignée et qui est transmise vers le bas, et celle directement transmise sans interaction avec le front avant de la saignée. La détermination de la superficie d'interaction avec le faisceau sur le front avant de la saignée (à l'aide d'une vision coaxiale) nous permet de distinguer ces deux composantes et d'estimer ainsi l'absorptivité sur le front avant de la saignée. L'absorptivité mesurée était environ 60% ; cette valeur est légèrement plus élevée que celle

prédite par la loi d'absorption de Fresnel. Mais il semble raisonnable de considérer que l'absorptivité pendant la découpe laser d'acier avec un gaz inerte est décrite par une loi de type Fresnel.

Introduction

Absorption of laser beam power on kerf front is the primary energy input process in laser cutting of steel assisted by an inert gas. Two features can be mentioned for the absorption process in laser cutting: high incidence angle of the laser beam to an inclined kerf front and high melt surface temperature on the kerf front. In the theoretical analyses of laser cutting process in the past, it has been assumed that the Fresnel absorption law can describe the absorptivity on kerf fronts. However, there are few studies that have investigated the applicability of the Fresnel absorption law to laser cutting which involves the above-mentioned particular features. The object of this section is to investigate the applicability of the Fresnel formula by experimental measurements of the absorptivity.

In the first experiment, the angular dependence of the absorptivity is measured for a high incidence angle (or, low inclination angle α of the kerf front). The results show reasonable agreement with the theory for both of the p and s polarisations. Second, the temperature dependence of the absorptivity is estimated from an experiment described in Annex 2. It will be shown that the absorptivity for pure iron is almost constant up to the boiling point T_v . The above two experiments conclude that the Fresnel absorption law can be extrapolated to a region of low α , using the complex refractive indices n and k that are obtained by an experiment with a high α near 90 degrees, and also to a high temperature range over the melting temperature T_m . Finally, the absorptivity in real cutting process is experimentally measured. The measured absorptivity is around 60%. The value is slightly higher than that predicted from the Fresnel absorption law. But it seems reasonable to conclude that the Fresnel law well describes the absorptivity during inert gas laser cutting of steel.

A1.1. Measurement of angular dependence

The object of this first experiment is to confirm the angular dependence of the absorptivity, especially for a high incidence angle, which corresponds to a low inclination angle α of kerf front. Angular dependence of absorptivity on a polished inclined surface of pure iron was measured using the setup shown in figure A1-1. A laser beam from the 10 kW disc laser was polarised with a polarising beam splitter. The measurement was carried out for each of the two polarisations s and p. The sample was placed above an integrating sphere and the reflected light was collected in the sphere. The surface temperature of the sample must have been below the melting point T_m , because melting could not be found after the measurement with a laser pulse irradiation.

The results are shown in figure A1-2 and compared with theoretical curves. The experimental results roughly agree with the theoretical curves. As predicted by the theory, the absorptivity strongly depends on the angle α and on the polarisation; the absorptivities for both the p and s polarisations increase with a decrease of incidence angle (an increase of α) and the absorptivity is much higher for the p-polarisation than for the s-polarisation. The present result agrees with a previous work [Touvrey 2006], where the increase of absorptivity was confirmed with the increase of α for Tantalum. For the s-polarisation (red ■), the experimental values are much larger than the theory. With more properly polished steel sample (red □), this discrepancy was decreased. This result suggests that, when the inherent absorptivity is very low (as is the case for the s-polarisation), even small surface roughness can greatly enhance the absorptivity. It can be added that this kind of influence of surface roughness on the absorptivity was theoretically investigated using a ray tracing analysis in [Bergström 2008].

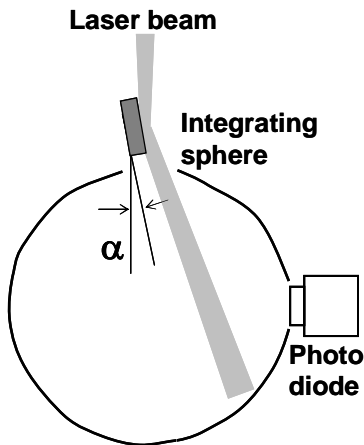


Figure A1-1 Experimental setup.

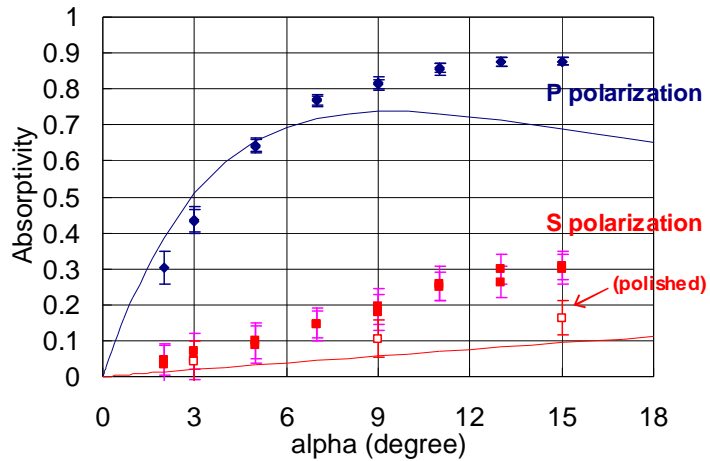


Figure A1-2 Angular dependence of absorptivity.

A1.2. Temperature dependence of absorptivity

In the second experiment influence of temperature dependence of the absorptivity was investigated. The details of this experiment, which is described in the next section Annex 2, can be summarised as follows. A sample of pure iron was placed under an integrating sphere, which collected the reflected light from the sample surface. The incidence angle ϕ_α of the laser beam was about 5 degrees ($\alpha = 85$ degrees). The time evolution of the absorptivity was measured during a single pulse irradiation by a disc laser beam. In another experiment with the same laser irradiation condition, the surface temperature of the irradiated spot was measured as a function of time by pyrometry using a high speed video camera. Combining these two results, the temperature dependence of the absorptivity could be estimated. The result shows that the absorptivity for pure iron is almost constant up to the boiling point T_v . The previous studies have shown that the absorptivity of steel for $1 \mu\text{m}$ does not change so much up to $1400 \text{ }^\circ\text{C}$ [Dausinger 1993] and to 2650 K [Kraus 1986]. The result in this work demonstrated for the first time that this extrapolation is valid up to T_v .

A1.3. Absorptivity on kerf front during laser cutting

Next the absorptivity in real cutting process was evaluated experimentally to confirm that the absorptivity can certainly be estimated from the Fresnel absorption law. To obtain the absorptivity during the cutting process, we collected power transmitted through a kerf with an integrating sphere using the setup shown in figure A1-3(a). The transmitted power is composed of two components: the power reflected on the kerf front and transmitted downwards to the sphere, and the power directly transmitted without any interaction with the kerf front. The measurement of the surface area of the kerf front that intercepts the laser beam allowed us to distinguish the two components and thus to estimate the absorptivity on the kerf front.

The absorptivity A was calculated from an equation

$$A = \frac{1-t}{s} \quad (\text{A1-1}),$$

where t is the measured transmittance through the kerf (transmitted power / input laser power), and s is the ratio of the overlapped region of the kerf front and the laser beam to the laser beam surface area. The latter was obtained from observation with a high speed video camera which was set coaxially with the laser beam (figure A1-3 (b)).

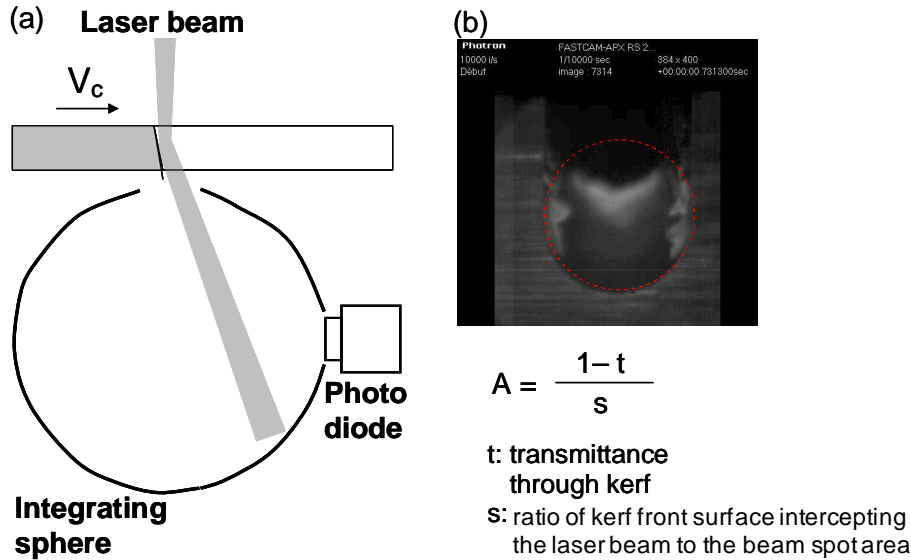


Figure A1-3 Experimental setup (a) and an example of coaxial observation with a high speed video camera (b).

Table A1-1 Parameters of laser cutting

Laser	Disc laser (Trumpf, TruDisc10002)
Laser power	8 kW (CW)
Polarisation	Random
Beam diameter	1.7 mm and 0.56 mm
Assist gas	Nitrogen
Sample thickness (material)	3 mm (low carbon steel) 12 mm (S355)

Operating parameters used in the experiment are summarised in Table A1-1.

Let us describe the experimental results. Figure A1-4 and A1-5 show transmitted power ratio for the beam diameters of 1.7 mm and 0.56 mm, respectively. Absorptivities were calculated from eq.(A1-1) using this data of transmitted power and the surface area intercepting the laser beam. The results are shown in Figure A1-6 and A1-7 for the diameters 1.7 mm and 0.56 mm, respectively.

Although the results are displayed for a large cutting velocity range, the following conditions limit the velocity range where absorptivity on the kerf can be properly estimated.

- (i) There must be no hump on kerf front (If there are humps, some portion of the laser power is reflected to the above from shelves.)
- (ii) Ratio of the beam area intercepted by the kerf front to the entire beam spot area must be smaller than 1. (If not, multi-reflections will occur.)

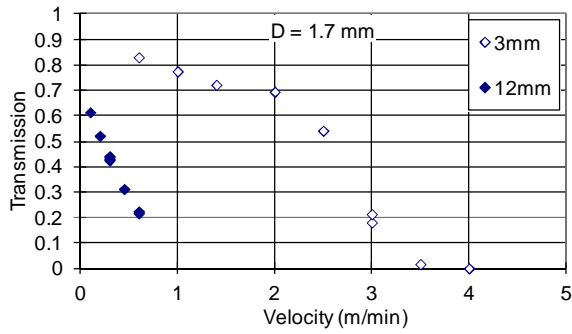


Figure A1-4 Transmission for $d_f = 1.7$ mm.

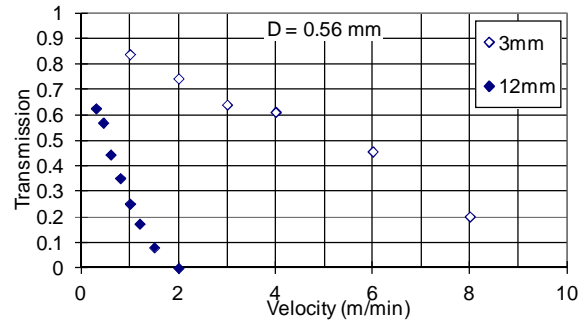


Figure A1-5 Transmission for $d_f = 0.56$ mm.

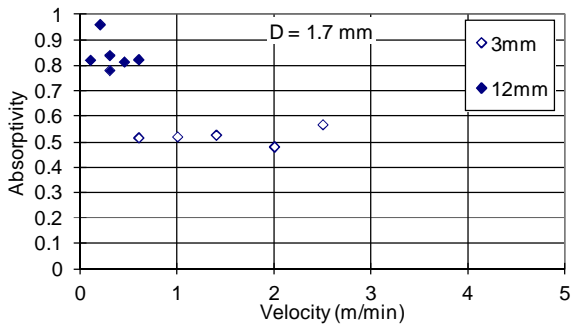


Figure A1-6 Absorptivity for $d_f = 1.7$ mm.

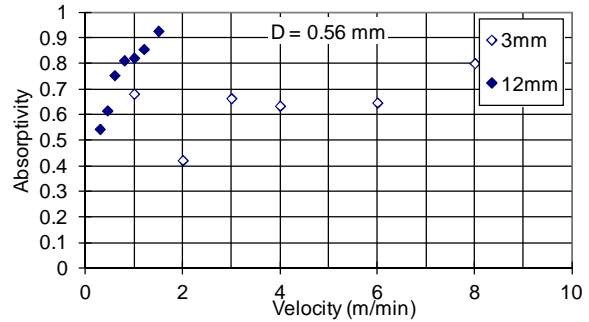


Figure A1-7 Absorptivity for $d_f = 0.56$ mm.

Table A1-2 Velocity ranges without humps (i) and without multi-reflection (ii).

	$d_f = 1.7$ mm		$d_f = 0.56$ mm	
	$h = 3$ mm	$h = 12$ mm	$h = 3$ mm	$h = 12$ mm
(i)	$V_c > 2$ m/min	$V_c > 2$ m/min	$V_c > 4$ m/min	$V_c > 4$ m/min
(ii)	$V_c < 3$ m/min	$V_c < 0.6$ m/min	$V_c < 8$ m/min	$V_c < 1.5$ m/min
(i) & (ii)	$2 < V_c < 3$	---	$4 < V_c < 8$	---

The velocity ranges where the above conditions (i) and (ii) are satisfied are shown in the row “(i)&(ii)” in Table A1-2. We have only the following two points that are considered to be reliable.

(a) $V_c = 2.5$ m/min for $d_f = 1.7$ mm and $h = 3$ mm

The obtained absorptivity A is 54%. Averaged inclination angle α of the kerf front is estimated to be 25 – 30 degrees. The obtained value is slightly higher than theoretical value.

(b) $V_c = 6$ m/min for $d_f = 0.56$ mm and $h = 3$ mm.

In this case, $A = 65\%$. The angle α of the inclination angle of the kerf front estimated from the coaxial camera image is about 10 degrees, very close to the Brewster angle. This may be a reason why the absorptivity is higher than the above case (a).

A1.4. Summary

To verify the applicability of the Fresnel formula to laser cutting process, several experimental measurements of absorptivity were conducted with a 1 μ m disc laser beam.

The first experiment was carried out to investigate the angular dependence of the absorptivity for a high incidence angle. The absorptivity on pure iron was experimentally measured for the p and s

polarisations. The obtained results show reasonable agreement with the theory. As the inclination angle α of a sample sheet increases, absorptivities for both the p and s polarisations increase. The absorptivity for the p-polarisation is higher than that for the s-polarisation.

Then temperature dependence of the absorptivity was investigated. The variation of the absorptivity during a single laser pulse irradiation was measured. For the same laser condition, fast evolution of the surface temperature on the irradiated spot was measured using a 2D camera-based pyrometry method with a high speed video camera. In this way, temperature dependence of the absorptivity was obtained. It was shown that the absorptivity of pure iron is nearly constant up to the evaporation temperature T_v .

The results of the above two experiments confirm the applicability of the theoretical Fresnel absorption law for an inclined surface with high temperature. That is, it is reasonable to extend the absorption law to a region of low α using the complex refractive indices n and k that are obtained by an experiment with a high α near 90 degrees. Also, the influence of the temperature change should be negligible.

Then the absorptivity in real laser cutting process was evaluated from experimental measurement of power transmitted through a kerf during the cutting process. The surface area of the kerf front under the beam irradiation was also measured, which allowed us to distinguish the two components of the power reflected on the kerf front and the power directly transmitted through the kerf. The obtained absorptivity was about 60%. Although the value is slightly higher than the value predicted from the Fresnel absorption law, we conclude that the Fresnel absorption law is a good approximation to estimate the absorptivity in inert gas laser cutting of steel. This law is thus assumed in theoretical analyses in this study.

Unfortunately, the evaluation of the absorptivity was limited in a small velocity range in the experiment in A1-3, since humps that appear on a kerf front reflect a portion of laser power to the above and prevent the accurate evaluation of the transmitted power. It will be interesting to measure this reflected power by setting another integrating sphere over the sample. This experiment will not only enable the evaluation of the absorptivity in the regime of humps but also a better understanding of energy coupling in this regime.

Annex 2. Study on recoil pressure

Résumé

La pression de recul issue de l'évaporation d'une surface irradiée par un laser est le principal moteur de mise en mouvement du métal fondu dans ces conditions pour une gamme d'intensités laser incidentes allant de 10^{-1} à 10^2 MW/cm². Il est donc essentiel d'estimer cette pression de recul afin de décrire convenablement des processus physiques en jeu, ou même d'effectuer des simulations numériques. Cependant, il n'existe aucune évaluation quantitative de la pression de recul pour des températures proches de la température d'ébullition (T_v), températures caractéristiques du procédé de soudage laser. Une des conséquences directe du manque d'information sur la dépendance de la pression de recul avec la température, concerne la relative indétermination de la température seuil nécessaire pour réaliser le soudage laser en régime de formation d'un capillaire (ou encore « keyhole »). Plusieurs études ont supposé que la température de surface de capillaire était égale à T_v , impliquant que c'est la température minimale pour déclencher le régime de soudage en présence d'un capillaire. Cependant, les travaux bien connus de Semak et Matsunawa [Semak 1997] décrivant le modèle dit du « piston », montrent que cette hypothèse n'était pas nécessaire. Ils affirment que le capillaire (« keyhole ») peut être obtenu pour une température bien inférieure à T_v , en fait, dès que la température est supérieure à la température de fusion T_m . Comme le montre cet exemple, une description appropriée de la dépendance avec la température superficielle de la pression de recul s'avère nécessaire. C'est donc l'objet de ce chapitre que d'étudier la pression de recul du fer pour une température proche de sa température d'ébullition T_v , sous une irradiation laser effectuée à la pression atmosphérique.

Tout d'abord, la formulation théorique de la pression appliquée à une surface de liquide est proposée et examinée. La pression résulte de deux pressions partielles : les pressions exercées par les vapeurs métalliques induite et par le gaz ambiant. La pression des vapeurs métalliques résulte en fait de la contribution du processus de vaporisation de la surface et du processus de condensation de la vapeur métallique située au-dessus de la surface. La pression de ces vapeurs métalliques est exprimée par une relation modifiée de type Clausius-Clapeyron. Le taux de condensation peut être théoriquement estimé dans le cas de l'évaporation sous vide ; par contre, à la pression atmosphérique ambiante, la dépendance de ce taux de condensation avec la température, pour une température proche de T_v n'est pas disponible. Il est donc difficile d'estimer la pression partielle de ces vapeurs métalliques. Pour ces mêmes conditions, à la pression atmosphérique, la dépendance de la pression partielle du gaz ambiant avec la température à la surface du liquide n'est pas connue. En raison de la difficulté d'une description de ces processus et du manque de données sur le taux de condensation des vapeurs métalliques et sur la pression partielle du gaz ambiant, il est donc impossible d'estimer théoriquement la dépendance de la pression totale appliquée à la surface avec la température; des études expérimentales sont donc nécessaires pour déterminer ces seuils.

Nos expériences ont eu pour objet de déterminer le seuil de température produisant une déformation de la surface du liquide. La déformation et la température de surface ont été mesurées pour deux configurations différentes avec les mêmes conditions d'irradiation laser (la puissance laser : 2 kilowatts, un diamètre de tache focale : 1,6 millimètres, durée d'impulsion : 80 ms). L'initiation de la déformation de la surface été observée 17 ms après le début de l'irradiation. Une technique de cartographie 2D par pyrométrie optique utilisant une caméra rapide a été utilisée pour la première fois afin d'étudier l'évolution rapide du profil de température de la surface de liquide, jusqu'au régime d'évaporation. Le rayonnement thermique émis par la surface chauffée a été analysé par la caméra rapide et a nécessité la détermination préalable de l'émissivité de la surface (obtenue dans une autre expérience). On a ainsi observé qu'à l'instant $t = 17$ ms, correspondant au début de la déformation de la surface, sa température était de 3250 K +/- 100 K, qui est donc juste au-dessus de T_v . Pour ces conditions expérimentales, la surface atteint un état un régime quasi-stationnaire entre 60 ms et 80 ms. Durant cette période, en mesurant la déformation de la surface, la différence entre la pression de recul appliquée au centre de la surface du liquide et la pression ambiante a été estimée à $\Delta P \approx 3 \pm 2 \times 10^3$ Pa et la température mesurée au centre de la surface était 3270 K +/- 100 K.

Le taux de condensation β des vapeurs métalliques, qui a été déterminé par la mesure de la masse perdue par l'échantillon, a été estimé à 0.9, sur période de $t = 60$ ms à 80 ms. Cette valeur élevée de β suggère l'interprétation suivante du rôle de la pression atmosphérique ambiante sur la surface : pour ces températures de surface proches de T_v , à la pression ambiante, le gaz ambiant ne contribue pas à la pression totale exercée sur la surface, mais joue un rôle de confinement des vapeurs métalliques en augmentant le taux de condensation de ces vapeurs métalliques.

La détermination du seuil de température pour initier la déformation de la surface d'un liquide sous irradiation laser aboutit à des conclusions intéressantes pour la compréhension des mécanismes physiques en jeu et à des conséquences pratiques dans leur description en particulier numériques. Elle fournit en tout cas les premières preuves expérimentales que la température de la surface d'un capillaire au cours du soudage laser en régime de pénétration profonde doit être au moins égale à T_v .

Pour ce qui concerne la découpe laser, ces résultats impliquent que le processus d'éjection latérale du liquide doit être négligeable tant que la température T_s de surface est inférieure à T_v . Une étude expérimentale récente sur la distribution de la température sur le front avant de la saignée [Onuseit 2011] indique que T_s atteint T_v pour des vitesses de découpe relativement élevées, proches de la vitesse limite du procédé, et dans une région située dans la partie basse de la saignée. On peut donc conclure que l'éjection latérale par la pression de recul est tout à fait négligeable pour des conditions de découpe optimisées. C'est un résultat important car dans certains modèles analytiques de découpe laser, la pression de recul a été prise en considération comme mécanisme contrôlant l'éjection latérale de liquide sur le front avant de la saignée, du centre vers les côtés. L'absence de l'éjection latérale suggère donc que le gaz d'assistance est le seul mécanisme d'éjection de liquide de la saignée. Ceci a été confirmé par nos observations décrites au chapitre 4, qui montrent que le liquide s'écoule vers le bas avec pratiquement aucune composante de vitesse latérale, excepté pour une gamme de vitesses de découpe élevées où T_s est probablement proche de T_v .

Bien évidemment l'éjection latérale induite par la pression de recul peut devenir importante lorsque T_s est plus élevée que T_v . Par exemple, dans la découpe à distance de laser de l'acier, où le gaz assistant n'est pas utilisé, T_s doit être élevée et l'éjection par la pression de recul doit être alors le mécanisme principal de l'éjection de liquide de la saignée.

Enfin, l'analyse de la dépendance de la pression de recul avec la température, décrite dans ce chapitre devrait permettre de réaliser des simulations numériques plus réalistes.

Introduction

Recoil pressure is the principal driving force of molten metal in laser metal processing in the intensity range of $10^{-1} \sim 10^2$ MW/cm². It is thus essential to estimate the recoil pressure in order to describe physical processes or to carry out numerical simulations. However, there exists no quantitative estimation of the recoil pressure near the boiling temperature (T_v), which is particularly important in welding process.

As discussed in this annex, the pressure is composed of two partial pressures: the pressures exerted by metal atoms and ambient gas, respectively. The pressure from metal atoms consists of two contributions from vaporising atoms and recombining atoms. The pressure from metallic atoms is basically expressed by a modified Clausius-Clapeyron relation. While the recombination rate can be theoretically estimated for the case of processing under vacuum, for a processing under the ambient atmospheric pressure, temperature dependence of the recombination rate for a temperature range around T_v is not available, so that we cannot express the partial pressure of metal atoms. Moreover, in the case of the atmospheric pressure, temperature dependence of the partial pressure of ambient gas on the melt surface is unknown for a surface temperature near T_v . Due to lack of this information on the recombination rate of vaporising metal atoms and the partial pressure of the ambient gas atoms, it is impossible to estimate theoretically the temperature dependence of the total pressure applied on the melt surface. Thus experimental studies are being required to clarify this aspect.

One of the arguments caused by the lack of information on the temperature dependence of the recoil pressure concerns threshold temperature required to perform keyhole laser welding. Not a few studies have assumed that the keyhole surface temperature is equal to T_v , implying that this is the minimal temperature in order to carry out the keyhole welding process. In the well-known paper by Semak and Matsunawa [Semak 1997], however, this assumption was denied. They claimed that the keyhole can be obtained at a temperature well below T_v . As this example shows, a proper description of the temperature dependence of the recoil pressure is necessary.

In this section, we investigate recoil pressure of iron in the temperature range around T_v during laser processing under atmospheric pressure is investigated. The main interest is the experimental determination of the threshold surface temperature for melt surface deformation due to the recoil pressure. For this purpose, camera-based pyrometric temperature measurement is combined with ordinary camera observation of melt surface during single laser pulse irradiation on a pure iron sample. The results provide the first experimental evidence that the surface temperature has to reach T_v to initiate the melt surface deformation.

A2.1. Recoil pressure during laser material processing

A number of laser metal processing such as welding, drilling, grooving utilise the intensity range of $10^{-1} \sim 10^2$ MW/cm², which are easily obtained by multi-kW class fibre, disc, Nd:YAG and CO₂ lasers. In this intensity range, materials are driven or removed in the form of liquid, while the fraction of vaporised material is limited. Understanding of hydrodynamics of molten material is thus essential to consider process efficiency or final quality achieved. Recoil pressure, which is sometimes called evaporation pressure or ablation pressure, is generated as a counter momentum to evaporation from the surface. It is widely accepted that the recoil pressure can be a dominant driving force of the molten material in various laser metal processing [Von Allmen 1987, Semak 1997], even though the evaporation itself contributes little to the mass removal.

It is well known that the recoil pressure exerted on the surface increases with the surface temperature T_s . One may then pose a question: what is the minimum surface temperature to initiate the driving process of molten material? This question is very important, since this temperature determines limit of energy efficiency of various processes. Although there exist a few experimental measurements of the recoil pressure for several metal species [Kuznetsov 1994, Batanov 1973, Apostol 1976, Golovin 1985, Lee 2004], these are limited to the ablation regime with high laser intensity (typically > 1 MW/cm² for iron) well above the threshold of the ejection process. It should be noted also that in these studies, the recoil pressure was determined only as a function of laser intensity and it could not be related to the

surface temperature. Consequently our understanding of the threshold temperature is not at all conclusive. Concerning a deep keyhole welding, for example, not a few studies have assumed that the keyhole surface temperature is equal to T_v [Dowden 1985, Kaplan 1994, Colla 1994, Solana 1997, Zhao 2003, Le Guen 2011], implying that this is the minimal temperature in order to carry out the keyhole welding process. In the well-known paper by Semak and Matsunawa [Semak 1997], however, this assumption was denied. They claimed that the keyhole can be obtained at a temperature well below T_v . This kind of debates is caused by the lack of information on the temperature dependence of recoil pressure, especially in the region near T_v .

As for theoretical description of the recoil pressure, the expressions proposed by Anisimov [Anisimov 1968] and Knight [Knight 1979] have often been used for numerical studies of laser welding, drilling and cutting [Semak 1997, Ki 2002, Pang 2011]. As explained in detail in the next subsection A2.2, an important assumption in their analyses is that the surrounding ambient gas does not touch the evaporating surface and thus does not contribute as a partial pressure to the total pressure at the evaporating surface. In this case, the total pressure is composed uniquely of the recoil pressure of metal evaporation. This assumption should be valid for the temperature range well above the boiling temperature T_v , where strong metal vapour jet emerging from the surface can completely expel the surrounding gas atoms. However, in the temperature range near T_v , where only weak evaporation takes place, the assumption is possibly not appropriate and the contribution of ambient gas may have to be considered to evaluate the total pressure exerted on the evaporating surface. But the problem is that, there exists no theoretical model that can take into account this contribution of the surrounding gas atoms to the total pressure at the surface in the case of laser processing under atmospheric ambient pressure. Experimental studies are thus required to clarify the temperature dependence of the total pressure at the surface.

Basu and DebRoy [Basu 1992] and later He *et al.* [He 2006] examined melt expulsion during laser spot welding of metals both experimentally and numerically. Their results indicated that ejection of spatters is initiated after melt surface temperature exceeds T_v . This hints that the total pressure at the surface becomes large enough to eject the melt layer only in the evaporation regime. The result, however, does not provide us precise information of the temperature dependence of the total pressure near T_v , because it is difficult to correlate the total pressure with the threshold of the spatter ejection. It should also be pointed out that the temperature distribution in their study was given by numerical simulations.

The present study investigates the total pressure exerted on the surface for the surface temperature range near T_v with experimental measurement of the temperature for the first time. Evolutions of surface shape and surface temperature are monitored with a high speed video camera during single impact irradiation on a pure iron sample. Special attention is paid to determination of the threshold temperature at which the surface starts to be deformed due to the pressure. This point should be contrasted with the above-mentioned works [Basu 1992, He 2006], where the melt ejection, which occurs after the deformation, was analysed. Our focus on the small initial melt surface deformation allows us to evaluate the corresponding total pressure more precisely and to determine the threshold temperature for surface deformation in a more fundamental sense. Difficulty of the temperature measurement should be one of the factors that have prevented this kind of fundamental investigation on the pressure at the surface. In this work, thermal radiation detected by the camera is processed using emissivity that is obtained experimentally, as reported in [Kraus 1986]. This accurate determination of emissivity enables us to reduce substantially error in the temperature measurement.

The outline of this section is briefly summarised as follows. In the next subsection A2.2, theoretical aspects of the recoil pressure and the total pressure at the surface are described. The experimental methods of the surface shape and temperature measurements are explained in subsection A2.3, and the results are presented in subsection A2.4. In subsection A2.5 we discuss the consequences of the results on our understandings of physical processes during laser welding and cutting.

A2.2. Theoretical background

It is schematically shown in figure A2-1 how the pressure applied on the surface deforms and ejects the molten material during a single laser pulse irradiation. We call the pressure measured at the laser beam centre the “total pressure” P_{tot} in this analysis. It is called “total”, because in general it is expressed as the sum of two partial pressures:

$$P_{tot} = p_r + p_g \quad (A2-1)$$

where the first contribution p_r comes from the conventional recoil pressure as a counter force of metal evaporation from the surface and the latter p_g is the partial pressure of surrounding gas.

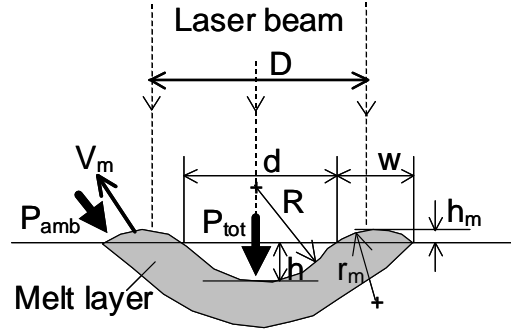


Figure A2-1 Pressure induced deformation of melt layer during irradiation of single laser pulse.

The value that is important to drive the melt is the pressure difference ΔP between P_{tot} at the centre and the pressure at the periphery of the melt layer. The latter can be given by the ambient pressure P_{amb} , because the periphery is normally out of the laser beam and so the evaporation does not occur. Thus

$$\Delta P = P_{tot} - P_{amb} \quad (A2-2)$$

The ambient pressure P_{amb} can vary but is usually the atmospheric pressure (1.01×10^5 Pa).

Using (A2-1) and (A2-2), one obtains

$$\Delta P = p_r + p_g - P_{amb} \quad (A2-3)$$

Please note that p_g is the partial pressure of surrounding gas measured locally at the target surface. Therefore, p_g can be different from P_{amb} and the two pressures do not generally cancel to each other.

The pressure difference ΔP is utilised to counteract the surface tension yielded from a deformation and to eject the material. Let us consider the case of figure A2-1, where the central part is depressed due to ΔP and the melt in the centre is redistributed to the periphery as an extruded rim [Semak 2006]. The curvatures of the melt deformation in the central and rim parts are expressed by R and r_m , respectively. As shown in figure A2-1, R and r_m are defined to be positive when the centres of the curvatures are situated above and below the melt surface, respectively. (In conditions of this study, both R and r_m become positive at any time.) When the melt is ejected from the rim with the velocity V_m , the pressure balance can be written using the Bernoulli equation.

$$\Delta P = \frac{2\sigma}{R} + \frac{\sigma}{r_m} + \frac{\rho_m V_m^2}{2} \quad (A2-4)$$

Please note that the factor 2 in front of (σ/R) comes from the fact that the deformation at the centre consists of the two same curvatures along two orthogonal directions on the sample surface.

In the following, we will examine dependence of p_r and p_g in ΔP (eq.(A2-3)) on the surface temperature T_s .

The recoil pressure p_r is a monotonously increasing function of the surface temperature T_s . Analytic expressions of p_r have been proposed by a number of authors. In a general form, the pressure can be approximated as [Samokhin 1990]

$$p_r = \frac{1 + \beta_R}{2} p_{sat}(T_s) \quad (A2-5)$$

where p_{sat} is the saturated pressure at $T = T_s$. It can be obtained from the well-known Clausius-Clapeyron's relation:

$$p_{sat} = p_0 \exp\left(\frac{\Delta H_v}{k_B T_v} \left(1 - \frac{T_v}{T_s}\right)\right) \quad (A2-6)$$

where T_v is the vaporisation temperature under the pressure p_0 and

$$\Delta H_v = mL_v \quad (A2-7)$$

is the enthalpy of phase transition from liquid to vapour per atom (m : mass per atom, L_v : latent heat of vaporisation, $L_v = 6.1 \times 10^6$ J/kg for iron). The coefficient β_R represents the fraction of re-condensing particles to evaporating ones. By its definition, β_R is related to the mass flow balance. The total mass flux from melt layer to gas phase can be estimated from modified Langmuir expression [Samokhin 1990, Bellot 2001]:

$$\rho_m V_v = (1 - \beta_R) \left(\frac{m}{2\pi k_B T_s}\right)^{1/2} p_{sat}(T_s) \quad (A2-8)$$

Here k_B is the Boltzmann constant. β_R is influenced by gas flow of evaporating particles above the surface. It depends on T_s , P_{amb} , three-dimensional surface profile around the considered surface point, and so on. When $T_s \approx T_v$ it is expected that the evaporation is not so strong and $\beta_R \approx 1$ (so $p_r \approx p_{sat}$). With the increase of T_s , β_R decreases while the upward velocity of metal vapour flow increases until it reaches the sound velocity. In this limit, β_R becomes 0.18 [Anisimov 1968, Knight 1979, Samokhin 1990]. According to eq.(A2-5), $p_r = 0.6p_{sat}$ in this regime. The equations (A2-5) and (A2-8) assume that atoms which recombine to the surface have the same temperature T_s as the evaporating ones. This assumption is valid only in weak evaporation regime where $\beta_R \approx 0$, but comparison with rigorous expressions in [Knight 1979], which take into account temperature decrease of the recombining atoms, shows that the error of p_r caused by the approximate expression (A2-5) is less than 10%, as shown in the following.

The expressions by Samokhin [Samokhin 1990] assume that temperature just out of the Knudsen layer is equal to that on the evaporating surface. We consider influence of this approximation, comparing more rigorous expression by Knight [Knight 1979]. According to eqs.(5) in the paper by Knight, mass and momentum balances can be written as follows.

$$\rho u = (1 - \beta_m) \rho_s \sqrt{\frac{RT_s}{2\pi}} \quad (A2-9),$$

$$\rho(u^2 + RT) = \frac{1 + \beta_p}{2} \rho_s RT_s \quad (A2-10),$$

where

$$\beta_m = -\beta \rho \sqrt{\frac{RT}{2\pi}} \left[\sqrt{\pi} \operatorname{erfc}(m) - e^{-m^2} \right] \quad (A2-11),$$

$$\beta_p = 2\beta \rho RT \left[\left(m^2 + \frac{1}{2} \right) \operatorname{erfc}(m) - \frac{m}{\sqrt{\pi}} e^{-m^2} \right] \quad (A2-12),$$

and

$$m = \sqrt{\frac{\gamma}{2}} M$$

Here γ is the adiabatic exponent and M is the Mach number. The coefficients β_m and β_p are the

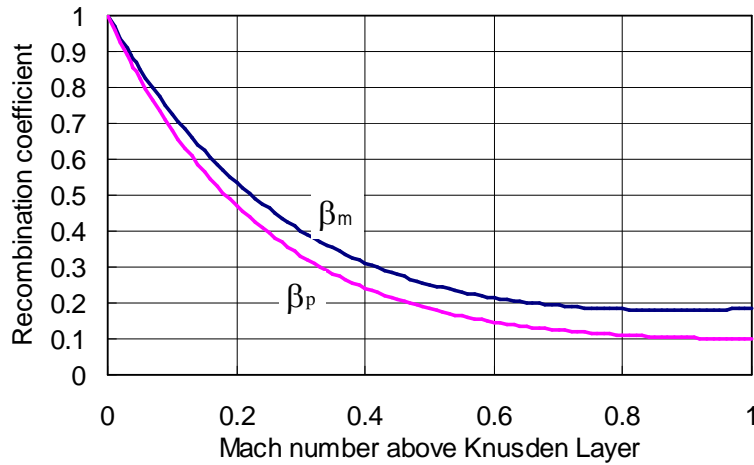


Figure A2-2 Recombination rates as functions of Mach number.

recombination rates defined with respect to the outward flux and the corresponding momentum, respectively. These are expressed as functions of the Mach number, as shown in figure A2-2. Please note that the two coefficients are generally different and the discrepancy increases with the Mach number. Samokhin used an approximation:

$$\beta_p \approx \beta_m \quad (\text{A2-13}).$$

As is evident from figure A2-2, the error induced by this approximation takes maximum at $M = 1$. However, the error is not so important, when one evaluates p_r : at $M = 1$, p_r is expressed as $(0.59 \cdot \rho_s RT_s)$ from Samokhin ($\beta_p = \beta_m = 0.18$) and $(0.55 \cdot \rho_s RT_s)$ from Knight ($\beta_p = 0.1$).

Now let us consider p_g in eq.(A2-3). It is considered that, when evaporation starts, p_g becomes smaller than P_{amb} , because evaporating metal particles reduces the number of surrounding gas atoms that impinge onto the surface. The only exception is processing under vacuum, where $p_g = P_{amb} = 0$ at any T_s . In most cases, where a metal target is placed under atmospheric pressure of 1.01×10^5 Pa, the estimation of ΔP is rather complicated, due to the fact that p_g and P_{amb} do not cancel to each other. This point is important for the following discussions.

The characteristics of p_g and resulting ΔP can be estimated for the two extreme cases of low and high temperatures with respect to T_v . First let us consider the case where T_s is so small that $p_r \approx 0$ (see eqs.(A2-5) and (A2-6)). In this case, there are very few evaporating metal particles. It can thus be assumed that $p_g = P_{amb} = 1.01 \times 10^5$ Pa. From eq.(A2-3) one obtains $\Delta P = p_r \approx 0$, which means that there is no driving force of molten material. On the other hand, if T_s reaches the strong evaporation limit of $\beta_R = 0.18$, the intense metal vapour flow prevents the surrounding gas atoms from reaching the surface. Thus $p_g \approx 0$ and consequently $\Delta P \approx p_r - P_{amb} = 0.6p_{sat} - P_{amb}$. In figure A2-3, ΔP in this limit is shown with the curve a for the case of iron. The problem is that we do not have enough information on ΔP in the intermediate temperature range near T_v , where with the increase of T_s , p_g decreases from P_{amb} to zero and p_r gains from zero depending on the magnitude of the unknown parameter β_R .

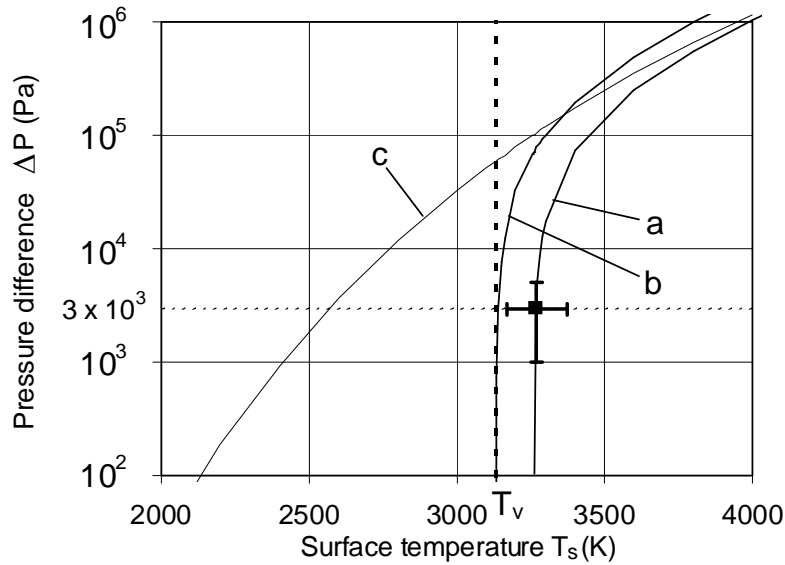


Figure A2-3 Pressure difference ΔP as function of the surface temperature T_s . The two curves a and b show theoretical equations in the case of processing of iron under $P_{amb} = 1.01 \times 10^5$ Pa (a: $\Delta P = 0.6p_{sat}(T_s) - P_{amb}$, b: $\Delta P = p_{sat}(T_s) - P_{amb}$). The curve a corresponds to the asymptotic curve in the limit of low β_R . The curve c shows the theoretical curve under vacuum conditions ($\Delta P = 0.6p_{sat}(T_s)$). The level of $\Delta P = 3 \times 10^3$ Pa corresponds to the minimal pressure difference needed to keep open a keyhole with the diameter of 1 mm. The rectangular dot (■) is the experimental point obtained in this work (see the sections A2.3 to A2.5 for details).

There exists no theoretical model that can predict this variation of ΔP around T_v in the case of processing under ambient pressure. The first analytical model by Anisimov [Anisimov 1968] was limited to the case of vaporisation into vacuum. Knight proposed another model [Knight 1979], which can take into account the existence of ambient gas. It was assumed, however, that ambient gas is completely screened out from the evaporating surface by metal vapour that covers totally the surface, which corresponds to the case of $p_g = 0$. As mentioned above, this assumption should be valid in strong evaporation regime, but its validity is not conclusive for weak evaporation in the vicinity of T_v . The consideration of mixing of the ambient gas and the metal vapour is still a challenging problem even with modern numerical techniques and there are very few works. Bellot and co-workers [Bellot 2001] numerically solved the Boltzmann equation to study the influence of surrounding gas pressure and geometrical scale factor for the evaporation problem of Cr from iron liquid. Unfortunately, the partial pressure of the surrounding gas they used, was limited approximately under 100 Pa. Due to the lack of theoretical model, experiments are indispensable to estimate the pressure ΔP in the temperature region near T_v .

It should be pointed out that little attention has been paid to the contribution of ambient gas on ΔP , which has been proposed as in eq.(A2-3). In a number of papers dealing with recoil pressure during laser material processing, the following type of expressions has been used.

$$\Delta P = p_r \tag{A2-14}$$

This should be a good approximation, when T_s is so high that $p_g = 0$ and $p_r \gg P_{amb}$. However, in order to describe lower temperature regime, such as the regime of a deep penetration keyhole welding, the validity of eq.(A2-14) must be questioned, since it implicitly assumes that $p_g = P_{amb}$. As already mentioned, in the case of processing under atmospheric pressure, p_g must decrease from P_{amb} , when evaporation starts.

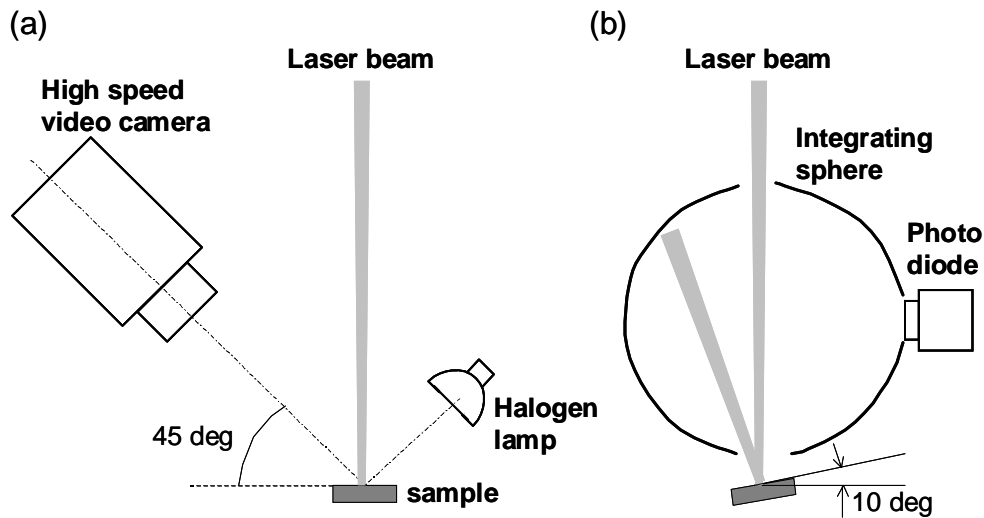


Figure A2-4 Schematics of the experimental setups for the observation of melt surface deformation or the measurement of NIR radiation from the surface (a), and for the absorptivity measurement (b).

A2.3. Methods of experiments

Schematic of the experimental setup is shown in figure A2-4. We investigated evolutions of surface shape and temperature during a single impact irradiation. The position of the laser beam was fixed during each irradiation. A disc laser (Trumpf, TruDisc10002) was utilised as the laser beam source. A non-polarised laser beam with the wavelength λ_L of 1030 nm, which was transmitted through an optical fibre with the core diameter of 600 μm , was imaged on a workpiece with a combination of a collimator lens ($f = 200$ mm) and a focusing lens ($f = 560$ mm). The obtained focus diameter D was 1.6 mm and the focus position was always set at the sample surface. The beam profile at the focus position was analysed with a commercial CMOS camera and the top-hat distribution of the intensity was confirmed. The samples were pure iron (Goodfellow FE000480; purity 99.95%). Their surfaces were polished with sand papers (# 2400) and cleaned with ethanol before the laser irradiation. Argon gas was provided as shielding gas to avoid undesirable oxidation. Different configurations were used to observe the evolutions of surface shape and surface temperature, with the above-mentioned processing conditions fixed.

As for the observation of the surface shape, we illuminated the surface with a halogen lamp and observed a reflected image with a high speed video camera (Photron, FASTCAM/APX-RS). As shown in figure A2-4(a), the angles of the illumination and the observation are set at 45 degrees. The spatial resolution per pixel was 6.0 μm x 8.5 μm . We placed a standard glass filter of the type KG3 in front of the camera lens to block the laser beam reflected from the irradiation spot. Therefore the entire visible spectrum region was utilised. The acquisition rate was set at 20 kHz and the shutter speed was 2 μs .

Two-dimensional distribution of surface temperature was monitored using a camera-based technique, which was reported for example in [Kraus 1986]. Thermal radiation from the surface was detected by a high speed video camera. Based on the Planck's law, the surface temperature was calculated from the measured radiation level and the emissivity that was obtained experimentally.

Thermal radiation level was measured with a CMOS sensor of the above-mentioned high speed video camera. We used the same optical system, observation angle (45 degrees) and acquisition rate as the observation of the surface shape, which allowed us the high spatial resolution (6.0 μm x 8.5 μm) and sampling rate (20 kHz). The differences from the surface shape observation were: we did not use the lamp for illumination; we selected a near infrared (NIR) spectrum band as specified below; and we used an adapted shutter speed (50 μs).

According to the Planck's radiation theory, the grey scale level G measured at a pixel of the CMOS sensor is generally expressed as

$$G = K\varepsilon(\lambda_0, T)B(T) \quad (\text{A2-15})$$

K is a constant, which depends on characteristics of the observation system, for example, numerical aperture of the lens system, transmittance of the thermal radiation from the laser spot to the sensor surface, shutter speed and the sensibility spectrum of the sensor. $\varepsilon(\lambda_0, T)$ is the emissivity of the surface at the central wavelength λ_0 of the spectrum band selected. $B(T)$ represents the temperature dependence of the black body radiation

$$B(T) = \int_{\lambda_0 - \Delta\lambda/2}^{\lambda_0 + \Delta\lambda/2} d\lambda \frac{2hc^2}{\lambda^5} \frac{1}{\exp\left(\frac{hc}{\lambda k_B T}\right) - 1} \quad (\text{A2-16})$$

where $\Delta\lambda$ is the width (FWHM) of the selected band, and h and c are the Planck constant and the speed of light, respectively. $B(T)$ can easily be calculated from eq.(A2-16), so that once the constant K and ε are obtained, the surface temperature T can be determined from the grey scale level G .

The emissivity ε is a function of wavelength and of temperature, which is then a function of time. Based on the Kirchhoff's law, the temporal evolution of ε was estimated from that of the absorptivity A , which was evaluated for the process laser wavelength λ_L (1030 nm), assuming that

$$\varepsilon(\lambda_0, T(t)) \approx A(\lambda_L, T(t)) \quad (\text{A2-17})$$

It can be mentioned here that this correspondence of ε and A has been recently utilised for monitoring of keyhole front profile during laser welding [Weberpals 2010-2]. Considering that ε in (A2-17) depends on the wavelength, it is better to use λ_0 near λ_L and small $\Delta\lambda$ for the NIR radiation observation by the video camera. We selected a spectrum band of $\lambda_0 = 0.9 \mu\text{m}$ and $\Delta\lambda = 0.07 \mu\text{m}$ using a band pass filter.

The setup for the measurement of A is shown in figure A2-4(b). The sample was placed just under an integrating sphere for the measurement. More details of the absorptivity A variation with materials and operating parameters can be found in [Muller 2012]. For the present study, the evolution of A was measured using exactly the same laser power and duration as those of the NIR radiation observation. The incidence angle was set at 10 degrees in order to capture the first reflection from the sample within the sphere. The angle was different from that of the NIR observation (45 degrees), but the influence is negligibly small. According to the theoretical Fresnel formula and the complex refraction index of iron, the difference of ε (or A) between 10 degrees and 45 degrees is very small for a non-polarised beam; less than 1% [Dausinger 1993].

The constant K of this observation system was calibrated at the melting points of Ta (3290 K) and Nb (2750 K) through the same scheme of the evaluations of G and A as the measurement for pure iron. As is deduced from eq.(A2-15), systematic error in a measured temperature can come from errors in K and ε . The error in the determination of K in the calibration processes with Ta and Nb was about $\pm 7\%$ ($= \Delta K/K$). This leads to the error of ± 50 K in T_s if it is evaluated at $T_s \sim T_v$. The experimental measurement of A allowed us to minimise the error of ε within $\pm 3\%$, which corresponds to the error of ± 50 K in T_s . By adding the two contributions, the total error in T_s is estimated to be ± 100 K.

The validity of the method of temperature measurement described above was confirmed by a comparison with temperature measured by a spectroscopic method, where the thermal emission spectrum in the visible range was correlated with the surface temperature based on the Planck's law [Muller 2012].

The present method of temperature measurement applies only to the case where the deformation is so small that one observes only a component of NIR light that is emitted from the surface and directly

transferred to the video camera. When the deformation becomes large, for example, as in the case of a keyhole, reflected component, which is emitted from another point, can be overlapped to the observed light in addition to the direct emission. The method in this study is based on a presumption that there is no such contribution from these reflections. In order to measure temperature also for the case where single or multiple reflections occur, it would be necessary to make the observation of the NIR image with the same angle as the incidence angle of the absorptivity measurement, for example, by installing the camera coaxially to the laser beam axis.

While a laser pulse is irradiated on the sample surface the surface temperature T_s is continuously elevated or stagnated. The surface shape strongly depends on $\Delta P (= P_{\text{tot}} - P_{\text{amb}})$, which is a function of T_s as explained above. Although the evolution of T_s is a dynamic phenomenon, it is considered that P_{tot} is dependent only on the instantaneous value of T_s , independent from any dynamical factor. This assumption is justified because the time needed for equilibrating P_{tot} for each instance is estimated to be as small as the order of 20 μs , if one estimates from (L/v_s) [Kaplan 2002], where L is the characteristic relaxation length of the uprising vapour ($\lesssim 10$ mm) and v_s is the sound velocity (≈ 500 m/s). As shown later, the characteristic time of the evolution of T_s is much longer in our experimental conditions.

Apart from the observations of deformation and temperature, in order to estimate the recombination rate β_R in eqs.(A2-5) and (A2-8), mass loss by evaporation was evaluated by measuring weight of samples before and after irradiation using a commercial balance (METTLER TOLEDO AT261). The precision of each weight measurement was ± 0.02 mg. Using the high speed video camera we confirmed that there was no droplet detached from the surfaces during the laser beam irradiation, which would have caused overestimation of the evaporation rate.

A2.4. Results

A2.4.1 Evolution of melt surface shape

Depending on the level of T_s , and thus on the level of P_{tot} , we can observe the melt pool evolution during the pulse irradiation in three stages: (i) flat, (ii) deformation, and (iii) key-hole. In the following, two typical conditions are shown. One is $P = 2$ kW, $\Delta t = 80$ ms, for which the system stagnates in the stage (ii). In the other condition of $P = 4$ kW, $\Delta t = 25$ ms, the system gets into the final keyhole stage (iii).

The evolution of surface shape observed for $P = 2$ kW and $\Delta t = 80$ ms is shown in figure A2-5(a). Please note that information on surface profile tends to be amplified with the illumination by the halogen lamp. From the observed video images, it was confirmed that melting starts at time $t = 1.7$ ms from the centre of the laser beam spot. The melted region spread with the elapse of time after that. In this first stage the liquid surface stays almost flat but is never stationary. As shown in the image of $t = 7$ ms, ring patterns, such that we observe when a raindrop plunges into water surface, were frequently observed. The detection of this phenomenon was made possible owing to the fast shutter speed of the camera (2 μs).

The second regime sets in at $t = 17$ ms, when one can confirm the initiation of concave deformation in the centre. The diameter d and the depth h of the deformation area gradually increase with time until the end of the pulse. At $t = 60$ ms, the diameter d of the deformed region was 1.1 mm \pm 0.2 mm. The depth h was estimated from small displacement of the centre of the circular deformed region that can be observed due to the inclined angle of visualisation of the high speed video camera (Figure A2-4(a)). Due to the inclination angle of 45° , h can be estimated by the displacement distance d_p of the centre measured in the plane of the sample surface (refer to an example at $t = 80$ ms in figure A2-5(a)). The measured depth h of deformation is shown as a function of time in figure A2-7. The depth h was measured also from the triangular method, where displacement of a centre of a HeNe laser beam spot irradiated from the above with a certain inclination angle was measured. As can be seen from figure A2-7, the two methods give approximately the same values of h . The regression line shows that $h = 80$ μm \pm 20 μm at $t = 60$ ms.

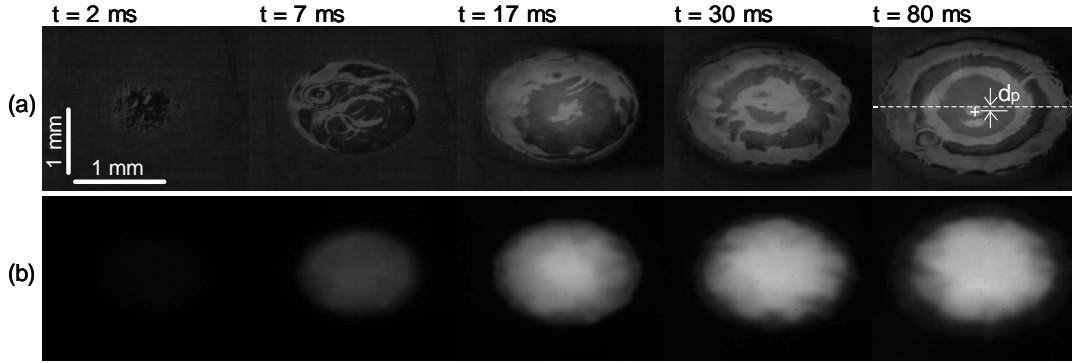


Figure A2-5 Temporal evolutions of surface shape (a) and NIR emission (b) observed with the high speed video camera in the case of $P = 2 \text{ kW}$ and $\Delta t = 80 \text{ ms}$. In the image at $t = 80 \text{ ms}$ of (a), it is observed that the centre of the circular deformed region (cross mark) is displaced by d_p from the initial level of the central line on the surface (dotted line). This value was used to estimate the depression depth h at the centre ($h \approx d_p$).

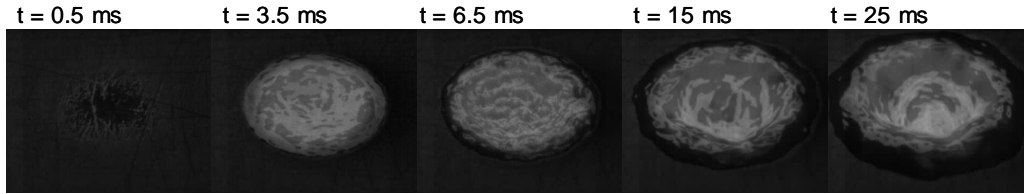


Figure A2-6 Temporal evolution of surface shape for $P = 4 \text{ kW}$ and $\Delta t = 25 \text{ ms}$. The scale of the images is the same as figure A2-5.

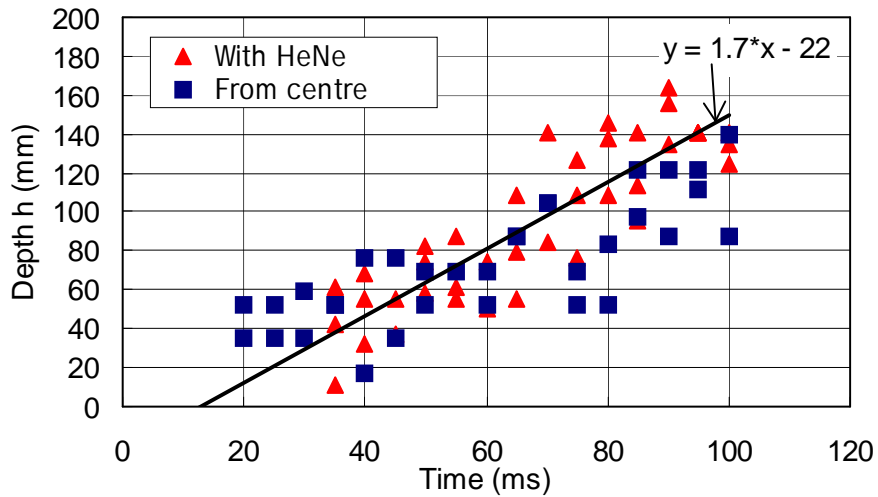


Figure A2-7 Results of measurements of the deformation depth h at the centre.

Let us estimate the pressure difference ΔP from the values d and h measured at $t = 60 \text{ ms}$. Using eq.(A2-4) with the ejection velocity $V_m = 0$, the pressure difference ΔP is estimated from the following equation

$$\Delta P \approx \frac{2\sigma}{R} + \frac{\sigma}{r_m} \quad (\text{A2-18})$$

The curvature R of the liquid surface at the bottom can be estimated from the geometrical formula $R = ((d/2)^2 + h^2)/2h$, which gives $R = 2 \pm 1$ mm. In order to estimate the curvature r_m of the rim, we assume that the rim extruded above the sample surface is represented by a part of a torus which is cut at the sample surface, as in [Semak 2006]. This extruded volume should be provided from the depressed volume in the central part. This volume balance can be approximated as

$$\frac{1}{3}\pi\left(\frac{d}{2}\right)^2 h \approx \left(\frac{1}{2}wh_m\right) \times 2\pi\left(\frac{d}{2} + \frac{w}{2}\right) \quad (\text{A2-19})$$

The width w is measured to be 0.5 ± 0.1 mm from the image at $t = 60$ ms. Substituting this value to eq.(A2-19), one obtains $h_m \approx 0.02 \pm 0.01$ mm. Then r_m is estimated to be 1.5 ± 1 mm from the geometrical formula $r_m = ((w/2)^2 + h_m^2)/2h_m$. Using $\sigma \approx 1.5$ Pa·m, we finally obtain $\Delta P \approx 3 \pm 2 \times 10^3$ Pa. (We neglect temperature dependence of σ .)

Images observed with $P = 4$ kW and $\Delta t = 25$ ms are shown in figure A2-6. Melting starts at $t = 0.4$ ms, and the second deformation stage begins at $t \approx 4$ ms. The concaved surface is modulated with small wavy structure as one can confirm in the image of $t = 6.5$ ms. Unlike the case of $P = 2$ kW, the evolution of the surface profile is not stationary, and finally at $t \approx 15$ ms, a keyhole is produced.

A2.4.2 Evolution of melt surface temperature

Because the method of temperature measurement cannot be applied to the case of strong deformation, we present only the result for the condition of $P = 2$ kW and $\Delta t = 80$ ms. Observed NIR images are shown in figure A2-5(b). Results of the absorption measurement and the calculated surface temperature T_s are plotted in figure A2-8 as a function of time. The grey scale level G was evaluated as an average in a small circle at the beam centre with the diameter of 0.2 mm. Variation of the temperature within the circle was typically ± 10 K. Considering that this variation can generally be caused by real temperature variation and/or noise of each pixel, it can be said that the value (± 10 K) defines the maximal value of the temperature variation.

As shown in figure A2-8, the temperature T_s in the central region increases and reaches $T_s = 3250$ K at $t = 17$ ms and stagnates after that at about $T_s = 3270$ K. This characteristic rising time of T_s can be explained by the following 1D analytical solution of heat conduction problem for surface heating of a semi-infinite body with constant intensity [Carslaw 1959]. The temperature increase at the centre on the surface is given by

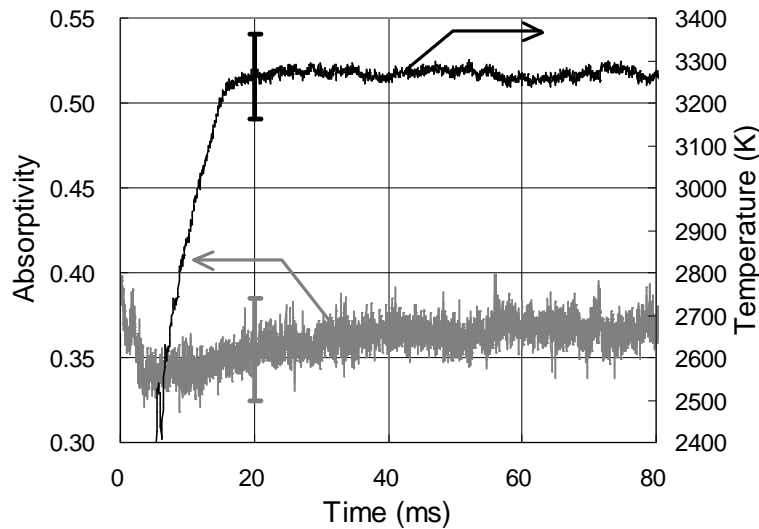


Figure A2-8 Results of measurements of absorptivity and surface temperature in the case of $P = 2$ kW and $\Delta t = 80$ ms.

$$T_s - T_a = \frac{2AI_L}{K} \sqrt{\frac{\kappa t}{\pi}} \quad (\text{A2-20})$$

where I_L is the incident laser intensity (0.1 MW/cm^2), K is the heat conductivity ($80 \text{ W/m}\cdot\text{K}$), κ is the thermal diffusivity ($2 \times 10^{-5} \text{ m}^2/\text{s}$), and T_a is the ambient temperature (300 K). This 1D equation neglects three-dimensional thermal diffusion, which is estimated to start at $\tau \sim 10 \text{ ms}$ based on the relation $2(\kappa\tau)^{1/2} \approx (D/2)$. We neglect the latent heats of melting and evaporation in this discussion. The assumption of no evaporation is justified, since it was experimentally confirmed that evaporated mass is negligibly small until $t = 17 \text{ ms}$, as is shown later. Using the experimentally obtained absorptivity ($A \approx 0.35$), the rising time to $T_s = 3250 \text{ K}$ is estimated to be 17 ms , which shows a good agreement with the experiment in spite of the approximations.

The observation of surface shape showed that the surface deformation starts at $t = 17 \text{ ms}$. Thus the threshold surface temperature for the melt surface deformation is determined to be $3250 \text{ K} \pm 100 \text{ K}$. It can be concluded that the surface deformation starts just above T_v (3134 K).

Whereas T_s at the centre stagnates, the 2D temperature field continues to evolve even after $t = 17 \text{ ms}$. Further analysis showed that the region with the maximum temperature ($= 3270 \text{ K}$) slightly spreads with time until $t \approx 60 \text{ ms}$. The diameter of this region stays constant at about 0.5 mm for $t = 60 \sim 80 \text{ ms}$. The temperature distribution was quasi-stationary during this period.

A2.4.3 Evaporation rate

Mass loss by evaporation measured for the case of $P = 2 \text{ kW}$ and $\Delta t = 80 \text{ ms}$ is shown in figure A2-9. Comparison with the evolution of T_s suggests that the mass loss by the evaporation only starts after T_s surpasses T_v . The mass loss rises roughly proportionally to the pulse duration after this moment. The mass evaporation rate in the quasi-stationary regime ($t = 60 \sim 80 \text{ ms}$) can be determined as $\dot{m} = 1.4 \times 10^{-5} \text{ kg/s}$ from the gradient of the plots. Based on the modified Langmuir eq.(A2-8), the recombination rate β_R was calculated from the following relation

$$\beta_R = 1 - \frac{\dot{m}}{\int \left(\frac{m}{2\pi k_B T_s} \right)^{1/2} p_{\text{sat}}(T_s) dS} \quad (\text{A2-21})$$

with the expression of p_{sat} taken from eq.(A2-6) and the integrated area defined by the beam diameter.

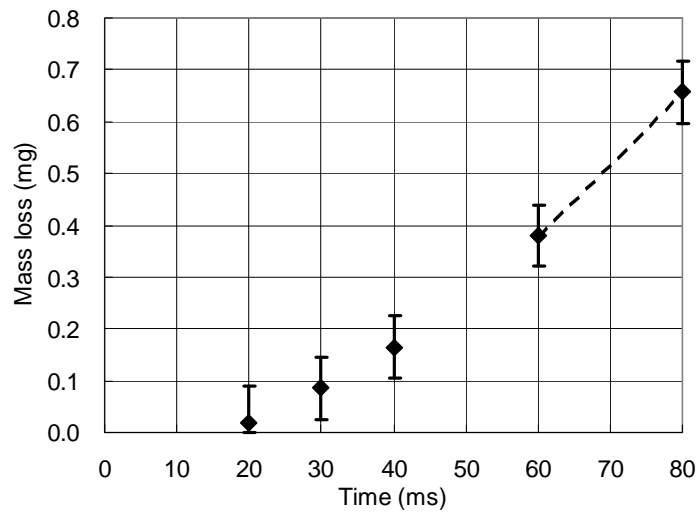


Figure A2-9 Results of measurement of evaporated mass in the case of $P = 2 \text{ kW}$ and $\Delta t = 80 \text{ ms}$.

For T_s , the temperature distribution at $t = 60$ ms was used. The obtained recombination rate β_R was 0.9.

Now let us discuss about the stagnation of T_s at the centre observed after $t = 17$ ms. It is considered that the stagnation of T_s at the centre is caused by increase of three-dimensional thermal diffusion and reduction of heat flux into the sample due to evaporation heat loss. If we consider surface heating of a semi-infinite body with a circular beam that has the intensity I_{abs} and the diameter D , the analytical solution predicts that the temperature increase at the centre stagnates at $(I_{abs}D/2K)$ because of the heat conduction. Taking also into account the reduction of the incoming energy flux due to evaporation loss, the temperature increase in the stationary regime is estimated from

$$T_s - T_a = \frac{2(AP_L - \dot{m}L_v)}{\pi DK} \quad (A2-22)$$

This equation gives $T_s = 3.5 \times 10^3$ K, which is close to the stagnation level observed experimentally.

A2.5. Discussion

A2.5.1 Temperature dependence of ΔP

As explained above, the pressure difference ΔP at $t = 60$ ms is estimated to be $\Delta P \approx 3 \pm 2 \times 10^3$ Pa, from the result of the surface shape observation. The measurement of surface temperature shows that T_s is quasi stationary at 3270 K around $t = 60$ ms. These results add an experimental point in figure A2-3, which shows the dependence of ΔP on T_s for the case of processing under $P_{amb} = 1.01 \times 10^5$ Pa. The important conclusion is that the melt surface deformation or the melt ejection due to the recoil pressure is obtained only above T_v , where ΔP becomes large enough. This finding allows us to understand better physical processes during laser welding and cutting, as discussed below in subsections A2.5.2 and A2.5.3.

The recombination rate determined from the mass loss measurement ($\beta_R = 0.9$) may seem to be high, but similar results can be found in the past works. Mundra and DebRoy [Mundra 1993] measured mass evaporation rate during conduction mode laser welding of stainless steel. It was reported that the evaporation rate of iron was only 15% of the value predicted from the Langmuir equation at $T_s \approx 3200$ K, which is about the same as the temperature in our case (3270 K), although their temperature was not measured experimentally but estimated from a numerical simulation. The rate β_R in their work was 0.85, which is very close to our result. As for numerical investigations of β_R , Bellot *et al.* [Bellot 2001] studied the dependence of β_R on ambient Ar pressure for evaporation of Cr from liquid iron surface in near vacuum condition. It was shown that, when the Ar pressure becomes comparable to the saturated pressure of Cr, β_R for Cr evaporation rises up and approaches 1. These previous results support the rather high value of β_R obtained in this study.

It must be mentioned, however, that the experimentally obtained ΔP and β_R at $T_s = 3270$ K are not completely consistent with the theoretical prediction. Indeed, using $\beta_R = 0.9$ obtained at $T_s = 3270$ K, p_r is calculated to be 1.6×10^5 Pa from eq.(A2-5). Considering that $P_{amb} = 1.0 \times 10^5$ Pa and $p_g \geq 0$, the right hand side of eq.(A2-3) is equal to or larger than 6×10^4 Pa, which is larger than $\Delta P (= 3 \times 10^3$ Pa). The errors in the experimental measurements of T_s and \dot{m} might have caused this inconsistency. Nevertheless, the fact that the term $(p_r - P_{amb})$ in the right hand side of eq.(A2-3) is already larger than ΔP suggests that $p_g \approx 0$. This means that the shielding Ar atoms are expelled from the surface of the beam spot already at $T_s = 3270$ K. This indicates that the effect of the ambient atmospheric pressure at $T_s \sim T_v$ is not the direct contribution as the partial pressure to the total pressure at the surface, but the confinement of metal vapours, which results in the high value of $\beta_R (= 0.9)$ compared with the vacuum case ($\beta_R = 0.18$).

Now let us discuss about the expression of ΔP as a function of T_s . Assuming that $\beta_R = 0.9$ and $p_g = 0$, the pressure difference ΔP in the range of $T_s \sim T_v$ may be expressed as $(0.95p_{sat}(T_s) - P_{amb})$, which is very close to the curve b $(p_{sat}(T_s) - P_{amb})$ in figure A2-3. As already mentioned in subsection A2.2, when T_s increases from T_v , it is predicted that β_R decreases down to 0.18 and correspondingly ΔP

approaches $(0.6p_{\text{sat}}(T_s) - P_{\text{amb}})$, which is shown with the curve a in figure A2-3. Further investigation on the dependence of β_R on T_s is out of the scope of this work, it may be worthwhile to mention that the asymptotic convergence at high temperature depends more or less on geometry around the considered surface point. Aden *et al.* [Aden 1992, Aden 1990] theoretically analysed metal vapour expansion dynamics in 3D geometry. It was shown that with the increase of the laser intensity and that of T_s , β_R approaches ~ 0.2 . It was also revealed that, when the beam diameter becomes larger, β_R reaches this limit at higher laser intensity and that this delay is most pronounced at the extreme of 1D case. Similar effect of evaporating surface size on the magnitude of β_R was also reported in [Bellot 2001]. It was shown that, when the area of the evaporating surface becomes small, one needs higher ambient pressure of Ar to restrict the evaporating mass of Cr, that is, to keep β_R at a high level. Apart from this surface size effect, we point out that the global geometry can also influence β_R . For example, in the case of a deep keyhole welding, it is considered that β_R effectively increases, since metal atoms vaporised from a keyhole wall can be absorbed again to the other side of the wall surface. As a result, ΔP will reach the strong evaporation limit of $(0.6p_{\text{sat}}(T_s) - P_{\text{amb}})$ at higher T_s compared with an open geometry.

As for practical interests such as boundary conditions of pressure for numerical simulations of melt pool dynamics driven by the recoil pressure, the variation of β_R from 1 to 0.18 with increase of T_s is possibly not so important, because the temperature difference between the curves a and b for a certain ΔP level is only ~ 100 K, as shown in figure A2-3. Therefore, it can be sufficient to use the curve a $(0.6p_{\text{sat}}(T_s) - P_{\text{amb}})$ with extrapolation down to $T_s \sim T_v$, if one accepts the corresponding error. The measured point ($\Delta P = 3 \times 10^3$ Pa at $T_s = 3270$ K), which lies near the curve a, supports the validity of this approximation. It should be emphasised that, in order to conduct accurate simulations, what is much more important than the variation of β_R is to really take into account the ambient atmospheric pressure P_{amb} , as discussed below.

A2.5.2 Welding

The present result allows us to correct our common understandings on some processes in which T_s becomes comparable to T_v . First let us discuss consequence on a deep penetration keyhole welding. The minimum pressure difference ΔP to carry out a keyhole welding can be estimated from the following relation.

$$\Delta P \approx \frac{2\sigma}{d_k} + \frac{\rho_m V_m^2}{2} \quad (\text{A2-23})$$

where d_k is the diameter of the keyhole. For example, if we take $d_k = 1$ mm and consider the limit of low velocity ($V_m \approx 0$), $\Delta P = 3 \times 10^3$ Pa. According to figure A2-3, it is predicted that T_s must be at least in the order of T_v to keep this keyhole open. In theoretical analyses of a deep penetration keyhole welding, it has often been assumed that the temperature T_s of the keyhole surface is equal to T_v . The present result provides the first experimental support to this assumption.

We have to point out, however, that this assumption has been sometimes doubted in the past. For example, Semak and Matsunawa [Semak 1997] denied this assumption and claimed that the recoil pressure can trigger lateral ejection at a lower temperature even near the melting temperature. Using the Bernoulli type equation (the equation number (10) in [Semak 1997])

$$p_r = \frac{\rho_m V_m^2}{2} \quad (\text{A2-24})$$

they claimed that a meaningful ejection velocity can be obtained even for $T_s < T_v$. As already discussed in subsection A2-2, the equation (A2-24) is based on the implicit assumption that $p_g = P_{\text{amb}}$. This assumption is not correct according to the present result which suggests that $p_g \approx 0$ at the threshold temperature for melt surface deformation.

It is predicted that the threshold temperature for keyhole welding strongly depends on the ambient pressure. In figure A2-3, we plot $\Delta P = p_r$ for the extreme case of processing under vacuum, assuming

that $\beta_R = 0.18$ (the curve c in figure A2-3). ΔP can take non-zero value even when $T_s < T_v$. For example, the above-discussed deep keyhole welding with the diameter of 1 mm, which requires $\Delta P = 3 \times 10^3$ Pa, will be realised at $T_s \approx 2600$ K. This decrease of the process temperature must be one of the reasons why the penetration depth achieved in a deep penetration welding under vacuum is larger than the case under the atmospheric pressure for the same laser condition [Katayama 2001, Mueller 2010].

The same discussion applies also to boundary condition of pressure in numerical simulations of a keyhole welding process, which have already been reported by several groups [Ki 2002, Pang 2011, Geiger 2009]. The result of our study highlights the importance of imposing the ambient atmospheric pressure P_{amb} to non-evaporating surfaces, although this boundary condition was not clearly described in these papers. If one omits P_{amb} for the non-evaporating surfaces, the calculation will represent the case of welding under vacuum, and it will predict that surface temperature threshold for keyhole regime can be lower than T_v .

Moreover, a striking difference in time-dependent fluctuations of a keyhole is expected by the difference in the temperature dependence of P_{tot} between atmospheric pressure and vacuum. A small fluctuation of keyhole surface profile can trigger a local change of surface temperature. Then local total pressure applied on the keyhole surface is changed. The magnitude of this variation depends on dP_{tot}/dT_s . The change of pressure perturbs melt flow around the keyhole. For example, local high pressure on the keyhole front can generate a strong vapour jet, which can disturb melt flow in a rear part of the keyhole. It is expected that a keyhole is less stable for the case under the atmospheric pressure, as this gradient dP_{tot}/dT_s is larger; the gradient dP_{tot}/dT_s calculated from $0.6p_{sat}(T_s)$ is about 18 times larger at $T_s = 3270$ K than at $T_s = 2600$ K. This means that a keyhole created under the atmospheric pressure is much more vulnerable to a small fluctuation of the system than a keyhole created under vacuum.

A2.5.3 Cutting

We have to correct our understanding also for laser cutting process. In some of the analytical models for laser cutting, the recoil pressure P_{recoil} have been taken into account as an important mechanism of melt ejection in lateral direction from the kerf front to the side region [Petring 1994, Mas 2003-2, Quintero 2005]. It has been shown that the fraction of the lateral ejection can be the same order as that of the longitudinal ejection by downward assist-gas force, even when the surface temperature T_s is well below T_v [Petring 1994, Mas 2003-1]. Our present result shows, however, that the lateral ejection by the recoil pressure cannot occur when $T_s < T_v$. A recent experimental investigation of temperature distribution on the kerf front [Onuseit 2011] indicates that T_s reaches T_v only for relatively high cutting speed near the process limit and this is restricted in a bottom part of the kerf. The absence of lateral ejection suggests that the downward melt flow by assist gas should be the only principal mechanism of melt ejection from the kerf. This was supported by our observation described in chapter 4 that the melt flows downwards with little lateral velocity component except for a high velocity range where T_s is possibly comparable to T_v . In the lowest velocity range, we observed interaction between melt accumulations in the central and side parts of the kerf front. It should be noted, however, that this interaction does not originate from the recoil pressure but from surface tension. Of course, the lateral ejection induced by the recoil pressure can be important when the surface temperature T_s becomes higher than T_v . For instance, in remote laser cutting of steel, where assist-gas is not utilised, the ejection by the recoil pressure should be the principal mechanism of melt removal from kerfs. Also in the case of normal gas assisted cutting, it is reported that the lateral ejection occurs depending on the surface temperature in pulsed laser cutting of ceramics [Quintero 2005].

A2.5.4 Future prospects

Whereas only pure iron samples were utilised in this study, it will be interesting to investigate the recoil pressure using practical materials with impurity elements. It is well acknowledged that volatile elements, which have lower boiling temperature than matrices, can cause process instabilities and defects. Fundamental investigations of the effect of additional elements on the characteristics of the recoil pressure will serve to understand the mechanisms of these problems.

We demonstrated a fast 2D measurement of melt surface temperature up to the range near T_v . This technique can also be applied to real time process monitoring or to development of numerical models, although at the present stage the technique is restricted to relatively flat surface, for example, melt surface around a keyhole. An important finding in this study is that the emissivity is almost independent of T_s up to $\sim T_v$. Consequently, even without measurement of the emissivity, one can estimate T_s with reasonable accuracy from thermal radiation intensity detected by a 2D sensor.

A2.6. Conclusion

In this Annex 2, we studied recoil pressure of iron around its boiling temperature T_v during laser processing under atmospheric pressure. In the experiment, single laser pulse irradiation on iron was investigated with a specific aim to determine the threshold temperature of the melt surface deformation. The surface deformation and the surface temperature were measured with two different configurations for the same laser irradiation conditions (Laser power: 2 kW, spot diameter: 1.6 mm, pulse duration: 80 ms). The initiation of surface deformation was confirmed at 17 ms after the start of the irradiation. The camera-based 2D temperature measurement technique was applied for the first time to investigate the fast evolution of melt surface temperature T_s up to the evaporation regime. The thermal radiation intensity was processed by emissivity obtained from another experiment. The threshold temperature for the surface deformation was determined to be 3250 K \pm 100 K, which is just above T_v . Under the laser condition used in this experiment, the system reached a quasi-stationary state for $t = 60$ ms to 80 ms. In this period, the driving pressure difference between that on the melt surface and the ambient pressure was estimated to be $\Delta P \approx 3 \pm 2 \times 10^3$ Pa. The surface temperature during this period was measured to be 3270 K \pm 100 K.

The recombination rate, which was determined from experimental mass loss measurement, was 0.9 for the above time period from $t = 60$ ms to 80 ms. This high value suggest the following role of ambient atmospheric pressure on the total pressure exerted on the surface. That is, at $T_s \sim T_v$, ambient gas atoms do not contribute to the total pressure at the surface by direct impingement, but they confine metal vapours. This results in the increase of the recombination rate.

The determination of the threshold temperature for melt surface deformation leads to some important conclusions for physical mechanisms in practical laser processing. It provides the first experimental evidence that the temperature on the keyhole surface during deep penetration laser welding must be at least T_v . As for laser cutting, it is suggested that lateral melt ejection process should be negligible as far as T_s does not reach T_v . A recent experimental investigation of temperature distribution on the kerf front [Onuseit 2011] indicates that T_s reaches T_v only for relatively high cutting speed near the process limit and this is restricted in a bottom part of the kerf. It can thus be concluded that one can neglect lateral ejection by recoil pressure for a normal condition. This is an important result, because, in some of the analytical models for laser cutting, the recoil pressure P_{recoil} have been taken into account as an important mechanism of melt ejection in lateral direction from the kerf front to the side region. The absence of lateral ejection suggests that the downward melt flow by assist gas should be the only principal mechanism of melt ejection from the kerf. This was supported by our observation described in chapter 4 that the melt flows downwards with negligible lateral component in the melt velocity except for a high velocity range where T_s is possibly comparable to T_v .

Finally we point out that the information on the temperature dependence of the recoil pressure obtained in this chapter will serve to conduct more realistic numerical simulations for laser metal processing under the atmospheric pressure.

Annex 3. Revised piston model

Résumé

Le modèle du « piston » est un modèle analytique qui décrit le procédé d'éjection latérale du liquide sous l'effet de la pression de recul. Il s'applique à une gamme d'intensité de laser assez large (en général de 10^{-1} à 10^3 MW/cm² dans le cas de fer). Il est ainsi présent dans divers processus laser tels que le perçage, le soudage, la découpe et la gravure. Von Allmen a initialement proposé un modèle du piston. Par la suite, Semak et Matsunawa ont mieux formalisé le problème et ont étudié la dépendance de la vitesse d'avancement de l'interface solide-liquide avec l'intensité de laser [Semak 1997]. Cependant, Semak et Matsunawa ont employé l'équation (A2-24) pour l'équation du bilan d'impulsion. Mais comme on l'a vu en annexe 2, cette expression n'est valable que si le processus laser est réalisé sous vide. C'est donc l'objet de cette section que de reprendre ce modèle en tenant compte de l'effet de la pression atmosphérique ambiante que nous avons analysé dans l'annexe 2.

Le processus de perçage est décrit dans une géométrie 2D axisymétrique. Les équations que nous avons utilisées sont presque identiques à celles de l'article original [Semak 1997]. Le bilan de masse et le bilan énergétique ont été appliqués à une couche de liquide d'une certaine épaisseur. La dépendance de la perte de chaleur par conduction vers le solide, qui dépend du nombre de Péclet, a été améliorée et est basée sur les résultats des simulations numériques décrites dans l'annexe 4 suivante. Mais la principale différence très importante se situe dans l'équation du bilan d'impulsion : Dans notre cas, la pression atmosphérique, qui était négligée dans l'article original [Semak 1997], est prise en considération dans l'équation de Bernoulli.

Les résultats de calcul pour ces nouvelles conditions sont bien sûr très différents de ceux obtenus par Semak 1997. Notre modèle montre que le perçage ne commence que lorsque la température de surface dépasse T_v . Dans l'analyse originale, qui ne prenait pas en compte la pression atmosphérique ambiante, le processus de perçage démarrait dès que la température de surface avait atteint la température de fusion T_m . Par ailleurs, la différence de vitesse de perçage entre les deux approches est importante pour les températures proches de T_v . Cette différence s'atténue bien sûr lorsque la température augmente, c'est-à-dire lorsque la pression de recul devient importante par rapport à la pression atmosphérique. Ce résultat montre donc que la considération de la pression ambiante est nécessaire, particulièrement pour le procédé de soudage en régime « keyhole », où la température de surface de liquide est censée être juste au-dessus de T_v .

Introduction

So called ‘‘Piston model’’ is an analytical model which describes the material removal process under recoil pressure. It applies to a wide range of laser beam intensity (typically $10^{-1} \sim 10^3$ MW/cm² in the case of iron), which is utilised in various laser processes, including drilling, welding, cutting and grooving. The piston model was firstly proposed by Von Allmen. Later Semak and Matsunawa mathematically formulated the problem and quantified the dependence of removal speed on the laser intensity [Semak 1997]. However, Semak and Matsunawa used the equation (A2-24) for the momentum balance. As was discussed in Annex 2, this expression is valid only for laser processing in the vacuum. The object of this section is to provide an analysis which is applicable for processing under the ambient atmospheric pressure. The obtained result is clearly different from the original result in [Semak 1997]; the present analysis predicts that the threshold surface temperature for the initiation of drilling process is above T_v , whereas the original analysis in [Semak 1997] predicts the threshold temperature to be T_m .

A3.1. Formulation for laser drilling

We consider the dependence of removal rate (V_d : drilling velocity) on the laser intensity, based on the 2D axially symmetric model depicted in figure A3-1. There are two mechanisms of material removal: the evaporation itself and lateral melt ejection by the local pressure gradient. The latter, which involves pressure exerted onto the liquid surface, is called ‘‘piston’’ mechanism.

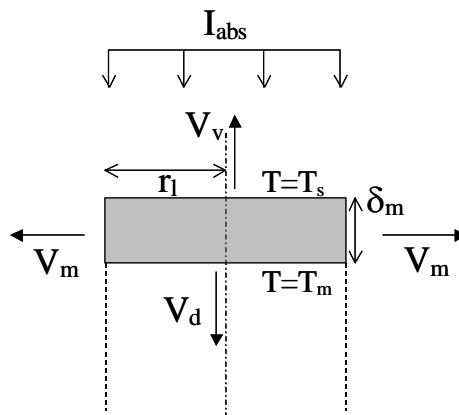


Figure A3-1. Piston model
(2D axi-symmetric)

Table A3-1 Definition of symbols and material parameters taken from [Semak 1997]

	Definition	Value
r_l	Laser beam radius	
ρ_s	Density of solid	7800 kg/m ³
ρ_m	Density of melt	6980 kg/m ³
C_{ps}	Heat capacity of solid	628 J/kg · K
C_{pm}	Heat capacity of melt	748 J/kg · K
T_m	Melting temperature	1808 K
T_v	Vaporisation temperature	3023 K
T_s	Surface temperature of melt layer	
L_m	Latent heat of melting	2.76×10^5 J/kg
L_v	Latent heat of evaporation	6.09×10^6 J/kg
δ_m	Thickness of melt layer	
κ_s	Heat diffusivity of solid	1.4×10^{-5} m ² /s
κ_m	Heat diffusivity of melt	7×10^{-6} m ² /s
V_v	Ejection speed by evaporation	
V_m	Speed of lateral melt ejection	

In this analysis, the intensity I_{abs} absorbed on the surface is used as a parameter describing the heat input, assuming that absorptivity A is known. The following analysis is composed of two steps: the first step is to clarify the dependence of V_d on the surface temperature T_s of melt layer. The second step is to express I_{abs} as a function of T_s . In this way V_d can be obtained as an implicit function of I_{abs} .

A3.1.1. Mass balance

The first step, which gives the dependence of V_d on T_s is obtained basically from mass balance consideration. As mentioned above, there are two contributions to the removal process: lateral ejection of liquid and evaporation. Mass balance can be written as

$$\rho_s (\pi r_l^2) V_d = \rho_m (2\pi r_l) \delta_m V_m + \rho_m (\pi r_l^2) V_v \quad (\text{A3-1})$$

where

$$\delta_m = \left(\frac{\kappa_m}{V_d} \right) \ln \left(1 + \frac{\rho_m C_{pm} (T_s - T_m)}{\rho_s [C_{ps} (T_m - T_0) + L_m]} \right) \quad (\text{A3-2})$$

is melt layer thickness. Substituting (A3-2) to (A3-1) we obtain a quadratic equation for V_d :

$$\begin{aligned} aV_d^2 - bV_d - c &= 0, \\ V_d &= \frac{b + \sqrt{b^2 + 4ac}}{2a} \end{aligned} \quad (\text{A3-3})$$

where

$$a = \rho_s r_l \quad (\text{A3-3.a})$$

$$b = \rho_m r_l V_v \quad (\text{A3-3.b})$$

$$c = 2\rho_m V_m \kappa_m \ln \left(1 + \frac{\rho_m C_{pm} (T_s - T_m)}{\rho_s [C_{ps} (T_m - T_0) + L_m]} \right) \quad (\text{A3-3.c})$$

To obtain the coefficients (A3-3.b) and (A3-3.c), it is still necessary to express V_m and V_v as functions of T_s . First, V_m can be estimated from the Bernoulli equation:

$$V_m = \sqrt{\frac{2(P_{\text{tot}} - P_{\text{amb}})}{\rho_m}} \quad (\text{A3-4})$$

where P_{amb} is the ambient atmospheric pressure (1.01×10^5 Pa). According to the study in Annex 2, the temperature dependence of the total pressure P_{tot} can be approximated as

$$P_{\text{tot}} = P_{\text{amb}} \quad (T_s < T_1) \quad (\text{A3-5})$$

$$= 0.6 p_{\text{sat}}(T_s) \quad (T_s > T_1) \quad (\text{A3-6})$$

where the temperature T_1 is given by

$$P_{\text{amb}} = 0.6 p_{\text{sat}}(T_1) \quad (\text{A3-7})$$

The expression of p_{sat} can be found in eq. (A2-6).

Taking into account the fact that a portion of material (β_R) is re-condensed to melt layer, total mass flow rate from melt layer to gas phase ($\rho_m V_v$ in eq.(A3-3.b)) can be estimated from

$$\rho_m V_v = (1 - \beta_R) \left(\frac{m}{2\pi k_B T_s} \right)^{1/2} P_{\text{sat}}(T_s) \quad (\text{A3-8})$$

Substituting the relations (A3-4)-(A3-8) to (A3-3.a)-(A3-3.c) one can solve the quadratic equation (A3-3) and obtain the dependence of V_d on T_s .

A3.1.2. Energy balance

The surface temperature T_s is a function of I_{abs} . This relation is obtained from energy conservation relation per unit time and per unit length along the drilling direction. The laser power input (p_{laser}) must

be equal to the sum of powers necessary to raise the temperature of solid part until T_m , melt it, and to heat up further the melt layer (p_m) or to evaporate it (p_v), and power lost by heat conduction to solid (p_{loss}).

$$p_{laser} = p_m + p_v + p_{loss} \quad (A3-9)$$

Inserting expression of each term, one obtains

$$\begin{aligned} I_{abs}(\pi r_l^2) = & \rho_m (2\pi r_l) \delta_m V_m [C_{ps}(T_m - T_0) + L_m + C_{pm}(T^* - T_m)] \\ & + \rho_m (\pi r_l^2) \mathcal{N}_v [C_{ps}(T_m - T_0) + L_m + C_{pm}(T_s - T_m) + L_v] \\ & + \rho_s (\pi r_l^2) \mathcal{N}_d C_{ps}(T_m - T_0) f(Pe) \end{aligned} \quad (A3-10)$$

where

$$Pe = \frac{r_l V_d}{\kappa_s} \quad (A3-11)$$

is the non-dimensional Péclet number and T^* is the average temperature of melt layer. Assuming linear temperature distribution along thickness of the melt layer, we use

$$T^* = \frac{1}{2}(T_m + T_s) \quad (A3-12)$$

The variable $f(Pe)$ in the last term for p_{loss} represents the ratio of the heat conduction loss to the heat necessary to heat the solid part, which will be removed, up to the melting temperature T_m . This factor is evaluated from a FEM calculation in the Annex 4. The result of the calculation is shown in figure A4-5, where one can confirm that f decreases monotonously with Pe . This function f can be approximated as

$$f(Pe) = 4.0Pe^{-0.84} \quad (A3-13)$$

It is interesting to note that this formula for the heat conduction loss in the case of the axi-symmetric 3D case is always larger than

$$f(Pe) = 1.3Pe^{-0.75}$$

which can be applied to the 2D case of laser cutting (see Figure A4-5).

In summary, when we assume a certain value of T_s , V_d and I_{abs} can be calculated from the equations (A3-3) and (A3-10), respectively. Repeating the process while varying T_s , we can easily obtain V_d as a function of I_{abs} .

A3.2. Calculation examples

Figure A3-3 shows the calculation results for two different diameters $r_1 = 0.85\text{mm}$, 0.28mm . In addition to V_d , ζ , which is the ratio of melt ejection to the total ejection, is shown.

$$\zeta = \frac{\rho_m (2\pi r_l) \delta_m V_m}{\rho_s (\pi r_l^2) V_d} \quad (A3-14)$$

This parameter represents process efficiency in terms of energy. In intensity range where V_d is high and heat conduction loss is small ($Pe \gg 1$), a smaller ζ indicates that larger portion of material is ejected in the form of vapour. This means that we have to provide more energy to drill unit thickness, so that the process efficiency is poorer.

As can be seen in figure A3-3, V_d increases monotonously with I_{abs} . It depends also on r_l . In lower intensity region ($I_{abs} < 0.5 \text{ MW/cm}^2$), V_d is greater for larger spot. In this range, V_d is not so large ($Pe < 1$), and heat conduction loss is important compared with the energy utilised to process the material. This conduction loss is smaller for a larger spot. Please note also that threshold condition for vaporisation can be approximated as

$$I_{abs-th} \approx \frac{K(T_v - T_0)}{r_l} \quad (A3-15)$$

The threshold becomes higher for a smaller spot.

On the other hand, in higher intensity region ($I_{\text{abs}} > 0.5 \text{ MW/cm}^2$), V_d is higher for a smaller spot. This can be understood in terms of ζ . As is evident from figure A3-1, whereas exit surface area of the melt ejection $[(2\pi r_1)\delta_m]$ linearly increases with r_1 , surface area for vaporisation (πr_1^2) is proportional to r_1^2 . This means that, as one increases the spot size, more material is removed in the form of vapour (in other words, smaller ζ), so that more intensity I_{abs} is required to reach a certain value of V_d .

Figure A3-4 shows the dependence of the surface temperature T_s and the total pressure P_{tot} on the absorbed intensity I_{abs} for the case of $r_1 = 0.28\text{mm}$.

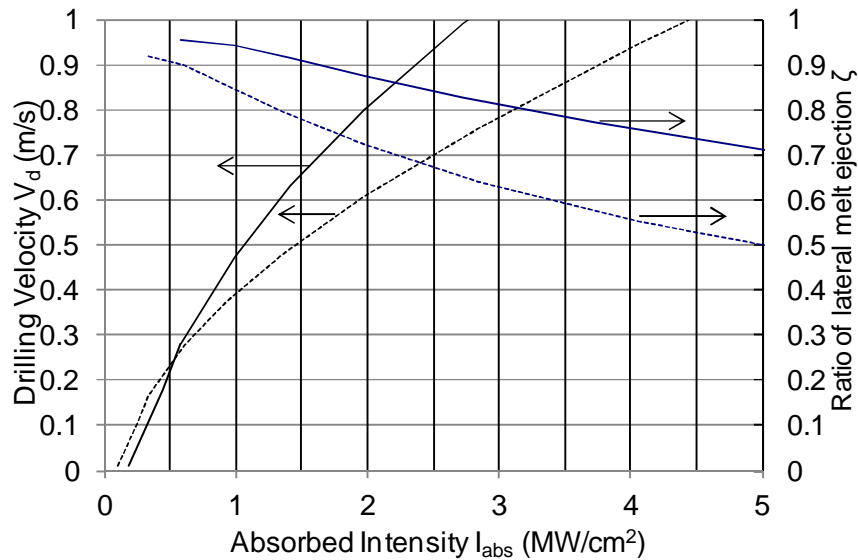


Figure A3-3. Results of calculations for $r_1 = 0.85\text{mm}$ (dotted lines) and $r_1 = 0.28\text{mm}$ (solid lines).

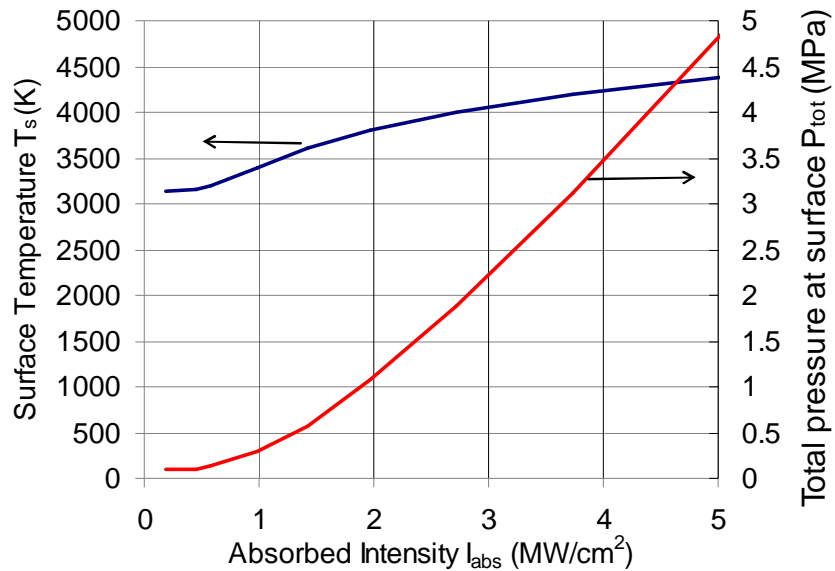


Figure A3-4. Calculated surface temperature and the total pressure in the case of $r_1 = 0.28\text{mm}$.

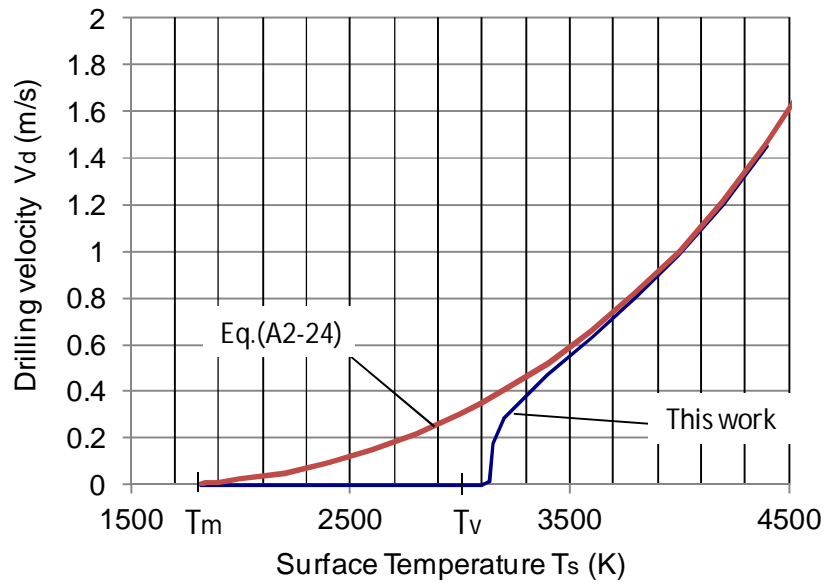


Figure A3-5. Calculated drilling velocity as a function of T_s in the case of $r_1 = 0.28\text{mm}$. The result obtained from the pressure balance eq.(A2-24) is also shown for comparison.

In figure A3-5, drilling velocity is plotted as a function of T_s in the case of $r_1 = 0.28\text{mm}$. One can see that drilling does not occur when T_s is below T_v . For comparison, the drilling velocity calculated from the pressure balance eq.(A2-24) is also shown in the figure. One can clearly recognise the difference; in this case, drilling can start as soon as T_s reaches T_m . However, this result is valid only for the case of processing in the vacuum as discussed in the Annex 2.

A3.3. Summary

In this Annex 3, the revised piston model, which is applicable to laser drilling under the ambient atmospheric pressure, was proposed. The modelling method was almost the same as the original paper [Semak 1997]. The mass balance and the energy balance were considered for a melt layer with a certain thickness. Dependence of heat conduction loss on the Péclet number was introduced based on results of numerical simulation described in the next section Annex 4. The important difference lied only in the equation of the momentum balance. In the present analysis, the atmospheric pressure, which was neglected in [Semak 1997], was taken into account to the Bernoulli equation.

The result of the calculations shows a clear difference from the analysis in the original paper [Semak 1997]. The present analysis predicts that drilling starts only after T_s exceeds T_v . On the other hand, the original analysis without consideration of the ambient atmospheric pressure lets the drilling process start just after T_s reaches T_m . The difference of the two results is prominent in the temperature range from T_m to just above T_v . This difference diminishes as T_s increases, as the recoil pressure becomes larger compared with the ambient atmospheric pressure. Thus the result demonstrates that the consideration of the ambient temperature is especially important for keyhole welding process, where T_s is supposed to be just above T_v .

Annex. 4 Analysis of heat conduction process

Résumé

Dans la découpe laser, une partie de la puissance laser absorbée sur le front avant de la saignée est perdue par la conduction de chaleur dans le solide et ne peut pas être utilisée pour fondre le matériau, qui est le principe même du procédé. Il est donc essentiel d'évaluer la fraction de l'énergie laser absorbée qui est perdue en conduction de chaleur si l'on veut évaluer l'efficacité du procédé ou prévoir la vitesse maximum de découpe, pour des paramètres opératoires donnés. L'objet de l'analyse présentée dans cette section est d'estimer cette perte de puissance.

L'un des intérêts de cette analyse est de déterminer le seuil d'intensité (ou encore la puissance seuil, pour une surface d'irradiation donnée) défini comme étant l'intensité minimum nécessaire à la réalisation d'une découpe laser, c'est-à-dire l'obtention de la température de fusion sur la surface irradiée. Intuitivement, ce seuil d'intensité diminue avec V_c . D'un point de vue mathématique, il est intéressant de voir si cette intensité seuil tend vers zéro lorsque V_c diminue. Par ailleurs, il est intéressant de noter que ce problème dépend de sa géométrie, car la solution de l'équation de la chaleur dépend fortement de la dimension 1D, 2D ou 3D utilisée. Dans ce contexte, nous discutons non seulement le cas « 2D » : chauffage par une source de chaleur en ligne, qui correspond au processus de découpe laser, mais également le chauffage « 1D » homogène d'une surface et le chauffage « 3D » par une tache de faisceau circulaire.

Tout d'abord, on traite le chauffage d'une surface avec un faisceau laser statique ($V_c = 0$). En géométrie 1D, il n'y a bien sûr aucune perte due à la conduction latérale de chaleur, et donc pas d'intensité seuil. En d'autres termes, la température de surface croît continument, même avec une intensité laser infiniment petite. Dans le cas de la géométrie 2D, bien que des pertes par conduction latérale de chaleur existent, une intensité seuil ne peut pas être définie à $V_c = 0$. Dans ces deux cas de 1D et 2D, même pour une faible intensité absorbée, la température de surface peut atteindre la température de fusion si on attend suffisamment longtemps. Enfin, dans le cas de la géométrie 3D, les pertes par conduction deviennent plus importantes que dans le cas de la géométrie 2D : Il existe alors une intensité seuil, en-dessous de laquelle la surface ne peut pas être fondue quelle que soit la durée d'irradiation.

Dans le cas général d'un déplacement relatif laser-pièce ($V_c \geq 0$), la puissance seuil a été déterminée pour ces trois géométries. La perte par conduction de chaleur latérale pour les cas de 2D et 3D ont été évaluées à partir de simulations numériques par la méthode des éléments finis, en utilisant le logiciel commercial COMSOL. Des expressions analytiques en fonction du nombre de Péclet du problème ont été obtenues dans ces deux cas. Pour le cas du 2D, le résultat de cette étude est conforme à l'expression proposée par Schulz [Schulz 1993] et sera utilisée dans nos analyses nécessitant la description de la conduction de chaleur dans la partie solide.

Introduction

In laser cutting, a part of the laser power absorbed on a kerf front is dissipated by heat conduction and cannot be utilised to melt the material. It is essential to evaluate this heat conduction when we discuss efficiency of the energy use or predict maximum cutting speed for a given set of operating parameters. The object of the analysis in this section is to quantify this power loss.

One of the interests of the analysis is to know about threshold intensity, which is defined as the minimum intensity required to carry out laser cutting for a given set of operating parameters. Intuitively, the threshold intensity is reduced with a decrease of cutting velocity V_c . From a mathematical point of view, it is interesting to see whether or not this threshold intensity becomes zero as V_c is decreased. Also, it is worthwhile to note that such a characteristic depends on the dimension of the problem, as a solution of heat conduction equation depends strongly on the dimension. In this context, we discuss not only “2D” heating by a line heat source, which corresponds to laser cutting process, but also “1D” homogeneous heating of a surface and “3D” heating by a circular beam spot.

In the following, surface heating with a static laser beam ($V_c = 0$) is discussed first. It is pointed out that the threshold intensity exists only for the 3D case. Then we analyse the power required for a general case of $V_c \geq 0$. Heat conduction loss for the cases of 2D and 3D is evaluated from FEM calculations. For the case of laser cutting (2D), the heat conduction loss obtained in this study agrees well with the expression previously proposed by Schulz.

A4.1. Surface heating with a static laser beam

First, let us consider surface heating by a static laser beam ($V_c = 0$) for the three cases shown in figures A4-1. Figure A4-1(b) corresponds to initiation of the cutting process. The surface is heated by a line source with the width of $2r_0$ and the intensity of I_0 . The 1D model (Figure A4-1(a)) and the 3D model (Figure A4-1(c)) are also analysed to investigate the dependence of the characteristics of heat conduction on the dimension of the problem. In the 1D model, whole the surface is heated homogeneously with the intensity of I_0 . For the 3D model the circular spot with the radius r_0 is assumed. This corresponds to the geometry in laser drilling process.

Figure A4-2 shows calculated evolutions of surface temperature under irradiation with a constant intensity of $I_0 = 10^6$ (W/m²), $r_0 = 0.1$ mm. The temperature on the central axis of the heat source line and that at the centre of the beam spot are shown for the 2D and 3D models, respectively. These two curves were obtained from FEM calculations using the commercial software COMSOL [COMSOL WEB]. The properties of material used in the calculations are summarised in Table A4-1.

For the 1D case (figure A4-1 (a)), surface temperature can be expressed analytically.

$$\Delta T(t) = \frac{2I_0}{K} \sqrt{\frac{\kappa t}{\pi}} \quad (\text{A4-1}).$$

The temperature increases proportionally to the square root of t . The time t_m needed to melt the surface

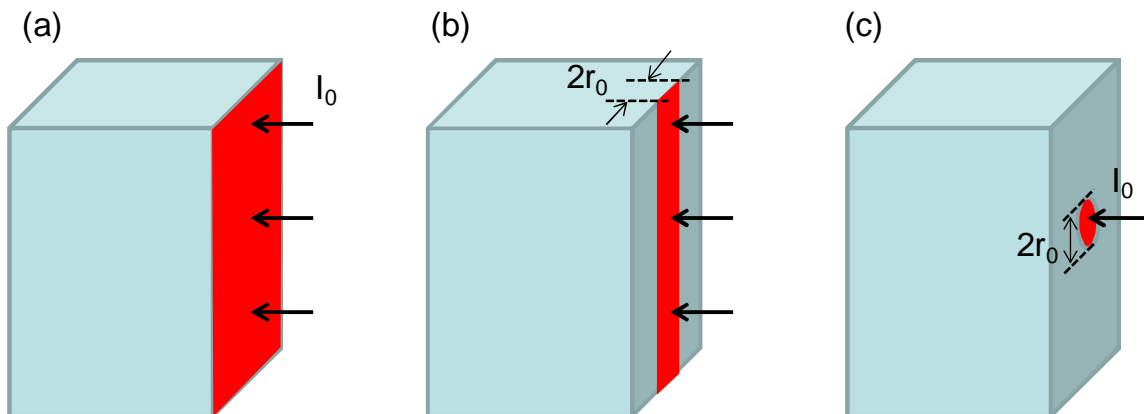


Figure A4-1 Surface heating with a static laser beam for the three different configurations.

Table A4-1 Material properties

Parameters	Values
Density	7.8×10^3 (kg/cm ³)
Heat Capacity	420 (J/kg·K)
Melting point	1500 (degrees)
Thermal Conductivity	40 (W/m·K)
Latent Heat	3.5×10^5 (J/kg)

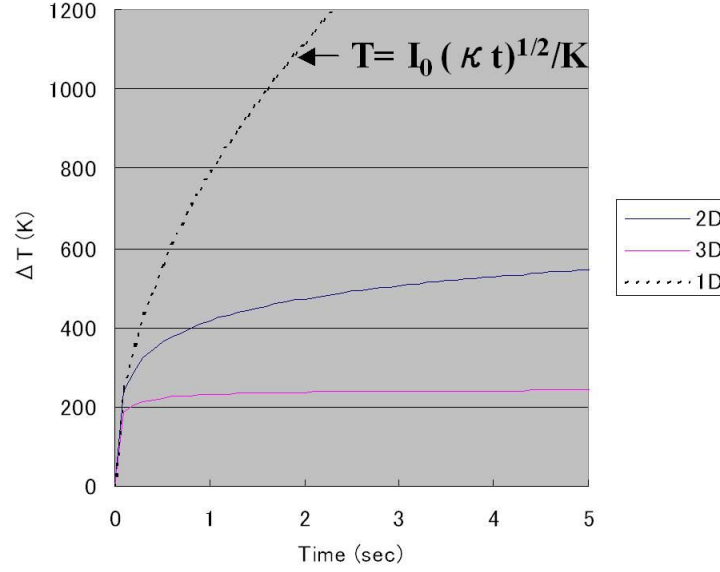


Figure A4-2 Transient behaviours of surface temperature for the three different configurations.

is given as

$$t_m = \frac{\pi}{\kappa} \left[\frac{K(T_m - T_0)}{2I_0} \right]^2 \quad (\text{A4-2}).$$

In the case of 3D (figure A4-1 (c)), an analytical expression of temperature development is available for the symmetry axis of the laser beam. Defining the depth x from the surface, the temperature is expressed as

$$\Delta T(x, t) = \frac{I_0 \delta}{K} \left\{ \text{ierfc} \left(\frac{x}{\delta} \right) - \text{ierfc} \left(\frac{\sqrt{x^2 + r_0^2}}{\delta} \right) \right\} \quad (\text{A4-3})$$

$$\delta = 2\sqrt{\kappa t}$$

There exists a saturated temperature and this value is expressed as

$$T_0 = \lim_{t \rightarrow \infty} T(x, t) \Big|_{x=0} = \frac{I_0 r_0}{K} \quad (\text{A4-4}).$$

One can define a threshold intensity under which melting cannot be achieved even for $t \rightarrow \infty$. This threshold intensity can be obtained as

$$I_{th}^{3D} = \frac{KT_m}{r_0} \quad (\text{A4-5}).$$

It can be seen from figure A4-2 that the 2D model (figure A4-1 (b)) for laser cutting is an intermediate case between the above two cases of 1D and 3D, although an explicit analytical expression is not available. The surface temperature continues to increase, but more slowly than the 1D case due to heat conduction. It will be shown later that the temperature is not saturated in this case of 2D and the threshold intensity cannot be defined.

A4.2. Melting with a moving laser beam

Next we consider continuous melting of a solid-liquid interface with a moving laser beam. We neglect melt layer, assuming that molten material is removed immediately after melting. Thus the temperature of the melting front is assumed to be T_m .

A4.2.1 1D model

In the case of the 1D model, there is no heat conduction loss and all the absorbed power is utilised for cutting process. The power balance can be written as

$$I_0 = \rho [C_p (T_m - T_0) + L_m] V_c \quad (\text{A4-6})$$

This equation defines the threshold intensity as a function of V_c .

A4.2.2 2D model

We analyse heat conduction on a plane (figure A4-3(a)) which is extracted from the kerf model shown in figure A4-3(b). For laser cutting this setting of the problem as 2D is usually assumed, since thickness of a cut sample is much larger than the characteristic distance (κ/V_c) of temperature distribution which spreads in front of the kerf front. As was pointed out in section 2.2, however, this is not the case for regions near the top and bottom surfaces, where heat flux in the direction of the thickness of the sample modifies the temperature field. This influence was discussed in section 2.2.

As shown in figure A4-3(a), the kerf front profile is assumed to be a semi-circle with a radius of r_0 , which is approximately equal to the laser beam radius.

The power balance per unit thickness can be written as

$$p_d = p_s + p_m \quad (\text{A4-7})$$

The first term p_s is the power necessary to raise the surface temperature on the kerf front up to T_m . This term consists of two components:

$$p_s = p_{heat}^{axial} + p_{loss} \quad (\text{A4-8})$$

where p_{heat}^{axial} is the energy necessary to heat axial region (figure A4-3(b)) in front of the kerf front

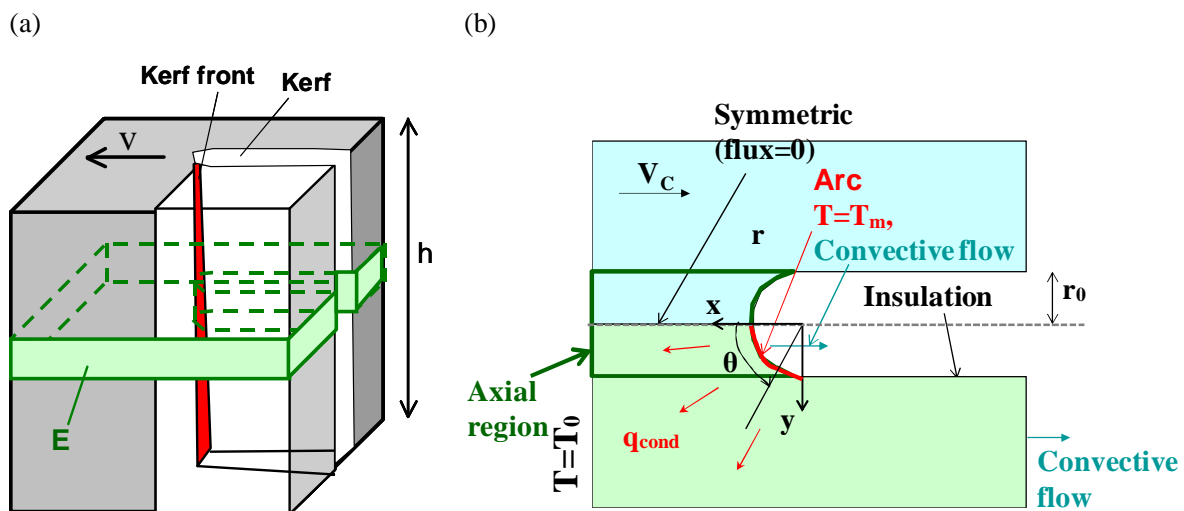


Figure A4-3 2D Model for heat conduction calculation.

and p_{loss} is the energy lost by heat conduction, in other words, the energy consumed to raise the temperature of the part outside the axial region. Defining a ratio f of p_{loss} to $p_{\text{heat}}^{\text{axial}}$ ($f = p_{\text{loss}} / p_{\text{heat}}^{\text{axial}}$), we rewrite eq.(A4-8) as

$$\begin{aligned} p_s &= (1 + f)p_{\text{heat}}^{\text{axial}} \\ &= (1 + f)\rho C_p (T_m - T_0)V_c (2r_0) \\ &= 2(1 + f)K(T_m - T_0)Pe \end{aligned} \quad (\text{A4-9}),$$

where

$$Pe = \frac{r_0 V_c}{\kappa} \quad (\text{A4-10}).$$

is the Péclet number, the non-dimensional parameter which represents the ratio of the kerf radius r_0 to the characteristic distance of temperature field (κ/V_c) which is created in the solid part in front of the laser beam.

The second term p_m in (A4-7) is the power needed for melting.

$$\begin{aligned} p_m &= \rho L_m V_c (2r_0) \\ &= St^{-1} K (T_m - T_0) Pe \end{aligned} \quad (\text{A4-11})$$

As will be shown later, f in (A4-9) is the function of Pe . Thus from the expressions (A4-9) and (A4-11) it is concluded that the power p_d required for cutting process is the function of Pe .

Let us calculate the heat conduction loss p_{loss} using the model shown in figure A4-3(b). The laboratory coordinate system where laser beam is fixed is adopted in this analysis. Temperature dependence of these parameters is neglected for ease of calculation.

Taking into account the convection term, which corresponds to displacement of material with the speed of V_c , the translation speed of laser beam, one obtains the heat transfer equation in stationary condition:

$$V_c \frac{\partial T}{\partial x} = \kappa \left(\frac{\partial^2 T}{\partial x^2} + \frac{\partial^2 T}{\partial y^2} \right) \quad (\text{A4-12}).$$

As already mentioned, only the solid part is taken into account and a part of material is assumed to disappear instantaneously once its temperature reaches T_m , the melting temperature. Thus boundary condition on the arc of the kerf front is

$$T = T_m \quad \text{on kerf front} \quad (\text{A4-13}).$$

On the other hand, insulated condition is imposed at the kerf sides.

The temperature at inlet in the left is

$$T = T_0 \quad \text{at inlet} \quad (\text{A4-14}).$$

Boundary condition of the heat flux on the kerf front is written as

$$q_{\text{cond}}(\theta) = -K \frac{\partial T}{\partial r} \Big|_{r=r_0} \quad \text{on kerf front} \quad (\text{A4-15}).$$

The power p_s required per unit depth is obtained by integrating the flux q_{cond} over the arc of the kerf front.

$$p_s = 2 \int_0^{\pi/2} q_{\text{cond}}(\theta) r_0 d\theta \quad (\text{A4-16}).$$

Let us mention here an important scaling law. First we introduce non-dimensional parameters as follows.

$$x' = \frac{x}{r_0}, \quad y' = \frac{y}{r_0} \quad (\text{A4-17}).$$

$$T' = \frac{T}{(T_m - T_0)} \quad (\text{A4-18}).$$

$$q'_{cond} = \frac{q_{cond}}{K \left(\frac{T_m - T_0}{r_0} \right)} \quad (\text{A4-19}).$$

$$= \frac{r_0}{K(T_m - T_0)} q_{cond}$$

Then eqs.(A4-12) and (A4-15) are rewritten as follows.

$$Pe \frac{\partial T'}{\partial x'} = \frac{\partial^2 T'}{\partial x'^2} + \frac{\partial^2 T'}{\partial y'^2} \quad (\text{A4-20}).$$

$$q'_{cond}(\theta) = - \left. \frac{\partial T'}{\partial r'} \right|_{r'=1} \quad \text{on kerf front} \quad (\text{A4-21}).$$

The important scaling law is that when the kerf radius r_0 is doubled, on the condition that the velocity V_c and the intensity q_{cond} are halved at the same time, the temperature field is not altered, except a modification in scale factors of space by two. It should be noted also that the power required per unit depth p_s [W/m] in eq.(A4-16) is conserved in this transformation of the operating parameters. In other words, when Pe is given, the power p_s that is required to maintain the temperature of the kerf front at T_m is uniquely determined, regardless of the combination of the parameters r_0 and V_c . Therefore, the threshold power p_d required per unit depth for laser cutting depends only on Pe . Referring to (A4-8) and (A4-9) one can conclude also that p_{loss} and f are functions of Pe .

FEM calculations of the heat conduction loss were carried out using the software COMSOL. In the calculation, the stationary temperature field was obtained by an iterative scheme of the software. After the calculation, the conduction heat flux on the kerf front was integrated to obtain p_s (W/m). Finally f was calculated from eq.(A4-9).

The results calculated by COMSOL are compared with the expressions proposed in the past.

(1) The expression in [Schulz 1993]

Using the equation (9) in the paper,

$$p_s = 4K(T_m - T_0) \left[\left(\frac{Pe}{2} \right) + \left(\frac{Pe}{2} \right)^{0.3} \right] \quad (\text{A4-22}).$$

$$f(Pe) = 2^{0.7} Pe^{-0.7} \quad (\text{A4-23})$$

(2) The expression in [Bazyleva 2002]

Using the equations (1) and (3) in the paper,

$$p_s = E_s V_c (2r_0) + 2E_m V_c x_{\perp}$$

$$= \rho C_p (T_m - T_0) V_c (2r_0) + 2\rho C_p (T_m - T_0) V_c \sqrt{\left(\frac{2\kappa}{V_c} \right) \left(2r_0 + \frac{\kappa}{V_c} \right)} \quad (\text{A4-24}).$$

$$= 2K(T_m - T_0) (Pe + \sqrt{2(2Pe + 1)})$$

$$f(Pe) = \sqrt{2Pe^{-1}(2 + Pe^{-1})} \quad (\text{A4-25})$$

(3) Rosenthal

We compared the calculation result also with the well-known analytical solution of Rosenthal. The assumption used is extremely thin line source and zero width of the kerf, the both of which correspond to $r_0 \rightarrow 0$. If the characteristic distance of temperature field (κ/V_c) is much larger than the kerf width $2r_0$ (i.e. Pe is very low), this solution must be a good approximation of the problem now under consideration. The Rosenthal solution is written as

$$\Delta T(x, y) = \frac{q}{2\pi K} \exp\left(-\frac{V_c x}{2\kappa}\right) K_0\left(\frac{V_c r}{2\kappa}\right) \quad (A4-26).$$

$$r^2 = x^2 + y^2$$

Under the condition of $Pe \ll 1$, the solution gives isothermal lines approximately circular around the line source. This fact enables us to set $\Delta T(x = r_0, y = 0)$ equal to T_m . Thus,

$$p_s = q = 2\pi K (T_m - T_0) \exp\left(\frac{V_c r_0}{2\kappa}\right) \left[K_0\left(\frac{V_c r_0}{2\kappa}\right) \right]^{-1} \quad (A4-27).$$

$$= 2\pi K (T_m - T_0) \exp\left(\frac{Pe}{2}\right) \left[K_0\left(\frac{Pe}{2}\right) \right]^{-1}$$

$$f = \pi Pe^{-1} \exp\left(\frac{Pe}{2}\right) \left[K_0\left(\frac{Pe}{2}\right) \right]^{-1} - 1 \quad (A4-28).$$

Escaping from adding the terms of modified Bessel function of zero-th order, we used the following expression, taking advantage of the assumption that $Pe = (V_c r_0 / \kappa) \ll 1$.

$$K_0(z) \approx -\ln\left(\frac{z}{2}\right) - \gamma \quad (A4-29).$$

with $\gamma = 0.577$ (Euler constant).

The equation (A4-27) shows that the power p_s required per unit depth approaches zero when $V_c \rightarrow 0$. This means that the threshold intensity cannot be defined at $V_c = 0$ for this 2D case.

These expressions are compared in figure A4-4. The function $f(Pe)$ calculated from the COMSOL can be approximated by

$$f(Pe) = 1.3Pe^{-0.75} \quad (A4-30)$$

It is seen that the expression by Bazyleva overestimates the conduction loss for the entire range of Pe . In this work the approximate expression by Schulz *et al.* is used to quantify the 2D heat conduction effect, since it is close to the results of FEM calculations in a wide range of Pe .

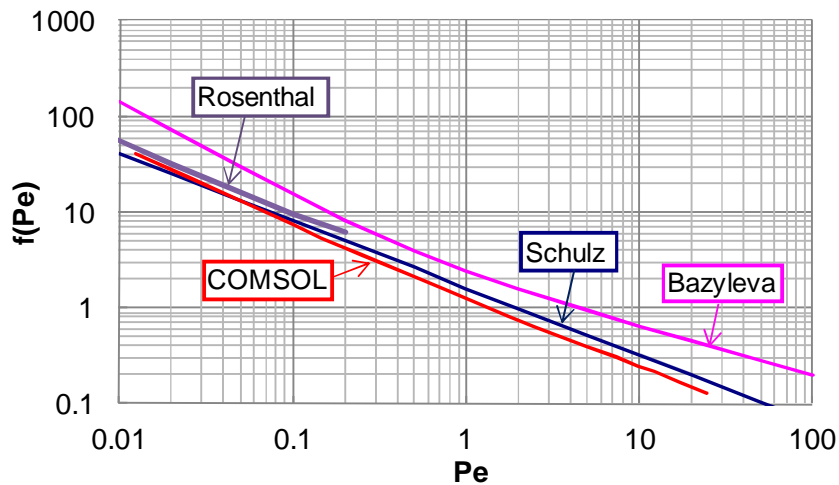


Figure A4-4 The function $f(Pe)$ obtained from the FEM calculation (COMSOL). The expressions obtained from the three models are shown for comparison.

A4.2.3 3D model

A similar calculation of heat conduction loss was carried out for the case of 3D using almost the same geometry as 2D (figure A4-3(b)) except that the central axis was changed to the axi-symmetric axis. The result of the calculations is shown in figure A4-5. The function f for 3D can be approximated as

$$f(Pe) = 4.0Pe^{-0.84} \quad (A4-31)$$

The function f is larger for 3D than that for 2D because of greater heat conduction.

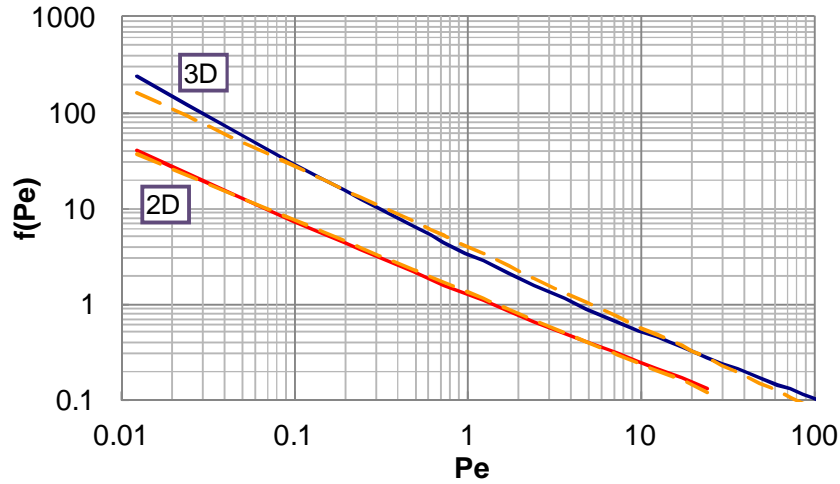


Figure A4-5 The function $f(Pe)$ obtained from the FEM calculations for the 2D and 3D models. The solid lines were obtained from FEM calculations by COMSOL. The orange dotted lines show linear approximations in the log-log scale.

A4.3 Summary

Heat conduction process was analysed for the cases of 1D, 2D and 3D. First, surface heating with a static beam ($V_c = 0$) was considered. In the case of 1D, there is no heat conduction loss, and there exists no threshold intensity. In the case of 2D, the heat conduction occurs. However, the threshold intensity cannot be defined either at $V_c = 0$. Surface can be melted even with an absorbed intensity infinitely small in these cases of 1D and 2D. Finally, in the case of 3D, the heat conduction loss becomes larger than the case of 2D. There exists a threshold intensity below which the surface cannot be melted even with a heating time infinitely long. Then the power required for melting was analysed for $V_c \geq 0$. The heat conduction loss in the cases of 2D and 3D were calculated by FEM analyses with the commercial software COMSOL. Approximate expressions were obtained for each case as a function of the Péclet number. For 2D, the result obtained in this study agrees well with the approximate expression previously proposed by Schulz *et al.* [Schulz 1993]. Thus this expression by Schulz *et al.* is used in this study.

References

- [Aden 1992] Aden M, Beyer E, Herziger G and Kunze H 1992 Laser-induced vaporization of a metal surface. *J. Phys. D: Appl. Phys.* **25** 57-65
- [Aden 1990] Aden M, Beyer E and Herziger G 1990 Laser-induced vaporization of metal as a Riemann problem. *J. Phys. D: Appl. Phys.* **23** 655-661
- [Ahmed 2009] Ahmed A M, Voß A, Vogel M M, Austerschulte A, Schulz J, Metsch V, Moser T and Graf T 2009 Radially polarized high-power lasers *Proceedings of SPIE* **7131** 713111
- [Amara 2012] Amara E H, Fabbro R and Hirano K 2012 Modelling of Cutting Velocity Influence on the Kerf Front During Laser Cutting Process *to be presented at the 31th Int. Congress on Applications of Lasers & Electro-Optics*
- [Anisimov 1968] Anisimov S I 1968 Vaporization of Metal Absorbing Laser Radiation *Sov. Phys. JETP* **27** 182-183
- [Apostol 1976] Apostol I, Vatanov V A, Mikheilesku I N, Morzhan I, Prokhorov A M and Fedorov V B 1976 Recoil impulse received by metal targets as a result of interaction with microsecond CO₂ laser radiation *Sov. J. Quantum Electronics* **6** 1119-1120
- [Arata 1967] Arata Y and Miyamoto I 1967 Generation and Applications of CW High power CO₂ Gas Laser *Technol. Repts. Osaka Univ.* **17**, No. 285.
- [Arata 1979] Arata Y, Maruo H, Miyamoto I and Takeuchi S 1979 Dynamic behavior in laser gas cutting of mild steel *Trans. JWRI* **8** 15-26
- [Basu 1992] Basu S and DebRoy T 1992 Liquid metal expulsion during laser irradiation *J. Appl. Phys.* **72** 3317-3322
- [Batanov 1973] Batanov V A, Bunkin F V, Prokhorov A M and Fedorov V B 1973 Evaporation of metallic targets caused by intense optical radiation. *Sov. Phys. JETP* **36** 311-322
- [Bazyleva 2002] Bazyleva I O, Galushkin M G, Golubev V S, Dubrovina E A and Karasev V A 2002 Thermal losses in process gas assisted laser cutting of metals *Proc. of SPIE* **4644** 73-81
- [Bellot 2001] Bellot J P, Duval H, Ritchie M, Mitchell A and Ablitzer D 2001 Evaporation of Fe and Cr from Induction-stirred Austenitic Stainless Steel. Influence of the Inert Gas Pressure *ISIJ International* **41** 696-705
- [Bergström 2008] Bergström D, Powell J and Kaplan A F H 2008 The absorption of light by rough metal surfaces – A three-dimensional ray-tracing analysis *J. Appl. Phys.* **103** 103515
- [Carslaw 1957] Carslaw H S and Jaeger J C 1959 *Conduction of Heat in Solids 2nd ed.* (Oxford University Press, New York) pp.75
- [Chen 1999] Chen K and Yao L 1999 Striation formation and melt removal in the laser cutting process *J. Manufacturing Processes* **1** 43-53
- [Chen 2000] Chen K, Lawrence Yao Y and Modi V 2000 Gas Jet-Workpiece Interactions in Laser Machining *J. Manuf. Sci. and Eng.* **122** 429-438
- [Colla 994] Colla T J, Vicanek M and Simon G 1994 Heat transport in melt flowing past the keyhole in deep penetration welding *J. Phys. D: Appl. Phys.* **27** 2035
- [COMSOL WEB] <http://www.comsol.com>
- [Craig 1966] Craig A D D 1966 Wind-generated waves in thin liquid films *J. Fluid Mechanics* **26** 269-392
- [Dausinger 1993] Dausinger F and Shen J 1993 Energy Coupling Efficiency In Laser Surface Treatment *ISIJ International* **33** 925-933
- [Dobler 2011] Dobler M, Kohl S, Leitz K H, Koch H, Otto A and Schmidt M 2011 Numerical Simulation of Laser Material Processing – Concepts and Progress *In: the 30th Int. Congress on Applications of Lasers & Electro-Optics* (Orlando, FL)
- [Dowden 1985] Dowden J, Davis M and Kapadia P 1985 The flow of heat and the motion of the weld pool in penetration welding with a laser *J. Appl. Phys.* **57** 4474-4479
- [Duan 2001-1] Duan J, Man H C and Yue T M 2001 Modelling the laser fusion cutting process: I. Mathematical modelling of the cut kerf geometry for laser fusion cutting of thick metal *J. Phys. D: Applied Physics* **34** 2127-2134
- [Duan 2001-2] Duan J, Man H C and Yue T M 2001 Modelling the laser fusion cutting process: II. Distribution of supersonic gas flow field inside the cut kerf *J. Phys. D: Applied Physics* **34** 2135-2142
- [Duan 2001-3] Duan J, Man H C and Yue T M 2001 Modelling the laser fusion cutting process: III. Effects of various process parameters on cut kerf quality *J. Phys. D: Applied Physics* **34** 2143-2150

- [Duan 2001-4] Duan J, Man H C and Yue T M 2001 Three dimensional modeling of the gas field distribution of a high-pressure gas jet used in laser fusion cutting *J. Laser Appl.* **13** 239-246
- [Eriksson 2011] Eriksson I, Powell J and Kaplan A 2011 Measurements of fluid flow on keyhole front during laser welding *Science and Technology of Welding and Joining* **16** 636-641
- [Ermolaev 2009] Ermolaev G V and Kovalev O B 2009 Simulation of surface profile formation in oxygen laser cutting of mild steel due to combustion cycles *J. Phys. D:Appl. Phys.* **42** 185506
- [Fabbro 2000-1] Fabbro R and Chouf K 2000 Keyhole modeling during laser welding *J. Appl. Phys.* **87** 4075-4083
- [Fabbro 2000-2] Fabbro R and Chouf K 2000 Dynamical description of keyhole in deep penetration laser welding *J. Laser Appl.* **12** 142-148
- [Fabbro 2005] Fabbro R, Slimani S, Coste F and Briand F 2005 Study of keyhole behaviour for full penetration Nd-Yag CW laser welding *J. Phys. D: Appl. Phys.* **38** 1881-1887
- [Fabbro 2006] Fabbro R, Slimani S, Doudet I, Coste F and Briand F 2006 Experimental study of the dynamical coupling between the induced vapour plume and the melt pool for Nd-Yag CW laser welding *J. Phys. D: Appl. Phys.* **39** 394-400
- [Fabbro 2010] Fabbro R 2010 Melt pool and keyhole behaviour analysis for deep penetration laser welding *J. Phys. D:Appl. Phys.* **43** 445501
- [Fieret 1986-1] Fieret J, Terry M J and Ward B A 1986 Aerodynamic interactions during laser cutting *Proc. of SPIE* **668** 53-62
- [Fieret 1986-2] Fieret J and Ward B A 1986 Circular and non-circular nozzle exits for supersonic gas jet assist in CO₂ laser cutting *Proc. of the 3rd Int. Conf. on Laser in Manufacturing* (Paris) 45-54
- [Fushimi 2000] Fushimi T, Horisawa H, Yamaguchi S, Yasunaga N and Fujioka T 2000 A fundamental study of laser cutting using a high speed photography *Proc. of SPIE* **3888** 90-95
- [Geiger 2009] Geiger M, Leitz K H, Koch H and Otto A. 2009 A 3D transient model of keyhole and melt pool dynamics in laser beam welding applied to the joining of zinc coated sheets. *Prod. Eng. Res. Devel.* **3** 127-136
- [Golovin 1985] Golovin A F and Petrukhin A I 1985 Some features of the evaporation of magnesium and lead by quasi-cw laser radiation. *Sov. J. Quantum Electron.* **15** 846-848
- [Golubev 1995] Golubev V S 1995 On possible models of hydrodynamical nonstationary phenomena in the processes of laser beam deep penetration into materials *Proc. of SPIE* **2713** 219-230
- [Golubev 2004] Golubev V S 2004 *Melt removal mechanisms in gas-assisted laser cutting of materials* Eprint No. 3 (Shatura: ILIT RAS)
- [Grigory 2010] Grigory E, Yudin P, Verna E and Jouanneau T 2010 Visualization and modeling of combustion effects at laser cutting of mild steel with oxygen *Proceedings of Pacific Int. Conference on Applications of Lasers & Optics 2010* (Wuhan, China) Paper 905
- [Greses 2004] Greses J, Hilton P A, Barlow C Y and Steen W M 2004 Plume attenuation under high power Nd:yttrium-aluminum-garnet laser welding *J. Laser Applications* **16** 9-15
- [Hansen 1994] Hansen F and Duley W W 1994 Attenuation of laser radiation by particles during laser material processing *J. Laser Appl.* **6** 137-143
- [He 2006] He X, Norris J T, Fuerschbach P W and DebRoy T 2006 Liquid metal expulsion during laser spot welding of 304 stainless steel *J. Phys. D: Appl. Phys.* **39** 525-534
- [Himmer 2007] Himmer T, Pinder T, Morgenthal L and Beyer E 2007 High brightness lasers in cutting applications *Proc. 26th Int. Congress on Applications of Lasers & Electro-Optics* 87-91
- [Hilton 2009] Hilton P A 2009 Cutting Stainless Steel with Disc and CO₂ Lasers *Proc. 5th Int. Congress on Laser Advanced Materials Processing* (Kobe, Japan) No. 306
- [Horisawa 2000] Horisawa H, Ashizawa H and Yasunaga N 2000 Plasma Characterization in Laser Cutting *Proc. SPIE* **3888** 82-89
- [Kaplan 1994] Kaplan A 1994 A model of deep penetration laser welding based on calculation of the keyhole profile *J. Phys. D: Appl. Phys.* **27** 1805-1814
- [Kaplan 1996] Kaplan A F H 1996 An analytical model of metal cutting with a laser beam *J. Appl. Phys.* **79** 2198-2208
- [Kaplan 1997] Kaplan A F H, Wangler O and Schuöcker D 1997 Laser Cutting: Fundamentals of the periodic striations and their on-line detection *Lasers in Engineering* **6** 103-126
- [Kaplan 2002] Kaplan A F H, Mizutani M, Katayama S and Matsunawa A 2002 Unbounded keyhole collapse and bubble formation during pulsed laser interaction with liquid zinc *J. Phys. D:Appl. Phys.*

- [Kasama 1983] Kasama A, McLean A, Miller W A, Morita Z and Ward M J 1983 Surface tension of liquid iron and iron-oxygen alloys *Canadian Metallurgical Quarterly* **22** 9-17
- [Katayama 2001] Katayama S, Kobayashi Y, Mizutani M and Matsunawa A 2001 Effect of vacuum on penetration and defects in laser welding *J. Laser Appl.* **13** 187-192
- [Kawahito 2007], Kawahito Y, Mizutani M and Katayama S 2007 Elucidation of high-power fibre laser welding phenomena of stainless steel and effect of factors on weld geometry *J. Phys. D: Appl. Phys.* **40** 5854-5859
- [Ki 2002] Ki H, Mohanty P S and Mazumder J 2002 Modeling of Laser Keyhole Welding: Part I. Mathematical Modeling, Numerical Methodology, Role of Recoil Pressure, Multiple Reflections, and Free Surface Evolution. *Metall. Mat. Trans. A* **33A** 1817-1830
- [Knight 1979] Knight C J 1979 Theoretical Modeling of Rapid Surface Vaporization with Back Pressure *AIAA J* **17** 519-523
- [Koch 2010] Koch H, Leitz K H, Otto A and Schmidt M 2010 Laser deep penetration welding simulation based on a wavelength dependent absorption model *Physics Procedia* **5** 309-315
- [Kovalenko 1985] Kovalenko V S, Romanenko V V, and Oleschuk L M 1987 *High Efficient Processes of Laser Material Cutting* (in Russian) (Kiev: Technika)
- [Kovalev 2001] Kovalev O B, Orishich A M, Fomin V M and Shulyat'ev V B 2001 Adjoint problems of mechanics of continuous media in gas-laser cutting of metals *Journal of Applied Mechanics and Technical Physics* **42** 1014-1022
- [Kovalev 2008] Kovalev O B, Yudin P V and Zaitsev A V 2008 Formation of a vortex flow at the laser cutting of sheet metal with low pressure of assisting gas *J. Phys. D: Applied Physics* **41** 155112.
- [Krasnyukov 1998] Krasnyukov A G, Kosyrev F K, Naumov V G and Shashkov V M 1998 Creation and application of mobile laser technological complexes *Proc. of SPIE* **3574** 41-48
- [Kraus 1986] Kraus H G 1986 Optical spectral radiometric method for measurement of weld-pool surface temperatures *Optics Letters* **11** 773-775
- [Kuznetsov 1994] Kuznetsov L I 1994 Recoil momentum at a solid surface during developed laser ablation *Quantum Electron* **23** 1035-1038
- [Lacroix 1997] Lacroix D, Jeandel G and Boudot C 1997 Spectroscopic characterization of laser-induced plasma created during welding with a pulsed Nd:YAG laser *J. Appl. Phys.* **81** 6599-6606
- [Lacroix 1998] Lacroix D, Jeandel G and Boudot C 1998 Solution of the radiative transfer equation in an absorbing and scattering Nd:YAG laser-induced plume *J. Appl. Phys.* **84** 2443-2449
- [Landau 1987] Landau L D and Lifshitz E M 1987 *Fluid Mechanics 2nd edition* (Oxford, UK: Butterworth-Heinemann) pp 316-320
- [La Rocca 1993] La Rocca A V 1993 Fluid-dynamics effects on laser processing *Proc. of SPIE* **2097** 100-111
- [Lee 2004] Lee D J and Jeong S H 2004 Analysis of recoil force during Nd:YAG laser ablation of silicon *Appl. Phys. A* **79** 1341-1344
- [Le Guen 2011] Le Guen E, Carin M, Fabbro R, Coste F and Le Masson P 2011 3D heat transfer model of hybrid laser Nd:Yag-MAG welding of S355 steel and experimental validation *Int. J Heat Mass Transfer* **54** 1313-1322
- [Lütke 2008] Lütke M, Mahrle A, Himmer T, Morgenthal L and Beyer E 2008 Remote-cutting – a smart solution using the advantages of high brightness lasers *Proc. 27th Int. Congress on Applications of Lasers & Electro-Optics* 695-702
- [Lüdi 2009] Lüdi A and Wittwer S 2009 Challenges of thick sheet metal cutting with fiber lasers *In: 5th International Workshop on Fiber Lasers* (Dresden, Germany)
- [Mahrle 2006] Mahrle A and Beyer E Hybrid laserbeam welding-classification, characteristics, and applications, *J. Laser Appl.* **18** 169-180
- [Mahrle 2009-1] Mahrle A and Beyer E 2009 Thermodynamic Evaluation of Inert-Gas Laser Beam Fusion Cutting with CO₂, Disc and Fiber Lasers *Proc. 28th Int. Congress on Applications of Lasers & Electro-Optics* 610-619
- [Mahrle 2009-2] Mahrle A and Beyer E 2009 Theoretical aspects of fibre laser cutting *J. Phys. D: Appl. Phys.* **42** 175507
- [Makashev 1992] Makashev N K, Asmolov E S, Blinkov V V, Yu Boris A, Buzykin O G, Burmistrov A V, Gryaznov M R and Makarov V A 1992 Gas hydrodynamics of metal cutting by cw laser radiation in

a rare gas *Sov. J. Quantum Electron.* **22** 847-852

[Makashev 1994] Makashev N K, Asmolov E S, Blinkov V V, Yu Boris A, Burmistrov A V, Buzykin O G and Makarov V A 1994 Gas-hydro-dynamics of CW laser cutting of metals in inert gas *Proc. SPIE* **2257** 2-9

[Man 1999] Man H C Duan J and Yue T M 1999 Analysis of the dynamic characteristics of gas flow inside a laser cut kerf under high cut-assist gas pressure *J. Phys. D: Applied Physics* **32** 1469-1477

[Mas 2003-1] Mas C 2003 *Modelisation physique du procede de decoupe de metaux par laser*, Ph. D. Thesis L'Universite Paris 6 (Paris).

[Mas 2003-2] Mas C, Fabbro R and Gouedard Y 2003 Steady-state laser cutting modelling *J. Laser Applications* **15** 145-152

[Matsunawa 1985] Matsunawa A and Katayama S 1985 High speed photographic study of YAG laser materials processing *Proceedings of 4th Int. Congress on Applications of Lasers & Electro-Optics* (San Francisco) 41-48

[Matsunawa 1997] Matsunawa A and Semak V 1997 The simulation of front keyhole wall dynamics during laser welding *J. Phys. D: Appl. Phys.* **30** 798-809

[Michalowski 2007] A. Michalowski, A. Heß, A. Ruß, and F. Dausinger 2007 *Proceedings of LIM2007* 357-361

[Miyamoto 1991] Miyamoto I and Maruo H 1991 The mechanism of laser cutting *Welding in the World* **29** (9/10) 283-294

[Mueller 2010] Mueller S and Bratt C 2010 Laser Beam Welding in Sub-Atmospheric Pressure *Proc. of the 29th Int. Congress on Applications of Lasers & Electro-Optics* (Anaheim CA) 1806

[Muller 2012] Muller M, Fabbro R, El-Rabii H and Hirano K 2012 Temperature measurement of laser heated metals in highly oxidizing environment using 2D single-band and spectral pyrometry, *J. Laser Appl.* **24** 022006

[Mundra 1993] Mundra K and Debroy T 1993 Calculation of Weld Metal Composition Change in High-Power Conduction Mode Carbon Dioxide Laser-Welded Stainless Steels. *Metall Trans* **24B** 145-155

[Ness 2012] Ness T 2012 IPG's Growth in Asian Market and Product Strategy *In: Photonix2012 Conference* (Tokyo, Japan)

[Niziev 1993] Niziev V G 1993 Theory of CW Laser Beam Cutting *Laser Physics* **3** 629-634

[Niziev 1999] Niziev V G and Nesterov A V 1999 Influence of beam polarization on laser cutting efficiency *J. Phys. D: Appl. Phys.* **32** 1455-1461

[Onuseit 2011] Onuseit V, Ahmed M A, Weber R and Graf T 2011 Space-resolved Spectrometric Measurements of the Cutting Front *Physics Procedia* **12** 584-590

[Pang 2011] Pang S, Chen L, Zhou J, Yin Y and Chen T 2011 A three-dimensional sharp interface model for self-consistent keyhole and weld pool dynamics in deep penetration laser welding. *J. Phys. D: Appl. Phys.* **44** 025301

[Petring 1988] Petring D, Abels P and Beyer E 1988 The absorption distribution as a variable property during laser beam cutting *Proc. of the 7th Int. Congress on Applications of Lasers & Electro-Optics* 293-302

[Petring 1991] Petring D, Preißig K U, Zefferer H, and Beyer E 1991 Plasma effects in laser beam cutting *DVS-Berichte* **135** 12-15

[Petring 1994] Petring D 1994 *Anwendungsorientierte Modellierung des Laserstrahl-schneidens zur rechnergestützten Prozeßoptimierung*, Ph. D. Thesis RWTH Aachen (Aachen: Verlag Shaker)

[Petring 2005] Petring D 2005 Computer simulation of laser cutting for the limiting-value-oriented development of robust processes *Welding and cutting* **4** 37-42

[Petring 2008] Petring D, Schneider F, Wolf N and Nazery V 2008 The relevance of brightness for high power laser cutting and welding," *Proc. 27th Int. Congress on Applications of Lasers & Electro-Optics* (Temecula, CA) 95-103

[Podgorski 2001] Podgorski T, Flesselles J M and Limat L 2001 Corners, Cusps, and Pearls in Running Drops *Phys. Rev. Lett.* **87** 036102

[Poprawe 2010] Poprawe R, Schulz W and Schmitt R 2010 Hydrodynamics of material removal by melt expulsion: Perspectives of laser cutting and drilling *Physics Procedia* **5** 1-18

[Powell 1998] Powell J 1998 *CO₂ laser cutting 2nd ed.* (London: Springer-Verlag)

[Powell 2009] Powell J, Petring D, Kumar R V, Al-Mashikhi S O, Kaplan A F H and Voisey K T

- 2009 Laser oxygen cutting of mild steel: the thermodynamics of the oxidation reaction *J. Phys. D: Appl. Phys.* **42** 015504
- [Powell 2011] Powell J, Al-Mashikhi S, Kaplan A and Voisey K 2011 Fibre laser cutting of thin section mild steel: An explanation of the 'striation free' effect *Optics and Lasers in Engineering* **49** 188-194
- [PRIMES WEB] http://www.primes.de/produkte/foc_e.htm
- [Quintero 2005] Quintero F, Varas F, Pou J, Lusquinos F, Boutinguiza M, Soto R and Perez-Amor M 2005 Theoretical analysis of material removal mechanisms in pulsed laser fusion cutting of ceramics *J. Phys. D: Appl. Phys.* **38** 655-666
- [Riveiro 2011] Riveiro A, Quintero F, Lusquinos F, Comesana R and Pou J 2011 Study of melt flow dynamics and influence on quality for CO₂ laser fusion cutting *J. Phys. D: Appl. Phys.* **44** 135501
- [Samokhin 1990] Samokhin A A 1990 First-order phase transitions induced by laser radiation in absorbing condensed matter. In Proceedings of the Institute of General Physics (Ed. by Prokhorov A M), Vol. 13: Effect of laser radiation on absorbing condensed matter (Commack, Nova Science Publishers) pp.1-161
- [Schneider 2006] Schneider M 2006 *Perçage profond par laser: Analyse des processus physiques*, Ph. D. Thesis L'Universite Paris 6 (Paris).
- [Schulz 1989] Schulz W and Becker D 1989 On laser fusion cutting: The self-adjusting cutting kerf width *Proc. of SPIE* **1132** 211-221
- [Schulz 1993] Schulz W, Becker D, Franke J, Kemmerling and Herziger G 1993 Heat conduction losses in laser cutting of metals *J. Phys. D:Appl. Phys.* **26** 1357-1363
- [Schulz 1999] Schulz W, Kostykin V, Nießen M, Michel J, Petring D, Kreutz E W and Poprawe R 1999 Dynamics of ripple formation and melt flow in laser beam cutting *J. Phys. D:Appl. Phys.* **32** 1219-1228
- [Schuöcker 1986] Schuöcker D 1986 Dynamic phenomena in laser cutting and cut quality *Appl. Phys. B* **40** 9-14
- [Schuöcker 1987] Schuöcker D 1987 The physical mechanism and theory of laser cutting, in Industrial Laser Handbook, pp.65-79
- [Schuster 2009] Schuster R and Dinkelmann M 2009 Observation of evaporating surfaces and vapour flows at capillary front geometries *Proc. of the 5th International WLT-Conference on Lasers in Manufacturing* 783-786
- [Scintilla 2010] Scintilla L D, Tricarico L, Mahrle A, Wetzig A, Himmer T and Beyer E 2010 A comparative study on fusion cutting with disc and CO₂ lasers *Proceedings of 29th Int. Congress on Applications of Lasers & Electro-Optics* (Anaheim, CA) 249-258
- [Scintilla 2011] Scintilla L D, Tricarico L, Wetzig A, Mahrle A and Beyer E 2011 Primary Losses In Disk And CO₂ Laser Beam Inert Gas Fusion Cutting *Journal of Materials Processing Technology* **211** 2050-2061
- [Semak 1997] Semak V and Matsunawa A 1997 The role of recoil pressure in energy balance during laser materials processing *J. Phys. D:Appl. Phys.* **30** 2541-2552
- [Semak 1999] Semak V 1999 Transient model for the keyhole during laser welding *J. Phys. D:Appl. Phys.* **32** L61-64
- [Semak 2006] Semak V V, Knorovsky G A, MacCallum D O and Allen Roach R 2006 Effect of surface tension on melt pool dynamics during laser pulse interaction *J. Phys. D: Appl. Phys.* **39** 590-595
- [Solana 1997] Solana P and Ocana J L 1997 A mathematical model for penetration laser welding as a free-boundary problem *J. Phys. D: Appl. Phys.* **30** 1300-1313
- [Sullivan 1967] Sullivan A B J and Houldcroft P T 1967 Gas-jet Laser Cutting *British Welding Journal* **14** 443-445
- [Touvrey 2006] Touvrey-Xhaard C 2006 *Etude thermohydraulique du soudage impulsif de l'alliage TA6V*, Ph. D. Thesis L'Universite de Provence (Marseille)
- [Tritton 1977] Tritton D J 1977 *Physical Fluid Dynamics* (New York: Van Nostrand Reinhold) pp. 27-29
- [Trumpf WEB] <http://www.trumpf-laser.com/en/products/solid-state-lasers/disc-lasers/trudisc.html>
- [Tsai 1993] Tsai M-J and Weng C-I 1993 Linear stability analysis of molten flow in laser cutting *J. Phys. D: Applied Physics* **38** 719-727

- [Woods 1999] Woods K J and Parker R 1999 Two-Color Imaging Pyrometer Temperature Measurements of the Kerf Front During Laser Cutting *Proc. 18th Int. Congress on Applications of Lasers & Electro-Optics* 96-105
- [Wandera 2006] Wandera C, Salminen A, Olsen F O and Kujanpää V 2006 Cutting of stainless steel with fiber and disc laser *Proceedings of 25th Int. Congress on Applications of Lasers & Electro-Optics* (Scottsdale, AZ) 211-220
- [Wandera 2011-1] Wandera C and Kujanpää V 2011 Optimization of parameters for fibre laser cutting of a 10 mm stainless steel plate *Proceedings of the Institution of Mechanical Engineers, Part B: Journal of Engineering Manufacture* **225** 641-649
- [Wandera 2011-2] Wandera C, Kujanpää V and Salminen A 2011 Laser power requirement for cutting thick-section steel and effects of processing parameters on mild steel cut quality *Proceedings of the Institution of Mechanical Engineers, Part B: Journal of Engineering Manufacture* **225** 651-661
- [Ward 1984] Ward B A 1984 Supersonic characteristics of nozzles used with lasers for cutting *Proceedings of 3rd Int. Congress on Applications of Lasers & Electro-Optics* (Boston) 94-101
- [Weberpals 2008] Weberpals J and Dausinger F 2008 Fundamental understanding of spatter behaviour at laser welding of steel *Proceedings of 27th Int. Congress on Applications of Lasers & Electro-Optics* 364
- [Weberpals 2010-1] Weberpals J P 2010 *Nutzen und Grenzen guter Fokussierbarkeit beim Laserschweißen, Ph. D. Thesis Universität Stuttgart* (München: Herbert Utz Verlag)
- [Weberpals 2010-2] Weberpals J, Schuster R, Berger P and Graf T 2010 Utilization of Quantitative Measurement Categories for Process Monitoring *Proceedings of 29th Int. Congress on Applications of Lasers & Electro-Optics* (Anaheim, CA) 44-52
- [Vicanek 1987-1] Vicanek M, Simon G, Urbassek H M and Decker I 1987 Hydrodynamical instability of melt flow in laser cutting *J. Phys. D:Appl. Phys.* **20** 140-145
- [Vicanek 1987-2] Vicanek M and Simon G 1987 Momentum and heat transfer of an inert gas jet to the melt in laser cutting *J. Phys. D:Appl. Phys.* **20** 1191-1196
- [Von Allmen 1987] Von Allmen M 1987 *Laser-Beam Interactions with Materials* (Berlin, Springer)
- [Vossen 2010] Vossen G, Schüttler J and Nießen M 2010 Optimization of Partial Differential Equations for Minimizing the Roughness of Laser Cutting Surfaces In *Recent Advances in Optimization and its Applications in Engineering* (M. Diehl *et al.* (eds.), Springer-Verlag, Berlin/Heidelberg, 2010), pp. 521-530
- [Yudin 2007] Yudin P and Kovalev O 2007 Visualization of events inside kerfs during laser cutting of fusible metal *Proc. 26th Int. Congress on Applications of Lasers & Electro-Optics* 772-779
- [Yudin 2009] Yudin P and Kovalev O 2009 Visualization of events inside kerfs during laser cutting of fusible metal *J. Laser Appl.* **21** 39-45
- [Zaitsev 2005] Zaitsev A V, Kovalev O B, Orishich A M and Fomin V M 2005 Numerical analysis of the effect of the TEM₀₀ radiation mode polarization on the cut shape in laser cutting of thick metal sheets *Quantum Electronics* **35** 200-204
- [Zefferer 1991] Zefferer H, Petring D and Beyer E 1991 Investigation of the gas flow in laser beam cutting *DVS-Berichte* **135** 210-214
- [Zhao 2003] Zhao H and DebRoy T 2003 Macroporosity free aluminum alloy weldments through numerical simulation of keyhole mode laser welding *J. Appl. Phys.* **93** 10089

List of publications

Publications in journals with peer reviews

- K. Hirano and R. Fabbro, "Experimental investigation of hydrodynamics of melt layer during laser cutting of steel", *Journal of Physics D: Applied Physics* **44** (2011) 105502.
- K. Hirano, R. Fabbro and M. Muller, "Experimental determination of temperature threshold for melt surface deformation during laser interaction on iron at atmospheric pressure", *Journal of Physics D: Applied Physics* **44** (2011) 435402.
- K. Hirano and R. Fabbro, "Possible explanations for different surface quality in laser cutting with 1 μm and 10 μm laser wavelengths", *Journal of Laser Applications* **24** (2012) 012006.

Participations in international conferences (Oral presentations)

- K. Hirano and R. Fabbro, "Study of fundamental aspects of thick section laser cutting", 12th International workshop on process stability in laser beam welding, 10-12 Feb 2010, Söllerhaus, Hirschegg, Austria.
- K. Hirano and R. Fabbro, "Visualisation of hydrodynamic instabilities during laser cutting of steel - Mechanism of striation generation", 13th International workshop on process stability in laser beam welding, 9-11 Feb 2011, Söllerhaus, Hirschegg, Austria.
- K. Hirano and R. Fabbro, "Experimental observation of hydrodynamics of melt layer and striation generation during laser cutting of steel", The 6th International WLT-Conference on Lasers in Manufacturing, 23-26 May 2011, Munich, Germany.
- K. Hirano and R. Fabbro, "Study on striation generation process during laser cutting of steel", The 30th International Congress on Applications of Lasers & Electro-Optics (ICALEO), 23-27 Oct 2011, Orlando, FL, USA.
- K. Hirano, R. Fabbro and M. Muller "Temperature dependence of recoil pressure during laser material processing", The 77th Laser Materials Processing Conference, Japan Laser Processing Society, 24-25 May 2012, Osaka, Japan.

Etude des mécanismes de génération des stries dans le procédé de découpe laser d'aciers

RESUME : Ce travail a pour objectif d'étudier les mécanismes de génération des stries habituellement observées lors de la découpe laser de l'acier, avec un gaz inerte. En dépit de son importance scientifique et surtout industrielle, l'origine de ce mécanisme est inconnue depuis la mise au point de ce procédé laser. Nous avons tout d'abord étudié expérimentalement l'hydrodynamique du métal fondu le long du front de découpe en utilisant une caméra video rapide. L'observation par la face supérieure de l'échantillon a montré pour la première fois l'origine de la génération de ces instabilités de l'écoulement du liquide métallique, qui présente deux types de discontinuités caractéristiques : la présence de « humps » dans la partie centrale de la saignée et d'accumulations de liquide, sur les côtés de la saignée. On observe clairement que les stries latérales sont générées périodiquement et résultent du déplacement vertical vers le bas, de ces accumulations de liquide produites le long des côtés de la saignée. L'observation transverse du front avant de la saignée (à l'aide d'une visualisation latérale, à travers une lame de verre simulant un côté de la saignée) montre également que les « humps » de la partie centrale peuvent perturber la dynamique du mouvement de ces accumulations de liquide et contribuer à la dégradation de la qualité des stries. L'origine de ces instabilités est ensuite discutée. Les caractéristiques des 2 types instabilités observées peuvent être expliquées d'une façon cohérente par un seul mécanisme lié à la tension superficielle du liquide métallique. Les stries sont ainsi créées par la fusion locale de la surface du solide en raison du transfert de chaleur à partir de ces accumulations de liquide. La rugosité finale de la surface a pu être estimée à partir d'une analyse du transfert de chaleur de ces accumulations, et est en accord satisfaisant avec les resultants expérimentaux. Finalement, à partir de ce modèle de la génération des stries, nous pouvons expliquer la différence observée de la qualité de la découpe lors de l'emploi de lasers de longueurs d'onde différentes, à 1 micron et à 10 microns. Nous mettons ainsi en avant les deux facteurs qui peuvent influencer cette dépendance avec la longueur d'onde: la stabilité de l'écoulement du liquide dans la partie centrale, qui est contrôlée par la loi d'absorption laser locale, et l'importance de l'absorption du rayonnement laser sur les accumulations du liquide le long des parois de la saignée. La validité de chacun de ces mécanismes est confirmée par une modélisation analytique des processus physiques impliqués.

Mots clés : découpe laser, hydrodynamique, stries

Study on striation generation process during laser cutting of steel

ABSTRACT : This study investigates the mechanism of striation generation in inert gas laser cutting of steel. In spite of its scientific and industrial importance, the mechanism has remained unknown for several decades. First, hydrodynamics of molten liquid on a kerf front is experimentally observed using a high speed video camera. Observation from the above of a sample reveals for the first time generation of melt flow instabilities from the sample surface. Unstable melt flow involves molten droplets: so called humps and melt accumulations, in the central and side parts of the kerf front, respectively. It is clearly observed that striations are generated by periodic generation and downward displacement of the melt accumulations along kerf sides. Lateral observation of a kerf front through a glass plate demonstrates that also humps in the central part can disturb the dynamics of the melt accumulations and degrade quality of striations. Then the origin of the observed instabilities is discussed. Characteristics of the melt flow instabilities observed both in the central and side parts can be explained coherently by a unique mechanism related to surface tension. We consider that striations are created by local melting of solid surface due to heat transfer from the melt accumulations. Surface roughness is theoretically predicted by a heat transfer analysis and the result roughly agrees with experimental results. Finally, using the newly revealed mechanism of striation generation, we discuss an interesting topic of cut surface quality difference between 1 and 10 microns laser wavelengths. We propose two factors which can cause the wavelength dependence: stability of melt flow in the central part and absorptivity of laser beam on melt accumulations along the kerf sides. The validity of each mechanism is confirmed by analytical modelling of related physical processes.

Keywords : laser cutting, hydrodynamics, striations